Freie Universität Berlin

HZB Helmholtz Zentrum Berlin

Silicon heterojunction solar cells:

From conventional concepts to a singlet fission multi-exciton generating hybrid approach

im Fachbereich Physik der
Freien Universität Berlin eingereichte

Dissertation

zur Erlangung des akademischen Grades
Doktor der Naturwissenschaften
- Dr. rer. nat. -

vorgelegt von M.Sc.

Martin Lutz Liebhaber

2017

Erstgutachter: (Betreuer)	Prof. Dr. Klaus Lips
Zweitgutachter:	Prof. Dr. Bernd Rech

Disputation am: 09.03.2017

"Ask not what your planet can do for you.
Ask what you can do for your planet."

- freely adapted from John F. Kennedy -

Contents

1 Introduction

It is predicted that the world's energy consumption will be nearly doubled in the next 30 years [5]. Therefore, it is a daunting task for mankind to solve this global energy challenge; providing sustainable energy doubly so. Besides wind, hydro, biomass, solarthermics, and some other niche technologies, photovoltaics (PV) plays an important role in the renewable energy mix. The pioneer programme of Germany, well known as the *"Energiewende"*, demonstrates already impressive results. In 2015, about 33% of Germany's electricity demand was delivered by renewable sources, whereby PV covered about 7% with 39.6 GWp installed [99].
With silicon (Si) being the most abundant inorganic semiconductor material, the PV market is dominated by crystalline silicon (c-Si) wafer based technologies. Both, multi and mono c-Si technologies together accounted for about 93% of the global market share in 2015 [99].
The first practical solar cell was presented by *Bell Laboratories* in 1954, based on Si, yielding an efficiency of $\sim$6% [56]. For mono c-Si technologies with diffused p/n-junctions the current record efficiency of this mature technology is 25.3% [123, 109].

By the turn of the millennium, *Sanyo* entered the market with the promising high-efficiency amorphous/crystalline Si heterojunction (SHJ) technology and reported device efficiencies exceeding 20% [291]. Instead of relying on a diffused p/n-homojunction, the SHJ approach uses doped and hydrogenated amorphous silicon (a-Si:H) layers. A full-area high quality passivation with minimal interface recombination losses is provided by implementing a thin intrinsic a-Si:H passivation layer in between the doped a-Si:H emitter and the c-Si absorber. Front contacting layers have to be as transparent as possible within the solar spectrum range to minimize parasitic absorption losses. This is achieved by (i) fabricating contact layers as thin as possible, and/or (ii) replacing conventional a-Si:H and transparent conductive oxide (TCO) contact layers with wider band gap materials such as Si carbide [343, 36] or Si oxide [102, 83, 262, 185] and MoO_x or WoO_x layers [35, 24, 191]. Another route might be the replacement of costly fabricated inorganic materials by cheaply, solution-processable organic materials [341, 232, 138].
By fabricating an interdigitated back contact (IBC) SHJ solar cell, the efficiency of this technology could be boosted to the current world record of 26.33% for single-junction c-Si based PV, reported by *Kaneka* in 2016 [91, 338].

The technological key aspect is to minimize the costs of electricity of a PV system. As a rule of thumb, a 1%-point efficiency gain justifies ∼25% higher cell processing costs [206, 123]. This points out the current PV trend towards high-efficiency technologies.

26.33% is already within ∼3% points of the fundamental single-junction limit which is determined by the band gap of the absorber material and the solar spectrum. For photon energies (E_{phot}) higher than the band gap (E_{g}), the excess energy is converted into heat by thermalization of excited charge carriers, while light with sub-band gap energies is not absorbed [267]. A theoretical limit for single-junction solar cells was first formulated by W. Shockley and H. J. Queisser in 1961, assuming black-body radiation from the sun (6000 K), perfect absorption and only taking into account the band gap and radiative recombination losses (so-called detailed balance calculation) yielding an efficiency limit of 30% for c-Si based solar cells at 25 °C [267]. In the latest calculation using the AM1.5G solar spectrum and taking Auger recombination – being a dominant intrinsic recombination mechanism in c-Si– into consideration, A. Richter et al. predicted an efficiency limit of 29.43% [243]. To circumvent the single-junction limit several technological strategies have been put forward.

The most obvious approach is to minimize thermalization and transmission losses by introducing absorber layer stacks with successively decreasing band gaps, thus absorbing different portions of the incident sun light in each layer [115]. This multi-junction concept is already successfully realized in III-V solar cell structures, since band gap engineering is relatively easy for III-V semiconductor compounds. By 508-fold light concentration onto a 4-junction device, the absolute world record for solar cell power conversion efficiency of 46.0% was reported by the *Fraunhofer ISE* in 2014 [98]. The fabrication of these multi-junction cells requires lattice matching layers and cost-intensive materials and fabrication. Large-scale unconcentrated installations are not yet competitive at modern latitudes.

For that reason, further concepts are needed which can tackle the single-junction limit, but at the same time rely on materials and processes compatible with large-scale production. Ideally, such high-efficiency concepts can easily be adapted to mature technologies, such as silicon PV.

In the last few years perovskite solar cells attracted much attention [166]. Especially their combination with c-Si based solar cells is a promising high-efficiency concept [187]. A big advantage of perovskites is that their band gap can be tuned to perfectly match c-Si. A monolithic perovskite/c-Si-heterojunction tandem solar cell with an efficiency of 19.9% is reported [10]. Efficiencies well above 30% are predicted by optical simulations [181, 9].

Combining solar cells with materials facilitating spectral conversion of light, i.e. photon upconversion (UC) or photon-induced multiple exciton generation (MEG) is an alternative route for high-efficiency photovoltaics.
Transmission losses can be reduced in UC enhanced devices which can harvest unused subthreshold photons by creating one higher-energy photon out of (at least) two photons in the UC medium. Up-converted light with $E_{\mathrm{phot}} > E_{\mathrm{g}}^{\mathrm{abs}}$ can then be harvested in the solar cell's main absorber, thus expanding the usable solar spectrum [259].
In the MEG concept the absorption of one high energy photon creates multiple excitons of lower

energy which then have to migrate to an interface to be harvested there. Thus, thermalization losses are reduced. The MEG medium has to be implemented on the device front side.
Combining both, photon up-conversion and photon-induced multi-exciton generation, Shpaisman et al. calculated a theoretical upper power conversion efficiency limit for non-concentrated single-junction PV of 49% [269].
For c-Si solar cells under AM1.5G illumination, multi-exciton generation has a theoretically larger potential in terms of efficiency gain than up-conversion [269]. There are two prominent approaches for photon-induced MEG:

(i) Inorganic colloidal Si nanocrystals [29] or quantum dots of compositions, e.g. PbSe, PbTe, CdS, InAs. A successful integration of PbSe quantum dots into solar cells exceeding 100% external quantum efficiency is reported [263, 207, 208, 27, 28].

(ii) Singlet fission (SF), a spin allowed process that splits a singlet exciton (S_1), created via absorption of a high energy photon, into a pair of two lower energy triplet excitons (T_1) with no, or only marginal loss of energy [276].

Singlet fission occurs in some organic molecular chromophores with the polyacenes anthracene, tetracene (Tc) and pentacene (Pc) being the most prominent candidates and extensively studied in the last decades [276]. Although singlet fission with $2E(T_1) \approx E(S_1)$ can ideally double the photocurrent, it also halves the potential voltage. Therefore, to increase solar cell efficiencies in a hybrid approach the triplet energy of the SF material has to match the band gap of the long wavelength absorber.
Tc with its triplet energy E_T^{Tc} = 1.25 eV [310, 54] is currently the most promising candidate which matches the band gap energy E_g^{Si} = 1.12 eV of c-Si [288]. Theoretically, Tc/c-Si hybrid solar cell efficiencies of $\sim$35% - 40%, therefore well above the single-junction limit of 29.43% [243], are predicted [269, 119, 300, 302, 301]. The most important prerequisites for a successful integration of a SF material into c-Si based solar cells are:

(i) Sufficiently good surface passivation quality of the hybrid Tc/c-Si interface.

(ii) Lifetime and diffusion length for triplet excitons created via singlet fission have to be long enough to reach the hybrid interface.

(iii) Efficient charge separation, i.e. dissociation of tightly bound triplet excitons in the organic layer at the hybrid interface.

(iv) Finally, separated free charge carriers have to be extracted via selective contacts.

The MEG concept introduced in this thesis is based on the direct harvesting of triplet excitons created via singlet fission, thus omitting additional loss channels which inherently arise in spectral down-conversion approaches where re-emission by phosphorescent emitters and radiative coupling of the down-converted light into devices is the underlying principle [147, 309].
The proof of principle for SF devices is already reported. Multi-exciton generation via singlet fission and direct exciton harvesting has been observed in low efficiency purely organic devices, e.g. Refs. [134, 64, 328], as well as in hybrid organic-inorganic nanocrystal systems, e.g. Refs. [133, 86, 172, 290, 307]. However, for a real breakthrough SF materials have to be implemented

on c-Si based devices, being the major PV technology at least in the midterm future.
The idea to use organic thin layers to sensitize inorganic absorbers was already proposed in 1979 by D. L. Dexter [82], but since conventional silicon PV technologies are reaching the theoretical limit, the interest in potential approaches to surpass this limit was renewed in the last few years.

Strategies followed in this work

Within the scope of this thesis conventional SHJ concepts, both, (i) inorganic amorphous/crystalline Si heterojunctions, and (ii) the novel hybrid PEDOT:PSS/c-Si junction were investigated. In the second part of this work the SF material Tc was incorporated in a c-Si based hybrid device structure.

One possibility to further improve the conventional high-efficiency SHJ technology is to reduce losses due to parasitic light absorption in the a-Si:H and TCO layers. To that end, potential wide band gap Si alloys, in particular amorphous Si suboxides (a-SiO_x:H) were investigated in the first part of this thesis. As there is a trade-off between widening the band gap and concomitantly increasing band offsets, measuring the valence band offset, ΔE_V, at the heterojunction which strongly influences hole extraction, was central to the study. By fabricating solar cells with identical prepared SHJs, ΔE_V is directly related to device performance. With this, hole transport mechanisms can be discussed.

Recently, it was reported that the polymer PEDOT:PSS is a promising organic hole selective contact which forms a hybrid p^+n-heterojunction with n-type c-Si [138]. Since PEDOT:PSS is highly conductive, no TCO layers are needed for efficient charge carrier extraction. However, comparatively high parasitic absorption and reflection losses are reported which significantly hamper device performance [348]. Within this thesis also the PEDOT:PSS/c-Si heterojunction was investigated in great detail. A complete band diagram of the hybrid junction was constructed. Moreover, hybrid interface formation and passivation quality was investigated. By fabricating hybrid devices with a PEDOT:PSS/c-Si front and a superior electron selective back contact adopted from the inorganic SHJ technology, the potential of PEDOT:PSS as a hole selective contact for n-type c-Si is discussed.

The objective of the second part of this thesis is to reduce the fundamental thermalization losses via multi-exciton generation by the incorporation of the SF material Tc being a promising candidate since its triplet energy matches the band gap of c-Si [310, 288]. A device architecture using PEDOT:PSS as the hole contact implemented on top of a hybrid thin film Tc/c-Si wafer absorber layer stack is introduced. The major challenge in this approach is to harvest the tightly bound triplet excitons created via singlet fission in the organic part at the hybrid interface to inorganic c-Si. Theoretically this concept features the prospect to surpass the single p/n-junction efficiency limit [269].

Furthermore, the potential of various hybrid device concepts were studied by optical simulations on real device layer stacks using experimentally derived (*n-k*) data sets. Within a basic model the potential of MEG via singlet fission in the proposed device architecture is derived. Moreover, optical losses due to reflection and parasitic absorption can be quantified and are discussed.

In brief, this thesis is structured as follows:

Chapter 2 introduces the basics of solar cell operation, loss mechanisms and selective heterocontacts. The SF process and possible triplet harvesting mechanisms are outlined. Furthermore, c-Si based SF device concepts are introduced.

Chapter 3 gives experimental details of device fabrication and various analysis methods utilized throughout this work.

Chapter 4 reports on the measured band alignment at a-SiO_x/c-Si (for $0 \leq x \lesssim 2$) heterojunctions and discusses the potential of wide band gap a-SiO_x passivation layers incorporated in conventional SHJ solar cells. The hole transport across the SHJ with varying ΔE_V is discussed.

Chapter 5 discusses the potential of various hybrid device concepts studied by optical simulations: (i) hybrid PEDOT:PSS/c-Si heterojunction solar cell; (ii) proposed MEG solar cell by the incorporation of the singlet fission material Tc in a c-Si based hybrid device structure.

Chapter 6 reports on experimental results of the novel PEDOT:PSS/c-Si organic-inorganic heterojunction. A band diagram is constructed and the buried hybrid interface formation is investigated. Herewith, the potential of the PEDOT:PSS/c-Si solar cell concept is discussed.

Chapter 7 presents thin film Tc morphology and singlet fission dynamic studies, as well as PEDOT:PSS/Tc/c-Si solar cell results. Furthermore, challenges of exciton harvesting at the hybrid Tc/c-Si junction are discussed.

The thesis closes with a **conclusion and outlook**. A short **abstract** in English and German is placed at the end.

2

Conventional heterojunction and singlet fission multi-exciton generating solar cells

With a solar cell sunlight is directly converted into electricity. By absorbing light in a semiconductor electrons are lifted over the band gap creating **electron-hole pairs, so-called excitons**. These electrically neutral quasi-particles, consisting of bound electron-hole pairs, are attracted to each other by electrostatic Coulomb forces. Therefore, excitons can transport energy without transporting net electric charges [230, 253].

Inorganic semiconductors generally exhibit high dielectric constants ($\epsilon_r > 10$) resulting in a screening of electric fields and thus, the Coulomb interaction between electrons and holes is reduced. This type of excitons are called **Wannier-Mott excitons**[1]. Typically Wannier-Mott excitons have binding energies in the order of 0.01 eV and large exciton radii of $\sim$100 $\mathring{A}$. Therefore, in most inorganic semiconductors Wannier-Mott excitons are immediately split into free charge carriers at room temperature [59]. Those free charges then can be separated via charge carrier selective contacts (cf. section 2.1).

On the contrary, **organic semiconductors** have a small dielectric constant ($\epsilon_r < 4$), so that the charges are much more tightly bound with binding energies between 0.1 - 1 eV and exciton radii of $\sim$10 $\mathring{A}$. This type of excitons are called **Frenkel excitons**[2]. Binding energies are much larger than k_BT at room temperature (0.025 eV). Thus, Frenkel excitons do not separate easily, i.e. an electron lifted into the lowest unoccupied molecular orbital (LUMO) is still coulombically bound to the corresponding hole in the highest occupied molecular orbital (HOMO). Frenkel excitons have to diffuse to an appropriate heterointerface, a so-called donor-acceptor junction, to be split into free charges [59] (cf. section 2.2).

[1] named after Gregory Wannier and Sir Nevill Francis Mott
[2] named after Yakov Frenkel

Finally, in all kinds of solar cells separated free charge carriers are collected at the metal contacts, generating the photocurrent. Solar cells are diodes under light illumination. The current-voltage, $j(V)$, curve can be described by the diode equation [288, 327, 274]:

$$j(V) = j_0 \cdot \left[exp\left(\frac{eU}{n_d k_B T}\right) - 1 \right] - j_{\mathrm{ph}}\,, \tag{2.1}$$

with the ideality factor n_d accounting for small deviations compared to an ideal diode. Fundamental solar cell parameters can be extracted from the $j(V)$-characteristics. The short-circuit current density $j_{\mathrm{sc}} \equiv j(V=0) = j_{\mathrm{ph}}$ is trivially determined, the open-circuit voltage, V_{oc}, can be deduced by solving Equation (2.1) for $j(V_{\mathrm{oc}}) = 0$:

$$U(j=0) \equiv V_{\mathrm{oc}} = \frac{n_d k_B T}{e} \cdot ln\left(\frac{j_{\mathrm{ph}}}{j_0} + 1\right) \approx \frac{n_d k_B T}{e} \cdot ln\left(\frac{j_{\mathrm{ph}}}{j_0}\right)\,, \tag{2.2}$$

where the approximation is justified because $j_{\mathrm{ph}} \gg j_0$. It is obvious from Equation (2.2) that V_{oc} is limited by the recombination current density, j_0 (also called dark saturation current). Therefore, V_{oc} directly reflects absorber and interface passivation quality [66]. The solar cell's fill factor, FF, is given by the ratio between the output power at the maximum power point $P_{max} = V_{\mathrm{mpp}} \cdot j_{\mathrm{mpp}}$ and the product of V_{oc} and j_{sc}:

$$\mathrm{FF} = \frac{V_{\mathrm{mpp}} \cdot j_{\mathrm{mpp}}}{V_{\mathrm{oc}} \cdot j_{\mathrm{sc}}}\,. \tag{2.3}$$

Lastly, the power conversion efficiency of the solar cell can be calculated by dividing its maximum power output by the incident power of light

$$\eta = \frac{V_{\mathrm{mpp}} \cdot j_{\mathrm{mpp}}}{P_{\mathrm{in}}} = \mathrm{FF} \cdot \frac{V_{\mathrm{oc}} \cdot j_{\mathrm{sc}}}{P_{\mathrm{in}}}\,. \tag{2.4}$$

Fundamental solar cell loss mechanisms

During charge generation, **thermalization and transmission losses** dominate the fundamental losses of single-junction photovoltaic devices resulting in an efficiency limit of ∼30% for c-Si based solar cells [267, 243].

Optical losses due to **parasitic light absorption** in various contact layers and **back reflection** of incident light decreases the fraction of incident photons reaching the main absorber and therefore lowers solar cell's j_{sc}. Obviously, to minimize parasitic absorption, contact layers have to be as thin as possible while maintaining essential layer functionalities. Reflection losses can be minimized by suitable anti-reflection (AR) coatings. A trade-off between layer thicknesses and AR behavior determines a minimum of optical losses for a given layer stack. Additionally, reflection losses can be drastically reduced by textured surfaces [274].

By various **recombination processes** the generated excess charge carrier density is reduced, reflected in j_0, and therefore solar cell's V_{oc} is decreased (cf. Eq. (2.2)). Depending on the

properties of the specific absorbing semiconductor material, different types of recombination will be more or less significant. Recombination mechanisms important for c-Si based solar cells can be divided into intrinsic radiative and non-radiative Auger recombination –i.e. processes that also take place in pure and defect-free semiconductors– and extrinsic processes evoked by defects and commonly described by the Shockley-Read-Hall (SRH) formalism. As rates corresponding to different recombination processes add up, the total effective charge carrier lifetime, τ_{eff}, is determined by the sum of all recombination processes. Obviously τ_{eff} is dominated by the fastest recombination process [327, 274]:

$$\frac{1}{\tau_{\text{eff}}} = \sum_i \frac{1}{\tau_i} = \underbrace{\frac{1}{\tau_{\text{rad}}} + \frac{1}{\tau_{\text{Auger}}}}_{\text{intrinsic}} + \underbrace{\frac{1}{\tau_{\text{SRH}}} + \frac{1}{\tau_{\text{surface}}}}_{\text{extrinsic}} . \tag{2.5}$$

Radiative recombination is the spontaneous relaxation of an excited electron from the conduction band back into the valence band. The energy is conserved by radiative emission. The rate constant for c-Si is rather low, as the involvement of phonons is required to fulfill momentum conservation for indirect band gap c-Si. Furthermore, the probability depends on excess carrier concentrations which are comparably low for commonly used doping concentrations $< 10^{17}$ cm^{-3}, resulting in radiative lifetimes $\tau_{\text{rad}} > 10^{-3}$ s [317].

Auger recombination becomes important, especially in indirect semiconductors such as c-Si. In this process, the excess energy and momentum resulting from a recombination event involving an electron and a hole is transferred to a third (quasi)particle which then successively transfers the energy into lattice vibrations (thermalization loss). The Auger recombination rate depends on doping concentration and significantly affects c-Si solar cell efficiencies [84, 153, 327, 274]. Nevertheless, it is an intrinsic process and cannot be prevented.

Non-radiative recombination that can be described by the **SRH model** [268, 117] is facilitated by recombination centers such as impurity atoms or lattice defects which introduce allowed energy levels within the forbidden gap acting as trap states. It is a two-step process with a successive capture of the electron and hole into the trap state whereby the excess energy is dissipated into lattice vibrations.

Surface recombination – The processes introduced so far are bulk related with fixed rates given by semiconductor properties and material quality. However, SRH-like defect recombination is strong at surfaces and interfaces. At the surface many valence electrons cannot find a partner to create covalent bonds resulting in dangling bonds. These surface trap states are roughly situated in the middle of the band gap, thus constituting ideal recombination-active defects. Especially for high efficiency devices using best quality c-Si wafers, recombination losses might be dominated by surface recombination [288, 327, 213, 174].

Lastly, **resistive effects** in solar cells reduce their efficiency by dissipating power. The most common parasitic resistances are the **series resistance** R_s and the **shunt resistance** R_{sh} [288].

2.1 Silicon heterojunctions

A heterojunction is basically characterized by its selectivity and passivation. The selectivity is provided by the potential barrier present for one type of charge carriers at the junction. A high interface passivation quality has to be ensured to minimize interface recombination losses.
The basic structure of an amorphous/crystalline silicon heterojunction (SHJ) solar cell is depicted in Figure 2.1 (a). The key for the very high power conversion efficiencies obtained in SHJ devices is the separation of the highly recombination-active (ohmic) metal contacts from the c-Si absorber [72, 23]. An excellent full-area surface passivation can be achieved by implementing thin layers of intrinsic a-Si:H. Thus, compared to defect rich diffused p/n-homojunctions, the overall defect density in the heterojunction can be drastically reduced resulting in minimized interface recombination and therefore high charge carrier lifetimes (cf. Eq. (2.5)). For charge separation a p-doped a-Si:H emitter layer is deposited on top of the passivation layer. A sketch of the corresponding band line-up of the hole selective SHJ front contact is given in Figure 2.1 (b). Due to the slightly difference of about 0.5 - 0.7 eV in the band gaps of a-Si:H and c-Si, band offsets between the conduction band (ΔE_C) and valence band (ΔE_V) are imposed at the SHJ. To ensure efficient separation of excess charge carriers, a large band bending (eφ) in the c-Si absorber, also called built-in potential (Ψ_{bi}), is essential. To achieve that in homojunction solar cells, doping concentrations have to be maximized. This leads to an increased (Auger) recombination and correspondingly V_{oc} is limited for highly doped emitter regions in c-Si homojunction devices. However, by introducing a heterojunction, comparably low doping concentrations in the c-Si absorber of about 10^{15} - 10^{16} cm^{-3} are acceptable to obtain sufficient Ψ_{bi} values. This leads to much higher minority carrier lifetimes in the c-Si bulk, being the second requirement besides the excellent surface passivation to obtain very high open-circuit voltages. Values up to 750 mV [292], which is already close to the maximum theoretical value of 769 mV, predicted by M. A. Green [114], and about 50 mV higher than the best Si homojunction solar cells are reported. On the SHJ solar cell's back side, an (i/n^{++})a-Si:H layer stack is implemented, acting as a back surface field (BSF) to ensure efficient electron (majorities) extraction [72, 294]. Since the a-Si:H layers have comparatively low conductivities which are not sufficient for loss-free carrier transport towards the metal grid fingers, transparent conductive oxides (TCO) are needed. Besides the electrical conductivity, TCOs with optimized thicknesses, can simultaneously act as anti-reflective coatings [72, 130]. Commonly indium tin oxide (ITO) [130] or aluminum doped zinc-oxide (AZO) [244] is used. Solar cells are completed by metal contacts.

Surface passivation by (i)a-Si:H – Intrinsic hydrogenated amorphous silicon thin films deposited on accurately cleaned c-Si wafers[3] reveal a very good and stable chemical passivation of electronic defect states (Si dangling bonds) at the a-Si/c-Si interface [218, 182]. The majority of dangling bonds can be passivated by covalent Si-Si bonds, whereby the remaining ones can be saturated by hydrogen provided in the (i)a-Si:H [103, 257]. During post-annealing steps additional thermal energy may provoke reorganization and diffusion of hydrogen close to the interface, thus further improving the interface passivation quality [256, 75, 197, 254, 85]. Moreover, an atomically sharp a-Si:H/c-Si interface is essential for a high quality passivation [73, 105, 334].

[3] standard RCA cleaning procedure and a HF-dip prior to deposition to strip off native oxide (cf. section 3.1)

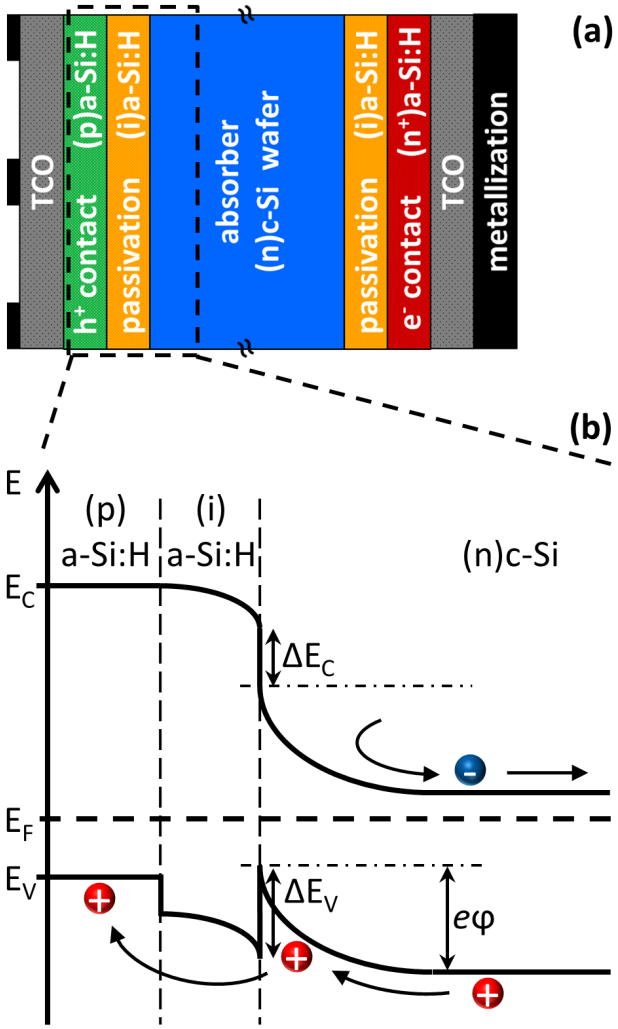

Figure 2.1: (a) Basic structure of an a-Si:H/c-Si heterojunction (SHJ) solar cell consisting of a c-Si absorber and well passivated charge carrier selected contacts formed by hydrogenated intrinsic and doped a-Si:H layer stacks. Charge carriers are extracted via TCO/metal contacts. (b) Band line-up of the hole selective hetero front contact. Electrons are repelled at the SHJ due to the potential barrier imposed by the band bending ($e\varphi$) and the conduction band offset (ΔE_C). Holes can be transferred across the (i)a-Si:H passivation layer to the (p)a-Si:H emitter to be collected at the TCO/metal front contact.

To fulfill those conditions, plasma enhanced chemical vapor deposition (PECVD) parameters have to be carefully adjusted. The excellent passivation with effective lifetimes in the range of several ms [80, 72] is a cornerstone for the high-efficiency SHJ technology.

Parasitic absorption in a-Si:H – However, besides the excellent selectivity and surface passivation with low recombination rates enabling high open-circuit voltages, a drawback of a-Si:H layers implemented on the front side of solar cells is a comparable high current loss due to parasitic absorption. Loss mechanisms in the amorphous silicon layers[4] include both, absorption that does not create an electron-hole pair (e.g. free-carrier absorption) and recombination before collection. The latter one is caused by the dangling bond defects in the amorphous materials, resulting in a-Si:H bulk lifetimes lower by orders of magnitudes than c-Si bulk lifetimes for typical dangling bond concentrations. Therefore, excess charge carriers generated in the a-Si:H layers recombine before they can be extracted. On device level, this has been proven experimentally by varying a-Si:H layer thicknesses [235, 105, 294, 140, 215]. In a modeling study, Z. C. Holman et al. predict a current loss of about 1 mA/cm^2 for a typical (i)a-Si:H layer thickness of 5 nm [129]. Obviously, to minimize parasitic absorption losses, a-Si:H layer thicknesses have to be as thin as possible while maintaining essential layer functionalities. In a study of H. Fujiwara and M. Kondo, a minimum i-layer thickness of 4 nm to obtain sufficient interface passivation was determined, whereas the p-layer thickness can be as thin as 3 nm [104]. Further improvements require the development of either new materials with reduced parasitic absorption or new structures that break away from the conventional SHJ design.

2.2 Donor-acceptor interface

As discussed previously, absorption of a photon with $E_{\mathrm{phot}} \geq E_{\mathrm{LUMO}}$ - E_{HOMO} in organic semiconductors results in a tightly bound electron-hole pair. To overcome the binding energy of the exciton and generate free charge carriers in an organic solar cell requires the use of a heterointerface [295, 59, 77]. Figure 2.2 depicts the energy level diagram of a so-called organic donor-acceptor junction. An oversimplified current photogeneration process is sketched in Figure 2.2 (a). The electron cannot be simply transferred across the interface into the acceptor since it is tightly bound to the hole remaining in the donor molecule, as indicated by the full-line oval. However, it is generally agreed that the initial charge separation step can be achieved by utilizing a suitable energy offset between the donor and acceptor LUMO levels. As illustrated in Figure 2.2 (b), enabling the initial electron transfer requires that the LUMO level energy offset is larger than the Coulomb binding energy of the exciton E_B^{exc}. Thus, the formation of an intermediate interfacial electron-hole pair, usually called charge-transfer (CT) state has to be energetically downhill. In a second step (not depicted in Fig. 2.2 (b)) CT states may split into separated electrons and holes which can then diffuse to the contacts to be extracted. OPV devices with near unity quantum yields of photocurrent generation are reported, suggesting that the interfacial CT state is not tightly bound ($E_B^{\mathrm{CT}} < E_B^{\mathrm{exc}}$), as indicated by the dashed-line oval [59].
CT states must overcome their Coulomb interaction in order to generate free charge carriers.

[4] especially pronounced in doped a-Si:H

If dissociation does not take place within the lifetime of the CT state, geminate recombination, which is known to be a significant loss mechanism in organic solar cells, may occur. The competition between dissociation of the CT state and its recombination back to the ground state depends upon the magnitude of the interfacial Coulombic attraction [214, 37, 59].

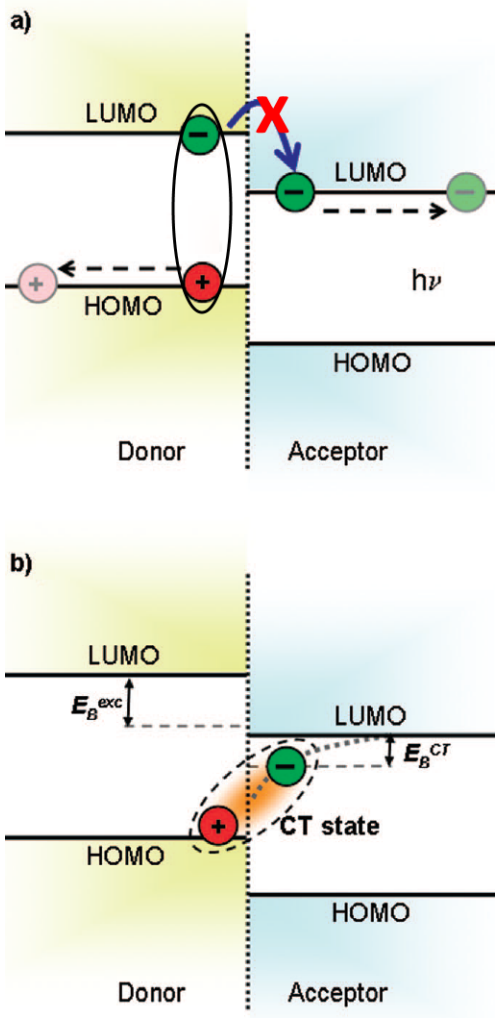

Figure 2.2: Energy level diagram of a donor-acceptor interface. (a) Sketch of an oversimplified current photogeneration process. Direct electron transfer from the donor into the acceptor LUMO is not expected due to the large binding energy of the exciton, indicated by the full-dashed oval. (b) Illustration of the formation of an intermediate interfacial charge-transfer (CT) state. The energy of this state depends upon the Coulomb attraction of the electron and hole and therefore their spatial separation, as illustrated by the dotted curve. Binding energies of the exciton (E_B^{exc}) and the CT state (E_B^{CT}) are also indicated, whereby $E_B^{\mathrm{CT}} < E_B^{\mathrm{exc}}$. Note that for simplicity, the energy of the exciton and the CT state are shown relative to the HOMO level. Slightly modified figure taken from Ref. [59].

2.3 Singlet fission and triplet harvesting

In the singlet fission process a singlet exciton, created by the absorption of a photon, is split into two triplet excitons with each approximately having half the energy of the initial excitation [276]. If those triplets can be harvested at a heterointerface, SF mediated multi-exciton generation solar cells have the potential to overcome the fundamental single-junction limit by reducing thermalization losses [269].

2.3.1 The singlet fission process

The conversion of singlets into two triplets has been a subject of interest since many decades. Already in 1965 singlet fission was first invoked to explain the photophysics of anthracene crystals [271] and then firmly established in tetracene crystals [287, 189, 107]. Pioneering work on both, the mechanism of singlet fission and how it is affected by the presence of a magnetic field was already done in the 1960/1970s by R. E. Merrifield, A. Suna, M. Pope, and C. E. Swenberg [188, 189, 107, 285, 146, 286].
In the SF process a photoexcited singlet (spin S = 0) exciton S_1 (process ① in Fig. 2.3) shares its energy with a neighboring ground state molecule, creating two triplet (spin S = 1) excitons T_1 (process ② in Fig. 2.3). As all physical processes, energy has to be conserved. Therefore, singlet fission is limited to systems in which the T_1 state is approximately half the energy of the S_1 state. Unlike intersystem crossing, the generation of triplet states via singlet fission is a spin-allowed process that does not require a spin flip. Since $T_1 \rightarrow S_0$ transitions are spin forbidden, triplets are rather long-lived states [276].

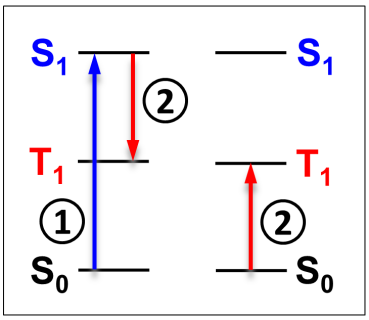

Figure 2.3: Singlet fission process. ① The chromophore on the left is initially photo-excited to the singlet state S_1. ② Subsequently, the excited chromophore shares its energy with the neighboring chromophore on the right, creating a triplet state T_1 on each [276].

The dynamics of singlet fission in single crystals, as well as polycrystalline thin films of polyacenes, with tetracene (Tc) and pentacene (Pc) being the most prominent candidates, have been studied extensively, but are currently still under debate [276, 349, 277, 299, 200]. Very fast SF rates in the range of fs - ps, thus outcompeting other decay channels like intersystem crossing, have been experimentally observed. Furthermore, SF quantum yields close to 200% with long-lived triplet states in the range of ns - μs have been reported [276, 277, 47, 45].
Note that for a given high efficient SF material, such as polycrystalline polyacenes thin films, SF dynamics are influenced by film morphology. It is hypothesized that the SF process is likely mediated by singlet exciton diffusion to defects or interfaces [15, 227].

The most common, but oversimplified description of singlet fission is described in the **conventional four-electron picture**. In Figure 2.4, the SF process within this model is sketched. The initially photoexcited S_0 + S_1 state on molecule a and molecule b, respectively, is first converted into an intermolecular pair of local coherently coupled triplet states, commonly written as $(T_1T_1)^l$. It can be seen as a coherent superposition of the nine (l = 1 ... 9) triplet pair states with overall singlet character [287, 107, 146]. In literature this intermediate state is variously also denoted as correlated triplet pair state, bound triplet state, or multi-exciton state. Finally, it is believed that the $(T_1T_1)^l$ state may separate into free individual triplets, T_1 + T_1, due to enthalpic and entropic driving forces, thus completing the SF process [200].

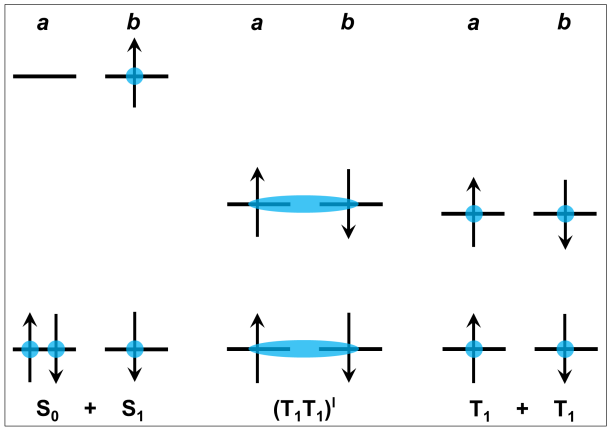

Figure 2.4: Conventional four-electron picture of the singlet fission process in two neighboring molecules a and b. The model involves a correlated triplet pair state, $(\mathrm{T_1T_1})^l$, with overall singlet character, before uncorrelated free triplets, $\mathrm{T_1}$ + $\mathrm{T_1}$, are generated. Figure adapted from Ref. [200].

The corresponding kinetic scheme, including various rate constants, k_i, is given by [276, 45]:

$$\mathrm{S_0} + \mathrm{S_1} \underset{k_2}{\overset{k_{-2}}{\rightleftharpoons}} (\mathrm{T_1T_1})^l \underset{k_1}{\overset{k_{-1}}{\rightleftharpoons}} \mathrm{T_1} + \mathrm{T_1} \quad . \tag{2.6}$$

It is obvious that for an efficient overall singlet fission process the forward rate, k_{SF}, has to outcompete the triplet fusion rate, k_{TF}, being the inverse process of singlet fission. Note that other loss channels, e.g. radiative relaxation of singlet states, non-radiative decay of triplets or triplet-triplet annihilation are not included in the simple description of Equation (2.6). In solids where exciton diffusion is present the ratio $\epsilon = k_2/k_{-1}$ is relevant, whereby the rate constant k_{-1} denotes the dissociation of the initially formed correlated triplet pair state, $(\mathrm{T_1T_1})^l$, into free triplets, $\mathrm{T_1}$ + $\mathrm{T_1}$, and k_2 the return of $(\mathrm{T_1T_1})^l$ to an $\mathrm{S_1}$ + $\mathrm{S_0}$ pair.

In a four-particle spin 1/2 system, there exist 16 possible spin states: two singlet (S_{tot} = 0), nine triplet (S_{tot} = 1), and five quintet (S_{tot} = 2). Recalling Equation (2.6), in the "classical" Merrifield theory, the kinetic rate equations are given by [286, 188, 228]:

$$\frac{d\left[S_1\right]}{dt} = -k_{-2}\sum_{l=1}^{9}\left|C_l^s\right|^2\left[S_1\right] + \sum_{l=1}^{9}k_2\left|C_l^s\right|^2\left[(\mathrm{T_1T_1})^l\right] \quad , \tag{2.7}$$

$$\frac{d\left[(\mathrm{T_1T_1})^l\right]}{dt} = k_{-2}\left|C_s^l\right|^2\left[S_1\right] - \left(k_2\left|C_s^l\right|^2 + k_{-1}\right)\left[(\mathrm{T_1T_1})^l\right] + k_1\left[T_1\right]^2 \quad , \tag{2.8}$$

$$\frac{d\left[T_1\right]}{dt} = 2k_{-1}\sum_{l=1}^{9}\left[(\mathrm{T_1T_1})^l\right] - k_1\left[T_1\right]^2 \quad , \tag{2.9}$$

whereby the rate constants, k_i, are multiplied by the coupling $\left|C_l^s\right|^2$ which is defined as $C_l^s = \left\langle S_1|(\mathrm{T_1T_1})^l\right\rangle$. Thus, $\left|C_l^s\right|^2$ represents the singlet character of the spin state of $(\mathrm{T_1T_1})^l$ and changes

under the influence of magnetic fields. Assuming steady-state conditions, $d\left[(\mathrm{T_1T_1})^l\right]/dt \approx 0$, one can solve for the time dependence of the $[S_1]$ and $[T_1]$ populations, finding [188, 48, 228]:

$$\frac{d\,[S_1]}{dt} = -k_{\mathrm{SF}}\,[S_1] + k_{\mathrm{TF}}\,[T_1]^2 \ , \tag{2.10}$$

$$\frac{d\,[T_1]}{dt} = 2k_{\mathrm{SF}}\,[S_1] - k_{\mathrm{TF}}\,[T_1]^2 \ , \tag{2.11}$$

where k_{SF} and k_{TF} are the rate constants for singlet fission and triplet fusion, respectively. They can be written as [188, 48, 228]:

$$k_{\mathrm{SF}} = \sum_{l=1}^{9} \frac{k_{-2}\,|C_l^s|^2}{1 + k_2/k_{-1}\,|C_l^s|^2} \ , \tag{2.12}$$

$$k_{\mathrm{TF}} = \frac{k_1}{9} \sum_{l=1}^{9} \frac{k_2/k_{-1}\,|C_l^s|^2}{1 + k_2/k_{-1}\,|C_l^s|^2} \ . \tag{2.13}$$

These are the "classical" results for singlet fission.

Magnetic field dependency – As an applied external magnetic field changes the number of triplet pair states $(\mathrm{T_1T_1})^l$ that have singlet character, it therefore changes steady-state rates involved in the SF process. The overall SF efficiency is reported to increase at low fields, before slowing down at intermediate fields and saturating in the high-field limit at about 0.4 T. This magnetic field dependency is an unique fingerprint of the SF process [230, 146, 93, 45, 328]. An example taken from literature is given in Figure 2.5 [328]. It shows results of a magnetic field modulation study on (i) fluorescence change of a pristine Tc crystal and polycrystalline thin film Tc in comparison to (ii) the photocurrent change in a Tc/C_{60} OPV cell. Singlet fission OPV devices will be introduced in section 2.4. The fluorescence signal monitors the singlet state population. The correlation between the measured fluorescence signal, SF dynamics, and $[S_1]$ & $[T_1]$ state populations will be explained in the next paragraph. The detected fluorescence signal increases for larger externally applied magnetic fields (Fig. 2.5 (top)). This is because singlet fission, which depopulates the emissive S_1 state by generating triplets, is slowed for increasing magnetic fields. On device level, a decreasing photocurrent is observed for increasing magnetic fields (Fig. 2.5 (bottom)). As the solar cell's photocurrent decreases while the singlet concentration increases, it is demonstrated that a significant portion of extracted charge carriers arises from triplets generated via singlet fission and harvested at the Tc/C_{60} heterointerface. Note that the initially increasing fission rate at low magnetic fields $\lesssim 0.05$ T can also be resolved within the here presented literature data [328].
Therefore, magnetic field modulated current, $I(B)$, measurements are capable to provide information on singlet fission and allow the distinction between singlet and triplet harvesting [134, 133, 64, 172, 328].

Singlet and triplet states assessed by transient fluorescence measurements – As sketched in Figure 2.6 (left), in SF materials the competing rate to multiple triplet generation via singlet

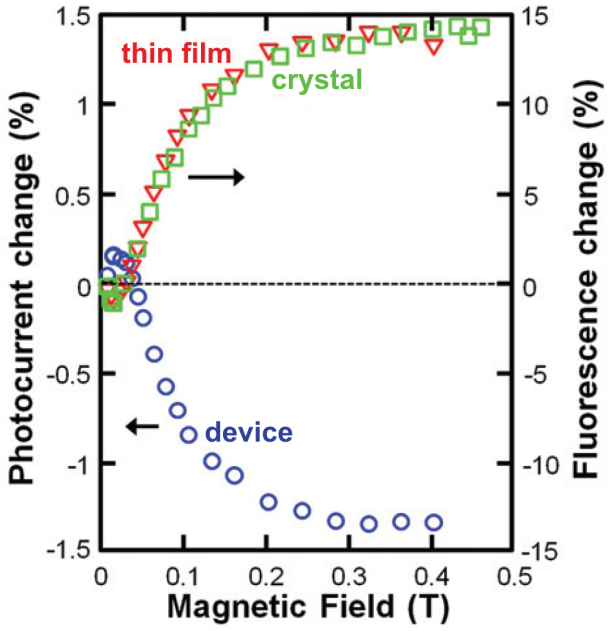

Figure 2.5: The magnetic field dependency of the fluorescence from a Tc crystal (squares) and polycrystalline thin film Tc (triangles). The corresponding change of solar cells photocurrent from an OPV cell with a 30-nm-thick Tc layer exhibits the opposite sign. Figure taken from Ref. [328].

fission (purple arrow) is radiative relaxation from the excited singlet state S_1 back to the ground state S_0 (blue arrow). This transition is called fluorescence and involves the emission of a photon. On the contrary, since $T_1 \rightarrow S_0$ transitions are spin forbidden, triplets are long-lived, so-called dark states. Therefore, the measure of emission is a proxy for the [S_1] state population and, if transient fluorescence signals are recorded, time-resolved dynamic processes can be monitored. In this study, the time-correlated single photon counting (TCSPC) method was conducted to detect transient signals. The setup is described in detail in section 3.2.6.

From the SF rate equations (2.10) and (2.11), a simple kinetic model for the mixed-process decay of a photo-excited singlet state coupling to a triplet channel is constructed. In addition to the singlet fission (k_{SF}) and triplet fusion (k_{TF}) rates a non-radiative decay rate (k_{nrad}) accounting for spontaneous losses of the long-lived triplet states is introduced. An example of the time evolution of [S_1] and [T_1] populations are plotted on the right side of Figure 2.6. The corresponding rate constants which were put into Equations (2.10 & 2.11) are given in the caption.

The initial decay of the [S_1] population which falls over two orders of magnitude is ascribed to the competing generation of T_1 states via singlet fission described by a fast forward rate k_{SF}. Coincidentally the [T_1] population rises (red line). In our simple model, the long-lived triplet state population slightly decreases due to (i) the introduced non-radiative decay rate, k_{nrad} (loss), and (ii) triplet-triplet fusion, k_{TF}, which results in a repopulation of the emissive singlet state. This causes delayed fluorescence.

Thus, measuring transient fluorescence stemming from the singlet state is an indirect but well established way to access SF dynamics [229, 227, 47, 45, 15]. The detection of a delayed fluorescence signal is an unambiguous proof that long-lived triplet states exist in the system under investigation. Figure 2.6 clearly demonstrates how triplet and singlet populations are directly connected to each other.

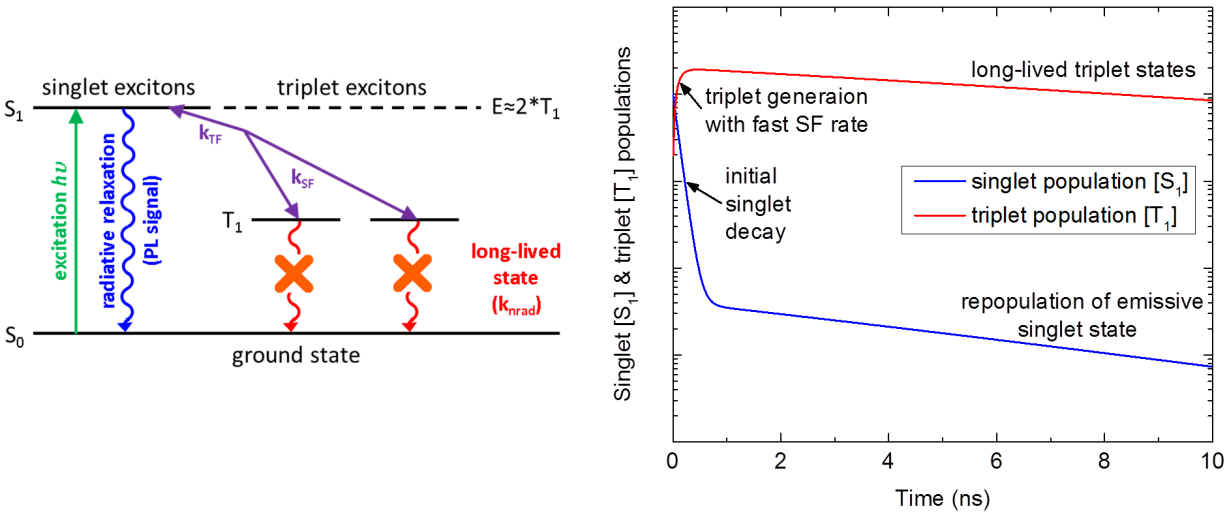

Figure 2.6: (left) Sketch of transition processes involved in a simple model of singlet fission (SF). Photo-excited singlet states S_1 can either produce two triplets via SF (purple arrow) or radiatively relax (blue arrow) to the ground state S_0, which is the competing process to SF. (right) Plot of singlet [S_1] and triplet [T_1] populations (log scale) according to rate equations (2.10 & 2.11) plus an additional non-radiative decay rate (k_{nrad}) for the triplet state. The here used rate constants are $k_{\mathrm{SF}} = 0.01$, $k_{\mathrm{TF}} = 1 \cdot 10^{-5}$, and $k_{\mathrm{nrad}} = 1 \cdot 10^{-4}$.

The photo-physical mechanism of singlet fission introduced in this section remains subject of active research [47, 46, 44, 45, 21, 53, 54, 55, 276, 277, 200] which is beyond the scope of this thesis. The interested reader is referred to the hitherto most comprehensive reviews of the field provided by M. B. Smith and J. Michl in 2010 [276] with a follow up due to rapid progress in 2013 [277]. The review by N. Monahan and X.-Y. Zhu from 2015 focuses on the key mechanistic question how a singlet exciton couples to the triplet pair [200].

2.3.2 Triplet harvesting and transfer mechanisms

For a successful implementation of SF materials in PV devices an efficient harvesting of triplet excitons is essential. Since singlet fission occurs in organic small molecules, excitons are tightly bound. To generate photocurrent, those Frenkel excitons have to be separated at a heterointerface. Besides direct ionization of excitons via charge transfer, at organic/inorganic heterointerfaces triplet energy transfer mechanisms have to be considered. In comparison to direct charge transfer, the entire exciton is transferred across the interface. As soon as a Frenkel exciton (organic part) is transferred across the hybrid interface, excitons in the inorganic part are delocalized resulting in free charge carriers already at room temperature. Free charges can then be extracted via selective contacts. Various transfer mechanisms are sketched in Figure 2.7 and will be briefly outlined in the following.

Electron transfer from the donor (D) to the acceptor (A) does usually not directly result in

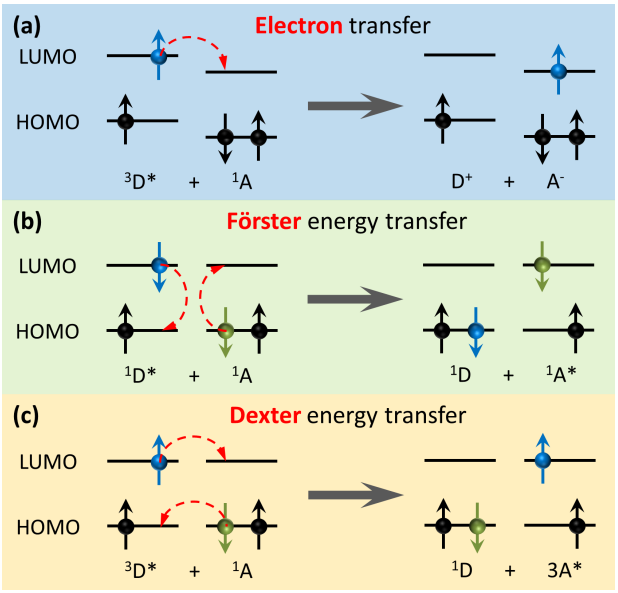

Figure 2.7: Schematic diagrams of (a) electron transfer from a triplet state, (b) Förster energy transfer from a singlet state, and (c) Dexter energy transfer from a triplet state. D and A denote donors and acceptors, respectively. The dashed arrows represent simultaneous rearrangement of the electronic configuration [195, 332].

fully separated charges, but rather occurs in a two-step process involving an intermediate charge transfer (CT) state (cf. section 2.2). Electron transfer involves a short-range interaction which requires significant spatial overlap of D and A wave functions. To overcome the Coulomb binding energy of bound excitons, suitable band offsets are required [59].
Both, electron transfer from singlet and triplet states might be possible (cf. Fig. 2.7 (a)).

Förster resonance energy transfer (FRET) is based on non-radiative dipole-dipole electromagnetic interaction and therefore a significant overlap of emission spectrum of the D with the absorption spectrum of the A is required [195]. It may be thought of as a virtual photon exchange between D and A (cf. Fig. 2.7 (b)). Additionally, the orientations of the transition dipoles must be approximately parallel. FRET efficiency decreases with the distance r between D and A $\propto r^{-6}$ as described by [101, 332]:

$$\eta_{\mathrm{FRET}} = \frac{{R_0}^6}{{R_0}^6 + r^6}\,, \tag{2.14}$$

with the Förster distance, R_0, i.e. the distance between D and A at which the energy transfer efficiency is 50%. FRET is a rather long-range process with typically observed D-A separations in the range of 1 - 5 nm [101, 195, 332, 252].
Usually only singlet excitons can be transferred via FRET since triplet-triplet transfer is spin forbidden according to Pauli's exclusion principle. An exception is given if the triplet exciton is located at a phosphorescent donor. However, for Tc at room temperature the oscillator strength for phosphorescence transitions is very low and therefore FRET is rather unlikely as a possible mechanism for triplet harvesting at the Tc/c-Si interface [195].

Dexter energy transfer – In contrast, an actual exchange of electrons between the D and A takes place during Dexter energy transfer (cf. Fig. 2.7 (c)). As the exchange interactions are dictated by the molecular (wave function) overlap, length scale of Dexter transfer is restricted to rather

short range $\lesssim$ 1 nm and exponentially decreases with distance r between D and A. The rate constant, k_{dex}, is given by [332]:

$$k_{\mathrm{dex}} = CJ \cdot \exp\left(\frac{-2r}{L}\right), \tag{2.15}$$

whereby C is an experimental constant, J is the normalized spectral overlap integral, and L is the sum of the van der Waals radii of the D and A.
If overall spin conservation is maintained, transfer from triplet states is allowed in the Dexter mechanism [81, 82, 195, 332].

In literature triplet exciton dissociation via electron transfer involving CT states at the organic donor-acceptor interface between the SF materials Tc and Pc and the electron acceptor C_{60} is reported [245, 52, 239, 64, 328].
Furthermore, the formation and dissociation of CT states also at hybrid organic-inorganic interfaces, therefore called "hybrid charge transfer (HCT)" states throughout this thesis, have been observed in literature [224, 20, 318, 241, 216].
Recently, two independent teams reported on efficient Dexter-type energy transfer of triplet excitons generated via singlet fission in the polyacenes Pc and Tc at the hybrid junction to inorganic PbS or PbSe nanocrystals. M. Tabachnyk et al. [290] point out the essential requirement of resonance condition between the nanocrystal band gap and the molecular triplet energy. N. J. Thompson et al. [307] report an exponential dependence of energy transfer efficiencies on ligand length, as expected for a Dexter-type process (cf. Eq. (2.15)). Triplet energy transfer was unambiguously proven and distinguished from singlet exciton transfer by the observation of the typical magnetic field dependency of the SF process, as introduced previously in this section. For resonance conditions triplet energy transfer efficiencies $\gtrsim$ 90% are claimed [307, 290].

Those results are promising for the hybrid Tc/c-Si interface. However, to the best of the author's knowledge, no triplet exciton harvesting at the Tc/c-Si interface is reported to date. In section 7.5 challenges of charge separation at the specific Tc/c-Si interface will be discussed with the aid of experimental results obtained throughout this work.

2.4 Singlet fission devices

In the last decade several groups have successfully implemented SF materials, namely Tc and Pc in organic photovoltaic (OPV) devices, e.g. Refs. [337, 217, 171, 134, 242, 289, 305, 64, 328, 306, 335, 172]. The efficiency of harvesting generated charges is reflected in the external quantum efficiency (EQE) of a solar cell as it constitutes the ratio of extracted charge carriers to the number of incident photons. Thus, comparing absorption spectra of the SF material with the corresponding EQE spectra of the device with an implemented SF layer give access to the contribution related to the SF material. In 2013, D. N. Congreve et al. reported for the first time a peak EQE exceeding 100% in a SF-based Pc/C_{60} bilayer OPV device (cf. Fig. 2.8 (b)). Their device architecture is depicted in Figure 2.8 (a) [64]. Accordingly, triplet excitons which are gen-

erated with a high quantum yield via singlet fission in the Pc thin film can diffuse and efficiently dissociate at the organic donor-acceptor Tc/C_{60} heterojunction. An EQE above unity reflects a net gain of multi-exciton generation via singlet fission which outcompetes the sum of all other possible loss channels. Nevertheless, bear in mind that the overall OPV device efficiency $\lesssim 2\%$ is rather low.

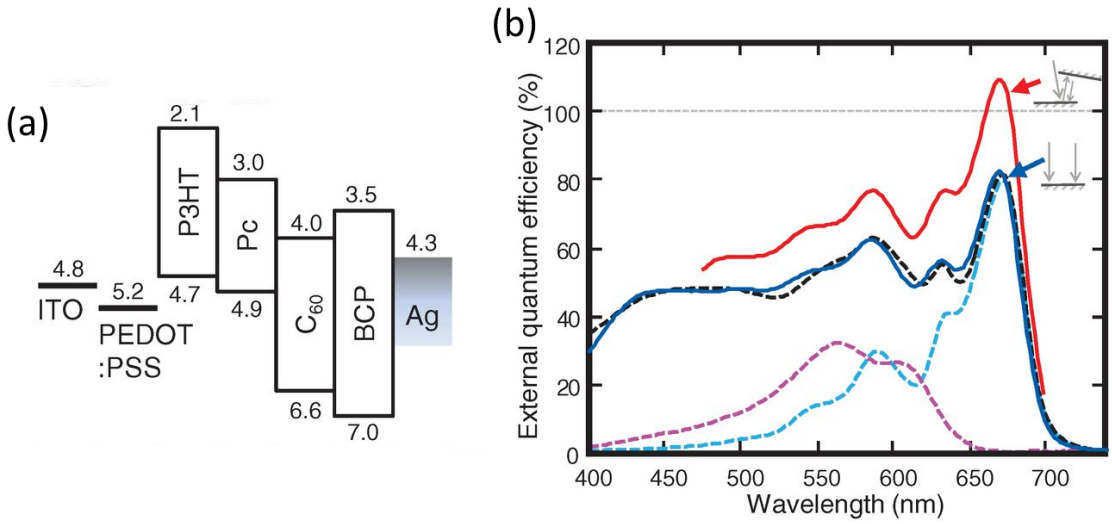

Figure 2.8: (a) Device architecture and HOMO/LUMO energy levels of the SF-based Pc/C_{60} bilayer organic solar cell. (b) Corresponding external quantum efficiency (EQE) measured without optical trapping (blue line) and multiple paths via back reflection with an external mirror (red line). This is the first report of a SF-based multi-exciton generating device with an EQE exceeding 100%. Figure taken from Ref. [64].

The SF materials Tc and Pc were also successfully integrated in hybrid devices with PbSe and PbS nanocrystals as triplet acceptors [133, 87, 88, 86, 172]. As pointed out in Ref. [290] and already discussed above (cf. section 2.3.2), by varying nanocrystal sizes the importance of resonance condition between the triplet energy and band gap of inorganic acceptor material, and the correct band line-up, was confirmed on device level by means of EQE measurements. If nanocrystal band gaps are in resonance with the energy of the T_1 state, absorption peaks of SF materials coincide with EQE maxima. If the T_1 energy is too low or too high, no charge separation is observed and the excitation disappears non-radiatively. Hence, the SF process is a loss mechanism which is reflected as a decrease of the EQE where the molecule absorbs. Despite initial success, also efficiencies of nanocrystal SF devices remained disappointingly low.

Tc/c-Si hybrid device concepts

The objective of the second part of this work is to integrate the SF material Tc into "conventional" c-Si based solar cells. A successful triplet exciton harvesting at the hybrid Tc/c-Si interface is

not reported to date. In Figure 2.9, three different concepts for the implementation of SF materials in n-type c-Si absorber devices are sketched. Obviously, in each concept the fundamental prerequisite for triplets generated via singlet fission is to reach the hybrid interface to be somehow separated there. Thus, Tc layer thicknesses should be within the same order as the triplet diffusion length which is reported to be ∼100 nm at room temperature [47].

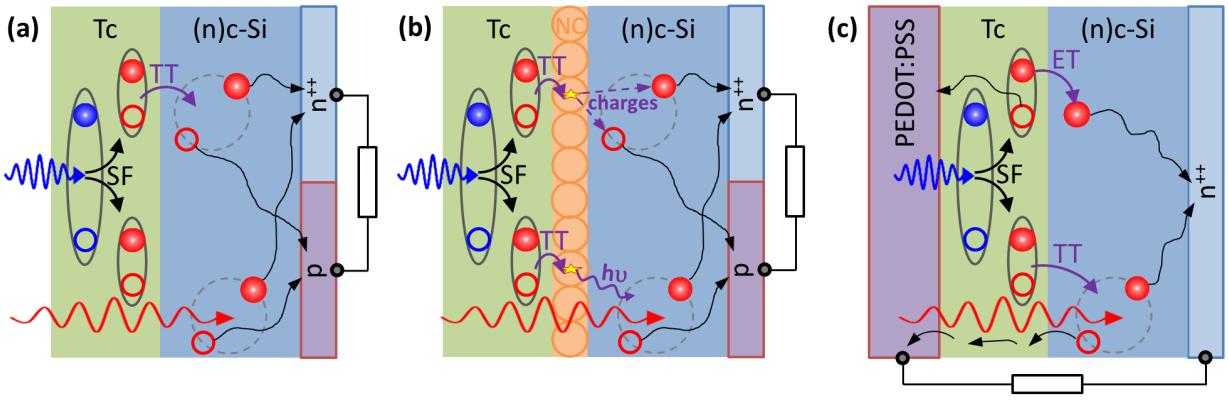

Figure 2.9: Various concepts for the implementation of Tc in (n)c-Si absorber solar cells. Via singlet fission (SF) in Tc, a high energy singlet exciton (blue) is split into two triplet excitons (red) of lower energy. (a) Tc implemented at the front side of a back contacted (n)c-Si solar cell. This concept requires an entire triplet transfer (TT). (b) Nanocrystal (NC) interlayer approach. TT into NCs is proven [290, 307]. In a 2nd step, (i) radiative energy transfer ($h\nu$), or (ii) ionization of excitons into free charge carriers which are then injected into c-Si is possible. (c) Tc sandwiched between the hole conductive PEDOT:PSS and (n)c-Si. Both, (i) electron transfer (ET), or (ii) TT is possible.

In the first approach, Tc is grown on top of a back contacted c-Si solar cell (cf. Fig. 2.9 (a)). Consequently, the entire triplet has to be transferred via Dexter-type energy triplet transfer (TT) across the hybrid interface to c-Si (cf. section 2.3.2). As soon as the triplet is transferred to inorganic c-Si, electrons and holes become delocalized and can be extracted at the solar cell's interdigitated back contacts. In a dynamic study by Piland et al., no evidence for triplet energy harvesting was found at the hybrid Tc/c-Si interface [229]. Also on device level no report is available to date.

The idea of the second approach is to use nanocrystals as a "relay" to shunt triplet exciton energy transfer from the organic into the conventional inorganic c-Si based part of the solar cell (cf. Fig. 2.9 (b)). Efficient TT into nanocrystals was proven recently (cf. section 2.3.2) [290, 307, 22]. After accepting triplet energy in the nanocrystals, bright state excitons might be generated. Their coupling into c-Si could be mediated in a second step by either emitting a photon that is absorbed in c-Si generating an electron-hole pair, or by Förster resonance energy transfer via exchange of virtual photons. Another possibility would be the ionization of excitons and generation of free electrons and holes in the nanocrystals, which are then injected into the c-Si absorber. Nevertheless, this two-step processes will always struggle with additional loss channels such as non-

radiative recombination or radiative recombination not directed into the absorber [22]. To date, no successful sensitization of c-Si via nanocrystals in a SF approach is reported.
In Figure 2.9 (c) the hybrid Tc/c-Si device idea that is followed in this work is sketched. The Tc layer is sandwiched in between the main c-Si absorber and the polymer PEDOT:PSS. In the concept proposed here, triplet harvesting via electron transfer (ET) from Tc into c-Si with the hole remaining in the organic part of the hybrid interface would be sufficient. The free electron is then extracted through a standard electron selective back contact, whereas the hole can be extracted through the hole selective PEDOT:PSS as commonly used in OPV devices. However, as indicated in the figure, also TT with a hole transfer back is a possible scheme in this device structure. The major challenges of this concept are:

(i) Sufficient passivation of the c-Si surface by thin film Tc.

(ii) Efficient charge separation, i.e. dissociation of tightly bound triplet excitons at the hybrid Tc/c-Si interface.

(iii) Efficient hole extraction, also from the c-Si absorber, has to be guaranteed.

3 Experimental methods

In this chapter details of device fabrication are given and various analysis methods utilized throughout this work are introduced.
The first step in the production of c-Si based solar cells is always a sufficient cleaning of the Si wafers, followed by various deposition methods for inorganic and organic layers. For instance, amorphous Si layers are fabricated by plasma enhanced chemical vapor deposition, Tc is thermally evaporated in vacuum, and PEDOT:PSS is spin-coated under ambient conditions followed by a subsequent annealing step.
A pool of analysis methods were used to characterize amorphous Si and organic layers as well as the corresponding heterointerfaces to c-Si. In particular, various modes of photoelectron spectroscopy were conducted to measure the band alignment at conventional a-SiO_x:H/c-Si as well as hybrid PEDOT:PSS/c-Si and Tc/c-Si heterojunctions. Stoichiometry x of a-SiO_x:H was investigated by core level spectroscopy. Using high excitation energies provided by synchrotron radiation the buried PEDOT:PSS/c-Si interface could be addressed. Surface photovoltage measurements were employed to determine the band bending in c-Si, minority-carrier lifetime was extracted from photoconductance decay meauserments. Optical transmission and reflection measurements as well as spectroscopic ellipsometry were conducted to determine absorption and (*n*-*k*) data of amorphous Si and organic thin films. By using the time-correlated single photon counting technique, the SF dynamics of thin film Tc could be monitored.
Complete solar cells were characterized with capacitance-voltage and current density-voltage measurements. For a thorough interpretation quantum efficiency spectra were recorded under various measurement conditions, such as temperature and external voltage.

3.1 Device fabrication

Figure 3.1 depicts the layer stacks of various solar cell approaches investigated in this work.
On the left of Figure 3.1, the layer stack of **conventional both-sides-contacted SHJ solar cells with wide band gap (i)a-SiO_x layers** incorporated is shown. The electron selective back contact

is formed by a ∼5 nm (i)a-Si:H passivation layer and ∼15 nm (n^+)a-Si:H acting as a back surface field. The amorphous layer stack is followed by a ∼80 nm ITO layer and a full area Ti/Ag metallization. In this thesis the 5 nm (i)a-Si:H passivation layer on the front side is replaced by wider band gap (i)a-SiO_x:H with varying stoichiometry x. The emitter is formed by ∼10 nm of (p)a-Si:H. The front contact is completed by ∼80 nm ITO and a Ti/Ag metal grid.
On the right of Figure 3.1, the layer stack of **hybrid organic/c-Si HJ solar cell concepts** is depicted. **(a) Hybrid PEDOT:PSS/c-Si HJ solar cell** without Tc layer. **(b) MEG hybrid PEDOT:PSS/Tc/c-Si device approach** by the incorporation of the SF-material Tc. Optional ultra-thin interlayers were investigated throughout this work which might help to harvest excitons at the hybrid junction between Tc and c-Si. The electron selective back contact is adopted from the conventional SHJ technology. Hybrid devices are completed with an Ag grid directly fabricated onto the highly conductive polymer PEDOT:PSS at the front side.
Details of various process steps during solar cell fabrication as indicated with the circled numbers in Figure 3.1 will be given in the following.

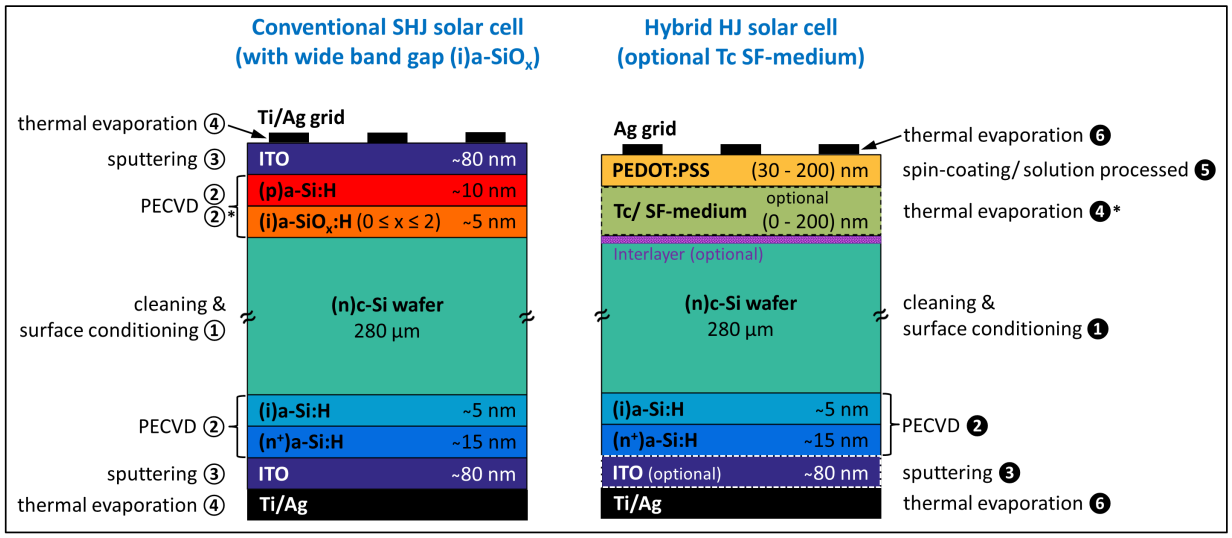

Figure 3.1: Sketch of layer stacks of various solar cell concepts. Circled numbers indicate the process step sequences. (left) Conventional both-sides-contacted SHJ solar cell. The electron selective back contact is formed by an (i,n^+)a-Si:H layer stack followed by an ITO layer and a full area Ti/Ag metallization. In the hole selective front contact, the standardly used (i)a-Si:H passivation layer is replaced by wider band gap (i)a-SiO_x:H, followed by a (p)a-Si:H emitter. The front contact is completed by an ITO layer and a Ti/Ag metal grid. (right) Hybrid solar cell concepts: (a) Hybrid PEDOT:PSS/c-Si HJ solar cell without Tc layer. (b) MEG hybrid PEDOT:PSS/Tc/c-Si concept by incorporation of the SF-material Tc. Optional ultra-thin interlayers are investigated. The back contact is adopted from the conventional SHJ technology. Hybrid devices are completed with an Ag front grid.

①/❶: c-Si wafer cleaning and surface conditioning

For all solar cells fabricated in this work, commercially available high quality float-zone grown c-Si wafers with (111) surface orientation and a resistivity of 1 - 5 $\Omega \cdot$cm (n-doped) were used. If necessary, 4" wafers were cut into the required sample sizes prior to the cleaning process.
Substrates were cleaned following the standard RCA procedure established by the Radio Company of America [152].
To strip off the native Si oxide, a 2 min dip in 1% diluted hydrofluoric (HF) acid was always performed immediately before follow-up processes, i.e. amorphous Si or organic layer depositions. After the HF-dip, Si dangling bonds are saturated with H atoms, thus providing an initially well passivated surface. Subsequently after exposure to ambient air, oxidation and reduction of passivation quality starts [14]. Therefore, the time between HF-dip and further process steps is kept as short as possible $\lesssim$ 5 - 10 min. Time is consumed e.g. for various evacuation cycles during sample transfer into the glovebox and mounting samples into the evaporator.

②/❷: PECVD growth of standard a-Si:H layers

Both, conventional SHJ and hybrid HJ devices consist of a well passivated (i,n^+)a-Si:H electron selective contact at the back side. For conventional SHJ solar cells also a (p)a-Si:H emitter layer on the front side is needed.
Intrinsic, p- and n-doped a-Si:H thin films are fabricated by PECVD in a conventional parallel plate reactor configuration using microwave excitation frequencies of 13.56 Mhz or 60 Mhz. Silane (SiH_4) is used as Si precursor gas, diborane (B_2H_6) and phosphine (PH_3) are used as p- and n-type dopant sources, respectively. For saturation of Si dangling bonds in the amorphous network, H_2 is added to the precursor gases. Besides the gas phase composition, PECVD strongly relies on other deposition parameters like power density, substrate temperature, total gas flow, deposition pressure, and plasma excitation frequency [175, 74, 219].
The fabrication of various a-Si:H layers by PECVD are standard and well-established processes at HZB. Further details can be found in Ref. [190] and references therein.

②*: PECVD growth of a-SiO_x:H layers

In conventional SHJ solar cells, the standardly used (i)a-Si:H passivation layer was replaced by wider band gap (i)a-SiO_x:H. The growth of thin film (i)a-SiO_x:H by PECVD was established for this study.
All (i)a-SiO_x:H layers were grown with conventional parallel plate (2 cm electrode distance) PECVD at 60 MHz excitation, a plasma power density of 56 mW/cm^2, a process pressure of 0.5 mbar, a substrate temperature of 175 °C, and precursor gas mixtures of $SiH_4/H_2/CO_2$. As it is depicted in Figure 3.2, in order to vary the stoichiometry x of (i)a-SiO_x:H layers, the ratio R = CO_2/SiH_4 was varied from 0, for standard (i)a-Si:H layers, to 4, which results in an increased stoichiometry x. For all depositions, the H_2 gas flow was kept constant at 5 sccm.
The deposition of a-SiO_x:H layers was carried out in the same PECVD cluster as used for a-Si:H fabrication.

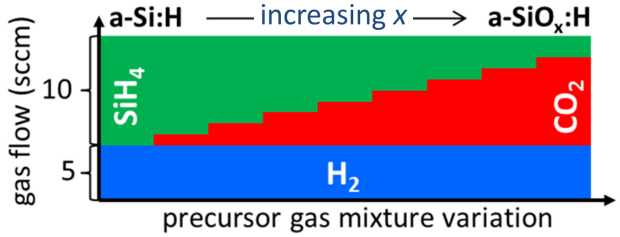

Figure 3.2: Schematic of precursor gas mixture variation during PECVD growth of (i)a-SiO_x:H layers. Precursor gas flows of SiH_4 and CO_2 always add up to a total of 10 sccm. The ratio R = CO_2/SiH_4 ranges from 0, for standard (i)a-Si:H layers, to 4, which results in an increased stoichiometry x of a-SiO_x:H films. The H_2 gas flow was kept constant at 5 sccm.

③/❸: ITO sputter deposition

In the SHJ technology TCO layers are needed between a-Si:H layers and metal contacts. For conventional SHJ solar cells ∼80 nm of ITO layers were reactively sputtered from an ITO target with 0.1% oxygen in the process gas flow. The ITO layer thickness is optimized in terms of anti-reflection properties and sufficient lateral conductivity [129, 192]. As indicated in Figure 3.1, for record PEDOT:PSS/c-Si HJ solar cells, we also utilized an ITO layer on the solar cell's back side. Standardly for organic/c-Si hybrid devices, ITO deposition was omitted to keep fabrication processes simple and to avoid organic materials in the sputter chamber. ITO layer fabrication is also a standard process at HZB carried out in a sputter system from the company *ROTH & RAU*.

❹*: Thermal evaporation of Tc

For the multi-exciton generating hybrid PEDOT:PSS/Tc/c-Si concept, thin film polycrystalline Tc was thermally evaporated on glass (for reference) and H-terminated c-Si wafers at ∼100 °C and base pressures $\lesssim 1 \times 10^{-6}$ mbar, which corresponds to deposition rates of about (0.5 - 1) $\mathring{A}$/sec, as determined with a quartz micro balance. During evaporation, no active cooling or heating of substrates was conducted. As is known from literature, these evaporation conditions result in island formation of Tc [204, 330, 169, 265, 303]. Sublimed grade Tc with a purity of 99.99% was used as received from the company *SIGMA-ALDRICH*.
Ultra-thin layers of the fullerene C_{60} (sublimed grade 99.9%, *SIGMA-ALDRICH*), as it constitutes a promising interlayer (cf. section 7.6, not yet introduced) were evaporated in the same setup at temperatures of ∼450 °C resulting in a deposition rate of about (0.1 - 0.3) $\mathring{A}$/sec.
The organic evaporation chamber is placed inside a glovebox, thus exposure to ambient during fabrication processes is minimized.

❺: Spin-coating of PEDOT:PSS

The highly conductive p^+-doped polymer PEDOT:PSS acts as the hole selective front contact in hybrid HJ solar cells. In this work the commercially available pre-mixed polymer dispersion *'F HC solar'* was used as delivered. To the polymer solution *'PH 1000'*, 5 vol% of dimethyl sulfoxide (DMSO) and a wetting agent (0.1 vol% FS31, Capstone) was added. Both PEDOT:PSS formulations are from the company *Heraeus Clevios*. As shown in our publication [136], both

solutions can be used interchangeable.
For MEG solar cells, immediately after Tc deposition PEDOT:PSS was standardly spin-coated at 1500 rpm for 10 sec under ambient conditions, resulting in layer thicknesses of about (100 - 150) nm. Subsequently after spin-coating, samples were annealed for 90 min in a vacuum oven at 60 °C, which is well below the Tc evaporation temperature.
Standardly PEDOT:PSS is annealed at higher temperatures well above 100 °C for shorter times, and often in ambient air [226, 179, 113]. Thus, for hybrid PEDOT:PSS/c-Si HJ solar cells without Tc, polymer films were dried at 130 °C for 15 min in ambient.
By increasing the spin-speed up to its maximum rotation of 10.000 rpm, PEDOT:PSS layer thicknesses of about 35 nm can be fabricated. Because these layers are too thick to access the buried interface by HAXPES measurements (cf. section 6.1), we followed a post-treatment procedure suggested in literature [58, 156, 331]. To this end, after the first annealing step, PEDOT:PSS layers were additionally immersed for 15 min in DMSO, followed by a second annealing step. Thus, layer thicknesses could be further reduced to about 20 nm. The detailed sample preparation procedure is given in our publication [137].

④/❻: metallization

Finally, all solar cells have to be metalized. At HZB metallization is done by thermal evaporation. In the both-side contacted device architectures a full area metal back contact is deposited. By the use of masks, a metal grid is fabricated on the cell's front side.
For conventional SHJ solar cells, metallization follows ITO sputtering. A 500 nm Ag contact with a ∼10 nm Ti adhesion layer in between Ag and ITO was evaporated on the back side. The front contact consists of a 1.5 μm thick Ag contact grid, also with a 10 nm Ti adhesion layer incorporated [192, 264, 121].
As already stated above, for hybrid organic/c-Si devices, standardly ITO deposition was omitted to keep fabrication processes as simple as possible. For that reason, 750 nm Ag was directly evaporated on the (i,n$^+$)a-Si:H layer stack leading to slightly reduced V_{oc} of solar cells due to enhanced surface recombination at the a-Si/Ag interface. Hybrid PEDOT:PSS/(Tc)/c-Si solar cells were completed by a 300 nm Ag front contact grid directly evaporated onto the polymer.

3.2 Analytical methods

By means of photoelectron spectroscopy (PES) the band alignment at various SHJs as well as chemical information of a-SiO$_x$ and PEDOT:PSS was obtained. The band bending in c-Si was extracted from surface photovoltage (SPV), carrier lifetime was extracted from photoconductive decay (PCD) measurements. The absorption of thin film Tc deposited on glass substrates was determined by transmission and reflection measurements using an absorption spectrometer with an integrating sphere attachment. Spectroscopic ellipsometry (SE) was conducted to obtain optical constants of a-Si and PEDOT:PSS. To investigate the SF dynamics of thin film Tc, transient PL spectra were recorded using the time-correlated single photon counting (TCSPC) technique. The following sections present more detailed descriptions of each of these experimental techniques.

3.2.1 Photoelectron spectroscopy

Throughout the works detailed in this thesis, various modes of PES at different setups were conducted. The basic principle of PES is sketched in Figure 3.3. Monochromatic light with an energy $h\nu$ is directed on the sample which excites electrons above the vacuum level E_{vac}. With an energy dispersive analyzer, these photoelectrons are then recorded and binned according to kinetic energy E_{kin}. Thus, a PES spectrum represents the sample's density of occupied states (DOS) [124, 240]. For low excitation energies $\lesssim$ 100 eV (UV range), photoelectrons are originating from valence band states near the Fermi edge E_F. For excitation energies $\gtrsim$ 1000 eV (X-ray range), photoelectrons can also escape from the more tightly bound core levels. The work function Φ_w is given by the difference of E_{vac} - E_F. As also indicated in Figure 3.3, a PES spectrum, consisting of core level peaks and the valence band region, is broadened due intrinsic and experimental broadenings. Intrinsic life-time broadening features a Lorentzian line shape, experimental broadening caused by the finite resolution of the excitation source and energy analyzer features a Gaussian distribution [124, 240].
By calibrating the PES setup, as it is commonly done with an Au reference sample, spectra are usually converted into electron binding energy by [124]:

$$E_{\mathrm{bind}} = E_{\mathrm{kin}} - (h\nu + \Phi_{\mathrm{det}}), \tag{3.1}$$

where the work function of the electron detector Φ_{det} is a setup specific constant [124].
PES measurements have to be performed in UHV systems for two reasons. (i) Free photoelectrons excited above E_{vac} have to be efficiently collected at the analyzer without loss of energy or change in momentum via scattering processes with residual gas atoms. (ii) Since PES is a surface sensitive technique, sample contamination by surface adsorbates has to be minimized.
Figure 3.4 shows the so-called universal curve which relates E_{kin} of the photoelectrons to their inelastic mean free path (IMPF) for various elements [260]. Therefore the universal curve provides a rough estimate for the information depth of PES measurements for different excitation energies with highest surface sensitivity and IMPFs of $\sim$1 nm using standard lab based excitation sources, i.e. He discharge lamp (blue) and Mg/Al X-ray tube (green). For excitation in the near-UV (orange range) or with tender/hard X-rays (red range), IMPFs can increase up to $\sim$10 nm. In a specific experiment, the effective information depth also depends on e.g. material density and setup sensitivity[1] [296]. Near-UV excitation was provided by a lab based light source, whereby tender/hard X-rays were provided by synchrotron radiation of BESSY II.

The band alignment at the a-SiO_x/c-Si, as well as hybrid PEDOT:PSS/c-Si and Tc/c-Si interfaces was investigated using various modes of ultraviolet PES (UPS). By the use of near-UV excitation the information depth is increased compared to conventional He-UPS measurements. Using X-ray PES (XPS) the stoichiometry x of a-SiO_x was determined. Furthermore, the chemical structure of the buried PEDOT:PSS/c-Si interface could be addressed by a tender/hard X-ray (HAXPES) study using high energy synchrotron radiation. Various PES modes conducted throughout this work will be briefly described below.

[1] few photoelectrons will always escape from deeper buried parts of the sample following an exponential decay

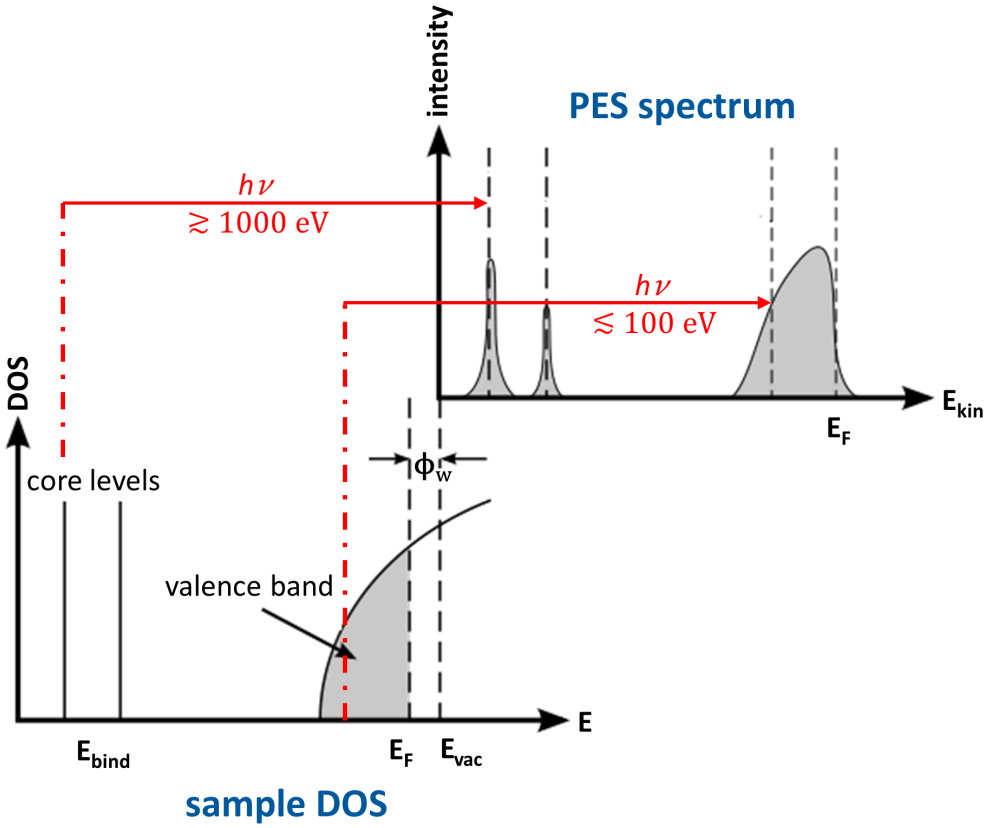

Figure 3.3: Sketch of the basic principle of photoelectron spectroscopy (PES) [124, 240]. (left) The occupied density of states (DOS) consists of core levels and valence band states near the Fermi edge, E_F. Monochromatic light with energy $h\nu$ directed on the sample excites electrons above the vacuum level, E_{vac}. Kinetic energies, E_{kin}, of those photoelectrons are then detected with an energy dispersive analyzer. Thus, the corresponding PES spectrum (right) represents the sample's DOS below E_F. The work function, Φ_w, is given by E_{vac} - E_F.

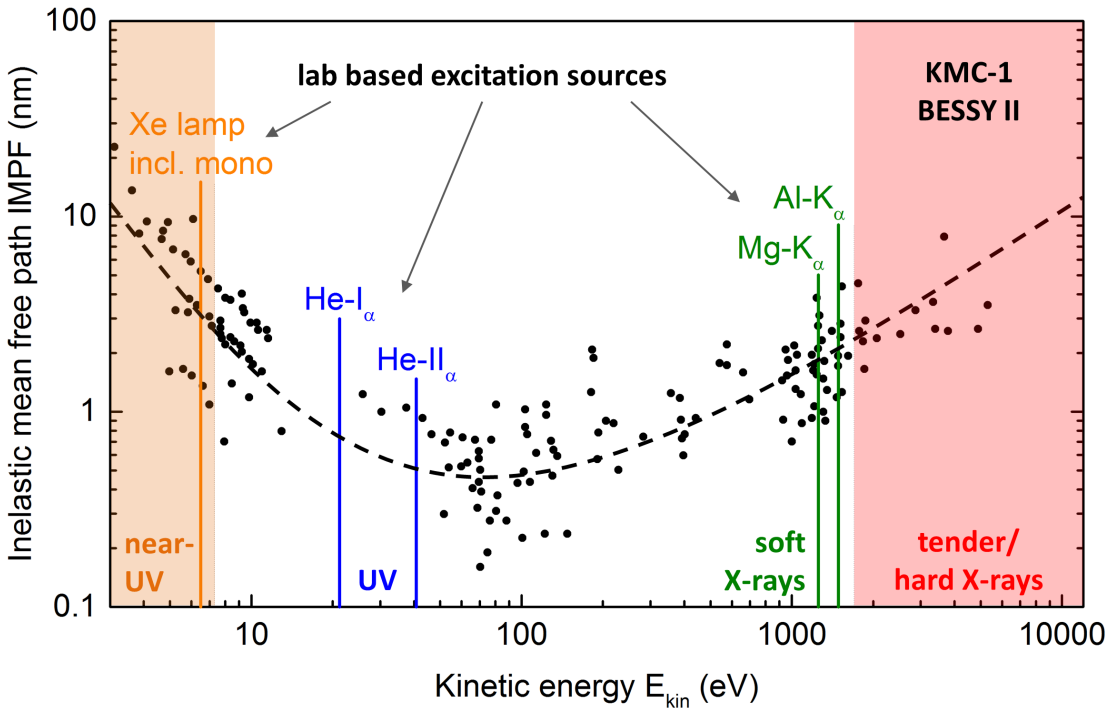

Figure 3.4: Universal curve which relates the kinetic energy (E_{kin}) of photoelectrons to their inelastic mean free path (IMPF) for various elements. Data digitized from Ref. [260]. Lab based excitation sources (Xe arc lamp, He discharge lamp, Mg/Al X-ray tube) and synchrotron radiation (this work KMC-1 bending magnet at BESSY II) are used. He-UPS and Mg/Al XPS are rather surface sensitive. An increased information depth can be obtained by using either *near-UV* or *tender/hard X-ray* excitation.

He-UPS and XPS (Mg/Ag)

The most common light source for UPS is a He gas discharge lamp directly connected to the UHV analytics chamber and differentially pumped. Throughout this project the He-I_α discharge line at $h\nu$ = 21.22 eV[2] was used. He-UPS is very surface sensitive and only probes a few atomic layers $\lesssim$ 1 nm (cf. Fig. 3.4). With this rather low excitation energy the valence band structure near E_F is probed, hence valence band maxima, E_{VBM}, and work function, Φ_w, from the secondary electron cutoff (SECO) can be determined [124].
In order to investigate chemical composition and stoichiometry, higher excitation energies in the X-ray range are needed to excite photoelectrons from element specific core level states. In this work the characteristic Mg-K_α ($h\nu$ = 1253.7 eV) and Al-K_α ($h\nu$ = 1486.7 eV) soft X-ray radiation from a conventional X-ray tube was used, resulting in $\sim$1 - 2 nm information depth (cf. Fig. 3.4). Stoichiometry can be determined by analyzing relative peak intensity ratios of core level peaks weighted with their element specific sensitivity factors [124, 321]. A change in chemical bonding, e.g. various oxidation states of a-SiO_x implicate a chemical shift of the Si core level peak. Core binding energies are determined by electrostatic interaction between the core electron and the nucleus. It is reduced by the electrostatic shielding of the nuclear charge from all other electrons in the atom, including valence electrons. Removal or addition of electronic charge as a result of changes in bonding, e.g. braking Si-Si bonds and incorporation of O into the amorphous Si network forming Si-O bonds, will alter the shielding [270, 124]. The result is a chemical shift of Si core level peaks towards higher E_{bind}. Thus, a quantitative analysis of the shift of Si peaks opens up another way to determine the stoichiometry x of a-SiO_x [126, 180].

Near-UV PES

The experimental setup of near-UV PES is sketched in Figure 3.5. Near-UV radiation is provided by a 100 W high-pressure Xe arc lamp monochromated with a double grating monochromator[3], providing photon energies up to 7.3 eV. This is determined by the cutoff of UHV window layers made of suprasil or LiF. The sample's work function determines the low-energy cutoff. The near-UV energy range leads to signals originating from the first 5 to 10 nm of the sample (cf. Fig. 3.4).
Two modes of near-UV PES were conducted throughout this work. *"Bulk sensitive"* N-UPS with a fixed excitation energy of typical 6.5 eV[4] which is identically to *"surface sensitive"* He(21.2 eV)-UPS, merely with a lower excitation energy. By contrast, in the so-called constant final state yield spectroscopy (CFSYS) mode the excitation energy is varied (3 eV $\lesssim h\nu \lesssim$ 7.3 eV) while the detection of photoelectrons is kept at a constant (final state) kinetic energy E^0_{kin}. As sketched in Figure 3.5, energy dependent changes in the photon flux $n_{\mathrm{phot}}(h\nu)$ provided by the Xe lamp and the reflectivity $R(h\nu) = n_{\mathrm{refl}}(h\nu)/n_{\mathrm{phot}}(h\nu)$ of the sample are measured with the reflection

[2] He-II_α discharge line at $h\nu$ = 40.8 eV is also available
[3] 1680 SpectraMate Double Spectrometer, Czerny-Turner type, manufactured by Yobin-Yvon/Spex. Gratings have a line density of 1200 nm^{-1}
[4] excitation energy of 6.5 eV selected by monochromator

sensor and the monitor diode, respectively. The internal photoelectron yield $Y_{\mathrm{int}}(E^0_{\mathrm{kin}}, h\nu)$ is then calculated via [159]

$$Y_{\mathrm{int}}(E^0_{\mathrm{kin}}, h\nu) = \frac{I^{\mathrm{CFSY}}_{\mathrm{tot}}(E^0_{\mathrm{kin}}, h\nu)}{e n_{\mathrm{phot}}(h\nu)\,[1 - R(h\nu)]}\,, \tag{3.2}$$

with the photoelectron current $I^{\mathrm{CFSY}}_{\mathrm{tot}}(E^0_{\mathrm{kin}}, h\nu)$ measured in constant final state yield. It is important to note that $Y_{\mathrm{int}}(E^0_{\mathrm{kin}}, h\nu)$ is directly proportional to the DOS [261, 159]. When the final state energy E^0_{kin} is chosen to yield the maximum flux of photoelectrons, the sensitivity of CFSYS is greatly superior to conventional UPS modes which enables to detect valence band tail and mid-gap defect states of amorphous semiconductors < 10^{20} $\mathrm{eV}^{-1}\mathrm{cm}^{-3}$. The valence band structure of a-SiO_x:H measured with conventional He-UPS and CFSYS will be presented and discussed in chapter 4.

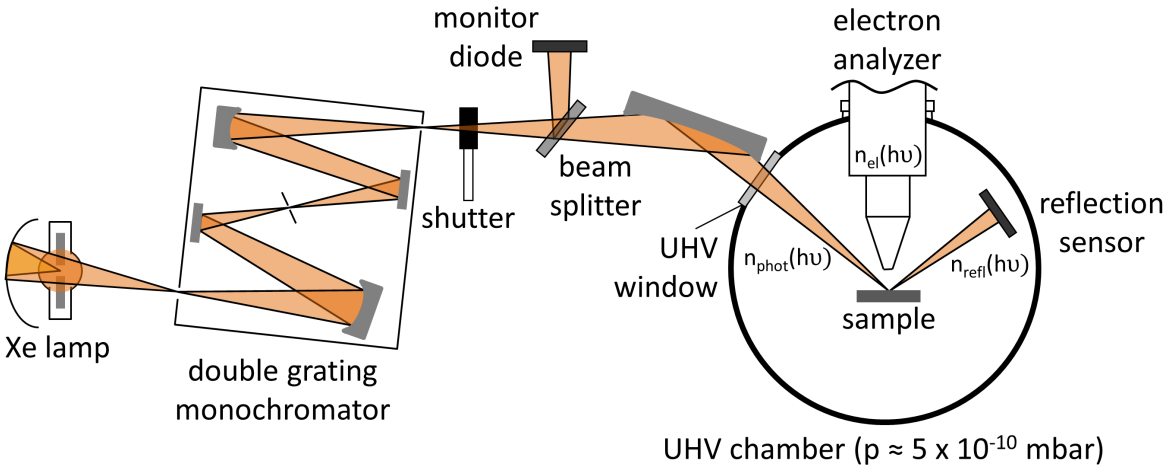

Figure 3.5: Sketch of near-UV PES setup. Two modes are possible: (i) Near-UV PES with an adjustable (typically 6.5 eV) constant excitation energy provided by the combination of a high-pressure Xe arc lamp and a double grating monochromator (left beam). (ii) Constant final state yield spectroscopy (CFSYS) mode. The photoelectron yield is determined by the ratio of detected photoelectrons $n_{\mathrm{el}}(h\nu)$ to incoming photons while measuring both, incident $n_{\mathrm{phot}}(h\nu)$ and reflected $n_{\mathrm{refl}}(h\nu)$ photon fluxes. Figure adopted from Ref. [159].

Obviously core level photoelectrons cannot be excited with near-UV radiation. In order to gain depth-resolved chemical information, tender/hard X-ray excitation is required.

Tender/hard X-ray PES at BESSY II

Tender/hard X-ray PES (HAXPES) measurements were performed at the HIKE[5] end-station installed at the KMC-1 bending magnet beamline located at the storage ring BESSY II in Berlin[6], a

[5] high kinetic energy electron spectroscopy
[6] BESSY II is part of Helmholtz-Zentrum Berlin für Materialien und Energie

state-of-the-art 3rd generation synchrotron radiation facility operated at an electron beam energy of 1.7 GeV [308]. KMC-1 beamline uses a double crystal monochromator operating in the range 1.7 - 12 keV, using different sets of crystals [247, 111]. By varying tender/hard X-ray excitation energies depth-resolved information of buried layers can be obtained, which is a great advantage for the study of real device structures. As the signal intensity of photoelectrons originating from buried layers is always significantly superimposed by near-surface signals, appropriate sample preparation and data deconvolution always play a crucial role in HAXPES data analysis.
In order to prevent beam-induced sample degradation of organic thin layers, HAXPES measurements were conducted during BESSY II's low intensity modes: (i) *'low-α multi bunch hybrid mode A'* with an initial ring current of 15 mA, and (ii) *'low intensity single bunch mode'* with 13.75 mA ring current. For comparison, the *'standard multi bunch hybrid top-up mode'* has a ring current of 300 mA. As it will be presented in section 6.1, within our HAXPES study of the buried PEDOT:PSS/c-Si interface, no degradation of the samples due to X-ray radiation was observed.

"Low dose" UPS at BESSY II

In addition, UPS experiments were performed at the end station SurICat (beamline PM4) at BESSY II [319]. This end station provides excitation energies in the UV range and offers the opportunity for in-system organic layer deposition. Samples can then be directly transferred from the preparation chamber (base pressure $< 5 \times 10^{-7}$ mbar) to the analysis chamber (base pressure $< 5 \times 10^{-9}$ mbar) without breaking vacuum. As it is a dipole beamline, the light intensity of SurICat is rather small, comparable to lab-based UPS using He radiation. The energy level alignment at the Tc/c-Si interface was investigated with this setup.

3.2.2 Surface photovoltage

The surface photovoltage (SPV) method [122] was employed to determine the equilibrium surface band bending eφ in c-Si of heterojunction a-Si/c-Si samples [160]. The principle of SPV is sketched in Figure 3.6. By placing an insulating mica plate in between a TCO coated ("metal-like") quartz glass and the semiconductor sample itself, a metal-insulating-semiconductor (MIS) structure is formed. A gold-plated chuck provides an Ohmic back contact. Upon intense illumination of the sample by a short laser pulse[7] excess charge carriers are generated in the sample, leading to flattening of the bands and a split-up of the quasi-Fermi levels of electrons, $E_{\mathrm{F,n}}$, and holes, $E_{\mathrm{F,p}}$, respectively (sketched red in Fig. 3.6). Since the chosen photon energy of E_{phot} = 1.37 eV is smaller than the a-Si band gap, generation predominantly takes place in c-Si. The corresponding change in the surface potential by the redistribution of photogenerated charge carriers is measured capacitively as a photovoltage pulse $V_{\mathrm{SPV}}(t)$. The illumination intensity is chosen high enough to reach flat-band conditions. This is the case for high injection conditions when charge carrier densities $n_{\mathrm{illum}}p_{\mathrm{illum}} \gg n_{\mathrm{dark}}p_{\mathrm{dark}}$. After correction for the Dember voltage resulting from the difference in mobilities of electrons and holes [79, 122], the initially detected

[7] in the here used setup: photon flux 10^{19} cm^{-2}s^{-1}, t_{pulse} = 150 ns

voltage signal right after the laser pulse $V_{\mathrm{SPV,corr}}(t{=}0)$, corresponds to the surface band bending eφ in the dark. Note that comparably slow recharging processes of a-Si:H defect states, which mainly occur through injection of charge carriers from photogenerated electron-hole pairs in c-Si are supposed to have a negligible effect on $V_{\mathrm{SPV,corr}}(t{=}0)$. Thus, thin a-Si only affect the SPV decay transient $(t{>}0)$ [255].

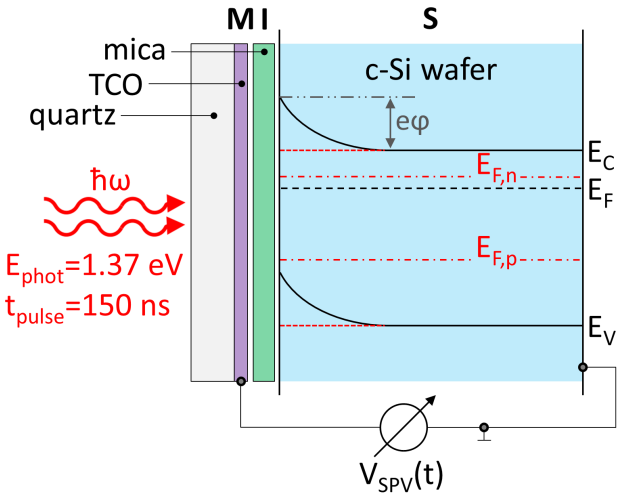

Figure 3.6: Schematic of the surface photovoltage (SPV) measurement setup. A metal-insulator-semiconductor (MIS) structure is formed by an insulating mica plate placed in between a TCO coated quartz glass and the sample itself. A short and intense laser pulse induces flat-band conditions in the c-Si wafer. After Dember voltage correction, the equilibrium band bending (eφ) can be determined from the capacitively detected change in surface potential.

3.2.3 Transient photoconductive decay

Measurements of minority-carrier lifetime in Si wafers are extremely valuable for process control and device optimization. The technique is based on the analysis of photoconductive decay (PCD) transients after a short light pulse. PCD is a well-established and fast method to access a-Si/c-Si interface passivation quality. In this work a commercially available *WCT-100 Sinton* setup is used. A Xe flash lamp generates free charge carriers in the sample. The injection dependent photoconductance, $\sigma_L(t)$, which is directly related to the minority excess carriers, Δn, is measured by placing the sample above an inductive coil. If the light flash is decaying at least a few orders of magnitude faster than the carrier lifetime, the injection dependent effective carrier lifetime, τ_{eff}, can be determined by [272]:

$$\tau_{\mathrm{eff}}(\Delta n) = \frac{\sigma_L}{j_{\mathrm{ph}}(\mu_n + \mu_h)} \,. \tag{3.3}$$

For c-Si the electron and hole mobilities (μ_n, μ_h) and their dependence on both, doping and injection level, are well known. The excitation photocurrent density, j_{ph}, has to be calibrated to the light intensity by a reference cell [272].
The mode described so far is called transient PCD (TRPCD). In the given setup, it allows to extract $\tau_{\mathrm{eff}} \gtrsim 400\ \mu$s. For shorter life times, when the decay times of carrier density and light flash are similar, the additional carrier excitation due to the light pulse has to be taken into account. In the so called quasi-steady-state mode (QSSPC) [272], by fitting the obtained injection-dependent

lifetime curve, $\tau_{\text{eff}}(\Delta n)$, with a semi analytical model derived by C. Leendertz et al., the interface defect density, D_{it}, and the interface charge, Q_{it}, can be quantified [173]. Therefore it is possible to discriminate between chemical passivation and field effect passivation at the a-Si:H/c-Si interface.
The excess carrier density of holes, Δp, and electrons, Δn, obtained by PCD measurements depend on the quasi Fermi level splitting under illumination. This splitting constitutes the maximum achievable V_{oc} of a solar cell with the corresponding lifetime. It is commonly called implied V_{oc} (iV_{oc}) and can be estimated by using the formula [272]:

$$iV_{\text{oc}} = \frac{k_B T}{q} \ln\left(\frac{\Delta n(N_A + \Delta p)}{{n_i}^2} + 1\right) . \tag{3.4}$$

Thus, from carrier lifetime measurements the V_{oc} potential of solar cell precursor layer stacks without metallization can be estimated.
Samples for PCD measurements must not be metallallized to allow for inductive coupling. Ideally they are symmetrically processed [272, 173, 190].

3.2.4 UV-VIS-NIR optical spectroscopy

To determine the absorption of thin film Tc, optical spectroscopy measurements in the UV-VIS-NIR range from 175 nm to 2500 nm were carried out using a commercial *Perkin Elmer Lambda1050* spectrophotometer. The UV light is provided by a deuterium lamp, a halogen lamp is used for the VIS-NIR spectral range. The incident light beam is monochromated by gratings. As sketched in Figure 3.7 (a), by placing the sample directly in front of the entrance slit of the integrating sphere, transmission (T) is recorded. Obviously, to measure transmission as described above, Tc layers have to be grown on transparent (quartz) glass substrates. By placing the sample behind the integrating sphere, reflection (R) is detected (Fig. 3.7 (b)). To account for and eliminate intensity fluctuations of the light, an additional reference beam is directed through a second port into the integrating sphere (not sketched in Fig. 3.7). Before each measurement, calibration and baseline corrections are performed and extracted from the recorded spectra. The absorption of a sample is then calculated by A = 100% - T - R.

3.2.5 Spectroscopic ellipsometry

Ellipsometry is an optical technique for investigating dielectric properties of thin films. Its principle is based on the material property to change polarization of electromagnetic waves upon reflection at the sample surface. As depicted in Figure 3.8, in spectroscopic ellipsometry (SE) measurements the sample is illuminated with monochromatic and circularly polarized light. The reflected light is elliptically polarized due to differences in the complex reflection coefficients for parallel and perpendicular polarization contributions. This change can be detected while sweeping the excitation energy.

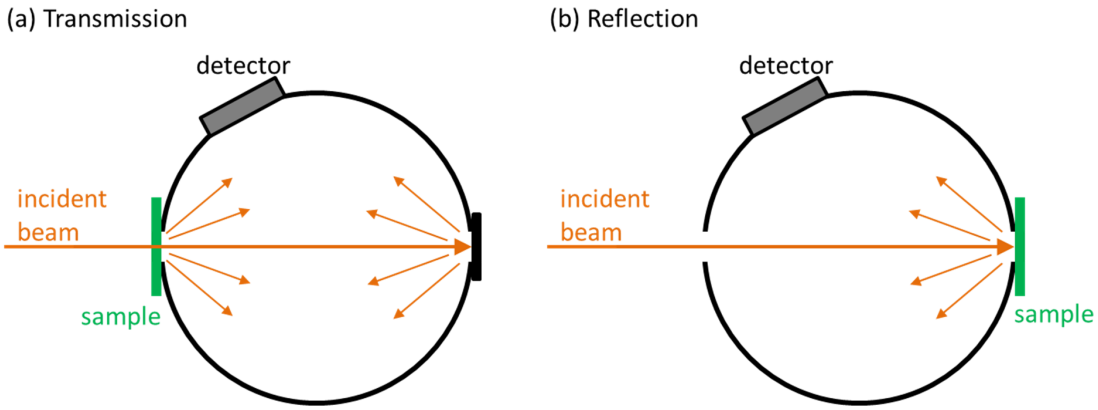

Figure 3.7: Sketch of a horizontal section through an integrating sphere as it is used for measuring (a) transmission and (b) reflection.

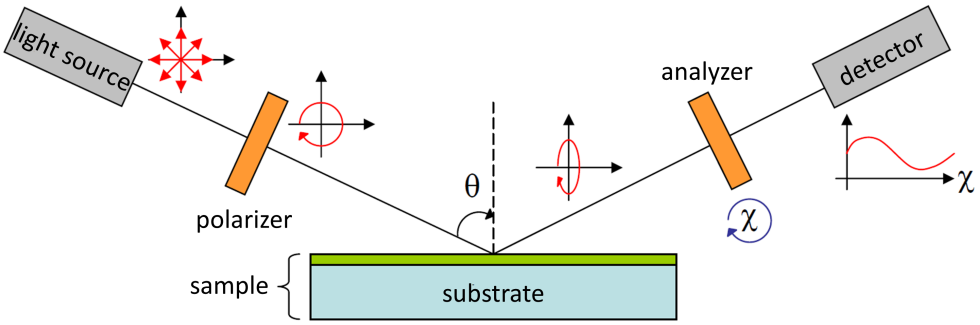

Figure 3.8: Scheme of the spectroscopic ellipsometry experiment. The sample is illuminated with monochromatic and circularly polarized light. The reflected light is elliptically polarized due to differences in the complex reflection coefficients for parallel and perpendicular polarization contributions. While sweeping the excitation energy, the polarization state of the reflected beam is analyzed by the combination of a rotatable linear polarizer and a detector. Figure adopted from Ref. [255].

Known as the fundamental equation of ellipsometry, the measured quantity is given by [12]

$$\rho = \frac{\tilde{r}_p}{\tilde{r}_s} \equiv \tan\Psi_{\mathrm{el}} \cdot \exp(i\Delta)\,, \tag{3.5}$$

with the complex Fresnel reflection coefficients $\tilde{r}_p$ and $\tilde{r}_s$. It defines the two quantities Δ and Ψ_{el} being a measure for change in phase difference and ratio of amplitudes, respectively. Ellipsometry is an indirect method, i.e. the measured quantities Δ and Ψ_{el} cannot be converted directly into the optical constants of the sample and a model analysis must be performed.
In this work, spectral ellipsometry was conducted to determine the optical constants of a-Si:H layers and PEDOT:PSS. Following G. E. Jellison et al., the model for the dielectric function of amorphous semiconductors like a-Si:H includes a Tauc fit of the band gap [298], a Lorentz oscillator which account for the absorption in the solid body [139], and a surface roughness layer with a-Si:H host matrix in the framework of the Bruggeman effective medium approach [41]. SE data of PEDOT:PSS was analyzed assuming uniaxial anisotropy of the spin-coated polymer on flat c-Si surfaces, following L. A. A. Pettersson et al. [221, 222]. For each component a model consisting of a Lorentz oscillator and a Drude term, accounting for free carrier absorption in the highly doped polymer film was used.
For further reading on the SE method and its model based data analysis, the reader is referred to Ref. [12].

3.2.6 Time-correlated single photon counting

As described in section 2.3.1 (cf. Fig. 2.6), dynamics of the SF process in Tc can be monitored by time-resolved detection of the fluorescence signal which stems from the emissive singlet state. For this purpose time-correlated single photon counting (TCSPC) measurements were conducted. TCSPC is a statistical method based on the detection of single photons with high sensitivity and picosecond time resolution, thus suitable to acquire transient photoluminescence (PL) decay curves.
The TCSPC setup used in this study is sketched in Figure 3.9. The optical arrangement is similar to that of a scanning confocal microscope. Through a neutral density (ND) filter the intensity of the pulsed laser beam can be adjusted. The incoming laser beam is focused onto the sample and the emitted PL is collected by the same lens L2. By inserting lens L1, the beam waist on the sample can be tuned. The power density at the sample position is measured with a photodiode. A mirror with a center hole spatially separates the PL signal from the excitation laser beam and directs it through filter wheels which efficiently block the residual laser light. Finally, L3 couples the light into a multimode fiber connected to the detector/monochromator.
A sketch of the TCSPC detection principle is shown in Figure 3.10. The sample is excited by a pulsed laser source[8] and the time difference between excitation and detection of a single photon stemming from a PL event is recorded. Over multiple detection events the photon distribution $n(t)$ over the detection times of the single photons in the signal period is then build up in a histogram [118]. As the electronics can only detect one event per trigger, it is therefore essential

[8] high repetition rates > 100 kHz

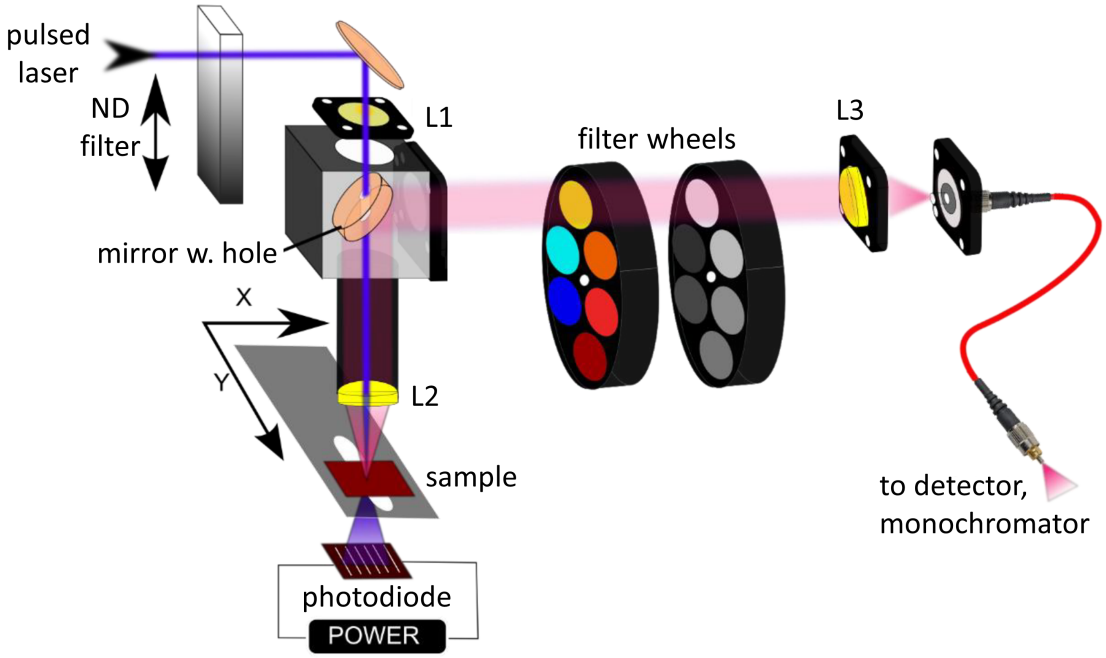

Figure 3.9: Time-resolved single photon counting (TCSPC) setup. Coincidentally, lens L2 focuses the incoming laser beam onto the sample and collects the emitted photoluminescence (PL) signal. A mirror with a center hole separates the PL signal from the excitation laser beam. Through filter wheels the residual laser light intensity is blocked from the PL signal before entering the detector. With a photodiode the excitation power density at the position of the sample is monitored.

to keep the rate of incoming PL events low to prevent distortion of the statistics. It is shown in literature that the counting rate should be $\lesssim 5\%$ of the laser repetition rate to sufficiently prevent this so called "pile-up" effect [209, 30, 31].

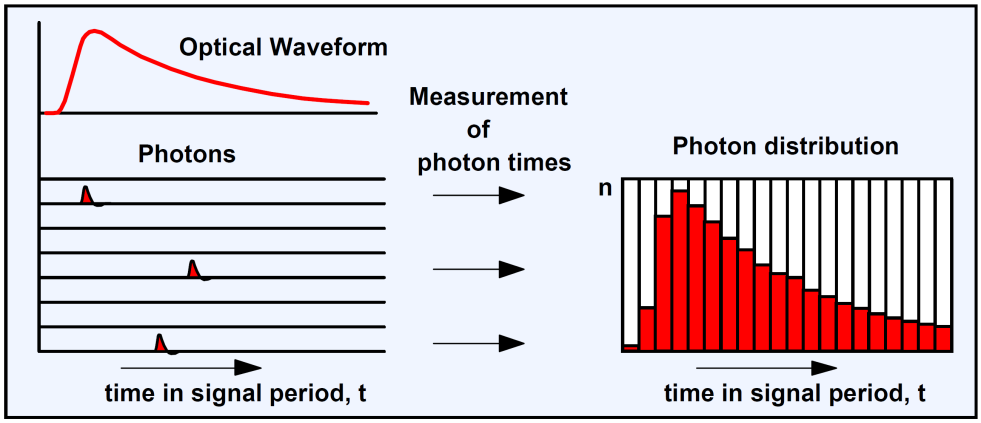

Figure 3.10: Principle of time-resolved single photon counting (TCSPC) method. Single photons of a periodic light signal are detected (left). Over multiple detection events the photon distribution over the detection times of the single photons in the signal period is then build up (right). Figure adapted from Ref. [118].

3.3 Solar cell diagnostics

Solar cells were analyzed by means of capacitance-voltage, C-V, and current density-voltage, $j(V)$, measurements. Quantum efficiency spectra as a function of wavelength were recorded under various measurement conditions, such as temperature and external voltage.

Capacitance-voltage measurements

C-V measurements in four-terminal contact configuration were carried out with a *Keithley* source-measure unit operating at 10 kHz with an ac amplitude of 10 mV and a voltage sweep between -2 V and 2 V[9]. Plotting 1/C^2-V and fitting the linear part according to [288]

$$\frac{1}{C^2} = \frac{2\left(\frac{k_B T}{q} - \Psi_{\mathrm{bi}} - V\right)}{qA^2\epsilon_0\epsilon_{Si}N_D}, \tag{3.6}$$

with the device area, A, and the permittivity of Si, $\epsilon_0\epsilon_{Si}$, allows the determination of the built-in voltage, Ψ_{bi}, at the SHJ as well as the doping concentration, N_D, of Si wafers. Ψ_{bi} can be extracted from the V-axis intercept and N_D from the slope, respectively [288].

[9] C-V measurements were carried out at the Max-Planck,Institute for the Science of Light, Erlangen

Current density-voltage characteristics

Dark and illuminated $j(V)$-curves were measured in a four-probe setup employing a *Keithley* source-measure unit. Devices are pneumatically fixed on a temperature controllable metal chuck serving at the same time as the electron back contact. The hole contact is realized via gold wires carefully pressed onto the solar cell's front contact grid. For calibration of the solar simulator a certified c-Si reference cell[10] was employed. Standard test conditions at 1000 W/m^2 light intensity (AM1.5G) were achieved by matching the short-circuit current density, j_{sc}, of the reference cell to its certified value by adjusting the electrical power input of the light source consisting of a Xe lamp for the short wavelength, and a halogen lamp for the long wavelength region, respectively. Standardly, the metal chuck is hold at 25 °C.

Quantum efficiency measurements

The spectral response, $SR(\lambda)$, of a solar cell is defined as the ratio of short-circuit current density, $j_{\mathrm{sc}}(\lambda)$, and monochromatic power density, $E(\lambda)$. It provides valuable additional information to the illuminated $j(V)$-curves. The external quantum efficiency, EQE, as a function of wavelength λ is defined as

$$\mathrm{EQE}(\lambda) = SR(\lambda) \cdot \frac{hc}{e\lambda}\,, \tag{3.7}$$

thus constitutes the ratio of created and extracted charge carriers to the number of incident photons [274]. For conventional c-Si based single band gap solar cells the EQE has values between 0 ... 1. However, as it is subject of the present work, EQE values > 1 are possible if multi-exciton generating materials can be successfully implemented in a device. EQE is measured using a lock-in technique with chopped monochromatic light[11]. During EQE measurements white bias light can be superimposed to imitate 1 sun illumination in order to provide realistic injection conditions. Furthermore, EQE measurements with external applied voltages (-2 V ... 2 V) as well as sample heating (RT ... 100 °C) can be performed. EQE setup details are given in Ref. [127]. By multiplying the EQE with the AM1.5G solar spectrum and integration over the wavelength range of interest, the photocurrent can be calculated.

[10] Fraunhofer Institute for Solar Energy Systems, Freiburg

[11] combination of halogen and Xe lamp with grating monochromator

4

Wide band gap a-SiO_x passivation layers in Si heterojunction solar cells

High efficiency Si heterojunction (SHJ) solar cells hold the current world record of 26.33% [91, 338] which is already close (∼90%) to the theoretical limit of ∼30% for single-junction c-Si based solar cells [267]. Those high efficiencies are possible because of excellent and full area passivated contacts provided by the incorporation of thin amorphous Si layers. However, a drawback in the standard both-side-contacted SHJ device architecture is the current loss due to parasitic absorption in the amorphous Si emitter and passivation layers on the solar cell's front side. Z. C. Holman et al. calculated total current density losses of about 2 mA/cm^2 in the 10 nm (p)a-Si:H emitter and about 1 mA/cm^2 in 5 nm (i)a-Si:H passivation layers [129]. Therefore, one possibility to further improve this technology could be the replacement of these a-Si:H layers by wider band gap and low absorption a-Si:H alloys like amorphous or microcrystalline Si oxides (a-SiO_x:H) [102, 83, 262, 185], or Si carbides [343, 36]. Unfortunately, larger band gaps might result in increased valence band offsets, ΔE_V, at the SHJ which impose a transport barrier for holes, thus counteracting the benefit of increased optical gaps.

In the study presented in this chapter wide band gap a-SiO_x was incorporated as passivation layers in both-side-contacted SHJ solar cells. A sketch of the specific device architecture is depicted in Figure 4.1 (a). For the absorber, commercially available n-doped c-Si wafers are used. The electron selective back contact is formed by an (i,n$^+$)a-Si:H layer stack. The hetero p-n junction is formed by a p-doped a-Si:H emitter and passivating intrinsic a-SiO_x:H layers with varying stoichiometry x. Solar cell contacts consist of an optimized ITO/Ti/Ag stack (cf. section 3.1).

At first, the stoichiometry x of various a-SiO_x layers and their passivation quality which is reflected in the interface defect density, D_{it}, were determined. Central to the study was the determination of ΔE_V at the a-SiO_x/c-Si heterojunction.

In a second step, (p)a-Si:H/(i)a-SiO_x:H/(n)c-Si heterojunction solar cells with intrinsic a-SiO_x:H passivation layers deposited using the same parameter sets were fabricated.

Figure 4.1 (b) depicts the band line-up of the SHJ solar cell at the front side. Hole transport from the c-Si absorber to the front contact can occur either by thermionic emission (TE) or by defect-

assisted tunnel hopping (TH) processes through the (i)a-SiO$_x$ passivation layers, depending on the transport barrier height imposed by ΔE_V [148, 237, 315].

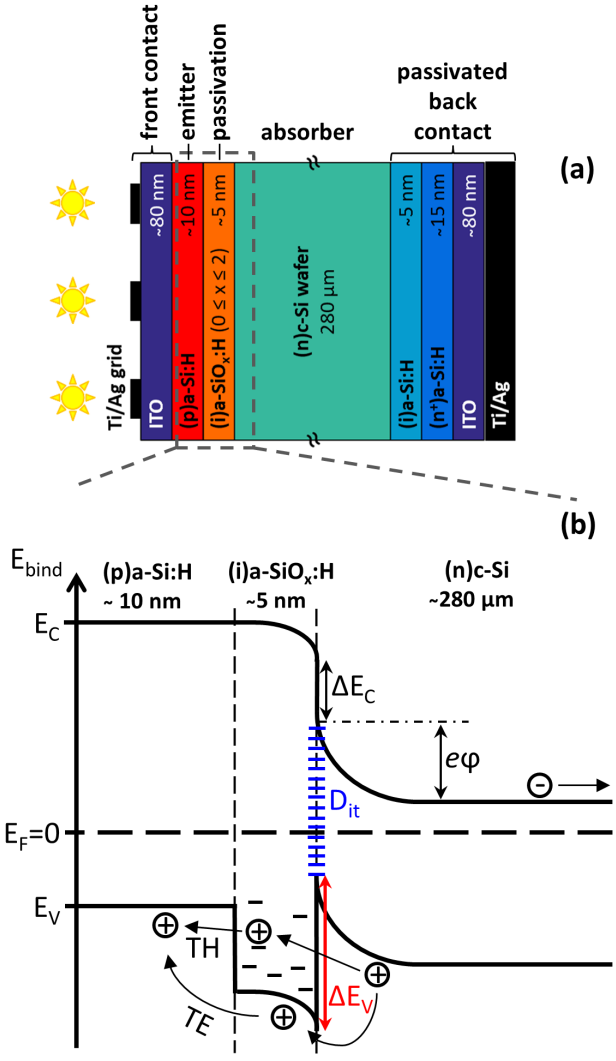

Figure 4.1: (a) Basic structure of the amorphous/crystalline SHJ solar cell (layer thicknesses not to scale). (b) Band line-up of the hole selective front contact of the SHJ solar cell. Holes which are generated in the (n)c-Si absorber can overcome the transport barrier imposed by the valence band offset (ΔE_V) either by thermionic emission (TE) or by tunnel-hopping processes (TH) through the thin (i)a-SiO$_x$:H passivation layer. They then travel in the (p)a-Si:H valence band and are collected at the TCO/metal(grid) front contact. The sketch also shows other relevant SHJ parameters like the c-Si band bending (eφ) and the interface defect density (D_{it}).

By combining both studies we can directly link the measured ΔE_V at the SHJ to solar cell performance. This direct correlation is a significant added value in comparison to former studies [102, 83, 262]. We are thus able to discuss the hole transport mechanisms across the SHJ, which is still an active field of research, in more detail.
Finally, we will comment on possibilities and strategies for a successful implementation of wide band gap materials to reduce the parasitic absorption in conventional both-side contacted SHJ solar cells.

Results presented in this chapter are published in a series of papers:

1. M. Liebhaber, M. Mews, T. F. Schulze, L. Korte, B. Rech, and K. Lips, *Valence band offset in heterojunctions between crystalline Si an amorphous Si (sub)oxides (a-SiO$_x$:H, 0<x<2)*,

Applied Physics Letters **106** (2015), 031601, http://dx.doi.org/10.1063/1.4906195, Ref. [177].

2. M. Mews, M. Liebhaber, B. Rech, and L. Korte, *Valence band alignment and hole transport in amorphous/crystalline Si heterojunction solar cells*, Applied Physics Letters **107** (2015), 013902, http://dx.doi.org/10.1063/1.4926402, Ref. [193].
3. M. Liebhaber, M. Mews, L. Korte, T. F. Schulze, B. Rech, and K. Lips, *Valence band offset and hole transport across a-SiO$_x$ (0<x<2) passivation layers in Si heterojunction solar cells*, 31st European Photovoltaic Solar Energy Conference and Exhibition (2015), 770, http://dx.doi.org/10.4229/EUPVSEC20152015-2AV.3.26, Ref. [176].

The study presented in this chapter is a co-operation project with M. Mews[1]. Amorphous SiO$_x$ layers were grown by M. Mews using PECVD. Analysis of the stoichiometry x of a-SiO$_x$ films and SHJ characterization, e.g. determination of the valence band offset, was carried out by the author of this thesis. SPV and PCD measurements were conducted by the author of this thesis and M. Mews. SHJ solar cell fabrication and analysis including "AFORS-HET" simulations, which constitute the basis for discussion of hole transport mechanism across SHJs, was carried out by M. Mews. All authors were involved in the interpretation and discussion of our results.
Sections 4.1 - 4.3 are based on papers [177, 176], Sections 4.3 - 4.5 on papers [193, 176].

4.1 Stoichiometry of a-SiO$_x$ layers

Amorphous SiO$_x$:H layers were grown with PECVD using $SiH_4/CO_2/H_2$ precursor gas mixtures. For passivation the gas flow of H_2 was kept constant at 5 sccm. SiH_4 and CO_2 gas flows added up to a total of 10 sccm. In order to vary the stoichiometry x of a-SiO$_x$ films, the ratio R = CO_2/SiH_4 was varied from 0 to 4. A more detailed description of layer deposition is given in section 3.1.
Conventional PES, i.e. XPS using Mg K$_\alpha$ or Al K$_\alpha$ radiation, as well as UPS using He-I$_\alpha$ radiation is surface sensitive (cf. Fig. 3.4 in section 3.2.1). Thus, to minimize surface oxidation and other contamination by surface adsorbates, a vacuum transfer of the samples from the PECVD cluster to the ultrahigh vacuum PES analysis chamber was employed.
Based on an XPS analysis, we monitor in a first step the evolution of the stoichiometry x of various (i)a-SiO$_x$ layers. XPS is a core level spectroscopy. Each element has specific core level peaks which are tabulated in literature, e.g. the NIST database [210].
Amorphous Si oxides consist of a composition of various Si suboxide states. On the bottom of Figure 4.2 various Si oxidation states are depicted. Depending on whether the central Si atom is bonded to 1, 2, 3, or 4 oxygen atoms, the oxidation states are denoted as Si^{1+} ... Si^{4+}. Thus, the near-field surrounding of the central Si atom is different in each oxidation state which results in a chemical shift of the Si 2p core level peak. Each oxidation state has its specific binding energy [126, 180].
Figure 4.2 (a) shows the XPS raw data using Mg K$_\alpha$ radiation of the Si 2p core level peak of various (i)a-SiO$_x$:H layers. For pure (i)a-Si:H (0 sccm CO_2, black curve in Fig. 4.2 (a)) there

[1] Institute for Silicon Photovoltaics, HZB

is only one peak in the spectrum located at about 99.4 eV. This is in accordance with literature values [210] and corresponds to pure amorphous Si, denoted as Si^{0+}. For an increasing CO_2 flow during layer deposition O is incorporated in the amorphous structure forming Si-O bonds. Thus, the Si^{0+} peak is gradually reduced and coincidentally peaks corresponding to core level signals from the various Si oxidation states (Si^{1+} ... Si^{4+}) appear on the higher binding energy side between 101 - 104 eV. For the highest CO_2 flow of 8 sccm (cyan spectrum in Fig 4.2(a)), the Si^{0+} contribution is almost vanished.

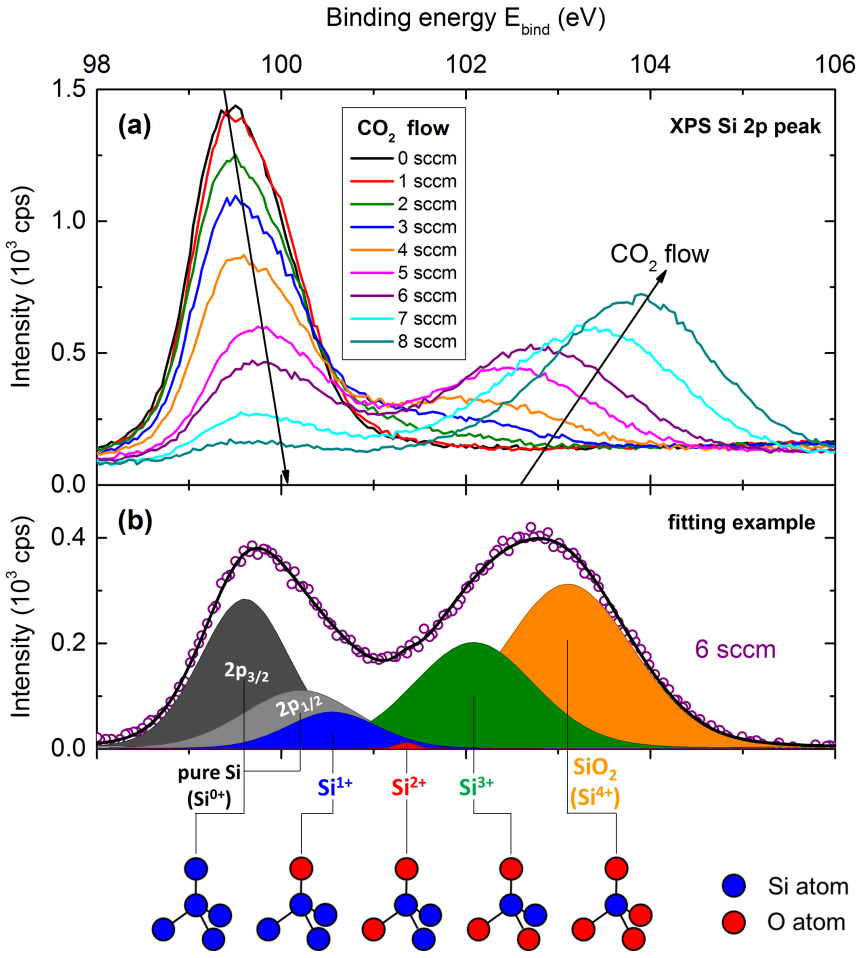

Figure 4.2: (a) XPS raw data of the Si 2p peak for (i)a-SiO$_x$:H layers deposited with different precursor gas flow rates of SiH_4/CO_2. (b) Exemplary peak fit for 6 sccm CO_2 flow showing the different Si oxidation states which are depicted on the bottom. The composition and shift of the Si 2p peak indicate pronounced changes in the Si chemical environment upon O incorporation. Figure adopted from publication [176].

XPS spectra were fitted with the software "XPS-Peak41" using tabulated peak positions for the different Si oxidation states [126, 180]. An exemplary fit is shown in Figure 4.2 (b) for a sub-stoichiometric a-SiO$_x$ layer grown with a CO_2 gas flow of 6 sccm. Prior to fitting, a Shirley

background [266] was subtracted. The Si^{0+} peak is spin-orbit split into Si $2p_{3/2}$ and Si $2p_{1/2}$ [210]. All peaks are fitted using Voigt profiles, thus accounting for both, the intrinsic life-time broadening of the core level state which has a Lorentzian line shape and a Gaussian distribution accounting for the experimental broadening [124].
Following this well established fitting analysis, the stoichiometry x of (i)a-SiO$_x$ films can be calculated based on the ratio of various suboxide peak areas using the formula [126, 180]:

$$\frac{O}{Si} = \frac{1}{2}\sum_{j=0}^{4} j \cdot \frac{A_j}{A_{\text{total}}}, \tag{4.1}$$

where j denotes the different oxidation states with their corresponding peak areas A_j. This procedure was crosschecked with a complementary method based on the O 1s/Si 2s peak ratios weighted with their respective atomic sensitivity factors [321].
Figure 4.3 shows the resulting calibration curve. PECVD precursor gas flows of SiH_4 (ranging from 10 to 2 sccm, visualized in green bars) and CO_2 (ranging from 0 to 8 sccm, visualized in red bars), respectively, can be related to stoichiometry x of corresponding a-SiO$_x$ layers. Values of blue points are deduced from XPS data analysis using the ratios of O 1s/Si 2s peak areas, black squares are determined from the relative contributions of the Si oxidation states in the Si 2p peak. Both methods yield comparable results. Our layers range from pure a-Si:H to nearly stoichiometric a-SiO_2. A non-linear dependency of stoichiometry x on PECVD gas phase composition is observed.
Note that the C concentration stayed well below 3% of the O concentration for all layers.

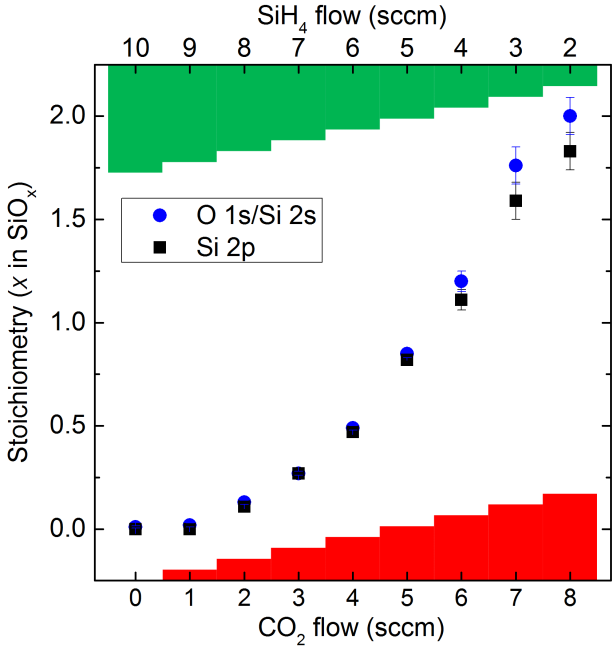

Figure 4.3: Stoichiometry x of (i)a-SiO$_x$:H films in dependence on SiH_4/CO_2 precursor gas flow ratios (green and red bars) during layer deposition as deduced from XPS data analysis using either the ratios of the O 1s to the Si 2s peak areas (blue points) or the relative contributions of the Si oxidation states of the Si 2p peak. Figure as published in Ref. [176].

4.2 Valence band structure of a-SiO$_x$ layers

In a next step, we assess the changes in the VB structure of the (i)a-SiO$_x$:H layers over the whole stoichiometry range by using various modes of UPS.
As introduced in section 3.2.1, the sensitivity of the CFSYS mode is greatly superior to the conventional He-UPS which enables to detect valence band tail and mid-gap defect states. An example for the valence band DOS of intrinsic a-Si:H, measured in the CFSYS mode, is shown in Figure 4.4 (black circles). The energetic distribution of the DOS, $N(E)$, consists of the valence band $N_V(E)$ (grey shaded), an exponential decaying valence band tail $N_V^t(E)$ (blue line) due to disorder in the atomic lattice [278], and a broad Gaussian dangling bond distribution $N_d(E)$ (red curve).

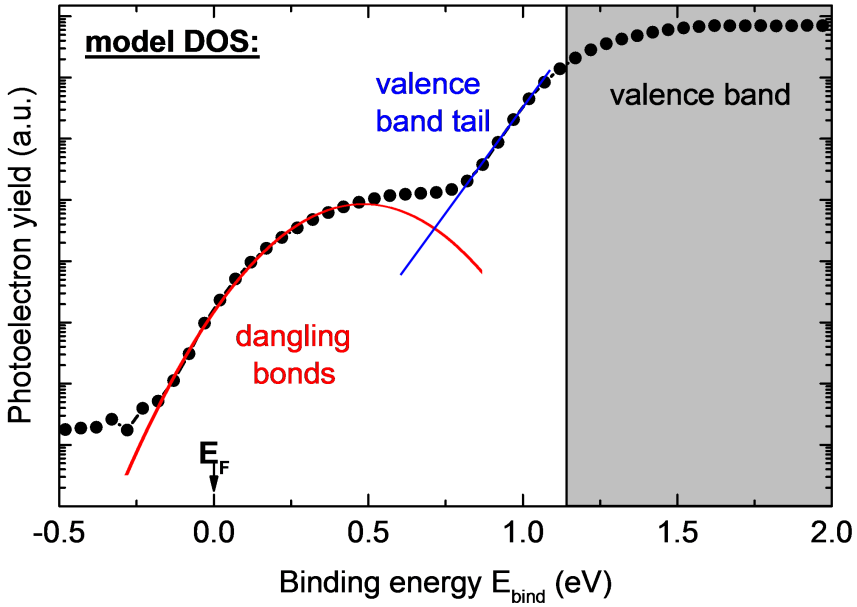

Figure 4.4: Constant final state yield spectrum (CFSYS) of a standard (i)a-Si:H sample (black circles). The measured density of occupied states (DOS) features the typical broad distribution of of dangling bond defect states in the band gap and the extended valence band tail states. By fitting a model DOS, valence band edge position, exponentially decaying (blue line) valence band tail slope (Urbach energy), and parameters of the Gaussian distribution (red curve) of dangling bonds can be extracted [159, 163].

A model DOS, $N(E) = N_V(E) + N_V^t(E) + N_d(E)$, can be fitted to the measured valence band structure, whereby the exponential decaying valence band tail is mathematically described by

$$N_V^t(E) = N_{0V}^t \cdot \exp\left(\frac{E_V^t - E}{E_{0V}}\right), \tag{4.2}$$

with the Urbach energy E_{0V} determining the slope of the decay [314, 165, 62]. The defect density in the band gap is modeled as

$$N_d(E) = N_{0d} \cdot \exp\left(-\frac{(E - E_d)^2}{2\sigma_d^2}\right), \tag{4.3}$$

with a Gaussian dangling bond distribution σ_d^2. The model parameters are varied, to obtain a best least-squares fit of the convolution of the model DOS, $N(E)$, with the experimentally determined transfer function. Further details of CFSYS measurements at (i)a-Si:H films and its model based analysis can be found in Refs. [251, 159, 161, 162, 163].
Figure 4.5 (a) shows near-UV CFSYS spectra, in panel (b) conventional UPS spectra using 21.2 eV He-I$_\alpha$ radiation are plotted. UPS measurements were performed on the same sample set as used in the XPS analysis presented above. Therefore, the legend is given in the deduced stoichiometry x and the color coding of various a-SiO$_x$ layers corresponds to Figure 4.2. The CFSYS spectra for the low-x samples in Figure 4.5 (a) show the typical a-Si:H DOS signatures as described above. The valence band extends into the exponentially decaying valence band tail which merges into a broad distribution of midgap dangling bond (DB) defects. At the Fermi edge (E_F), the DB signal is cut off smoothly due to experimental broadening caused by the finite resolution of the excitation source and energy analyzer. Valence band edge positions (relative to E_F) obtained by fitting CFSYS data with the model DOS are marked with points. As seen in Figure 4.5 (a), for increasing O concentration the valence band edge position steadily shifts to higher E_{bind}, while the valence band tail is getting shallower. The amplitude of the DB-related peak increases before it saturates, while its width steadily increases. The net result is a steady increase of DB density for increasing stoichiometry x, consistent with the increasing density of strained bonds manifesting in the valence band tail. For stoichiometries x > 0.84, the valence band edge position is shifted too far towards higher binding energies and thus beyond the range accessible with the UV lamp used in this study providing excitation energies between $\sim$ 4.0 - 7.3 eV. Therefore, to further track the evolution of the valence band edge position, the standard He-UPS mode with a higher excitation energy of 21.2 eV was used. As seen in Figure 4.5 (b), the valence band edge positions, marked with arrows, are determined by a linear extrapolation of the DOS leading edge to zero. Since He-UPS is less sensitive than CFSYS, valence band tails or dangling bonds cannot be resolved within the signal-to-noise of those measurements. Moreover, at the a-SiO$_{0.84}$:H sample both methods were applied for the determination of the valence band edge position and an agreement within 0.3 eV was found. This value is taken as an estimate for the systematic error for the determination of the valence band edge in the PES study.

4.3 Discussion of a-SiO$_x$/c-Si valence band offset and interface passivation

By fitting CFSYS data with a model DOS as described above, the valence band edge positions $E_V^{\mathrm{a-Si}}$ relative to E_F were obtained. It is obvious from Figure 4.1 (b) that in order to deter-

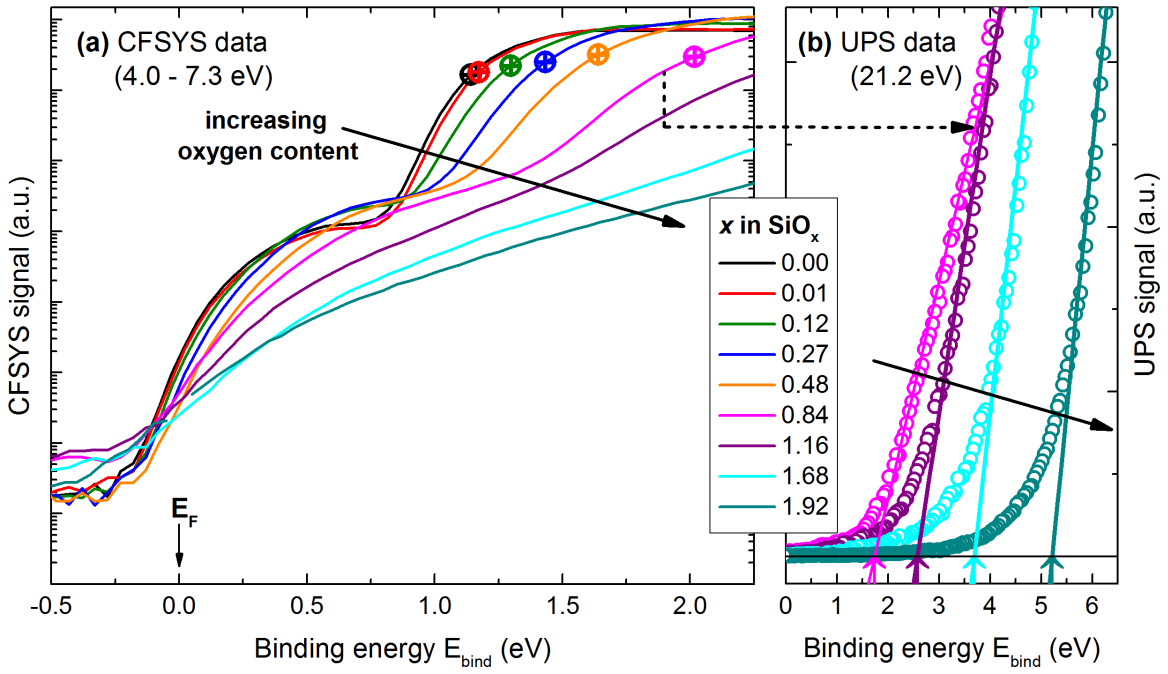

Figure 4.5: (a) CFSYS spectra of the valence band (VB) DOS of a-SiO$_x$:H layers with different stoichiometries x, starting from a typical a-Si:H DOS featuring a broad distribution of dangling bonds and an exponentially decaying band tail. The dots denote the position of the VB edge as obtained by fitting a model DOS to the CFSYS data. The DOS features and model fitting is described in Figure 4.4. A continuous shift to higher binding energies for increasing O contents is observed. (b) UPS data in which the VB edge positions (arrow marks) are obtained by linear extrapolation of the DOS leading edge to zero. Figure adopted from publication [176].

mine the valence band offset, ΔE_V, at the a-SiO$_x$/c-Si HJ, we need to further consider possible changes in the band bending, eφ, in the c-Si wafer. For that reason the SPV technique (cf. section 3.2.2) was utilized to measure eφ on the PES samples immediately after removal from the UHV system. We find eφ < 0.15 eV for all the samples. By taking these values into account, ΔE_V can be calculated by using the formula $\Delta E_V = E_V^{\mathrm{a-Si}} - E_V^{\mathrm{c-Si}} + \mathrm{e}\varphi$ (cf. Fig. 4.1 (b)) [258, 177]. The results obtained so far are summarized in Figure 4.6 (a). The panel displays the calculated ΔE_V combining PES (in the CFSYS and He-UPS mode) and SPV results. Values are plotted against stoichiometry x of a-SiO$_x$ layers, which was determined by XPS measurements. We report values starting from $\Delta E_V \approx 0.3$ eV for pure a-Si:H, which monotonously increase to more than 4.0 eV for near-stoichiometric a-SiO$_2$. As stated above, in the low-x regime ($x \leq 0.84$, grey shaded area), the valence band edge positions were obtained by CFSYS (filled circles). The excitation energy of 4.0 - 7.3 eV in this mode is too low to extract the valence band edge positions in the high-x regime (cf. Fig. 4.5). Thus, we conducted the less sensitive, conventional He-UPS method using an excitation energy of 21.2 eV to further track the evolution of the valence band

edge. For x = 0.84 both methods were applied and an agreement within 0.3 eV was found. Note that the uncertainty in the determination of the VB edge position for He-UPS data is larger than for CFSYS experiments. This is reflected in the error bars of Figure 4.6 (a).
Concerning the *end points* of the stoichiometry series, the results are in line with previous works. In a theoretical study of band offsets between crystalline and amorphous Si, C. G. Van de Walle and L. H. Yang calculated ΔE_V = 0.2 eV for 11%-hydrogen containing a-Si:H on c-Si [71]. In previous studies conducted at HZB, values for ΔE_V between 0.3 - 0.45 eV for a-Si:H layers grown in the same PECVD cluster tool, which mostly revealed a higher H concentration, were determined [258, 163]. Given the wide variety of different possible H microstructures in PECVD grown a-Si:H layers, which affects the bandgap and band offsets [71, 258], $\Delta E_V \approx 0.3$ eV for our pure a-Si:H fits well with the existing data. For the stoichiometric a-SiO$_2$/c-Si heterojunction, $\Delta E_V \approx 4.4$ eV has been established experimentally [151, 205], which is also in line with the results presented in Figure 4.6 (a).
Following the study of T. F. Schulze et al. [258], the H content in our a-SiO$_x$:H layers was quantified using Fourier transform infrared spectroscopy. A decrease of the H content from about 20% for pure (i)a-Si:H to ∼0% for high-x a-SiO$_x$:H films, with a particularly steep decrease at around $x \approx 0.5$ was found. Theoretical [71], as well as experimental studies [258] report an increasing ΔE_V for raising H contents in a-Si:H layers. Thus, from the evolution of the H content alone, a net *decrease* of ΔE_V with a magnitude of ∼0.25 - 0.6 eV depending on the assumed correlation of the H content with ΔE_V would be expected for our a-SiO$_x$:H ($0 \leq x < 2$) series [71, 258]. In contrast, we observe a pronounced *increase* of ΔE_V with x by more than 3.5 eV which therefore proves that the O content is the main driver for ΔE_V in the samples considered here. However, as will be discussed in the next paragraph, H incorporation may play an important role for SHJ passivation.
As also indicated in Figure 4.6, SHJ solar cells were fabricated in the low-x regime. Device results will be presented in the next sections. The passivation behavior of a-SiO$_x$ layers will be discussed in the following.

For the investigation of the a-SiO$_x$:H passivation behavior we fabricated double-sided polished c-Si wafers symmetrically[2] passivated with identically prepared a-SiO$_x$:H layers as used for ΔE_V determination and conducted photoconductance decay (PCD) measurements as described in section 3.2.3. The interface defect density, D_{it}, can be extracted by fitting the data with a semi-empirical model describing interface recombination which was previously developed by C. Leendertz et al. [173]. In Figure 4.6 (b) the resulting D_{it} values for the as-deposited state (black circles) as well as after a subsequent 300 °C forming gas (H$_2$/N$_2$) annealing step (orange circles) are plotted against a-SiO$_x$:H layer stoichiometry x. Obviously, the passivation quality starts from an excellent level for the standard (i)a-Si:H at x = 0 and decreases for increasing x. A forming gas anneal is detrimental for low-x values, while D_{it} can be significantly decreased for higher x. The latter is consistent with previous studies on PECVD-grown a-SiO$_2$ [57] albeit on a low level. This indicates suboptimal PECVD parameters in the high-x regime regarding the resulting interface passivation quality. The observed trend in D_{it} is accompanied by a decreasing valence-band tail slope which corresponds to an increased Urbach energy $E_{0\mathrm{V}}$ [281], obtained by fitting

[2] PCD measurements require symmetric samples [173]

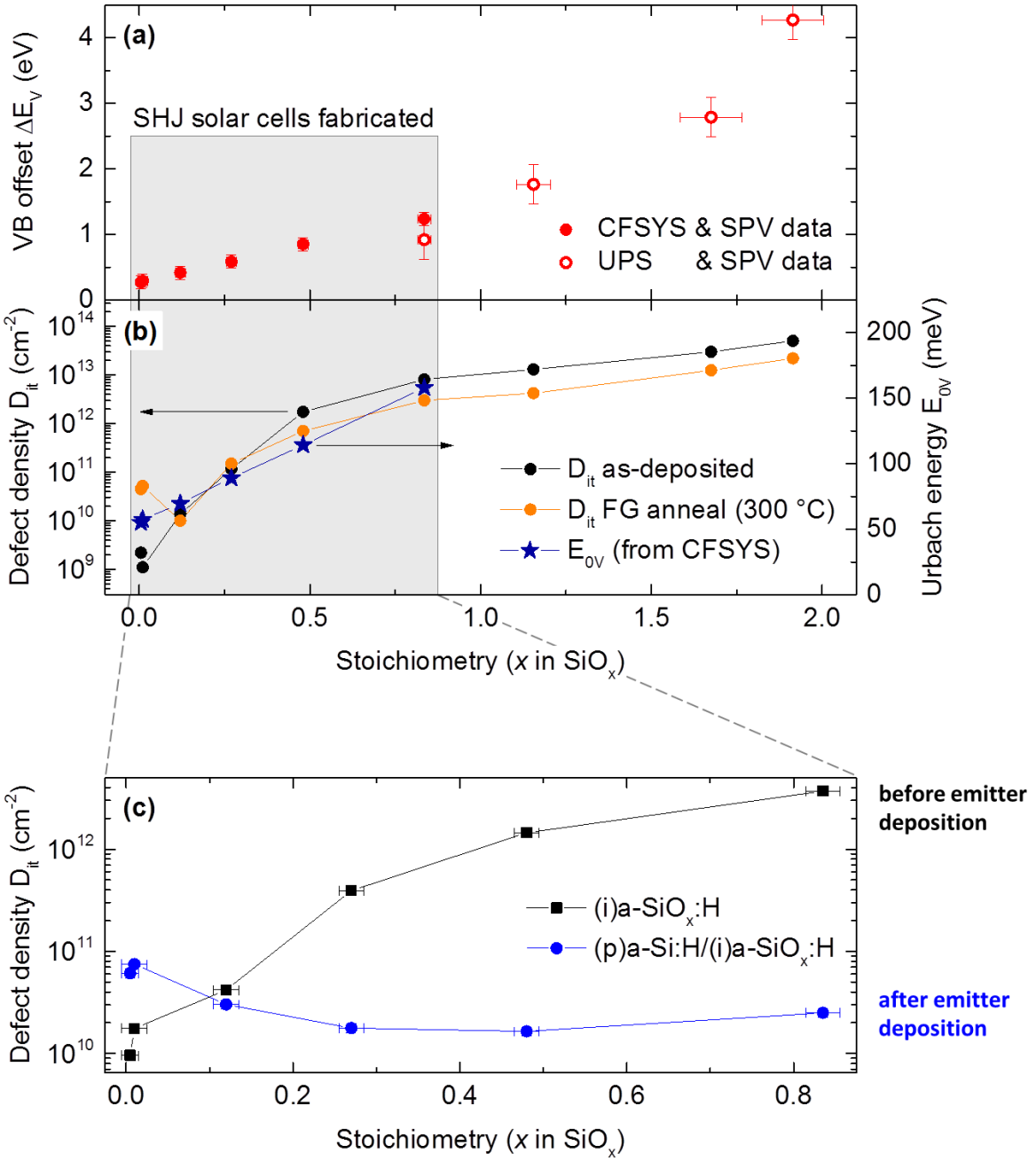

Figure 4.6: (a) Valence band offset, ΔE_V, at the a-SiO$_x$:H/c-Si heterojunction derived from combining PES and SPV data upon varying the O fraction in the layers. (b) Interface defect density, D_{it}, (left axis) as deduced from PCD measurements and Urbach energy, $E_{0\mathrm{V}}$, (right axis) determined from CFSYS data, marking the deterioration of a-SiO$_x$:H bulk electronic quality upon increased O incorporation. (c) D_{it} in the low-x regime: c-Si passivated with (i)a-SiO$_x$:H (black squares), and after additional (p)a-Si:H emitter deposition (blue circles). Figure adopted from our publications [177, 193, 176].

of CFSYS data (cf. Fig. 4.4) and plotted as stars in Figure 4.6 (b). This is consistent with the idea that D_{it} is closely related to the bulk defect density in the amorphous films [256]. PECVD parameters were optimized for pure (i)a-Si:H layers and, as described in section 3.1, only the ratio of SiH_4 and CO_2 precursor gases was varied to grow various a-SiO$_x$ layers. Non optimized deposition parameters for increasing O incorporation likely contribute to higher strain/disorder and thus increased bulk defect density in the a-SiO$_x$:H films [61] via the conversion of strained bonds into dangling bonds [231], manifesting in deteriorated interface passivation.

Finally, we turn to the discussion of interface passivation of SHJ solar cell relevant layer stacks in the low-x regime. Figure 4.6 (c) shows D_{it} values of device precursor structures consisting of a stack of (i)a-Si:H passivation and a (n$^+$)a-Si:H layer on the back, and (i)a-SiO$_x$:H (low-x regime) layers on the front side (black squares). D_{it} increases drastically for rising O content, but also decreases to the same order of magnitude after (p)a-Si:H emitter deposition on top of the (i)a-SiO$_x$:H passivation layers for x above 0.2 (blue circles), thus revealing a similar passivation quality as for the standard (i)a-Si:H/c-Si interface.
As a sufficient interface passivation for high-efficiency solar cells is essential, this is promising for the implementation of (i)a-SiO$_x$:H passivation layers in SHJ devices. During (p)a-Si:H layer fabrication using PECVD, the sample temperature stays below 200 °C. This is below the temperature which is required for thermal activation of bond reconfiguration in a post annealing step. Thus, it can be surmised that the lowered dangling bond concentration at the heterointerface, as evidenced by the reduced D_{it} after emitter deposition, is likely due to the saturation of dangling bonds with H which is provided during the additional plasma process [193, 176].
Note that the applied model for extraction of D_{it} from PCD measurements assumes symmetric samples [173], whereas the device precursor structures discussed here were not symmetric. This may lead to a slightly, below 10%, overestimation of the extracted D_{it} values [193].

4.4 Implementation of a-SiO$_x$ passivation layers in SHJ solar cells

So far we have analyzed and discussed a-SiO$_x$ bulk properties, as well as a-SiO$_x$:H/c-Si heterojunction parameters in the full stoichiometry range ($0 \leq x \lesssim 2$). In the second part of this study, (p)a-Si:H/(i)a-SiO$_x$:H/(n)c-Si heterojunction solar cells as depicted in Figure 4.1, with intrinsic a-SiO$_x$:H passivation layers deposited using the same parameter sets, were fabricated. The corresponding $j(V)$-characteristics measured under AM1.5G illumination are depicted in Figure 4.7. With the results presented above (cf. Fig. 4.6 (a)), we can discuss the SHJ solar cell results with respect to the determined ΔE_V, given in the legend of Figure 4.7.
V_{oc} is only slightly decreasing for increasing ΔE_V which manifests a sufficient c-Si surface passivation for all (i)a-SiO$_x$ layers, but j_{sc} stays constant at (28.6 $\pm$ 0.7) mA/cm^2. j_{sc} is rather low because flat substrates were used. We do not observe an increasing j_{sc} for wider band gap a-SiO$_x$ layers. Since we only exchange the very thin (5 nm) amorphous Si passivation layer with higher band gap Si suboxides, an increase in photocurrent well below 1 mA/cm^2 is expected [129]. However, with the sputter process used, ITO layers can only be fabricated within a thickness

accuracy of (80 ± 10) nm. This ITO thickness variation causes photocurrent variations up to ∼1.2 mA/cm^2 which makes it impossible to resolve small changes due to the incorporation of wider band gap a-SiO$_x$ layers.
The most prominent feature is the strongly decreasing FF (corresponding to an increasing s-shape of $j(V)$ curves) for rising ΔE_V. The reason is an increase of the barrier height for holes at the (i)a-SiO$_x$:H/(n)c-Si heterojunction. This behavior was predicted on the basis of numerical simulations, e.g. in Refs. [262, 148, 315], but so far no systematic experimental evidence had been presented. For that reason, the direct correlation of the measured ΔE_V with SHJ device performance in the here presented study constitutes a significant added value.

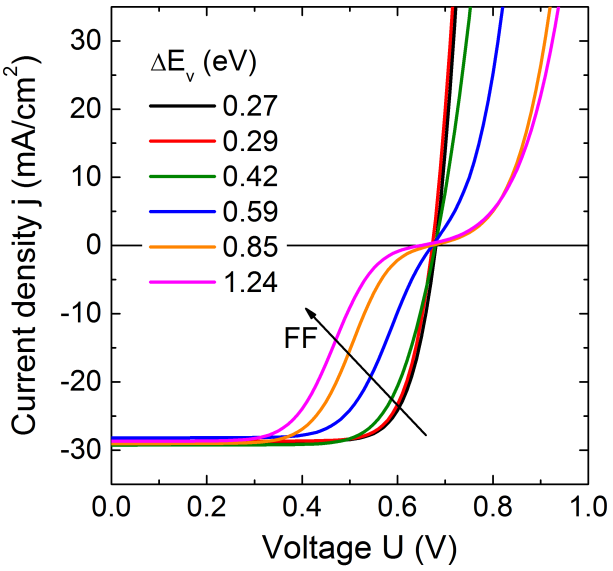

Figure 4.7: Influence of the valence band offset, ΔE_V, at the Si heterojunction, SHJ, on the current-voltage characteristics, $j(V)$, of SHJ solar cells with different a-SiO$_x$:H passivation layers. ΔE_V was measured previously on identically prepared a-SiO$_x$:H layers. Figure adopted from our publications [193, 176].

4.5 Discussion of SHJ solar cells and hole transport mechanism

Throughout this section, solar cells V_{oc} and FF will be discussed with special emphasis on the hole transport mechanism across the SHJ. Moreover, the idea to split the total VB offset into a sequence of smaller offsets will be introduced and discussed. Finally, further perspectives beyond the scope of this work to incorporate wide band gap materials at the front side of conventional both-sides-contacted SHJ solar cells will be presented.
In Figure 4.8 solar cell parameters corresponding to the $j(V)$ curves of Figure 4.7 are plotted against the previously determined ΔE_V. Figure 4.8 (a) depicts the solar cells V_{oc} and implied V_{oc} (iV_{oc}) as extracted from PCD measurements conducted on cell precursor layer stacks before ITO deposition and metallization. V_{oc} decreases monotonously with increasing ΔE_V, whereas iV_{oc} is constant for ΔE_V > 0.4 eV. This behavior can be related to an increased layer porosity and density of dihydrides and H filled voids for a-SiO$_x$:H layers with higher O fractions [89]. Depending on the specific a-SiO$_x$:H film microstructure, H can be driven out during ITO sputter

processes [78]. This would explain why layers with higher O contents degrade more strongly during follow-up processes than layers with lower O concentrations, causing a slightly poorer passivation quality which results in the observed decrease of V_{oc}.

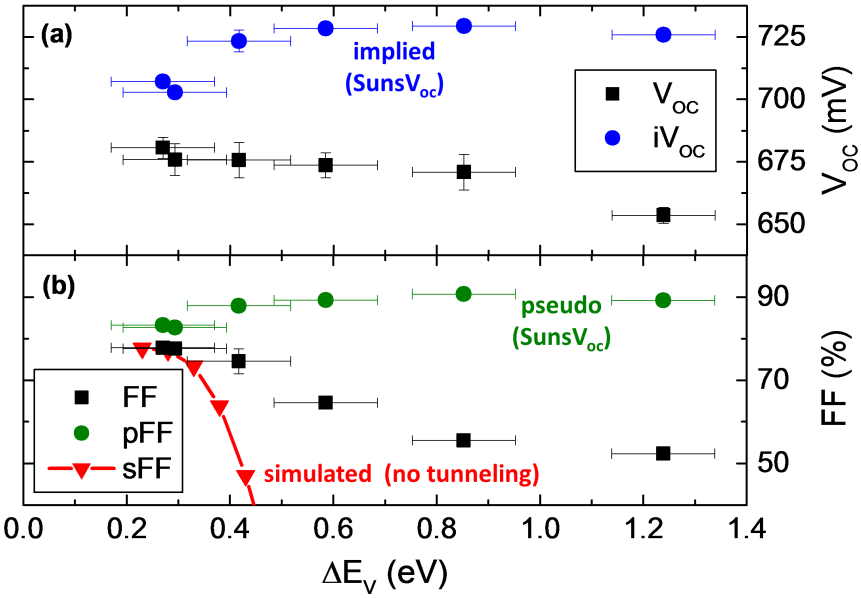

Figure 4.8: SHJ solar cell parameters, corresponding to $j(V)$ curves of Figure 4.7, with different (i)a-SiO$_x$:H passivation layers and thus varying valence band offset (ΔE_V). (a) Open circuit voltage (V_{oc}) and implied V_{oc} (iV_{oc}). (b) Solar cell fill factor (FF) and SunsV_{oc} pseudo FF (pFF) of the same solar cells, and simulated FF (sFF) using AFORS-HET. Figure adopted from our publications [193, 176].

Valence-band offset and hole transport across the SHJ

In Figure 4.8 (b) FF and pseudo FF (pFF) of the solar cells, as well as simulated FF (sFF) are plotted against ΔE_V. We observe a pronounced difference between the strongly decreasing FF and the slightly rising pFF with increasing ΔE_V. pFF is measured using SunsV_{oc}, a method were no external current is extracted from the device. Thus, pFF reflects the maximum possible FF excluding charge carrier transport related effects [273]. Consequently, the strongly decreasing FF from 78% at ΔE_V = 0.27 eV for the standard a-Si:H passivation layers to 52% for ΔE_V = 1.24 eV corresponding to a-SiO$_{0.8}$:H can be related to an increasing transport barrier for holes due to the increased ΔE_V. A possible explanation for the increase of pFF with decreasing FF is that the transport barrier improves the passivation at low injection densities and no net current flow [193].

To gain further insight, numerical simulations using "AFORS-HET" [316] were conducted. In AFORS-HET only thermionic emission is employed, being the main transport mechanism in SHJ solar cells [262, 60, 6, 68]. Simulated FFs (red in Fig. 4.8 (b)) fit the experimental data for

ΔE_V < 400 meV, supporting the assumption that thermionic emission is the dominant transport mechanism. However, the deviation for larger ΔE_V indicate that additional pathways for minority charge carrier transport become prevalent, e.g. tunneling through the interface [148, 237] or defect-assisted tunnel hopping processes across the junction [315, 65].

We conclude that for $\Delta E_V \geq 400$ meV the contribution of tunneling processes at the heterointerface become dominant. However, this additional transport path is not conductive enough to prevent degradation of FF. This transport deficiency for larger ΔE_V, which are intrinsic for wide band gap Si alloys [258, 177, 40, 94], hampers their application as hole selective contacts for SHJ solar cells.

Valence-band stairwell in SHJ solar cells

To mitigate this transport problem of high band gap alloys we pursue the idea to split the total VB offset at the c-Si/wide-gap material interface into a sequence of smaller offsets. This concept is referred to as *"valence-band stairwell"*.
As a proof of concept, we fabricated SHJ solar cells with a passivation layer stack on the front side consisting of a 2 nm (i)a-Si:H layer with ΔE_V = (270 $\pm$ 50) meV, followed by a 3 nm (i)a-SiO$_{0.3}$:H layer with an additional ΔE_V = 315 meV, yielding a total ΔE_V = (585 $\pm$ 50) meV. Figure 4.9 (a) shows the experimental $j(V)$ characteristics of the *"passivation stairwell"* approach (black solid line) and the single passivation layer reference cell (red dashed line). A sketch of the stairwell layer stack is given in the inset of Figure 4.9 (b). The identical V_{oc} of both cells indicate a comparable surface passivation quality. It is obvious that the transport barrier –reflected in FF– in the passivation layer stack is reduced by splitting the effective ΔE_V between two interfaces. However, the higher FF in the stairwell device is still significantly lower compared to the standard SHJ cell with a 5 nm (i)a-Si:H passivation layer (FF = 78%).
Figure 4.9 (b) shows simulated FF values. For the stairwell layer stack, the total VB offset is plotted on the abscissa. As expected, the stairwell stack does not change the overall trend of decreasing FF for increasing ΔE_V. But, compared to the single layer, the stairwell stack improves FF. Since experimental results are in accordance with simulations, although no tunneling processes were included, this constitutes a clear indication that the experimentally observed increased FF (cf. Fig. 4.9 (a)) is most likely due to more efficient thermionic emission along the layer stack than for the single interface with only one large VB offset. Note that within the simulations we cannot account for any tunnel-hopping effects in the 3 nm reduced Si oxide layer thickness as compared to the standardly used 5 nm (i)a-Si:H in the conventional single layer approach.

In summary, simulated and experimental results of the *"stairwell approach"* demonstrate that transport across the two-step stairwell works far better than across the one-step barrier with the same overall VB offset. By implementing appropriate layer stacks the effective ΔE_V can be split to more interfaces which can facilitate hole transport most likely due to an increased thermionic emission rate across each single interface. The more efficient hole transport across a valence-band stairwell can tolerate larger VB offsets. This may allow the implementation of wider band gap Si alloys into SHJ solar cells which then reduce the parasitic absorption significantly.

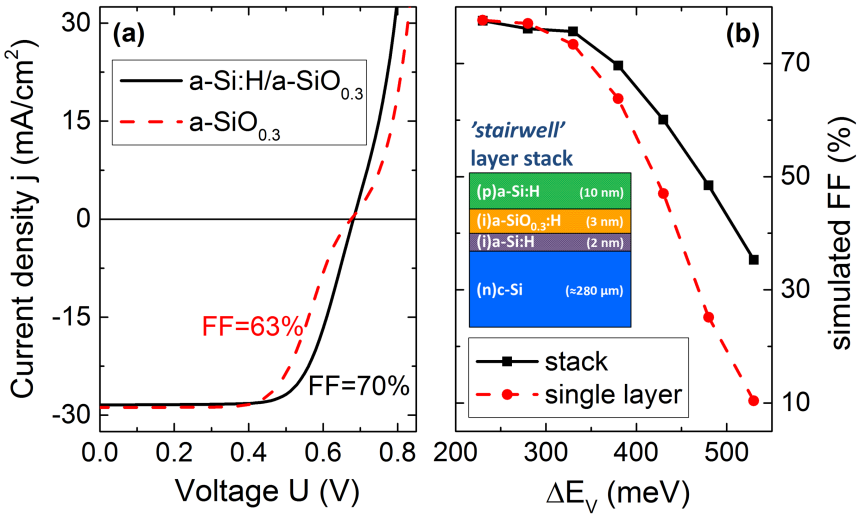

Figure 4.9: (a) $j(V)$-characteristics under AM1.5G illumination of SHJ solar cells with a single 5 nm (i)a-$SiO_{0.3}$:H passivation layer (dashed red line) corresponding to ΔE_V = (585 $\pm$ 50) meV and a *"stairwell"* passivation layer stack (black line) with the same overall ΔE_V but split into 2 nm (i)a-Si:H with ΔE_V = (270 $\pm$ 50) meV and 3 nm of (i)a-$SiO_{0.3}$:H. (b) Simulated FF extracted from "AFORS-HET" implementing only thermionic emission over the (i)a-SiO_x:H/c-Si interface for variable ΔE_V (dashed red line). For the (i)a-SiO_x:H/(i)a-Si:H/c-Si *"stairwell"* layer stacks (black line) the total ΔE_V is plotted on the abscissa. Figure adopted from our publications [193, 176].

Ultra-thin Si tunnel oxide passivation and alternative metal oxide contact layers in SHJ solar cells

We have shown that upon O incorporation into PECVD grown a-SiO_x:H layers the valence band offset increases drastically upon gap widening (cf. Fig. 4.6 (a)). This imposes a transport barrier at the SHJ counteracting the benefit of an increased band gap. Unfortunately, this physical behavior seems to be a generic feature for various a-Si:H alloys [258, 177, 40, 94]. However, the stairwell approach as discussed above may mitigate this transport problem and might allow a successful incorporation of wider band gap PECVD grown a-Si:H alloys in the front contact of SHJ solar cells.

In another promising concept the $\sim$5 nm (i)a-Si:H passivation layers are replaced by ultra-thin, near-stoichiometric SiO_2 tunnel oxides with layer thicknesses of $\sim$1 nm [34, 262, 211, 279]. In 2016, *Fraunhofer ISE (Freiburg)* reported 25.3% power conversion efficiency of a both sides-contacted c-Si based solar cell with tunnel oxide passivated contacts implemented [123, 109]. Besides the reduction of parasitic absorption due to (i) the reduced layer thickness, and (ii) the high band gap of those ultra-thin tunnel oxides, their growth is comparatively simple, thus providing alternative industry relevant fabrication processes. The main challenge is to achieve a high quality passivation by the preparation of stable and homogeneous ultra-thin SiO_2 layers with a structural abrupt interface to the c-Si wafer and low electronic defect density [279]. High quality

tunnel oxide layers can be grown by e.g. ozonized DI-water or by UV radiation induced photo oxidation [198, 199], thus omitting the more costly PECVD process.
Additionally, wide band gap metal oxides replacing the (p)a-Si:H emitter layer constitute a promising alternative for an increased current yield. In the SHJ community, recent interest has shifted towards the application of high work function metal oxides as hole contacts on (i)a-Si:H passivation layers [35, 24, 191]. An efficiency of 22.5% for a MoO_x hole contact is reported [108]. In a study by C. Battaglia et al. [24], a substantial current gain of 1.9 mA/cm^2 for a 10 nm MoO_x layer compared to a standard 10 nm (p)a-Si:H emitter layer was identified.

4.6 Summary

One possibility to further improve the high efficiency SHJ solar cell technology is to reduce the parasitic absorption in its front contact layers by implementing wider band gap materials. However, this will also modify the band alignment at the heterointerface. In the study presented here, we investigated a-SiO_x:H, ranging from pure a-Si:H to wide band gap near-stoichiometric a-SiO_2. Film stoichiometry x and valence band alignment at the SHJ were investigated via various modes of *in-system* photoelectron spectroscopy. A continuous increase of the valence band offset starting from ΔE_V = 270 meV for the a-Si:H/c-Si to 4.3 eV for the near-stoichiometric a-SiO_2/c-Si heterointerface was determined. It was shown that all layers reveal a sufficient surface passivation.
In a second step, SHJ solar cells with identically prepared layers were fabricated allowing to relate ΔE_V to device efficiency. Rising ΔE_V causes an increased transport barrier for holes. This is reflected in reduced solar cell FFs. With the aid of numerical simulations it was shown that the increased transport barrier leads to a reduction of thermionic emission rate. Simultaneously, the contribution of tunneling processes increases.
Although large valence band offsets constitute a general problem for SHJ solar cells, we demonstrate that a stacked passivation layer approach mitigates the transport problem. Therefore, splitting the valence band offsets is shown to be a promising concept. Especially the combination of a medium band gap passivation layer and a high band gap hole contact layer could allow the successful application of wide band gap Si alloys in SHJ solar cells.

5

The potential of hybrid device concepts studied by optical simulations

PEDOT:PSS which has recently been shown to provide a hole selective contact to Si [232, 226, 138], offers the possibility to directly integrate tetracene (Tc) as an interlayer in hybrid SHJ devices. In the following optical simulations of the proposed hybrid front junction, with and without an incorporated Tc interlayer, are conducted to evaluate the potential of various hybrid device concepts:

(i) PEDOT:PSS/c-Si heterojunction solar cell

(ii) PEDOT:PSS/Tc/c-Si approach featuring the potential of multi-exciton generation via singlet fission in the Tc layer

Current densities are calculated by integrating simulated absorption/reflection profiles of hybrid layer stacks over the solar spectrum. As input for the simulations experimentally derived optical (*n-k*) data are used. The electrical contribution of Tc is considered within a basic MEG model. Thus, the ultimate gain in j_{sc} achievable due to singlet fission in the proposed PEDOT:PSS/Tc/c-Si device architecture can be estimated.
Figure 5.1 depicts a schematic representation of the simulated hybrid device structure. It consists of a standard 280 μm c-Si absorber. The electron selective back contact is adopted from the SHJ technology, formed by a well passivated (i/n$^+$)a-Si:H layer stack acting as a back surface field, followed by Ag metallization. Organic layers incorporated on the cell's front side are simulated within the range of thicknesses as indicated in the figure. For simulations planar hybrid layer stacks are assumed.
Optical simulations allow to deduce maximum achievable solar cell short-circuit current densities and identify optical losses, namely parasitic absorption and reflection. However, device efficiencies, fill factors or open-cirucit voltages cannot be extracted from these simulations.

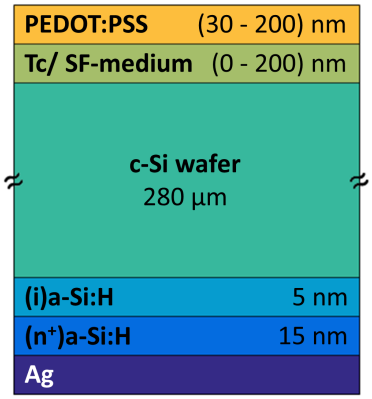

Figure 5.1: Schematic representation of the simulated hybrid device structure including fixed c-Si and a-Si:H layer thicknesses. The range of simulated thicknesses for Tc and PEDOT:PSS are depicted in the respective layers.

Parts of the results presented in this chapter regarding the hybrid PEDOT:PSS/c-Si device are published in:

- S. Jäckle, M. Liebhaber, C. Gersmann, M. Mews, K. Jäger, S. Christiansen, and K. Lips, *Potential of PEDOT:PSS as a hole selective front contact for silicon heterojunction solar cells*, submitted to Scientific Reports (2017), `http://arxiv.org/abs/1701.05368`, Ref [136].

Optical simulations were carried out by the author of this thesis and K. Jäger. Optical constants of Tc were derived from a backwards calculation of reflection/transmission data by the author of this thesis and C. Gersmann, optical constants of PEDOT:PSS were deduced from ellipsometry measurements by S. Jäckle in discussion with the author of this thesis. For the analysis and discussion of the potential of hybrid PEDOT:PSS/c-Si solar cells S. Jäckle and the author of this thesis equally contributed.

5.1 Simulation of absorption/reflection profiles and basic MEG model

Absorption profiles of planar thin-film layer stacks on c-Si were simulated within a transfer-matrix algorithm [183] implemented in the MATLAB software package "GenPro4" [246, 9, 135], developed at the Delft University of Technology. Since the coherence length of sunlight is much smaller than the 280 μm thick c-Si wafer, light interaction is treated non-coherently [246]. "Air" and the Ag back contact were assumed as infinitely thick layers.

Optical (*n-k*) data

As input for the simulations experimentally determined optical (*n-k*) data are used. Optical properties of the c-Si wafer, (i)a-Si:H and (n^+)a-Si:H thin films were previously determined by ellipsometry at HZB, Ag values are taken from literature [145]. To obtain the optical properties of PEDOT:PSS and Tc, layers were prepared with the same recipe as for solar cell fabrication.

(*n-k*) data for PEDOT:PSS were derived from spectroscopic ellipsometry (cf. section 3.2.5). Following the analysis of L. A. A. Pettersson et al. [221, 222] the data was analyzed assuming uniaxial anisotropy of the polymer film. It is surmised that the anisotropy in PEDOT:PSS layers stems from a geometric anisotropy of the polymer chains itself. Furthermore, if spin-coated on flat c-Si surfaces it is assumed that the main part of the polymer chains are lying flat and parallel to the surface plane but randomly oriented, giving rise to uniaxial anisotropy with the optical axis parallel to the sample normal [221, 222]. Thus, the optical response of thin film PEDOT:PSS can be described by an ordinary complex index of refraction perpendicular, and an extraordinary complex index of refraction parallel to the surface plane.
In Figure 5.2 (a) the experimentally determined (*n-k*) data for PEDOT:PSS are plotted. Absorption, assigned to free carrier absorption [225, 184, 284, 348, 17], is reflected in the increase of the extinction coefficient k towards the infrared. It is much higher for the ordinary component (normal incidence of light) than for the extraordinary component. This is most likely due to free carriers that can only move in direction of the polymer chains which are aligned parallel to the surface [221, 222]. Since under standard test conditions solar cells are measured in normal incidence of light, for the simulations only the ordinary component is considered.

Absorption and reflection data of Tc films deposited on quartz glass were used to derive (*n-k*) data for Tc by means of a backwards calculation of the transfer-matrix approach [120]. This is implemented in the MATLAB program "APCSA" [110], developed at the University of Potsdam. Within the program the transfer-matrix-method [120] is employed to compute theoretical reflection and transmission of the layer stack. A simulated annealing algorithm [238, 110] is implemented to minimize the deviation of computed and measured data. As further input, optical properties and thickness of the quartz substrate have to be known.
Figure 5.2 (b) depicts experimentally obtained (*n-k*) data of thin film Tc. The extinction coefficient k, clearly reveals the characteristic vibrational structure of thin film Tc in the range of 400 - 550 nm [299]. The weak absorption feature to the red of 550 nm is not related to Tc absorption [299] but is rather attributed to diffusely scattered light at rough surfaces. Since we assume flat surfaces, it is not considered in the simulations.

Absorption and reflection profiles

The optical data presented above was used to simulate absorption and reflection of various solar cell structures. Figure 5.3 displays simulated absorption and reflection profiles of hybrid device layer stacks, whereby the individual absorption contribution of each layer is added.
In Figure 5.3 (a), an example for a 95 nm PEDOT:PSS/c-Si device without Tc is shown. Assuming that PEDOT:PSS is electrically "dead", only light absorbed in the c-Si wafer (green area) contributes to the photocurrent. A significant fraction of light is reflected at the hybrid layer stack (yellow area) or is parasitically absorbed in PEDOT:PSS (orange area). The corresponding current losses will be quantified and discussed in section 5.2. Absorption in the a-Si:H layers and Ag back contact is very small and will be neglected for further discussion.
Figure 5.3 (b) depicts absorption and reflection contributions for a solar cell with a 30 nm PEDOT:PSS/100 nm Tc/c-Si layer stack. Obviously, Tc incorporated on the device front side

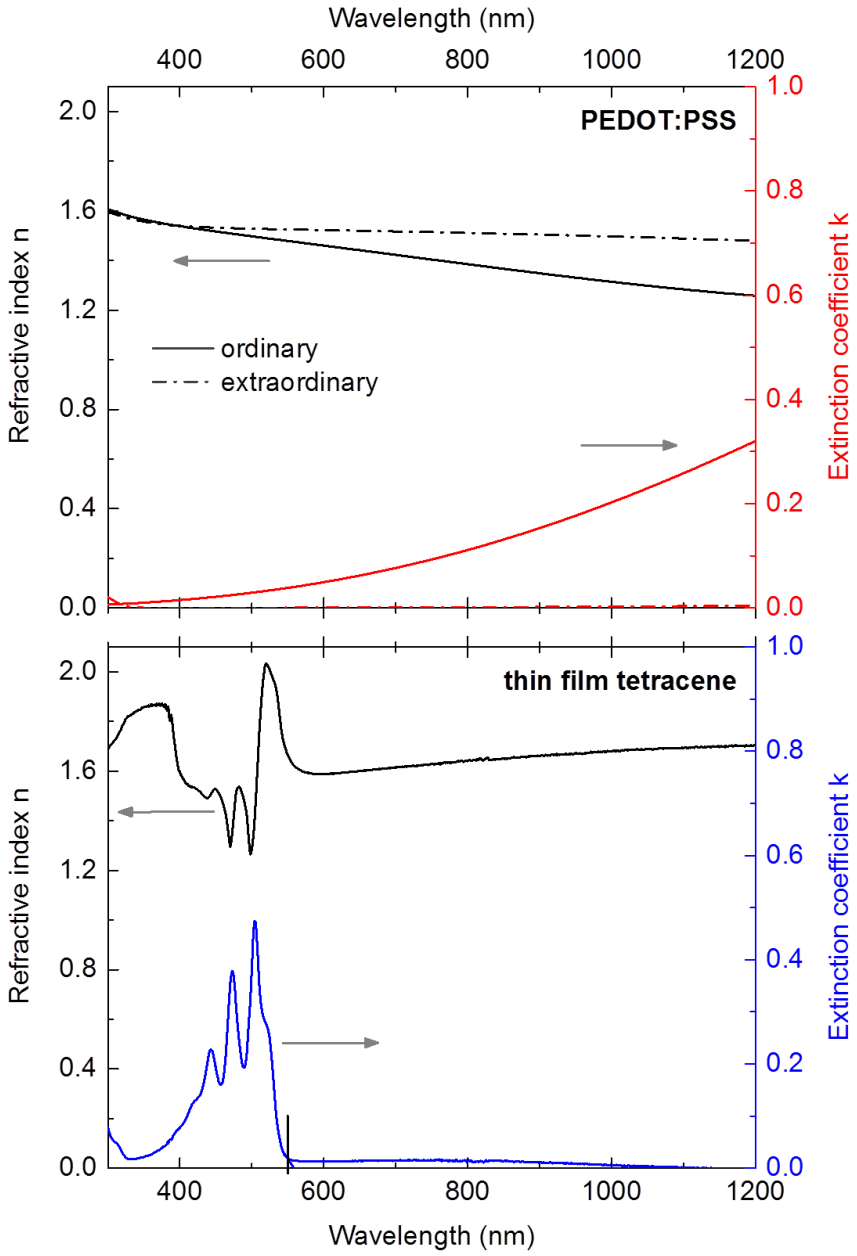

Figure 5.2: (a) (*n*-*k*) data for PEDOT:PSS derived by spectroscopic ellipsometry, following the analysis of L. A. A. Pettersson et al. [221, 222]. PEDOT:PSS is a birefringent material revealing ordinary and extraordinary optical components. Data published in Ref. [136]. (b) (*n*-*k*) data of thin film tetracene derived from absorption and transmission spectra. Layers were prepared identically as for solar cell fabrication.

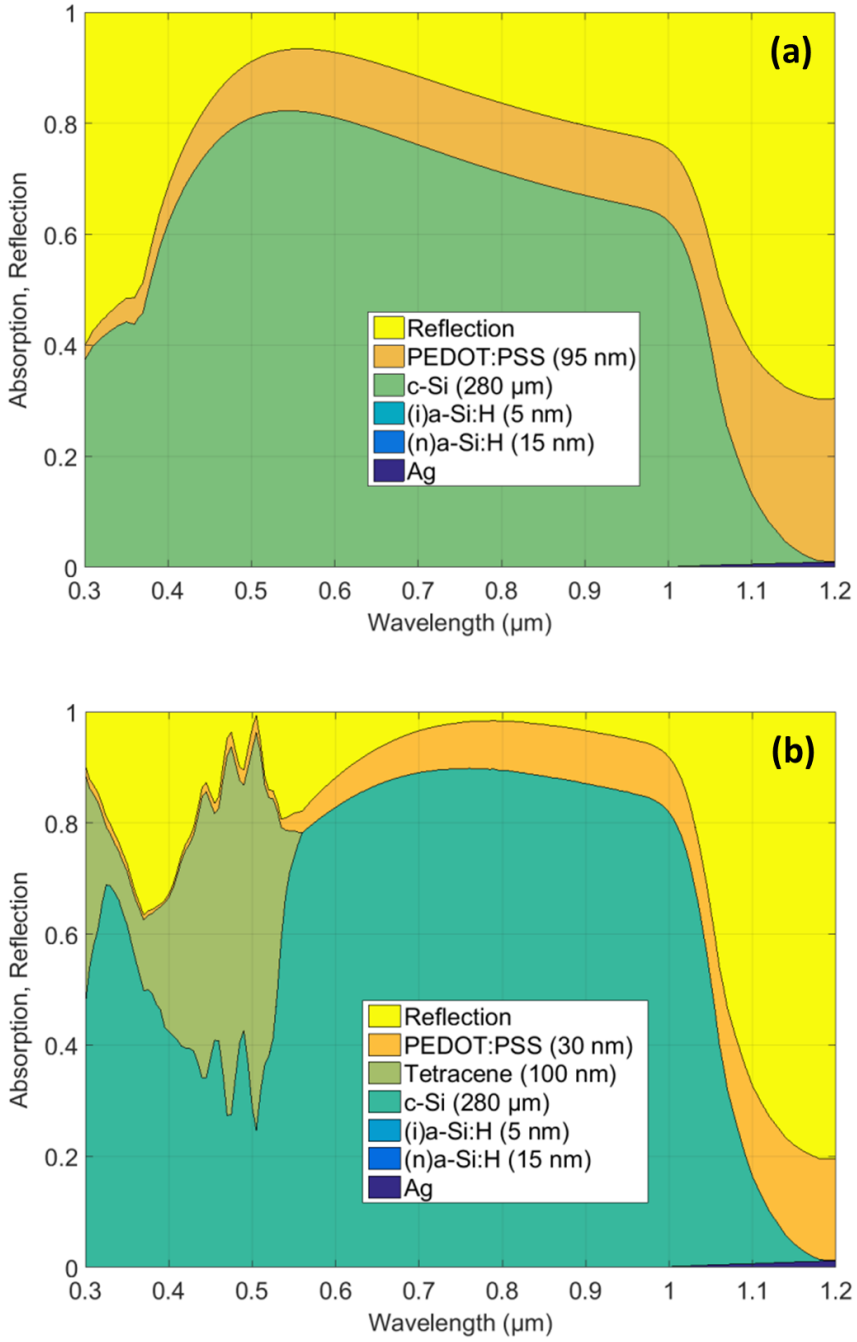

Figure 5.3: Absorption and reflection profiles versus wavelength for hybrid solar cells as sketched in Figure 5.1, simulated under illumination in normal incidence. (a) Example for a 95 nm PEDOT:PSS/c-Si heterojunction solar cell without Tc, and (b) 30 nm PEDOT:PSS/100 nm Tc/c-Si hybrid device.

acts as an optical filter for the c-Si absorber. Light absorbed in the Tc layer (light-green area) leads to a decreased absorption in the c-Si wafer. Consequently, as it is clearly observed in Figure 5.3 (b), the characteristic vibrational structure of Tc absorption is inversely reflected in the c-Si absorption profile (dark-green area).

As it will be described in the following, simulated absorption profiles can then be used to derive the EQE of a PEDOT:PSS/Tc/c-Si device. Finally, device j_{sc} can be calculated by integrating the EQE over the solar spectrum. A basic MEG model was developed to account for any current contribution of the SF material Tc.

Basic MEG model

We now describe how simulated absorption profiles are related to device performance assuming different Tc contributions. Given the case that the absorption in Tc is completely parasitic ($EQE_0^{Tc} \equiv 0$), the EQE of a hybrid cell is only determined by absorption in the c-Si absorber. It is calculated by:

$$EQE_0^{Si}(\lambda) = A_{Si}(\lambda)\eta_{opt}^{Si}\eta_{el}\,, \tag{5.1}$$

with the absorption profile of c-Si, $A_{Si}(\lambda)$, the optical efficiency, η_{opt}^{Si}, for creating an electron-hole pair, and the electrical efficiency, η_{el}, for the probability to extract generated charge carriers. $\eta_{opt}^{Si}\eta_{el}$ is referred to as the internal quantum efficiency IQE.
In a second step, the electrical contribution of the Tc layer is taken into account through multi-exciton generation via singlet fission which is referred to as $EQE_{MEG}^{Tc/Si}$. It is given by:

$$EQE_{MEG}^{Tc/Si}(\lambda) = EQE_0^{Si}(\lambda) + A_{Tc}(\lambda)\eta_{MEG}^{Tc}\eta_{el}\,, \tag{5.2}$$

with the absorption profile of Tc, $A_{Tc}(\lambda)$, and:

$$\eta_{MEG}^{Tc} := \overset{1-2}{\eta_{SF}} \cdot \overset{0-1}{\eta_{diff}} \cdot \overset{0-1}{\eta_{diss}}\,. \tag{5.3}$$

η_{MEG}^{Tc} is determined by the SF efficiency, η_{SF}, which can vary from 1 - 2, the probability that created triplet excitons reach the Tc/c-Si interface through diffusion described by η_{diff} (range 0 - 1), and their dissociation probability, η_{diss}, (range 0 - 1) at the hybrid junction resulting in free charge carriers. Free charges are then extracted at the device contacts with the efficiency η_{el}. η_{MEG}^{Tc} may vary from zero for solely parasitic absorption of Tc to a maximum of two which corresponds to 200% SF quantum yield[1], 100% exciton dissociation at the hybrid Tc/c-Si interface, and no losses during exciton diffusion in the Tc layer.
As a figure of merit we use the maximum achievable short-circuit current density, j_{sc}, by assuming IQE = 1 ($\eta_{opt}^{Si} = \eta_{el} \equiv 1$). j_{sc} is calculated by integration over the relevant λ_1 ... λ_2 wavelength range[2] of the $EQE_{MEG}^{Tc/Si}$ multiplied by the photon flux for AM1.5G solar irradiation

[1] definition of SF quantum yield: 100% SF effect → 200% quantum yield (1 photon in → 2 e-h pairs out)
[2] relevant spectral range for c-Si absorber: 300 nm - 1180 nm

$\Phi_{AM1.5G}$ [135]:

$$j_{\mathrm{sc}} = -e \int_{\lambda_1}^{\lambda_2} \mathrm{EQE}_{MEG}^{Tc/Si}(\lambda)\Phi_{AM1.5G}(\lambda)d\lambda\,. \tag{5.4}$$

Combining Equations (5.4), (5.2) and (5.1), j_{sc} is given by:

$$j_{\mathrm{sc}} = \underbrace{-e\int_{\lambda_1}^{\lambda_2} A_{Si}(\lambda)\Phi_{AM1.5G}(\lambda)d\lambda}_{\equiv j_{ph}^{Si}(\mathrm{IQE=1})} + \eta_{MEG}^{Tc}\underbrace{(-e)\int_{\lambda_1}^{\lambda_2} A_{Tc}(\lambda)\Phi_{AM1.5G}(\lambda)d\lambda}_{\equiv j_{ph}^{Tc}(\mathrm{IQE=1})}\,. \tag{5.5}$$

Finally, j_{sc} simplifies to:

$$j_{\mathrm{sc}}(\eta_{MEG}^{Tc}) = j_{ph}^{Si} + \eta_{MEG}^{Tc}\cdot j_{ph}^{Tc}\,, \tag{5.6}$$

with the maximum photocurrent density in the c-Si absorber j_{ph}^{Si}(IQE=1) and the photocurrent density of Tc j_{ph}^{Tc}(IQE=1). η_{MEG}^{Tc} ranges between 0 ... 2, thus accounting for any current contribution of Tc on hybrid device performance.
In addition to j_{sc} which is determined by c-Si and possible Tc photocurrent contributions (cf. Eqs. (5.4) - (5.6)), current losses due to parasitic absorption in the polymer and reflection at the hybrid layer stack can be quantified by integration over the absorption spectra of PEDOT:PSS and the infinite "air-layer", respectively.

5.2 The potential of hybrid PEDOT:PSS/c-Si solar cells

In this section, limitations and the potential of PEDOT:PSS implemented as the hole selective contact on the front of c-Si based solar cells will be discussed.
Figure 5.4 depicts the maximum achievable j_{sc}, as well as current density losses due to reflection and parasitic absorption in PEDOT:PSS calculated by integration of simulated absorption profiles for hybrid PEDOT:PSS/c-Si devices. An example absorption profile was already presented in Figure 5.3 (a). In the simulations layer thicknesses of PEDOT:PSS range from 30 - 200 nm. From Figure 5.4 it is clear that current losses strongly depend on PEDOT:PSS layer thickness. The loss current due to parasitic absorption steadily increases from 1.0 mA/cm^2 for 30 nm up to 15.4 mA/cm^2 for 200 nm of PEDOT:PSS. Simultaneously, reflection losses monotonously decrease from 17.7 mA/cm^2 (30 nm) to 7.6 mA/cm^2 (200 nm) for increasing PEDOT:PSS layer thicknesses. As a result, the maximum extractable j_{sc} of 30.6 mA/cm^2 generated in the c-Si absorber is obtained for a 80 nm thick PEDOT:PSS layer.
In order to maximize device performance, the parasitic absorption in PEDOT:PSS has to be kept as low as possible, hence the polymer layers have to be as thin as possible while at the same time low reflection can be achieved by an additional anti-reflex coating, e.g. MoO_x or LiF. Both exhibit refraction indices between those of PEDOT:PSS and air [179, 348, 9].
The reflection losses mainly originate from internal reflection at the planar interface between

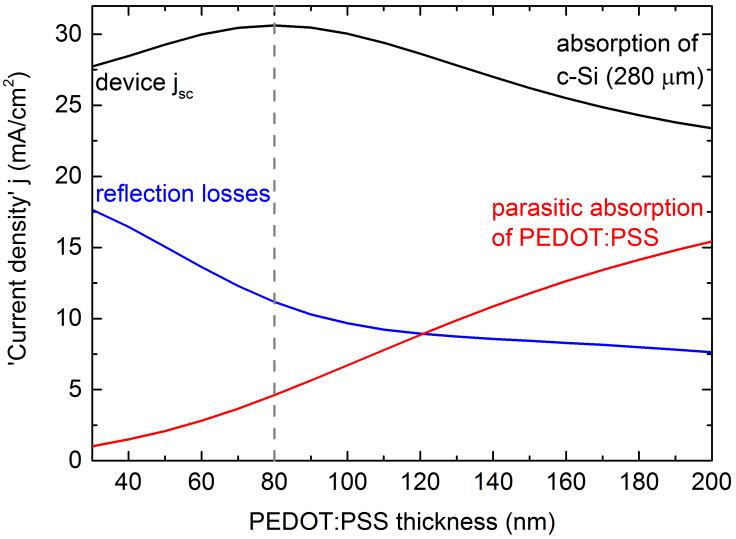

Figure 5.4: Current densities calculated via integration (300 nm $\leq \lambda \leq$ 1180 nm) of simulated absorption/reflection profiles (example profile see Fig. 5.3 (a)) multiplied by AM1.5G solar spectrum for a thickness series of (30 nm - 200 nm) PEDOT:PSS/(280 μm) c-Si hybrid solar cells. The extractable device j_{sc}, generated in the c-Si absorber, has its optimum for 80 nm PEDOT:PSS. Current is lost via reflection and parasitic absorption in PEDOT:PSS. Data published in Ref.[136].

PEDOT:PSS and c-Si due to their large difference in refractive index. Structuring the c-Si surfaces would drastically reduce reflection losses due to multiple incidence of light. This has an additional benefit because it also reduces the parasitic absorption in the PEDOT:PSS layer as a significant part of the incident light hitting the tilted surface would oscillate in direction of the polymer's extraordinary component which exhibits a drastically reduced extinction coefficient (cf. Fig. 5.2 (a)). For instance, standard KOH etching leads to a pyramidal surface texture with a tilting angle of 54.74° with respect to the c-Si $\langle 100 \rangle$ plane [26]. Assuming an alignment of the polymer chains along the textured surface would then result in a reduction of the parasitic absorption in the PEDOT:PSS layer of about 40% [136].

5.3 Potential of the MEG hybrid PEDOT:PSS/Tc/c-Si device concept

To determine the maximum achievable gain in j_{sc} due to multi-exciton generation in thin film Tc incorporated in the proposed PEDOT:PSS/Tc/c-Si device structure (cf. Fig. 5.1), absorption/reflection profiles were simulated for possible thickness combinations of PEDOT:PSS (30 nm - 200 nm) and Tc thin films (0 nm - 200 nm). An exemplary profile was already presented in Figure 5.3 (b). Corresponding photocurrent densities are then calculated via integration of simulated absorption/reflection profiles multiplied with the photon flux of the solar spectrum.

Therefore, short-circuit currents, $j_{\mathrm{sc}}(\eta_{MEG}^{Tc})$, and current density losses due to reflection and parasitic absorption in PEDOT:PSS are extracted. In our basic MEG model (cf. Eq. (5.6)), we account for MEG contribution in the Tc layer by the parameter η_{MEG}^{Tc} which ranges from 0 (solely parasitic absorption) to 2 (200% quantum yield, i.e. 1 photon in $\rightarrow$ 2 e-h pairs out, cf. Eq. (5.3)). Simulation results are plotted in 2d color maps with x- and y- axes corresponding to Tc and PEDOT:PSS layer thicknesses, whereas the color bars indicate photocurrent densities.

In a first step, we quantify the current losses as a function of the layer thicknesses of Tc and PEDOT:PSS. Figure 5.5 depicts the simulated current density losses due to (a) light reflection at the hybrid layer stacks, and (b) parasitic absorption in PEDOT:PSS layers. Reflection losses strongly vary from $\sim$5 mA/cm^2 to $\sim$18 mA/cm^2. The parasitic absorption rises for increasing PEDOT:PSS layer thicknesses within the range of $\sim$1 mA/cm^2 for 30 nm to $\sim$16 mA/cm^2 for 200 nm. In Figure 5.5 (c) the sum of reflection and parasitic absorption losses is plotted. By considering both loss mechanisms, a local current loss minimum of 10.8 mA/cm^2 is found for a 90 nm Tc/30 nm PEDOT:PSS layer stack. The discussed losses are interdependent and have to be taken in consideration designing the solar cell.

In the next step, the local photocurrent densities in the Tc layer and the c-Si wafer, j_{ph}^{Tc} (Fig. 5.6 (a)) and j_{ph}^{Si} (Fig. 5.6 (b)), respectively, are considered assuming no electric losses (IQE(λ) = 1). Obviously, j_{ph}^{Tc}(IQE=1)[3] is increasing for rising Tc layer thicknesses (Fig. 5.6 (a)). As indicated in the figure, for the thickest Tc film of 200 nm and a thin PEDOT:PSS layer, a maximum photocurrent density of j_{ph}^{Tc}(IQE=1) = 5.7 mA/cm^2 is extracted from the simulations. In Figure 5.6 (b) the photocurrent density j_{ph}^{Si} is plotted assuming an IQE(λ) = 1. The dashed line indicates the thickness combinations in which reflection and "parasitic" absorption losses of PEDOT:PSS/Tc layer stacks is minimized[4]. Simulations reveal highest values of j_{ph}^{Si}(IQE=1) for the sum of organic layer thicknesses d_{PEDOT} + d_{Tc} in the range of 80 nm - 100 nm. Due to the interplay of reflection and absorption in the organic top layer stacks, j_{ph}^{Si}(IQE=1) of 30.6 mA/cm^2 for the d_{PEDOT} = 80 nm reference cell (w/o Tc incorporation) is slightly lower than 32.2 mA/cm^2 for the d_{PEDOT} + d_{Tc} = 30 nm + 70 nm layer stack combination.

So far, various losses, namely reflection and parasitic absorption in PEDOT:PSS (cf. Fig. 5.5), and local current densities in Tc and c-Si assuming an IQE = 1 (cf. Fig. 5.6) were quantified. To address the potential of the here proposed PEDOT:PSS/Tc/c-Si device architecture the contribution of multi-exciton generation in Tc is taken into account in the basic model by η_{MEG}^{Tc}. As a figure of merit we use the maximum achievable j_{sc} of hybrid devices which is given by $j_{\mathrm{sc}}(\eta_{MEG}^{Tc}) = j_{ph}^{Si} + \eta_{MEG}^{Tc} \cdot j_{ph}^{Tc}$ (cf. Eqs. (5.4) - (5.6)). Figure 5.7 shows exemplary plots for three efficiencies η_{MEG}^{Tc} = 0, 1, 2. In Figure 5.7 (a), light absorption in Tc is solely parasitic and correspondingly $j_{\mathrm{sc}}(\eta_{MEG}^{Tc}$ = 0) only originates from light absorbed in the c-Si wafer. Figure 5.7 (b) displays $j_{\mathrm{sc}}(\eta_{MEG}^{Tc}$ = 1). Obviously, the maximum $j_{\mathrm{sc}}(\eta_{MEG}^{Tc}$ = 0) = 32.2 mA/cm^2 (indicated by the isoline) is now exceeded. Finally, in Figure 5.7 (c) we assume a Tc layer that is capable of multi-exciton generation with maximum efficiency of 200%. The maximum $j_{\mathrm{sc}}(\eta_{MEG}^{Tc}$ = 2) = 39.3 mA/cm^2 is obtained for a 30 nm PEDOT:PSS/100 nm Tc layer stack. Thus, maximum

[3] meaning: 1 photon in $\rightarrow$ 1 e-h pair out ($\leftrightarrow$ no MEG)

[4] note: regarding the absorption in c-Si, Tc acts as an optical filter ($\leftrightarrow$ "parasitic" absorption, cf. Fig. 5.3 (b)).

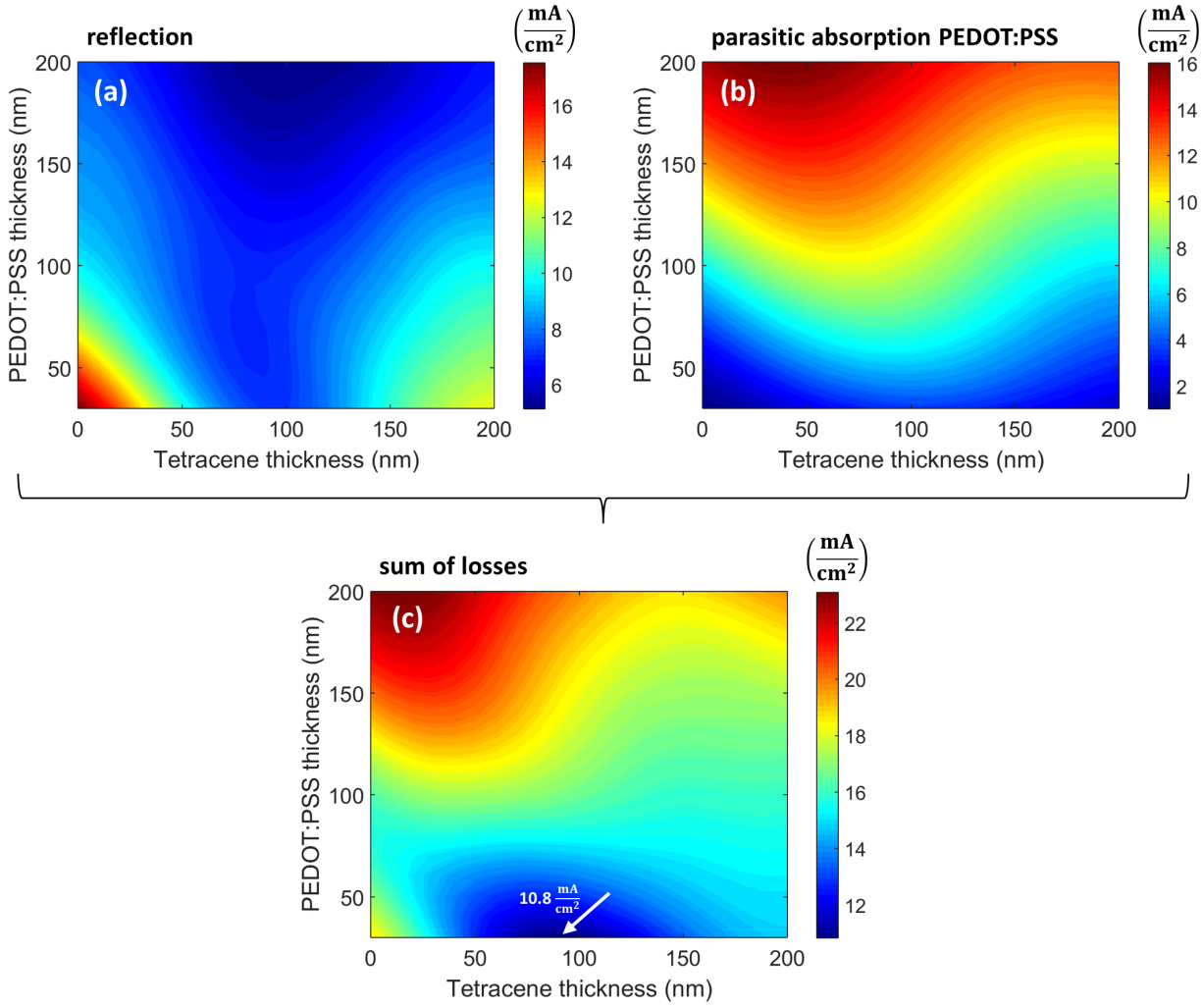

Figure 5.5: Simulation results are plotted in 2d color maps with x- and y- axes corresponding to Tc and PEDOT:PSS layer thicknesses, respectively. Color bars indicate photocurrent densities. (a) Reflection losses, (b) parasitic absorption in PEDOT:PSS, and (c) sum of both loss mechanisms.

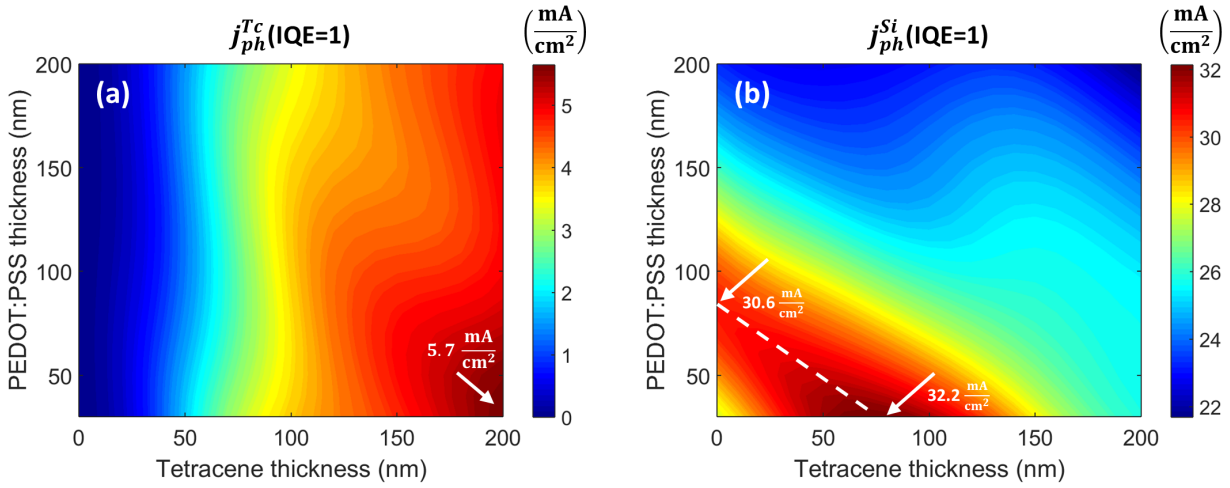

Figure 5.6: 2d color maps with x- and y- axes corresponding to Tc and PEDOT:PSS layer thicknesses, respectively. Color bars indicate photocurrent densities. (a) j_{ph}^{Tc} in thin film Tc, and (b) j_{ph}^{Si} for 280 μm c-Si absorber, assuming IQE(λ) = 1. The dashed line indicates thickness combinations in which reflection and "parasitic" absorption losses of PEDOT:PSS/Tc layer stacks incorporated on top of the c-Si absorber is minimized.

MEG results in an absolute increase of j_{sc} by 7.1 mA/cm^2, corresponding to a relative gain of $\sim$20%, in the here presented device architecture.

Nevertheless, the simulated 39.3 mA/cm^2 is still below the maximum achievable j_{sc} of 43.3 mA/cm^2 calculated for single junction c-Si solar cells [243] assuming optimum light harvesting but no 3rd generation effects. The here conducted optical simulation study reveals significant current losses of 3.6 mA/cm^2 due to parasitic absorption in the PEDOT:PSS layer and 7.3 mA/cm^2 due to reflection at the entire PEDOT:PSS/Tc/c-Si planar layer stack. Taking these values into account a maximum achievable j_{sc} = 50.2 mA/cm^2 could be achieved, thus exceeding the single junction limit.
This points out the importance of light management while implementing new materials on the front side of solar cells. Optical losses always have to be taken into account and must be minimized. For the PEDOT:PSS/Tc/c-Si layer stack the same routes apply as for the hybrid PEDOT:PSS/c-Si stack, which are briefly summarized in the following:

- Minimizing reflection losses by an optimized AR-coating through the incorporation of additional, optically transparent layers with suitable refractive indices.
- Minimizing parasitic absorption by fabrication of PEDOT:PSS layers as thin as possible while maintaining low sheet resistance.
- Using textured c-Si wafers, since this enhances the fraction of light (for normal incidence) that hits the less absorptive extraordinary component of birefringent PEDOT:PSS. In addition, structured wafers enhances light incoupling.

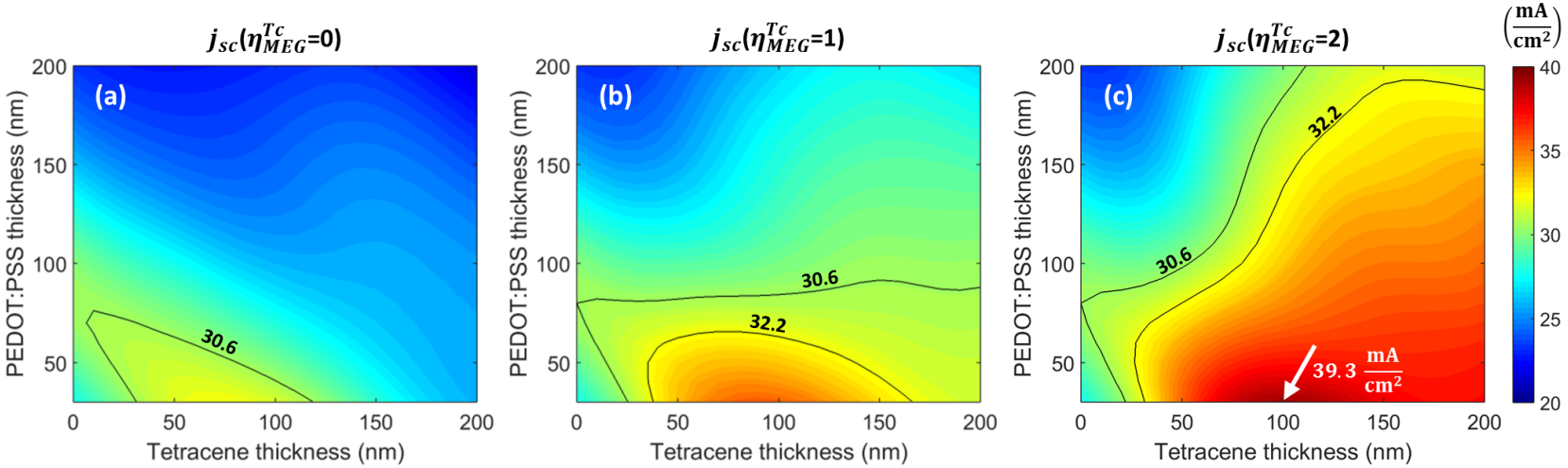

Figure 5.7: 2d color maps with x- and y- axes corresponding to Tc and PEDOT:PSS layer thickness, respectively. Color bars indicate j_{sc} obtained by $j_{\mathrm{sc}}(\eta_{MEG}^{Tc}) = j_{ph}^{Si} + \eta_{MEG}^{Tc} \cdot j_{ph}^{Tc}$ (cf. Eq. (5.6)) for three η_{MEG}^{Tc} efficiencies. For a better comparison, the color bar is equally scaled from 20 - 40 mA/cm^2 for all three figures. Isolines indicate maximum achievable j_{sc} for (i) the PEDOT:PSS/c-Si reference cell of 30.6 mA/cm^2, and (ii) PEDOT:PSS/Tc/c-Si of 32.2 mA/cm^2 assuming an electrically inactive Tc layer (η_{MEG}^{Tc} = 0). The arrow indicates the maximum j_{sc} that can be achieved with the here presented device layout assuming perfect multi-exciton generation at planar interfaces but with insufficient light harvesting.

From the above discussion it is clear that an improved design concept is mandatory. Possible design strategies with an enhanced light management are depicted in Figure 5.8. In the more conventional two-side contact scheme (Fig. 5.8 (a)), PEDOT:PSS as before is the hole selective front contact. To minimize optical losses wafer structuring and an optimized AR-coating is implemented. The replacement of PEDOT:PSS by conventional inorganic transparent conductive oxides such as ITO has not yet been tried because ion bombardment during sputter deposition will most probably damage organic thin film Tc [167, 181]. Using an IBC solar cell concept, as sketched in Figure 5.8 (b), renders the use of PEDOT:PSS unnecessary since a-Si:H selective contacts can be used instead. Thus, its parasitic absorption is nullified. In this concept, shadowing by the front contact grid is additionally omitted. Obviously, also in this approach surface texturing and an effective AR-coating have to be implemented for best efficiencies. However, as discussed in section 2.4, in the IBC concept the complete triplet exciton has to be transferred from Tc across the hybrid junction into c-Si, whereas for the both-sides contact scheme (Fig. 5.8 (a)) an electron transfer with the hole remaining in Tc is sufficient.

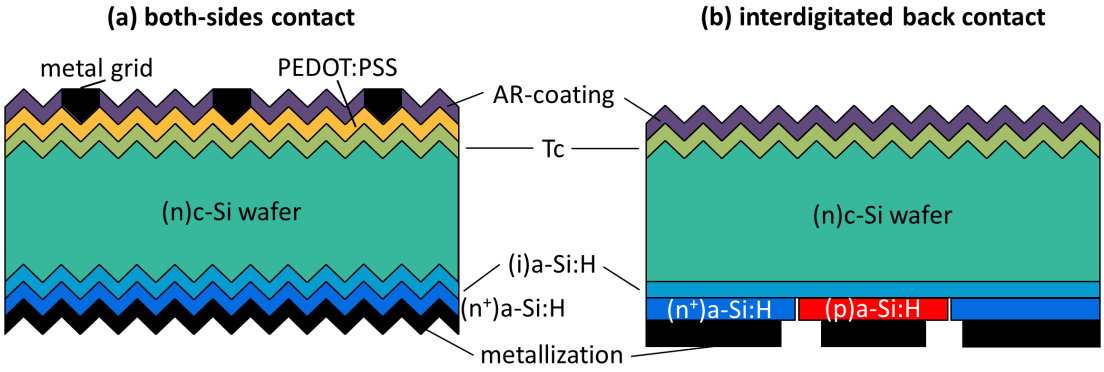

Figure 5.8: Proposed Tc/c-Si solar cell structures with improved light management. (a) Both-sides contacted concept using PEDOT:PSS as a hole selective front contact. To minimize parasitic absorption losses, the polymer layer has to be fabricated as thin as possible. (b) Interdigitated back contact approach, thus omitting PEDOT:PSS at the cell's front side. Optical losses are minimized by (i) surface texturing and (ii) anti-reflection (AR) coatings.

For a more detailed discussion of the performance of the above concepts more simulations are mandatory.

5.4 Summary

Experimental derived (n-k) data were used to simulate absorption and reflection profiles of specific hybrid layer stacks. In a second step, the photocurrent was extracted via integration over the solar spectrum. Hereby, maximum device short-circuit current densities as well as current losses due to reflection and parasitic absorption were quantified. For the simulations, planar device structures without additional anti-reflex layers were assumed.

For hybrid PEDOT:PSS/c-Si heterojunction solar cells simulations reveal a maximum j_{sc} of 30.6 mA/cm^2 for 80 nm PEDOT:PSS. Significant current is lost due to reflection (11.2 mA/cm^2) at the hybrid layer stack and parasitic absorption (4.6 mA/cm^2) in the polymer layer.
In PEDOT:PSS/Tc/c-Si devices which have the potential of multi-exciton generation via singlet fission in the Tc layer[5], simulations reveal that optical losses are minimal for combined organic thin layer thicknesses $d_{PEDOT} + d_{Tc} \approx 100$ nm. Optical light harvesting is accomplished by the variation of the PEDOT:PSS and Tc layer thicknesses. Optimal electrical efficiency is determined by the Tc layer thickness alone. By assuming the maximum singlet fission quantum yield of 200% and no recombination losses during exciton diffusion and their dissociation into free charges at the Tc/c-Si interface, the best j_{sc} of 39.3 mA/cm^2 is achieved for a 30 nm PEDOT:PSS/100 nm Tc layer stack. This corresponds to a relative photocurrent gain of $\sim$20% due to multi-exciton generation. However, in this planar layer stack 10.9 mA/cm^2 is lost due to reflection and parasitic absorption. Taking this into account, j_{sc} can be as high as 50.2 mA/cm^2 which is well above the maximum j_{sc} of 43.2 mA/cm^2 calculated for single junction c-Si solar cells [243]. Assuming literature values for device fill factor, FF, and open-circuit voltage, V_{oc}, of the world record single junction c-Si based solar cell (η = 26.33%, j_{sc} = 42.25 mA/cm^2, FF = 83.78%, V_{oc} = 743.8 mV [91, 338]) would result in an efficiency of 31.3%.
These significant current losses in a planar hybrid organic/c-Si solar cell structure demands for a better light management. Reflection losses can be minimized by both, surface texturing and by the incorporation of additional, non-absorbing AR-coating thin layers with suitable refractive indices. To minimize parasitic absorption, PEDOT:PSS layers have to be fabricated as thin as possible while maintaining electrical properties and ensuring a sufficient overall AR-behavior. In addition, textured surfaces may further decrease parasitic absorption losses as a significant fraction of incident light hits the less absorptive extraordinary component of birefringent PEDOT:PSS.
Optical simulations cannot predict device efficiencies, fill factors or open-circuit voltages. Therefore electrical simulations have to be performed. Finally, the concept has to be proven experimentally. Device results are presented and discussed in the following chapters.

[5] created triplet excitons have to be harvested at the Tc/c-Si interface

6

Hybrid PEDOT:PSS/c-Si heterojunction solar cells

The highly conductive polymer PEDOT:PSS is commonly used as a hole selective contact in organic solar cells. In particular, it was utilized in organic multi-exciton generating devices with Pc and Tc incorporated as the singlet fission material, e.g. Refs. [134, 328, 64, 305, 172, 171]. More recently, it has been shown that PEDOT:PSS is also a promising candidate as an organic hole-selective contact for n-type Si. Within the proposed multi-exciton generating PEDOT:PSS/Tc/c-Si device concept (cf. section 2.4) we make use of both properties by incorporating the singlet fission material Tc in between the hole selective PEDOT:PSS and the n-type c-Si absorber (experimental results, see chapter 7). In this chapter the novel PEDOT:PSS/c-Si heterojunction is investigated in great detail.

First devices with PEDOT:PSS implemented in c-Si solar cells have been presented by M. J. Price et al. in 2010 [232]. Efficiencies of solar cells with a planar device structure beyond 12% have been reported [226, 202, 179]. D. Zielke et al. reached about 17% in their "BackPEDOT" concept [348]. This proves that a reasonable passivation of the c-Si surface is possible. Recently, it was shown by S. Jäckle et al. that the PEDOT:PSS/(n)c-Si junction behaves as an abrupt p^+n-heterojunction [138], and not as commonly assumed as a Schottky junction [232, 142, 346].

A heterojunction contact is fundamentally characterized by its selectivity and passivation quality. The selectivity can be provided by the potential barrier present for one type of charge carriers. The barrier height was obtained by the construction of a complete band diagram of the PEDOT:PSS/(n)c-Si heterojunction. For this we combined experimental results (C-V and UPS measurements) and, where necessary, literature values. To study the passivation mechanism for standardly prepared hybrid junctions by means of solution processing of water based PEDOT:PSS on initially H-passivated c-Si surfaces, a tender/hard X-ray PES (HAXPES) study was conducted which allows to directly probe the buried PEDOT:PSS/c-Si interface on device relevant layer stacks.

By fabricating hybrid solar cells utilizing high quality c-Si absorbers and a superior electron selective back contact adopted from the highly efficient SHJ technology, we report on a record V_{oc}

$>$ 660 mV with an estimated interface recombination velocity $<$ 1000 cm/s.
HAXPES data are in-line with the estimated interface recombination velocity of hybrid solar cells, suggesting an immediate formation of a moderately passivating sub-stoichiometric SiO_x layer at the c-Si surface during standard sample processing.
Furthermore, by comparing experimental results with the simulations presented in chapter 5, optical losses at the hybrid layer stack on the solar cell's front side are quantified and discussed.

The results presented in this chapter contributed to the following publications:

1. S. Jäckle, M. Mattiza, M. Liebhaber, G. Brönstrup, M. Rommel, K. Lips, and S. Christiansen, *Junction formation and current transport mechanisms in hybid n-Si/PDEOT:PSS solar cells*, Scientific Reports **5** (2015), 13008, `http://dx.doi.org/10.1038/srep13008`, Ref. [138].
2. S. Jäckle, M. Liebhaber, J. Niederhausen, M. Büchele, R. Félix, R. G. Wilks, M. Bär, K. Lips, and S. Christiansen, *Unveiling the Hybrid n-Si/PEDOT:PSS Interface*, ACS Applied Materials & Interfaces **8** (2016), 8841, `http://dx.doi.org/10.1021/acsami.6b01596`, Ref. [137].
3. S. Jäckle, M. Liebhaber, C. Gersmann, M. Mews, K. Jäger, S. Christiansen, and K. Lips, *Potential of PEDOT:PSS as a hole selective front contact for silicon heterojunction solar cells*, submitted to Scientific Reports (2017), `http://arxiv.org/abs/1701.05368`, Ref. [136].

The studies presented in this chapter were done in collaboration with S. Jäckle[1]. HAXPES experiments were carried out under the lead of the author of this thesis with beam time support by S. Jäckle, R. Wilks and R. Félix. Sample preparation was done by S. Jäckle. HAXPES data analysis was performed by S. Jäckle, J. Niederhausen and the author of this thesis. Near-UV PES measurements and data analysis was performed by the author of this thesis. S. Jäckle and the author of this thesis equally contributed to the work on record hybrid solar cells. For record devices a-Si:H layers were grown by M. Mews. C. Gersmann was involved in the fabrication of the hybrid front contact and device characterization. C-V measurements were conducted by S. Jäckle. Optical simulations were carried out by the author of this thesis and K. Jäger. Manuscripts were written under the responsibility of S. Jäckle. All authors of above papers were involved in the discussion and interpretation of our results.
Section 6.1 is based on paper [138], Section 6.2 on paper [137] and Section 6.3 on paper [136].

6.1 Investigation of the buried PEDOT:PSS/c-Si interface

To investigate the passivation mechanism, a HAXPES study using an excitation energy (E_{ex}) of 3 keV was conducted to probe the buried PEDOT:PSS/c-Si interface on device relevant hybrid layer stacks. As PEDOT:PSS is usually directly fabricated on initially H-passivated c-Si surfaces, we investigated this interface.

[1] Max-Planck-Institute for the Science of Light & Institute of Nano-architectures for Energy Conversion, HZB

6.1.1 HAXPES sample preparation and degradation

To study a buried interface with HAXPES, photoelectrons from that interface have to escape through capping layers without being scattered. Therefore, capping layers have to be thin, in the order of ∼10 nm, depending on the specific experimental setup, e.g. excitation energy, light intensity, analyzer sensitivity, and material density (cf. section 3.2.1). However, the thinner the layers get the more probable pinholes will exist that can lead to signal artifacts caused by signals related to the underlying substrate. Standard spin-coating of PEDOT:PSS at maximum rotation speed of 10.000 rpm produces an average layer thickness of ∼35 nm. Because these layers are too thick to detect any signal from the buried interface, we followed a DMSO post-treatment procedure as suggested in literature [58, 156, 331]. Thus, layer thicknesses could be further reduced to ∼20 nm. The detailed sample preparation is described in section 3.1.

Figure 6.1 shows the comparison between (a) "bulk sensitive" Si 2s (E_{bind} = 150 eV) and (b) "surface sensitive" Si 1s (E_{bind} = 1840 eV) core level XPS spectra (E_{ex} = 3 keV) for thin film PEDOT:PSS on c-Si. The different information depth of the core level peaks originates from their difference in E_{bind}. For the same E_{ex}, higher E_{bind} results in lower E_{kin} of photoelectrons. Hence, the IMPF of photoelectrons related to Si 1s is significantly smaller compared to photoelectrons related to Si 2s core levels (cf. Fig. 3.4 in section 3.2.1). The Si 2s peak is clearly observed for ∼20 nm thin PEDOT:PSS layer on c-Si substrate (red data in Fig. 6.1 (a)), while at the same time the Si 1s peak –related to more surface sensitive signals– is not detected (noise in Fig. 6.1 (b)). This proves that the Si 2s signal exclusively stems from the buried PEDOT:PSS/c-Si interface. Therefore, we can exclude that the Si 2s signal is related to bare c-Si substrate. We therefore conclude that no pinholes or scratches in the PEDOT:PSS layer exists and no Si-related contaminants on the surface are probed. The ∼35 nm PEDOT:PSS layers are too thick to detect a significant Si 2s signal of the buried interface (black data in Fig. 6.1).

A rough estimate for the IMPF of photoelectrons in PEDOT:PSS can be calculated with the "TPP2M" formula [297], using the chemical formula of the polymer and assuming a density of 1 g/cm^3 [90, 1]. For an excitation energy of 3 keV the deduced IMPF for photoelectrons in the polymer stemming from Si 2s (E_{kin} = 2.85 keV) and Si 1s (E_{kin} = 1.15 keV) are ∼6.5 nm and ∼3 nm, respectively. Assuming a homogeneous coverage and considering that the Si signal is exponentially attenuated to 1/e^3 (i.e. ∼5%) compared to the signal of the bare c-Si wafer, this approximation suggests to obtain detectable buried Si related intensities for PEDOT:PSS coverages in the range of 10 - 20 nm [137]. For soft organic materials, in particular porous materials, the IMPF can be greatly increased [111]. This rationalizes why significant signals related to buried Si on samples with ∼20 nm PEDOT:PSS capping layers can be detected.

Using high excitation energies and high intensity synchrotron radiation may cause degradation of organic samples. To exclude beam-induced sample degradation during HAXPES measurements, single scan spectra of thin film PEDOT:PSS/c-Si samples were recorded. Figure 6.2 shows core level spectra of S 2p, which are related to PEDOT:PSS bulk material, and the Si 2s signal which stems from the buried interface and c-Si substrate. The black/white image depicts all single scans in an intensity plot. The scan sum is plotted in the bottom panel. No change in intensity, shape or position of the peaks is observed over 20 scans which corresponds to ∼1 h of X-ray irradiation.

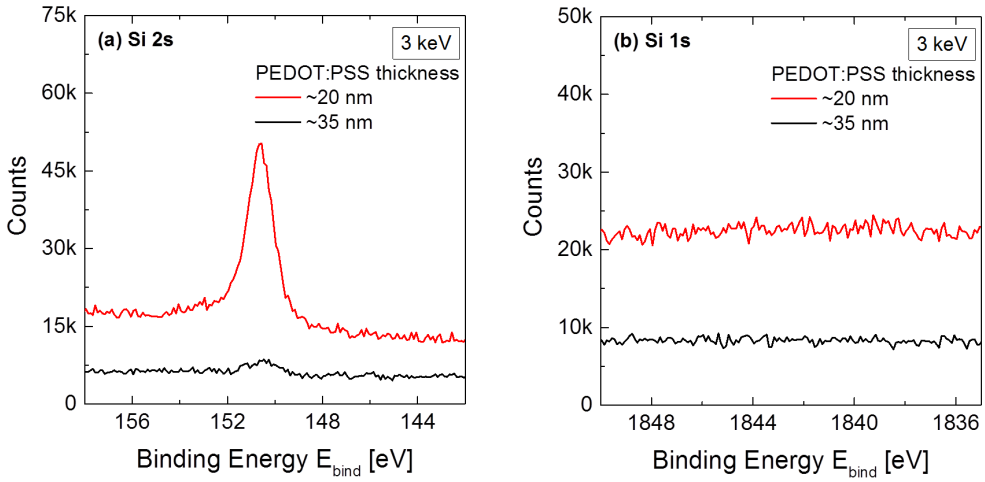

Figure 6.1: (a) "bulk sensitive" Si 2s and (b) "surface sensitive" Si 1s core level XPS spectra (E_{ex} = 3keV) of thin film PEDOT:PSS on c-Si. Standardly processed layers with a thickness of ∼35 nm (black data) and DMSO post-treated films of ∼20 nm (red data) were studied. Figure adopted from our publication [137].

Within the signal-to-noise, scan #1 (green spectrum) is identical to scan #20 (blue spectrum).

Samples with thicker PEDOT:PSS films reveal no c-Si related peaks even for long exposure times (data not shown here). In addition, no energy shift or changes in peak shape or intensity ratios were detected for C, S, and O core level peaks of bulk PEDOT:PSS (data not shown here). Furthermore, at the spot of irradiation no obvious change of the samples could be observed in an optical microscope.

In summary, there are no indications for any beam-induced PEDOT:PSS degradation while exposed to a moderate flux of 3 keV photons in the low intensity modes of BESSY II[2] used throughout the HAXPES studies. Therefore, all prerequisites for a meaningful HAXPES experiment –thin but closed layers and no beam-induced sample degradation– are fulfilled. HAXPES results will be presented and discussed in the following.

6.1.2 Effect of DMSO post-treatment on chemical composition of PEDOT:PSS

The chemical formula of the used PEDOT:PSS blend (Clevios PH 1000) is given in Figure 6.3 [1]. It consists of different species, PEDOT and PSS. The three chemical states of S related to the thiophene ring in PEDOT and to sulfonic acid groups in the neutral PSSH and charged PSS^- state are indicated in the figure.
In a first step, the change in chemical composition of PEDOT:PSS after the DMSO post-treatment is investigated. In addition to the S 2p core level peak located at $E_{bind} \approx 165$ eV, the HAXPES

[2](i) *'low-α multi bunch hybrid mode A'*, and (ii) *'low intensity single bunch mode'*

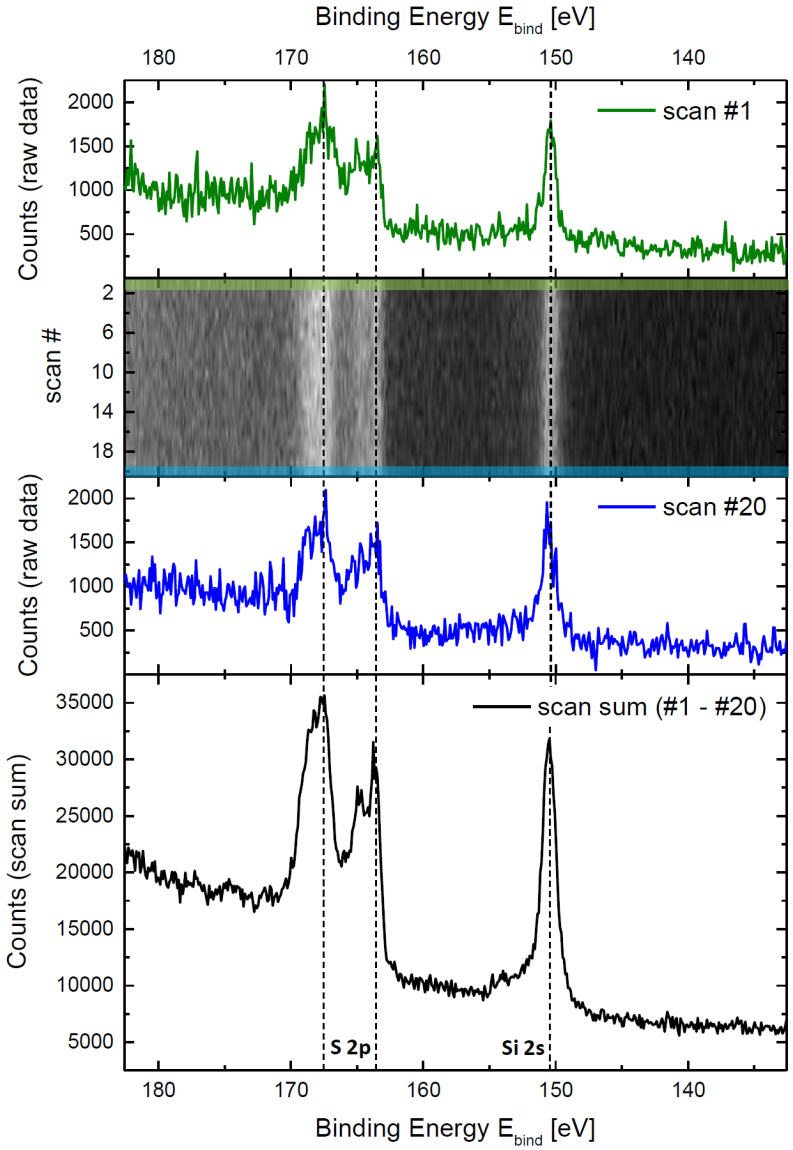

Figure 6.2: S 2p/Si 2s core level spectra (E_{ex} = 3 keV) of ∼20 nm thin film PEDOT:PSS/c-Si samples taken in the low intensity mode of BESSY II. Comparison of the first (green data) and last (blue data) single scan, and the summed up spectrum (black data). The black/white image depicts all single scans in an intensity plot. No significant change of the spectra can be observed over 20 scans. Figure as published in Ref. [137].

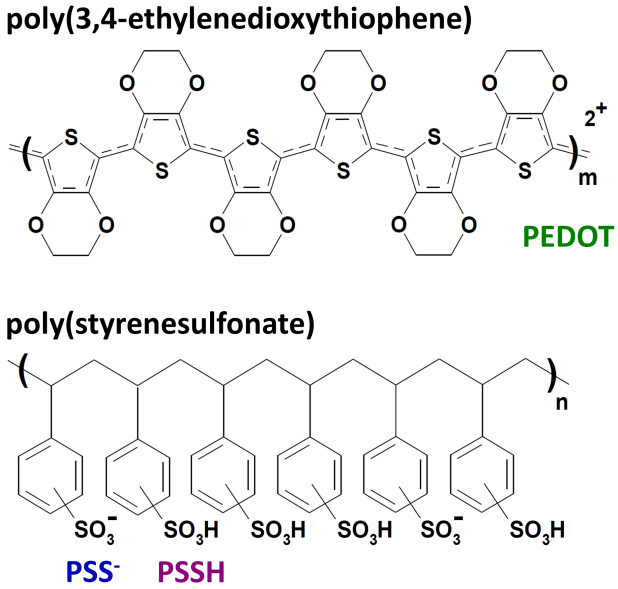

Figure 6.3: Chemical formulation of the PEDOT:PSS blend (Clevios PH 1000 [1]) consisting of different species, poly(3,4-ethylenedioxythiophene), PEDOT, and poly(styrenesulfonate), PSS, respectively. The dashed line in PEDOT shows the conjugation path through the backbone. 2^+ cationic charge in the PEDOT polymer chain is delocalized over several adjacent thiophene rings. As labeled, the PSS part consists of ionic PSS^- and neutral PSSH species [1].

study using 3 keV synchrotron radiation also allows to probe the S 1s core-level peak located at $E_{\mathrm{bind}} \approx 2475$ eV. Since no spin-orbit splitting has to be considered for s-shell core-level spectra, data analysis is slightly simplified compared to higher-order shell core-level spectra.

Figure 6.4 shows the S 1s core level spectra of PEDOT:PSS (a) before, and (b) after the additional DMSO immersion treatment. The three different chemical states of S as indicated in Figure 6.3, (i) PEDOT, (ii) neutral PSSH, and (iii) charged PSS^-, were deconvolved following the analysis of G. Greczynski et al. [113]. The signals related to the S atoms bonded in the thiophene ring (PEDOT) are at lower E_{bind} than the signals related to the strongly positive S atoms in the PSS species. The PEDOT peak exhibits an asymmetric tail on the higher binding energy side due to cationic charge in the PEDOT polymer chain being delocalized over several adjacent thiophene rings (indicated as 2^+ in Fig. 6.3) [113, 313]. The PSS signal is split into the neutral PSSH component located at a slightly higher E_{bind} than the ionic PSS^- component. Both S 1s spectra, i.e. before (Fig. 6.4(a)), and after the additional DMSO immersion (Fig. 6.4(b)) of PEDOT:PSS films exhibit distinct signals from PEDOT and PSS components. Spectra are fitted with the PSS^- peak shifted by 5.06 eV and the PSSH peak shifted by 5.63 eV with respect to the PEDOT peak. Intensity ratios of PEDOT-to-PSS signals can be deduced from the fitted peak areas.
For the "standardly" prepared polymer film a PEDOT:PSS ratio of 1:2.5 is derived from the S 1s spectrum (Fig. 6.4 (a)). This is identical to the molar ratio given by the supplier (Clevios PH 1000 [1]). In literature, phase segregation is reported for equivalently prepared PEDOT:PSS films using identical or similar polymer dispersions. The morphology consists of a shell of excess PSS segregating at the surface of PEDOT:PSS grains [225, 333, 132, 313, 113]. As discussed in the previous section (cf. Fig. 6.1), photoemission signals from high E_{bind} core level peaks such as S 1s are rather surface sensitive. For that reason a significantly higher PSS contribution in surface-sensitive S 1s photoemission data is expected. However, the molar ratio given by the supplier corresponds to the pristine polymer dispersion. In the present case, the PH 1000 suspension is mixed with 5 vol% DMSO, which has been shown to increase the PEDOT-to-PSS ratio

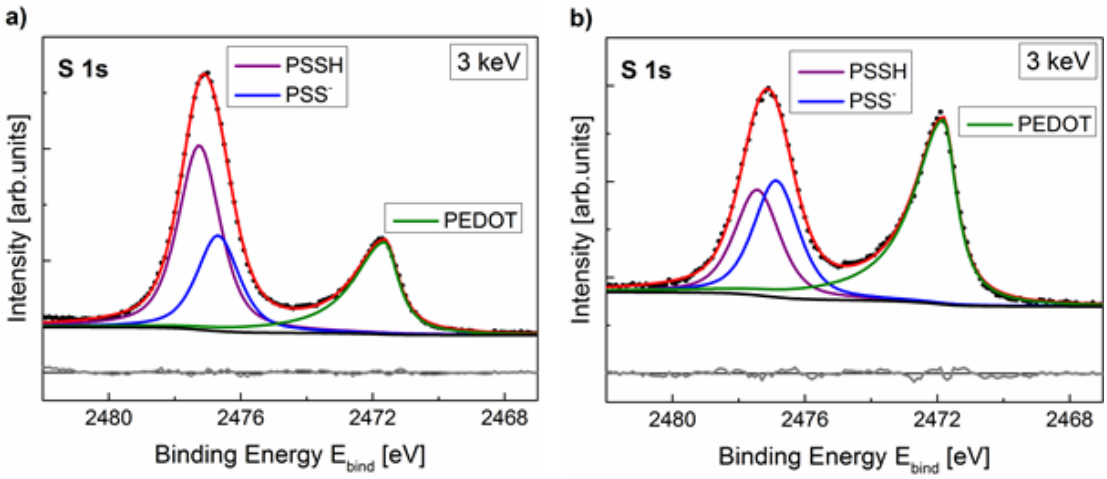

Figure 6.4: S 1s core level spectra (E_{ex} = 3 keV) of PEDOT:PSS (a) before and (b) after the additional DMSO treatment. Fitting of the spectra is based on the analysis of G. Greczynski et al. [113]. In PEDOT:PSS three different chemical states of S, i.e. PEDOT, PSSH and PSS^{-}, exist. The residual of the fit is shown in gray. Figure as published in Ref. [137].

[225, 313]. This may explain the measured ratio of 1:2.5.
By visual inspection of both spectra, it is obvious that the PEDOT-to-PSS signal ratio drastically changes after the additional immersion of PEDOT:PSS in DMSO. The intensity ratio obtained for the post-treated polymer is 1:1.1. This is in agreement with the observation by other groups that immersion of PEDOT:PSS in polar solvents or acids strongly reduces the PSS content [225, 329, 313, 76].

Furthermore, the sheet resistivity of the PEDOT:PSS films increases only slightly from 170 Ω/sq (∼35 nm) to 200 Ω/sq (∼ 20 nm) after the post-treatment. This indicates that the excess PSS removed by the additional immersion in DMSO was not actively taking part in the charge transport through the polymer layer [137].

Figure 6.5 visualizes the results presented so far. The well-known core-shell phase segregation with PEDOT:PSS grains (indicated in blue) surrounded by a PSS shell (indicated in red) is sketched [113, 225, 132]. HAXPES results suggest, that the excess PSS material in the shell is drastically reduced, or removed entirely, after the DMSO post-treatment leading to a thickness reduction of the polymer of approximately 40%. As shown in the previous section (cf. Fig. 6.1) and indicated by the arrows in Figure 6.5, those thin polymer layers allow to detect signals related to buried c-Si or interlayer within our HAXPES study using 3 keV excitation energy.

6.1.3 HAXPES study of the buried PEDOT:PSS/c-Si interface

The main result of the HAXPES study is depicted in Figure 6.6. For the investigation of the hybrid PEDOT:PSS/c-Si interface formation, the Si 2s core level signal was recorded with high

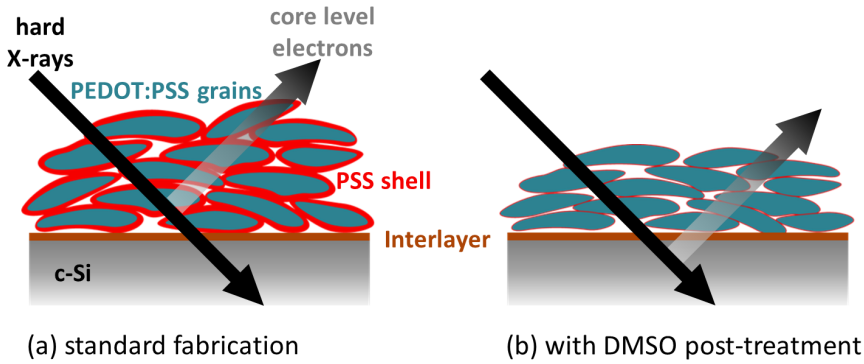

Figure 6.5: Sketch of PEDOT:PSS deposited on c-Si substrates. In the polymer, PEDOT:PSS grains (blue) are surrounded by a PSS shell (red) [113, 225, 132]. The PSS shell thickness is reduced by an additional immersion in DMSO leading to a thickness reduction of the polymer film of ∼40%. As indicated by the arrows, the thinner polymer films allow to detect signals from c-Si substrate and the interlayer. Figure adopted from our publication [137].

resolution and best signal-to-noise ratio feasible within reasonable integration times. Spectra are background corrected and normalized. For fitting and a thorough data interpretation various reference spectra without PEDOT:PSS capping layers are important and will be discussed.
Fig 6.6 (a) shows the Si 2s peak of a freshly HF-dipped c-Si wafer. The time between dip and sample loading into vacuum was ∼ 5 - 10 min. As expected for the H-passivated c-Si substrate the spectrum exhibits only one core level peak which is related to elemental Si (Si^0) [32, 210].
As a second reference (Fig. 6.6 (b)), a spectrum of a HF-dipped c-Si wafer that was oxidized for two weeks in ambient air (clean room conditions) was recorded. A distinct shoulder arises at higher E_{bind} which is related to Si oxide natively grown at the c-Si surface [126]. The spectrum can be fitted with two peaks whereby the oxide peak (orange trace, Fig. 6.6 (b)) is located at ∼3.6 eV higher E_{bind}. This is in good agreement with reported energy position of Si^{4+} as present in SiO_2 [32] and dominating native oxide growth on c-Si surfaces [116]. As already discussed in section 4.1 (cf. Fig. 4.2), SiO_x suboxide (x < 2) signals would appear in between the Si^0 and Si^{4+} peaks [32, 126]. However, since we are not probing thick PECVD grown SiO_x layers (cf. chapter 4), signals related to thin surface oxides are overlaid by intense c-Si bulk signals. As a general trend, suboxide related signals are hardly detectable for natively oxidized c-Si wafers [198].
In Figure 6.6 (c,d) Si 2s spectra of (c) a freshly prepared PEDOT:PSS/c-Si sample and (d) an identical prepared sample but stored for two weeks in an inert gas (N_2) atmosphere are plotted. Photoemission signals related to buried layers are effectively attenuated by capping layers. Thus, the signal-to-noise ratio of polymer capped samples is strongly reduced compared to the reference spectra, especially visible in the noise of the peak shoulders.
However, the Si 2s spectrum of the freshly prepared PEDOT:PSS/c-Si sample (Fig. 6.6 (c)) also reveals a peak shoulder at the higher binding energy side of Si^0. The spectrum could be adequately fitted assuming two components (Si^0, SiO_x). The shoulder is less shifted (ΔE ∼2.4 eV,

red trace) compared to the SiO_2 shift of the natively oxidized reference sample, pointing to the presence of suboxide species (i.e. Si^{2+} and/or Si^{3+} [32, 126]) at the interface.
The Si 2s core level peak of a PEDOT:PSS/c-Si sample stored for two weeks in N_2 is depicted in Figure 6.6 (d). Compared to the freshly prepared sample, a more pronounced shoulder is observed. The fitting procedure indicates also the presence of SiO_2 species (orange trace) in addition to Si suboxides species (red trace).

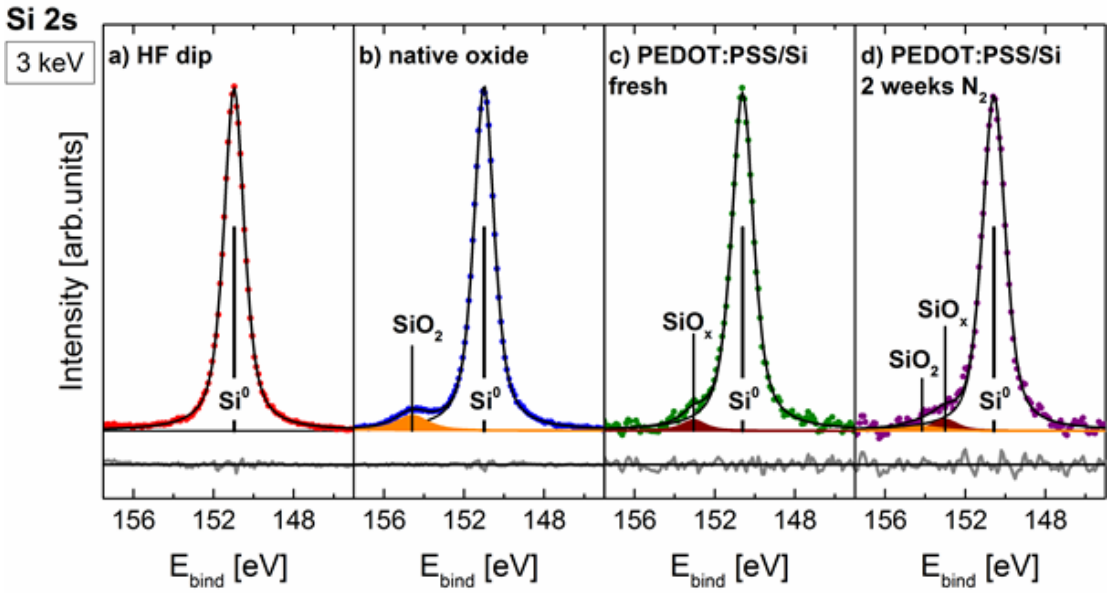

Figure 6.6: Background subtracted and normalized Si 2s core level spectra (E_{ex} = 3 keV) of (a) freshly HF-dipped, (b) oxidized, as well as covered c-Si wafers with thin (∼20 nm) layers of PEDOT:PSS measured (c) directly after preparation and (d) after storage in N_2 for two weeks. Various Si oxidation states are indicated. The residual of the fit is indicated in gray. Figure as published in Ref. [137].

6.1.4 Discussion of PEDOT:PSS/c-Si interface formation

Figure 6.7 summarizes the results of the HAXPES study. In a first step the colloidal dispersion of core-shell PEDOT:PSS in water (Fig. 6.7 (a)) is spin-coated on H-passivated c-Si substrates and annealed in ambient air. This leads to polymer films too thick to allow probing the buried interface with HAXPES. So we cannot gain information on its nature (indicated in brown in Fig. 6.7 (b)). After the additional DMSO immersion, including a second annealing step, excess PSS material is removed and the polymer film thickness can be further reduced by ∼40%. In such samples photoemission signals related to the buried interface are detected (Fig. 6.7 (c)).
Data analysis of the Si 2s core level peaks as presented in Figure 6.6 indicates that upon deposition and processing of PEDOT:PSS on an initially H-passivated c-Si substrate, the latter partially oxidizes. A rough upper estimate of the thickness of the interfacial oxide layers ($d \approx$

1.5 nm) can be deduced by the comparison of the intensity ratio of elemental and suboxide peaks of PEDOT:PSS/c-Si samples with the intensity ratios of Si 2s and Si 1s peaks of the natively oxidized c-Si wafer reference sample [137, 326]. For comparison, a monolayer of Si oxide is only about 0.3 nm thick [116]. A moist atmosphere can greatly enhance oxide formation on c-Si surfaces [201]. Furthermore, it has been shown that oxidation of c-Si in hot DI water is a very fast process [14]. Both, water from the water-based polymer dispersion and temperatures above 100 °C during mandatory annealing steps, are provided during PEDOT:PSS layer fabrication. This is believed to generate conditions that lead to a fast c-Si surface oxidation.
Note that possibly also other PEDOT:PSS-related species might bind to the c-Si surface forming e.g. Si-C or Si-S bonds which cause chemical shifts of the Si core level peak in the same region as the Si suboxide species [18, 322, 7]. However, as those species can at most form a monolayer on the Si surface their intensity would be lower than for the observed oxide peak. We interpret the observed chemical shift of the Si core level peak as a clear indication of an immediate formation of an interfacial suboxide layer (indicated in yellow in Figure 6.7 (c)).
Moreover, we observe that the initial suboxide layer increases in thickness, as well as in degree of oxidation state, even when samples are stored in inert gas atmosphere (Fig. 6.7 (d)). SiO_2 species are detected in addition to SiO_x. A mixed SiO_2/SiO_x interfacial oxide layer thickness of $\sim$1.9 nm was estimated [137].

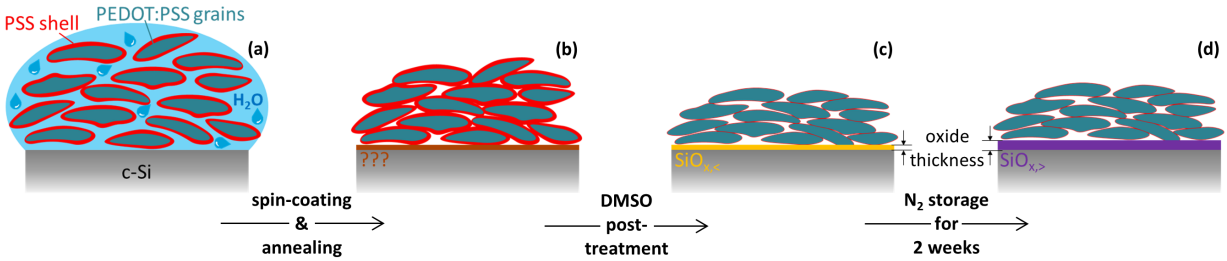

Figure 6.7: Sketch of the results from the HAXPES experiment. The colloidal dispersion of core-shell PEDOT:PSS in water (a) is spin-coated on H-passivated c-Si substrates and dried at temperatures > 100 °C leading to polymer films of $\sim$35 nm (b). By the DMSO post-treatment (incl. a 2nd annealing step) excess PSS material is removed and the film thickness is reduced by $\sim$40% (c). For post-treated samples the buried interface is accessible with HAXPES. Data analysis indicate an initial formation of an interfacial SiO_x layer (indicated in yellow) which increases in thickness and degree of oxidation state with time (indicated in violet), even when samples are stored in inert gas atmosphere (d).

As sketched in Figure 6.8, a likely explanation of this finding is residual water which accumulates at the interface, and/or the diffusion of residual water from pores in the polymer film to the interface. It is shown that PEDOT:PSS can easily take up water because of the hygroscopic behavior of PSS [90, 156]. Within a XPS study, evidence for residual water molecules in PEDOT:PSS films dried at 120 °C for 2 h in vacuum was found [113]. Although excess PSS material is drastically removed after the additional DMSO immersion, it is still likely that the polymer takes up some water during processing in ambient conditions. Water on the c-Si surface then causes

further oxidation with time [13]. This model could explain that even if stored in N_2, the interface is not stable and the c-Si surface continues to oxidize.

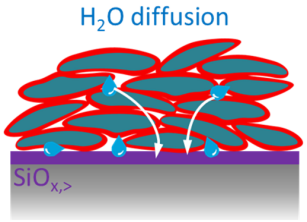

Figure 6.8: Model of continuous c-Si surface oxidation at the hybrid PEDOT:PSS/c-Si interface due to residual water left over at the interface, and/or the diffusion of residual water in the polymer film to the interface. Water on the c-Si surface then causes further oxidation with time.

The passivation quality of the natively grown interfacial suboxide layer at the PEDOT:PSS/c-Si junction is addressed in the discussion of hybrid devices presented in section 6.3. However, the observed continuous oxide growth can deteriorate the initial electronic quality of the interface with time. Therefore, in terms of long-term hybrid PEDOT:PSS/c-Si device stability this implies that in addition to a proper encapsulation of the polymer itself, also a stable and well passivating interface prior to solution processing has to be ensured. Possible candidates are inorganic ultrathin aluminium oxides [234], stoichiometric Si tunnel oxides [109, 106], or organic methyl passivation [178, 345, 344].
Another possibility to prevent oxide formation is to use non-water based PEDOT:PSS dispersions which recently became commercially available. Two polymer dispersions from the company Heraeus Clevios, i.e. *HTL Solar 3* (dispersion in toluene [3]) and *S V 3 Stab* (dispersion in glycols [2]), are candidates to be investigated[3]. In addition, to prohibit water uptake during fabrication, the whole preparation should be done in inert atmosphere such that no water is provided to the layer stack at all.

6.2 Valence band / HOMO of PEDOT:PSS

The valence band / HOMO and the sample's work function, Φ_w, of PEDOT:PSS (Clevios PH 1000 [1]) is probed by UPS measurements using a near-UV excitation energy of 6.5 eV. Details on sample preparation and the UPS experiment are given in chapter 3. Immediately after polymer fabrication, samples were loaded into the UHV analytics chamber.

Figure 6.9 depicts the measured UPS spectrum: (a) close to the secondary electron cut-off (SECO), and (b) the zoom into the valence band leading edge close to E_F.
From an UPS spectrum, Φ_w is determined by the difference between the excitation energy and E_{bind} at the SECO [124]. The steep rise of photoemission signal was fitted with a sigmoidal function using the Boltzmann Equation $y(x) = \left\{[A_1 - A_2] \,/\, \left[1 + e^{(x-x_0)idx}\right]\right\} + A_2$ [138, 191], whereby y changes drastically within the width dx. The y value at x_0 is half way between the two limiting values A_1 and A_2. The center position x_0 is defined as the SECO. The corresponding fit is shown in blue and the SECO is indicated as a vertical black line in Figure 6.9 (a). From the data Φ_w = (5.15 eV $\pm$ 0.02) eV for PEDOT:PSS is extracted. This is in good agreement

[3] note that the conductivity is strongly reduced compared to water based *PH 1000* and *F HC solar* polymer solutions used within this thesis

with literature values reported between 5.0 eV $\lesssim \Phi_w \lesssim$ 5.2 eV for similar mixed and treated PEDOT:PSS [340, 131, 157, 42, 132]. The rather small error of 20 meV corresponds to the fitting error. However, Φ_w is very sensitive to surface adsorbates. As shown by N. Koch et al., residual or adsorbed water from the ambient decreases the work function compared to polymer films dried in vacuum [157].

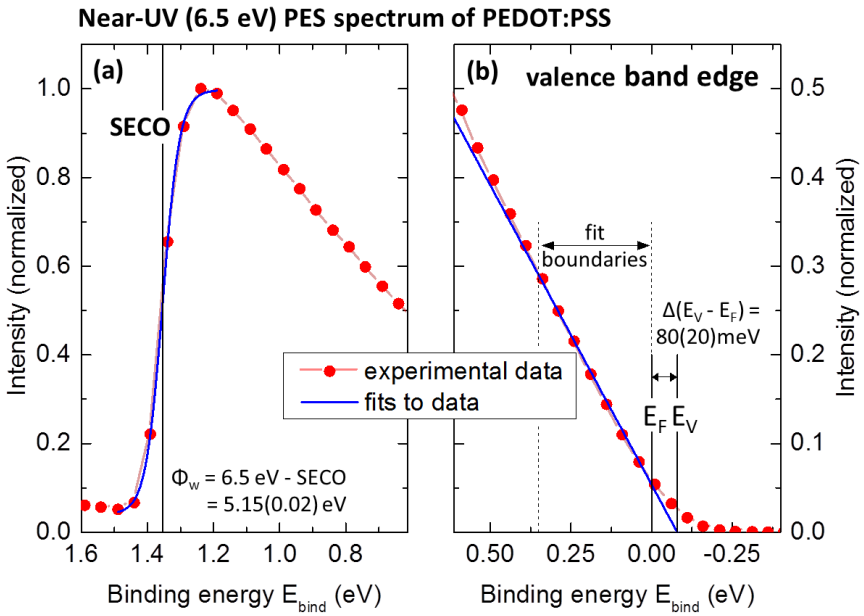

Figure 6.9: Near-UV photoelectron spectroscopy spectrum of a PEDOT:PSS film using 6.5 eV excitation energy. (a) Secondary electron cut-off, SECO, fitted by a Boltzmann sigmoid function for extraction of the work function, Φ_w (for details see text). (b) Valence band states near the Fermi level, E_F. The valence band edge, E_V, is determined by a linear extrapolation of the leading edge to zero. Figure adopted from our publication [138].

Figure 6.9 (b) shows the valence band leading edge. Often, surface sensitive UPS spectra are dominated by the insulating PSS shell instead of by the conductive PEDOT:PSS grains (bulk material) [113, 132]. The use of a rather low excitation energy of 6.5 eV compared to commonly used He-UPS (21.2 eV) leads to a higher information depth (cf. Fig. 3.4, section 3.2.1). Note that in the binding energy range $0 \lesssim E_{\text{bind}} \lesssim 2$ eV surface-segregated PSS species show no signal, but strongly attenuate signals originating from the conductive PEDOT:PSS bulk material [113]. Thus, in the here conducted "bulk sensitive" near-UV PES study, a significant signal response stems from PEDOT:PSS bulk material. As expected for a highly p-doped material as the here used PEDOT:PSS (*PH 1000* [1]), the spectrum exhibits filled valence states up to the Fermi level, E_F. The valence band edge position, E_V, was extracted by a linear extrapolation of the measured valence DOS leading edge to zero. The fit, including fit boundaries, is depicted in blue in Figure 6.9 (b). The determined E_V position lies (80 $\pm$ 20) meV above E_F. Thus, PEDOT:PSS appears to be degenerately doped. A similar UPS spectrum was reported recently by O. Bubnova et al. showing a significant DOS at E_F for the highly conductive PEDOT-Tos [42]. This could be

ascribed to the existence of bipolaron states within the energy gap forming bands at high doping levels [39, 38, 33, 90, 42].

The values extracted from UPS experiments will be used to construct the band diagram of the PEDOT:PSS/c-Si heterointerface (cf. next section).

6.3 PEDOT:PSS/c-Si hybrid solar cells

The first PEDOT:PSS/c-Si solar cell was presented in 2010 [232], followed by numerous reports on modifications of this junction, e.g. Refs. [142, 141, 323, 234, 339, 226, 138]. Hybrid solar cell results reported in literature are often achieved on so-called "long base" wafers, in which the diffusion length of minority charge carriers is smaller than the wafer thickness. Also ohmic metallic back contact schemes featuring high recombination velocities can lead to a reduction of charge carrier lifetimes. However, the full potential of PEDOT:PSS as a hole selective front junction on n-type c-Si can only be determined if the device is not limited by the intrinsic properties of the c-Si wafer or the implemented back contact. Therefore, we combine the hybrid PEDOT:PSS/c-Si front junction with a superior, very selective and well passivated electron back contact and use high quality c-Si wafers with a minority carrier diffusion length larger than the wafer thickness.

6.3.1 PEDOT:PSS/c-Si solar cell results

A sketch of the hybrid device is given in the inset of Figure 6.10 (a). The electron back contact consists of an (i,n$^+$)a-Si:H layer stack, followed by an ITO/Ti/Ag metallization adopted from the high-efficiency SHJ technology [194, 191]. PEDOT:PSS is fabricated on the front side followed by Ag-grid metallization. The detailed description of the hybrid device fabrication is given in section 3.1.
The $j(V)$-curve of the record PEDOT:PSS/c-Si solar cell, including characteristic device parameters, is depicted in Figure 6.10 (a). We report on an efficiency of 14.8%, j_{sc}[4] = 31.9 mA/cm^2, V_{oc} = 663 mV, and FF = 70%. To the best of the author's knowledge, this is the highest V_{oc} achieved for hybrid solar cells using PEDOT:PSS as a hole selective front contact to date. SHJ solar cells fabricated at HZB with identically-prepared electron back contacts but conventional inorganic ITO/(p)a-Si:H/(i)a-Si:H hole selective front contacts exhibit V_{oc}s up to 708 mV [191] and efficiencies above 16% [194]. Hence we conclude, that the achieved V_{oc} of 663 mV is truly limited by the hybrid PEDOT:PSS/c-Si front contact. This is supported by a similarly V_{oc} of 657 mV reported for the so-called "BackPEDOT" hybrid device concept using PEDOT:PSS as a hole selective back contact in a high-efficient front homojunction c-Si solar cell [250, 347]. Although PEDOT:PSS does not perform as well as the inorganic a-Si:H/c-Si front junction, it shows by far the best performance of all organic materials tested on c-Si. Using P3HT as an organic hole selective front contact and a similar inorganic SHJ electron back contact, a V_{oc} of only 617 mV is reported [341].

[4] solar cell active area of 0.85 cm^2, front metal grid subtracted

Figure 6.10 (b) depicts the corresponding $1/C^2$-V plot obtained by C-V measurements. As described in section 3.3, fitting of the linear part allows to determine the built-in voltage, Ψ_{bi}, and the doping concentration, N_D. The extracted values are given in the figure and will be used in the following section for the construction of the band diagram.

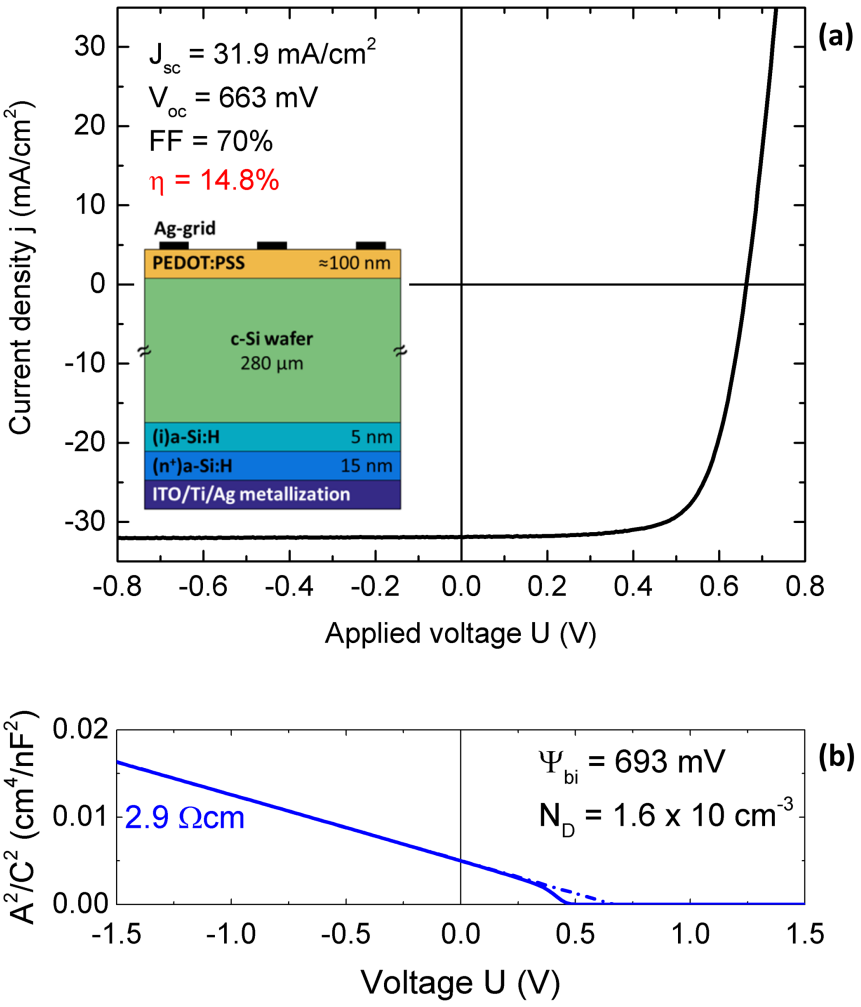

Figure 6.10: (a) $j(V)$-characteristics under AM1.5G illumination of the best hybrid PEDOT:PSS/(n)c-Si solar cell. The electron back contact is adopted from the high-efficiency SHJ technology. The exact hybrid layer stack is sketched in the inset. (b) Corresponding C-V characteristics. The built-in voltage, Ψ_{bi}, and the doping concentration, N_D, is extracted from the A^2/C^2-V plot according to Eq. (3.6) (cf. section 3.3). Data published in Ref. [136].

6.3.2 Junction formation at the PEDOT:PSS/(n)c-Si interface

In Figure 6.11 the band diagram of the hybrid PEDOT:PSS/(n)c-Si junction of the device under discussion is constructed by combining experimental data and literature values. For bulk c-Si

the electron affinity, χ_{Si} = 4.05 eV, and the band gap, E_g^{Si}(300K) = 1.12 eV, are well established values [288]. The built-in potential, $\Psi_{\mathrm{bi}} \approx 690$ mV, and the energy difference $\Delta(E_C - E_F) = \frac{k_B T}{q} \ln \frac{N_C}{N_D} \approx 250$ meV in c-Si is deduced by C-V measurements[5]. The energetic position of the conduction band / LUMO of PEDOT:PSS was recently determined by IPES to be at ∼3.6 eV, and the corresponding conduction band / HOMO is ∼4.9 eV [203]. Taking into account the measured $\Delta(E_V - E_F) \approx 80$ meV, the work function, Φ_w, is assumed to be ∼5.0 eV. The corresponding band offsets are indicated in red in Figure 6.11.

It is clearly seen in Figure 6.11 that due to Ψ_{bi} the intrinsic Fermi level of c-Si, E_I^{Si}, crosses E_F forming an inversion layer, IL, near the surface (indicated in blue). Moreover, even a strong inversion of c-Si, defined as $\Psi_{\mathrm{bi}} > 2|E_F - E_I|$ [288, 92], is observed at the PEDOT:PSS/(n)c-Si junction. Thus, the construction of the band diagram suggests the formation of a pn-junction within c-Si itself. A device operating in strong inversion is less sensitive to interface defects than a Schottky barrier or a weak inversion device. This gives rise to high V_{oc}'s and manifests the potential of the polymer PEDOT:PSS as an organic hole selective contact for (n)c-Si based photovoltaics.

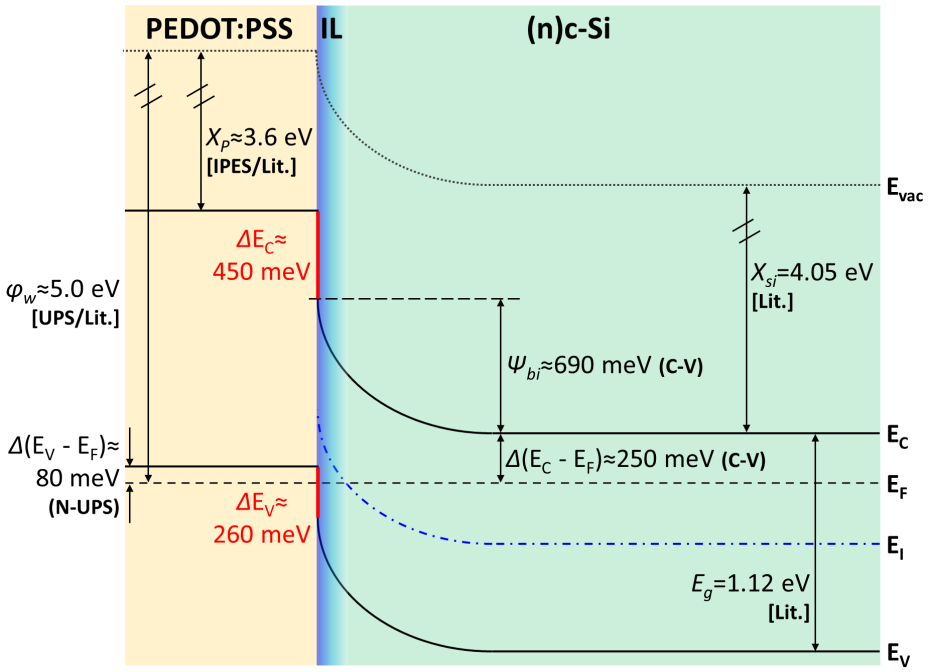

Figure 6.11: Constructed band diagram of the hybrid PEDOT:PSS/(n)c-Si junction by combining literature values for c-Si [288], PEDOT:PSS (IPES/UPS) [203], and values obtained by N-UPS(6.5 eV) and C-V measurements. The inversion layer (IL) caused by the built-in potential (Ψ_{bi}) is indicated in blue.

[5] with the effective density of states, N_C, in the conduction band. $N_C(300\ \mathrm{K}) = 2.8 \times 10^{19}\ \mathrm{cm}^{-3}$ [288]

6.3.3 Discussion of limiting properties of the PEDOT:PSS/(n)c-Si front contact

Based on the results presented above, the potential of PEDOT:PSS as a hole selective front contact for SHJ (n-type c-Si) solar cells will be discussed in this section.

Selectivity and passivation of the PEDOT:PSS/(n)c-Si junction

Basically, a heterojunction in solar cells is characterized by its selectivity and passivation.
The **selectivity** is provided by the **potential barrier** present for one type of charge carriers. The electron blocking barrier height at the PEDOT:PSS/(n)c-Si junction is given by (cf. Fig. 6.11) [288, 136]:

1. $\Delta(E_C - E_F) \approx 250$ meV (C-V data)
2. $\Psi_{\mathrm{bi}} \approx 690$ meV (C-V data)
3. $\Delta E_C \approx 450$ meV (IPES/UPS literature results [203])

The **passivation** of a heterojunction is determined by the **surface recombination velocity** (ν_S) and the **interface recombination velocity** (ν_I).
Considering all contributions listed above, this leads to the assumption of the dark saturation current density (j_0). It is derived by both contributions [136]:

$$\begin{aligned} j_0 \;\approx\; & qN_C\nu_I \cdot \exp\left\{-\frac{q}{k_BT}\Big[\Psi_{\mathrm{bi}} + \Delta(E_C - E_F)\Big]\right\} \\ + \;\; & qN_C\nu_S \cdot \exp\left\{-\frac{q}{k_BT}\Big[\Delta E_C + \Psi_{\mathrm{bi}} + \Delta(E_C - E_F)\Big]\right\}, \end{aligned} \tag{6.1}$$

whereby the probability of electrons to surpass the respective potential barrier is given by the exponential term.
Furthermore, j_0 can be approximated by the ideal diode equation at open-circuit [288]:

$$j_0 \approx \frac{j_{\mathrm{sc}}}{\exp\left[\frac{qV_{\mathrm{oc}}}{k_BT}\right] - 1} = 2 \times 10^{-13}\,\frac{\mathrm{A}}{\mathrm{cm}^2}\,, \tag{6.2}$$

with the measured V_{oc} and j_{sc} given in Figure 6.10 (a).
Finally, ν_I can be estimated from Equation (6.1) by assuming [136]:

- j_0 is only determined by the hybrid PEDOT:PSS/c-Si front junction.
- ν_S is given by thermionic recombination at the Ag/PEDOT:PSS (metal-semiconductor) interface, whereby all electrons which surpass the potential barrier recombine with $\nu_S \approx A^{**}T/qN_C$ [288][6].

[6] with the reduced effective Richardson constant A^{**}

This leads to an approximated interface recombination velocity of $\nu_I \approx 365$ cm/s.
For comparison, the recombination velocity at the c-Si surface with natively grown oxide is in the order of 1000 cm/s, but strongly depends on the time after H-passivation [186]. Unpassivated c-Si wafers have surface recombination velocities of $\sim 10^6$ cm/s. A high quality passivation with recombination velocities in the range of 10 - 30 cm/s and record values < 1 cm/s are reported for thermally grown stoichiometric SiO_2/c-Si, ALD fabricated Al_2O_3/c-Si, or PECVD processed a-Si/c-Si interfaces [4, 154, 69, 248, 324, 203]. Thus, the estimated ν_I of about 400 cm/s points out the further potential of the PEDOT:PSS/c-Si junction if a better passivation of the hybrid interface is achieved.
The estimated j_0 of $\sim 2 \times 10^{-13}$ A/cm^2 is slightly higher than the dark emitter saturation current density, $j_{0,e}$, extracted from PCD measurements on PEDOT:PSS/SiO_x/c-Si samples featuring a native SiO_x layer which was intentionally grown by storing the wafer for 24 h in air prior to PEDOT:PSS fabrication [249]. The difference may result from the fact that in our calculation of j_0 (Eq. (6.2)) contributions of the whole device are included. But also a different chemical state of interfacial SiO_x with varying passivation quality is a possible explanation.

Solar cell and HAXPES results both indicate the formation of an interfacial, sub-stoichiometric SiO_x layer during water-based solution processing of PEDOT:PSS on initially H-passivated c-Si substrates. Improving the wafer passivation and introducing a more controllable and stable interlayer is beneficial for V_{oc} and the long-term stability of PEDOT:PSS/c-Si solar cells.

Optical losses at the PEDOT:PSS/c-Si front contact

Simulations presented in chapter 5 demonstrate that optical losses are significant in PEDOT:PSS/c-Si solar cells. To quantify these losses optical simulations are compared with device performance. The PEDOT:PSS layer thickness of the device under discussion was determined to $\sim$93 nm[7]. Figure 6.12 depicts the simulated absorption and reflection profile for a 95 nm PEDOT:PSS/c-Si solar cell in comparison to the measured EQE proving that the assumption of uniaxial optical anisotropy of PEDOT:PSS films on flat c-Si surfaces under normal incidence of light is correct.
Through integration over the solar spectrum j_{sc} = 30.3 mA/cm^2 is obtained. This is 1.6 mA/cm^2 below j_{sc} = 31.9 mA/cm^2 extracted from $j(V)$ measurements (cf. Fig. 6.10). Possible causes for this deviation are (i) errors in substracting the front contact grid area or (ii) insufficient AM1.5G solar spectrum imitation used in the measurements. However, optical simulations predict about 6 mA/cm^2 current loss due to parasitic absorption in PEDOT:PSS (orange area in Fig. 6.12) and about 10 mA/cm^2 reflection losses at the hybrid layer stack (yellow area in Fig. 6.12). We have already shown that with a DMSO post-treatment it is possible to reduce PEDOT:PSS layer thickness to $\sim$35 nm while maintaining the same sheet resistance [137]. This will reduce parasitic absorption losses to $\sim$1.5 mA/cm^2 (cf. Fig. 5.4, section 5.2). Reflection can be minimized by adding an additional wide-bandgap layer with suitable refractive index. Possible candidates are e.g. LiF or MoO_x [179, 348, 9]. With demonstrated V_{oc} = 663 mV and FF = 70% efficiencies well above 16% are expected for planar layer stacks. Since the reflective losses mainly originate

[7] measured with AFM at the center of the device

from the PEDOT:PSS/c-Si interface, further improvement can be achieved by using textured wafers. As discussed in section 5.2, also parasitic absorption is expected to decrease as a significant part of incident light would then oscillate in direction of the extraordinary component of the extinction coefficient of PEDOT:PSS, which is smaller than the ordinary component. A further reduction of parasitic absorption of ∼40% for KOH etched c-Si substrates was estimated (cf. section 5.2). However, polymer deposition on structured surfaces has been shown to be difficult [142, 249, 323]. Eventually other deposition methods like drop-casting or spray-coating [63] might be utilized for a better polymer coating on textured substrates. Possibly, also other polymer formulations featuring different viscosities could enable a successful deposition of thin film PEDOT:PSS on structured c-Si wafers.

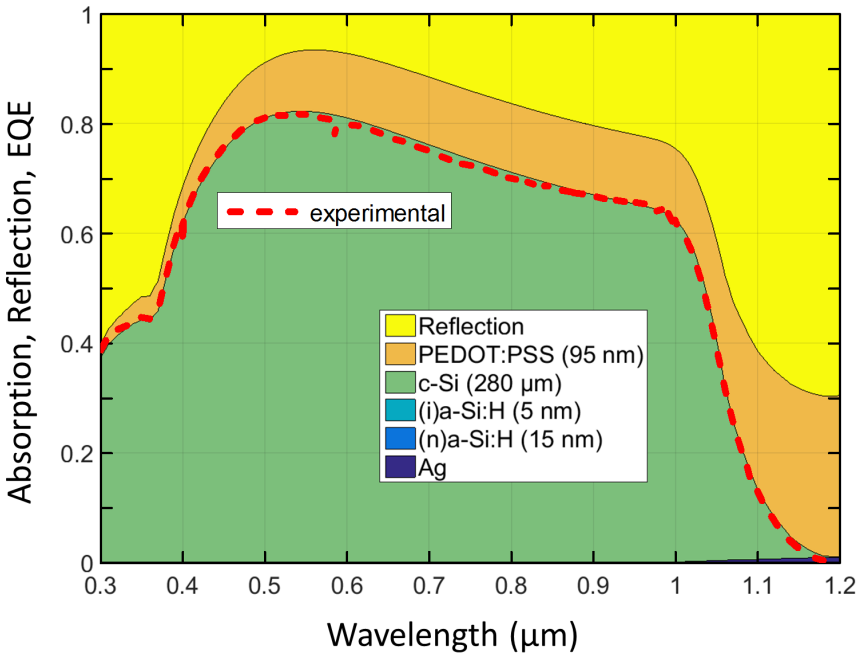

Figure 6.12: Optical simulated absorption and reflection profiles for a hybrid solar cell with 95 nm PEDOT:PSS. The experimental EQE of the device under discussion is shown as red dashed line. Data published in Ref. [136].

6.4 Summary

The promising PEDOT:PSS/c-Si hybrid solar cell approach was investigated in great detail. By combining capacitance-voltage measurements, near-UV photoelectron spectroscopy (PES) and literature values a complete band diagram of the PEDOT:PSS/(n)c-Si heterojunction was constructed showing that c-Si is strongly inverted at the hybrid interface. This is in-line with the finding that the PEDOT:PSS/(n)c-Si junction can be described as an abrupt p^+n-heterojunction [138] giving rise to high solar cell's V_{oc}.

Besides the proper band alignment of a heterojunction, the chemical structure of its interface is important. A tender/hard X-ray PES (HAXPES) study was conducted to probe the buried hybrid PEDOT:PSS/c-Si interface. The results show that after standard fabrication of PEDOT:PSS on H-passivated c-Si, a thin sub-stoichiometric SiO_x layer is always present at the interface. Moreover, we also find that this SiO_x layer is even not stable when stored in inert gas atmosphere. It is observed that the thickness and oxidation state of the SiO_x layer increases with time which may negatively affect the electronic quality of the hybrid interface.
PEDOT:PSS/(n)c-Si hybrid front junction solar cells utilizing high-quality c-Si wafers and a superior, well passivated electron selective back contact adopted from the SHJ technology, result in best solar cell efficiencies of 14.8% and a record V_{oc} of 663 mV. The cell's performance is limited by the hybrid PEDOT:PSS/c-Si junction. Assuming that the dark saturation current density, j_0, is only determined by the hybrid junction and that the surface recombination velocity is given by thermionic recombination, an interface recombination velocity, ν_I, of $\sim$400 cm/s was estimated. For comparison, ν_I in conventional inorganic SHJs is usually in the range between 10 - 30 cm/s [154]. This is the result of the poor interface, as observed in the HAXPES study.
This points out that the PEDOT:PSS/c-Si junction is limited by interface recombination and V_{oc} of hybrid SHJ solar cells could be further improved by providing a better passivating and stable interlayer.
Additionally, a significant device improvement is possible with a better light management. For the best solar cell, the comparison between measured device EQE and optical simulations predicts a short-circuit current density loss of $\sim$6 mA/cm^2 due to parasitic absorption in PEDOT:PSS and $\sim$10 mA/cm^2 due to reflection at the planar hybrid layer stack. Minimizing parasitic absorption by reducing PEDOT:PSS layer thicknesses will on the other hand enhance reflection. This can be compensated by implementing wide bandgap layers with suitable refractive indices. Device efficiencies above 16% are predicted. A further increase in photocurrent can be achieved by using structured surfaces which reduce reflection losses. Because a significant fraction of incident light will oscillate within the less absorptive extraordinary component of birefringent PEDOT:PSS, an additional reduction of parasitic absorption is expected for textured devices.
For a better surface passivation and hence improved V_{oc}, and to ensure a long-term stability of the PEDOT:PSS/c-Si hybrid interface, we suggest implementing a well-defined, stoichiometric and stable SiO_2 tunnel oxide with excellent surface passivation quality [279, 199, 97]. A so-called "TOPCon" device with such a layer currently yields a record efficiency of 25.3% for conventionally contacted c-Si solar cells [123, 109].

All above discussed device improvements lead to the proposed solar cell structure depicted in Figure 6.13. It consists of the "TOPCon" electron rear contact featuring a very low $j_{0,rear}$ = 7 fA/cm^2 [109]. On the front side the proposed hybrid device takes advantage of the high-quality SiO_2 tunnel oxide as utilized in the back contact. MoO_x or LiF are possible candidates for an anti-reflex coating.

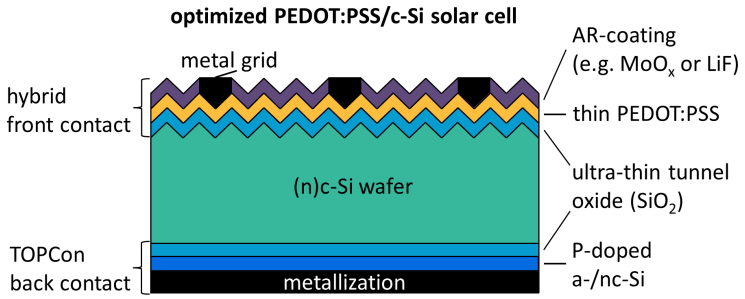

Figure 6.13: Proposed PEDOT:PSS/SiO_2/c-Si/TOPCon hybrid solar cell. The hybrid interface is passivated by a well-defined and stable SiO_2 tunnel oxide. For best device efficiencies PEDOT:PSS as thin as possible and an optimized AR-coating should be implemented [97, 109].

7

Multi-exciton generating hybrid PEDOT:PSS/Tc/c-Si device concept

Making use of multi-exciton generation (MEG) via singlet fission (SF) is one possibility to overcome the fundamental single junction photovoltaic limit. One of the central objectives of this thesis is to exploit MEG for the already mature Si based photovoltaic technology by implementing an appropriate SF material on the front side of conventional c-Si based solar cells. Tetracene (Tc) with its triplet energy of E_T^{Tc} = 1.25 eV [310] is a promising candidate as E_T^{Tc} is a little larger than the band-gap energy E_g^{Si} = 1.12 eV [288] for c-Si at room temperature.
The highly conductive polymer PEDOT:PSS is commonly used as the hole selective contact in singlet fission OPV devices [134, 328, 64, 305, 172, 171]. Furthermore, as demonstrated in the previous chapter, PEDOT:PSS is also a promising organic candidate forming a hole-selective hybrid contact with n-type c-Si which can be described as an abprupt p^+n-heterojunction [138]. Within the proposed hybrid PEDOT:PSS/Tc/c-Si device architecture (cf. section 2.4) we make use of both properties by implementing thin film Tc in between the hole selective PEDOT:PSS and the n-type c-Si main absorber.

The present chapter is organized as follows:
Morphology of thin film Tc, SF dynamics and the energy level alignment on device relevant Tc/c-Si layer stacks were investigated in great detail, as it is important for the interpretation of solar cell results.
As the central result of this study, PEDOT:PSS/Tc/c-Si solar cells with efficiencies $\gtrsim 10\%$ are reported. Devices were analyzed by means of $j(V)$ characteristics and EQE measurements. For a thorough interpretation the measured EQE spectra were fitted with the singlet fission EQE optical model introduced in chapter 5. To further assess whether the dissociation of triplet excitons and charge transfer across the hybrid interface to c-Si is a feasible scheme, EQE spectra were recorded under various measurement conditions, such as temperature and externally applied voltages. So far, no clear evidence for triplet exciton harvesting at the Tc/c-Si interface is found. Reasons which hamper an efficient charge separation at the hybrid interface are discussed.
Finally two interlayers approaches, (i)a-Si:H passivation and intermediate C_{60} layers were tested.

7.1 Morphology and growth mode of thin film Tc

For a profound interpretation of SF dynamics in polycrystalline thin film Tc (cf. section 7.2) and PEDOT:PSS/Tc/c-Si solar cell performance (cf. sections 7.4.1 & 7.4.2), insight into Tc film morphology and growth mode is essential.

7.1.1 Polymorphism in Tc thin films

The morphology of thin film Tc strongly depends on thermal evaporation deposition conditions [15, 265]. It has been reported that polycrystalline Tc can be classified in two polymorphs, namely Tc I and Tc II [15]. Furthermore, it is shown that Tc film morphologies influence SF dynamics [15, 227].

Polarization dependent absorption measurements were performed at various measurement geometries using a spectrophotometer. As sketched in Figure 7.1 (right), the incident light with wave vector $\vec{k}$ forms an angle with respect to the sample's surface normal $\vec{n}$. Sample rotation (here 10° and 65°) was achieved by a rotatable sample holder placed inside the integrating sphere. Thus, transmission T and reflection R is measured simultaneously and the absorption, A = 100% - (T + R), is plotted. Measurements at 10°, close to normal incidence (0° tilt), were performed. At normal incidence the specularly reflected beam exits the integrating sphere through the hole for the incident beam.
Figure 7.1 shows polarization dependent absorption spectra of a nominally 10 nm Tc film deposited on a glass substrate. The absorption spectra reveal the characteristic vibrational progression of polycrystalline Tc [15, 299]. The $S_0 \rightarrow S_1$ transition occurs between λ = 400 - 550 nm, whereby the two lowest energy transitions at ∼524 and ∼505 nm are assigned to Davydov splitting as a result of H- and J- type molecule aggregation [299, 212, 70]. For 10° tilt no significant difference for both polarizations is observed. In contrast, a pronounced change of Davydov split peak shares (cf. next paragraph) appears for 65° tilt.

Discussion of polymorphism and Davydov splitting

During growth of organic thin films, molecules tend to aggregate due to attractive intermolecular interactions like van der Waals forces. The optical absorption properties of molecular aggregates can be qualitatively modeled using the exciton coupling model that treats molecules as dipole oscillators which interact depending on the position and orientation of neighboring molecules [150, 149]. Using this model, absorption features can be related to structural motifs of the molecular aggregates. Figure 7.2 depicts the fundamental aggregate types. When two dipoles (indicated by the green double arrows) are aligned side-by-side (H-aggregate), parallel dipoles repel each other leading to a higher energy state S_1^+, whereas anti-parallel dipoles attract each other which lowers the energy of that state (S_1^-). An optical transition is only allowed if the transition dipole moment m is greater than zero. As also indicated in Figure 7.2, parallel alignment of dipoles results in $m > 0$, whereas anti-parallel dipoles cancel each other resulting

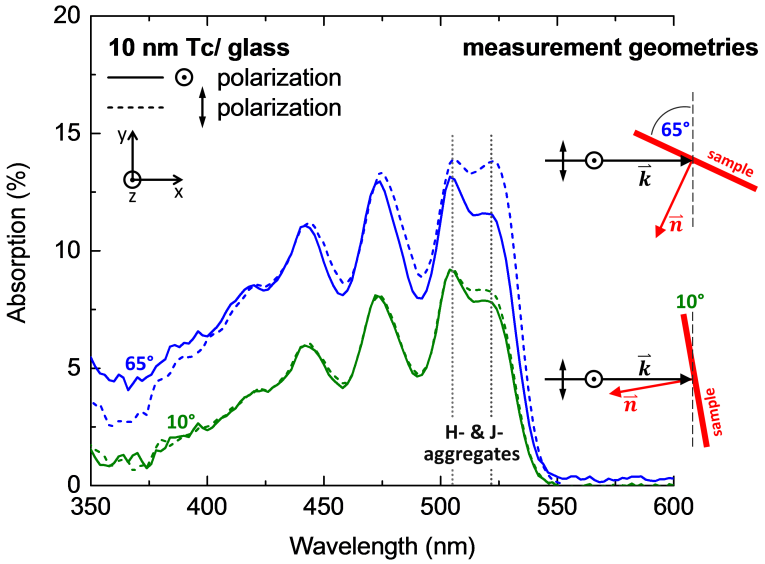

Figure 7.1: Absorption spectra of nominally 10 nm Tc deposited on glass. The measurement geometries for polarizations of incoming light with respect to the surface normal $\vec{n}$ are sketched for tilt angles of 10° (green line) and 65° (blue line). Vertical dotted lines indicate Davydov splitting as a result of H- and J- type aggregates. The polarization is given in the inset.

in $m = 0$. Thus, the fundamental absorption in H-aggregates is blue-shifted (higher energy $S_0 \rightarrow S_1^+$ transition allowed) with respect to the monomer. Similarly, if the two dipoles are oriented head-to-tail (J-aggregates) a red-shift (lower energy $S_0 \rightarrow S_1^-$ transition allowed) in the absorption is observed. In any intermediate case, the formation of oblique dimers, projections of various orientations yield a H-J-band splitting which is called Davydov splitting [70]. The oscillator strength is shared between the two transitions and their relative contributions depend on the orientation of the crystallites [149, 150, 196, 233, 342].
Accordingly, we can interpret the observed Davydov splitting in the absorption spectra of thin film Tc (Fig. 7.1) as being due to the fact that the polycrystalline Tc films consist of both, H- and J- type aggregate shares. Furthermore, by controlling the polarization of incident light with respect to the sample orientation and therefore the alignment of transition dipole moments, the preferential aggregate excitation can be tuned. The results reveal a pronounced change of Davydov split peak ratios for different polarizations in the off-axis (65° tilt) alignment, whereas for near-parallel (10° tilt) alignment of $\vec{k}$ and $\vec{n}$ no significant changes are detected. This behavior shows an isotropic aggregate distribution in the substrate plane. In this case various polarizations at normal incidence are not distinguishable. In contrast, the pronounced change of Davydov splitting for off-axis incidence (65° tilt) is a clear evidence for anisotropy of H- and J- type Tc aggregation along the surface normal $\vec{n}$.

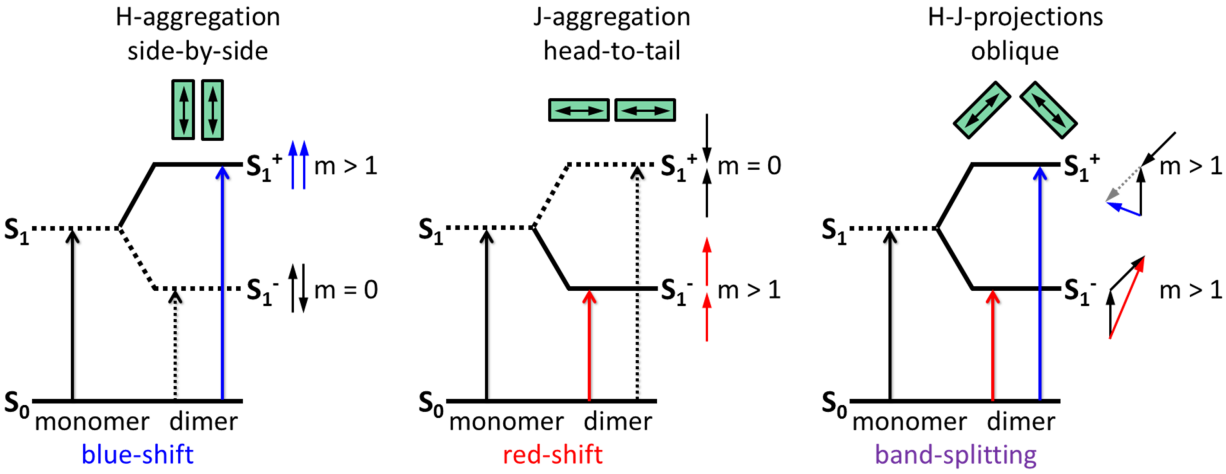

Figure 7.2: Energy level diagrams of molecular dimers in side-by-side (H-aggregation), head-to-tail (J-aggregation) and oblique (H-J-projections) geometrical arrangements (indicated by double arrows), and the allowed (solid arrows) or forbidden (dotted arrows) transitions. Small arrows denote the transition dipoles [149].

In addition, Tc absorption spectra for a thickness series of films deposited on glass ranging from nominally 10 nm up to 200 nm were recorded. For these measurements samples were placed in front of the integrating sphere, as it is commonly done to record transmission data. Thus, reflection is discarded and the approximated absorption A = 100% - T is plotted in Figure 7.3. All films exhibit the characteristic Davydov splitting with changing peak ratios depending on film thickness. As observed previously, intensity ratios of Davydov split peaks are evidence for various Tc polymorphs [128, 15]. In a recent study of D. H. Arias et al. [15], Tc polymorphs are classified into Tc I and Tc II types with H-type aggregation being more pronounced in Tc I and J-type aggregation being stronger in Tc II polymorphs. As shown in Ref. [15], Tc I : Tc II polymorph ratios strongly depend on growth conditions, i.e. deposition rate and substrate temperature, as well as on film thickness. Since all Tc films in this thesis are grown using the same deposition parameters with only varying the deposition time, the here presented absorption data show only the effect of changing film thickness. Thus, the change in Davydov split peaks of Figure 7.3 is assigned to varying Tc I : Tc II shares, whereas thicker films favor the enrichment of Tc I character (H-type split peak).

XRD analysis of thin film Tc

Figure 7.4 shows the X-ray diffractograms of nominally 100 nm and 300 nm Tc films grown on c-Si(111). XRD allows for a simple identification of crystal structures. The peaks at 7.3° and 6.9° can be assigned to diffraction from the (001) planes of Tc I and Tc II polymorphs, respectively [15]. XRD data clearly show contributions from both polymorphs. By fitting XRD peaks with Voigt profiles (for reasons of clarity fits are not shown in Fig. 7.4) peak area ratios were obtained. The 100 nm Tc film reveals a Tc I : Tc II polymorph ratio of ∼4:3, whereas the 300 nm Tc film

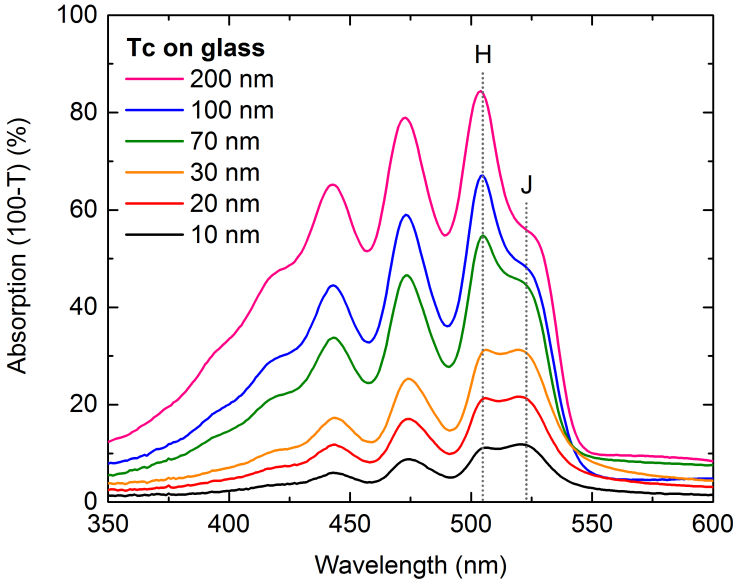

Figure 7.3: Absorption spectra of a thickness series ranging from nominally 10 nm to 200 nm of thin film Tc deposited on glass. Davydov splitting of H- and J- type aggregation is indicated.

is predominantly Tc I type with a strongly enhanced ratio of ∼16:1. Thus, the trend of higher Tc I shares for thicker films, which was already observed in the Tc absorption study (cf. Fig. 7.3), is confirmed. This is in line with the reported dependence of an increasing Tc I : Tc II ratio for thicker films in Ref. [15].

7.1.2 Thin film Tc growth on c-Si(111)

Detailed knowledge about Tc layer formation on H-passivated c-Si(111) surfaces will be essential for hybrid solar cell performance and interpretation of results. An important question is, if Tc films completely cover the c-Si substrate, or if point contacts between hole selective PEDOT:PSS and c-Si are possible. Therefore, as presented and discussed in the following, AFM topography images of Tc/c-Si layer stacks and corresponding SEM cross section images of hybrid stacks capped with PEDOT:PSS were taken. To manifest an upper limit of a possible point contact ratio, XPS measurements were additionally conducted.

Figure 7.5 (a) shows AFM topography images of nominally 10 nm (left) and 100 nm (right) Tc deposited on H-passivated c-Si(111). For nominally 10 nm coverage we observe 3d island formation with Tc crystallites of widths parallel to the surface in the range of ∼1 μm and heights of up to 60 nm. Approximately 60% of the surface area is not covered by such 3d crystallites. Additionally, for three crystallites the height profiles corresponding to the numbers in the AFM image are given. An analysis of the height profiles reveal Tc island edge angles of ∼60°. The nominally 100 nm Tc film also exhibits a 3d crystal grain structure with a RMS of ∼16 nm. Analysis of the height profiles yield the same ∼60° edge angle. As indicated by the red arrows

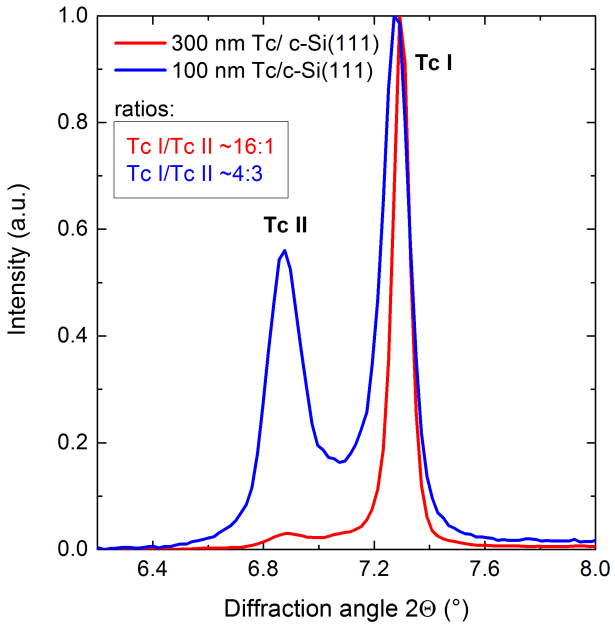

Figure 7.4: X-ray diffractograms for nominally 100 nm and 300 nm Tc films deposited on c-Si(111). Tc I and Tc II phases [15] are observed. The given intensity ratios are obtained by fitting two Voigt peaks in each data set (fits not shown here).

on the height profile color bar, after leveling of the image an ∼4.5% share of deep valleys have thicknesses below 40 nm, but only ∼0.1% less than 20 nm.
In addition, XPS measurements were conducted to determine the amount of photoelectrons stemming from the c-Si substrate that make it through the Tc film to the detector. As expected from the AFM image, a pronounced Si core level signal (Si 2p) is detected for the "thin" 10 nm Tc film (Fig. 7.5 (b,left)). Note that –in view of the inelastic mean free path of photoelectrons at the corresponding kinetic energy (> 1 keV) of 1 - 2 nm– this does not exclude a closed Tc wetting layer. For the "thick" 100 nm layer no Si related signal could be detected (background noise shown in Fig. 7.5 (b,right)).
Finally, Figure 7.5 (c) shows SEM cross section images of identical prepared Tc films with PEDOT:PSS capping layer used as the front contact in the hybrid device. The image on the left side depicts one Tc island of the nominally 10 nm film. It is clearly observed that spin-coated PEDOT:PSS covers the island. At its edges the polymer layer is aligned along the ∼60° Tc island edge and is in contact to the substrate. In contrast, the SEM cross section image for the nominally 100 nm Tc film show that the PEDOT:PSS layer is clearly spatially separated from the c-Si substrate by the Tc layer. During SEM imaging the entire cross section was scanned and no direct contact between PEDOT:PSS and c-Si wafer was found on a distance of about 2 mm. However, the SEM cross section study was conducted at randomly cracked samples. Thus it is likely that no deep valley of the Tc film emerged at the cross section under investigation even if there was a small fraction of contact area.

Discussion of Tc growth mode and point contacts

As sketched in Figure 7.6, there are three main types of film growth: (i) Volmer-Weber [320] (ii) Stranski-Krastanov [280], and (iii) Frank-Van Der Merwe [100]. In thermodynamic equilibrium,

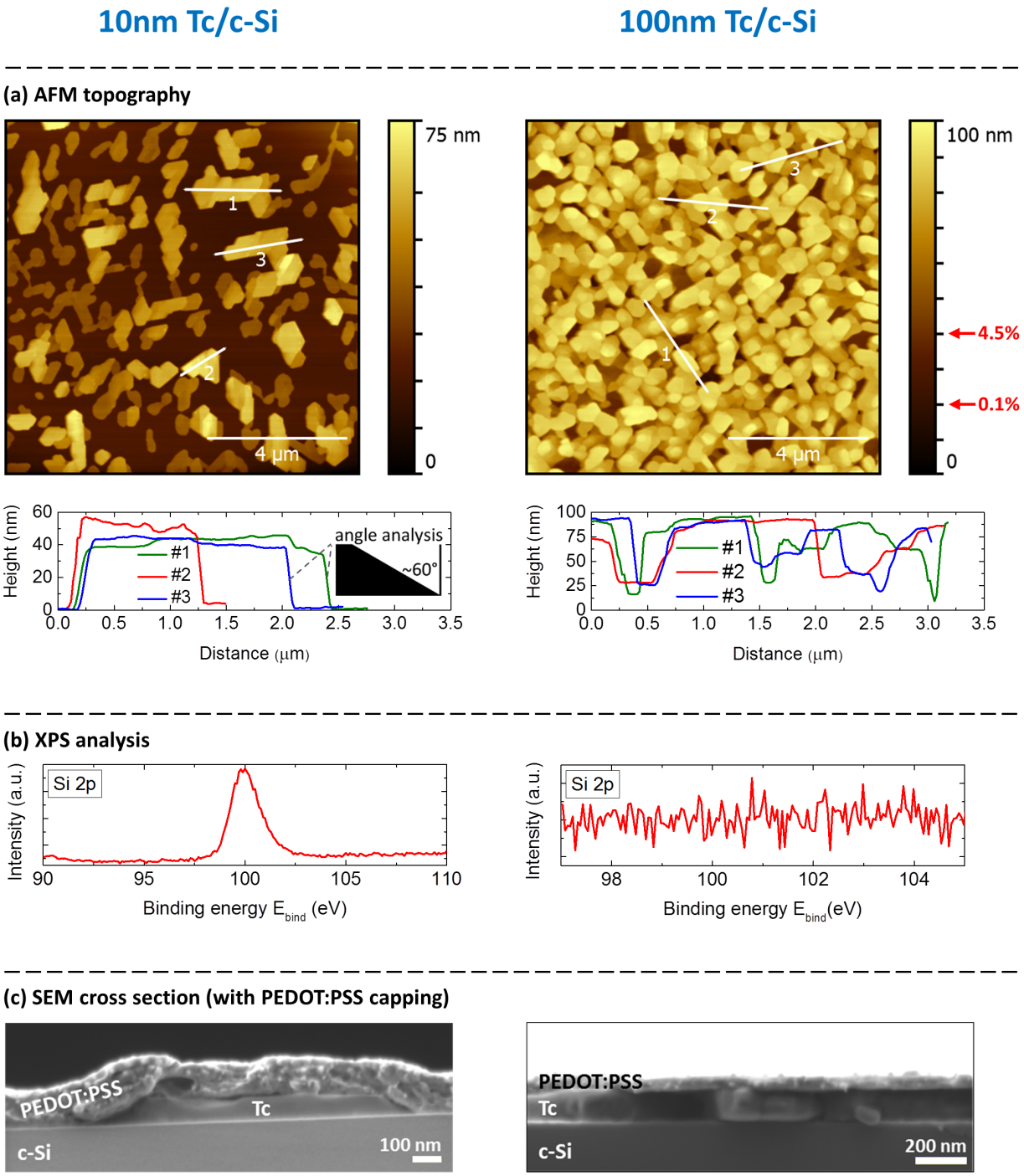

Figure 7.5: (a) AFM topography of nominally 10 nm Tc (left) and 100 nm Tc (right) deposited on H-passivated c-Si(111). Color bars indicate the height. Exemplary height profiles of Tc crystallites (left) and deep valleys (right) extracted from the AFM images at positions indicated in the images. (b) XPS spectra taken at E_{bind} of the Si 2p core level peak for identical prepared films. (c) SEM cross sections of the corresponding PEDOT:PSS/Tc/c-Si layer stacks.

growth modes can be explained macroscopically by a simple thermodynamic picture in terms of surface energies [25, 236]. The Volmer-Weber model considers an initial nucleation at a certain spot followed by a 3d island growth. This bulk island growth originates from the fact that the surface energy of the substrate, γ_s, is smaller than the sum of the surface energy of the molecular adsorbate, γ_m, and the interfacial energy, γ_i. In contrast, in the Frank-Van Der Merwe mode, 2d molecular layer-by-layer growth is favored for γ_s larger than the sum of γ_m and γ_i. However, there exists an intermediate regime, the Stranski-Krastanov mode, in which an initial layer formation is followed by 3d island growth. Note that γ_m and γ_i strongly depend on system specific molecule-surface interactions [236].

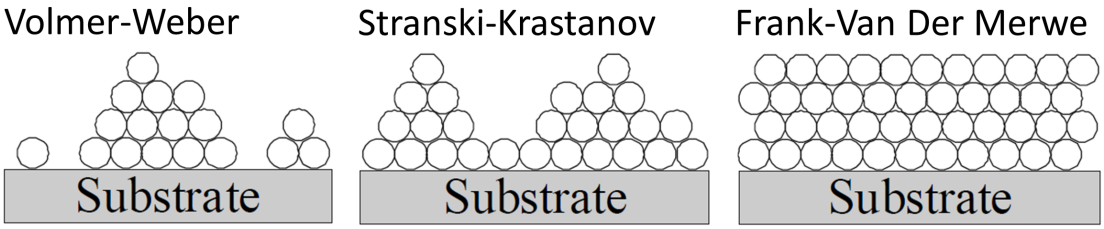

Figure 7.6: Cross-section views of the three modes of thin-film growth: (i) Volmer-Weber (island formation), (ii) Stranski-Krastanov (layer-plus-island), and (iii) Frank-Van Der Merwe (layer-by-layer). Figure taken from Ref. [16].

In literature both island formation growth modes, Volmer-Weber-like for thin film Tc deposited on SiO_2 surfaces [204, 330], as well as Stranski-Krastanov-like growth for Tc deposited on Ag(111) [169] have been reported. Furthermore, it has been shown that Tc thin film growth mode on H-passivated c-Si(100) substrates at room temperature strongly depends on the deposition rate [265, 303]. J. Shi et al. [265] report layer-by-layer growth within a narrow range of deposition rate of $\sim$1 nm/min. However, a sufficiently high deposition rate of $\sim$8 nm/min results in a high-aspect-ratio 3d grain morphology which indicates that rapid deposition causes multilayer-island growth before effective island coalescence takes place. In this regime they observe bare substrate regions coexisting with 3d grains pointing to a weak interaction between Tc admolecules and H-passivated c-Si(100) substrate [265, 312]. Furthermore, it is predicted by first-principles calculations that isolated Si dangling bonds of a H-passivated c-Si surface act as efficient initial nucleation centers [312]. In summary, the exact growth mode of thin film Tc strongly depends on specific substrate surface condition, substrate temperature and evaporation rate.

For the Tc films deposited on H-passivated c-Si(111) substrates, a layer-by-layer growth mode can be excluded from the AFM and SEM studies presented in Figure 7.5. A 3d island formation is unambiguously observed.

However, for the "thin" 10 nm Tc/c-Si sample the formation of an ultra-thin Tc monolayer prior to 3d island growth (Stranski-Krastanov mode) cannot be excluded from the here presented AFM and SEM imaging study. Although lab based XPS is rather surface sensitive, the detected Si 2p signal for the 10 nm Tc/c-Si sample could also emerge from buried Si with only a monolayer of Tc coverage which would allow to detect photoelectrons stemming from the c-Si substrate.

For the "thick" 100 nm Tc/c-Si sample one important question is whether the film is completely closed, or if some deep holes reach the c-Si surface. AFM analysis gives no indication for the existence of such holes but is limited due to cantilever length and diameter. To manifest an upper limit and to exclude AFM tip artifacts at deep pinholes, an XPS analysis was performed. With XPS no Si related signal could be detected. AFM height profile analysis reveal crystallite edge angles of deep holes of $\sim$60°. This is well above the photoelectron acceptance angle of 12° of the here used PES setup. Thus, no attenuation of photoelectron signal by Tc grain edges is expected. Assuming the typical sensitivity of XPS of 0.1% [275], from the here presented data an upper limit of 0.1% share of deep pinholes possibly reaching the c-Si substrate is given.
For a further investigation of thin film Tc growth mode within our specific deposition parameters and c-Si surface conditioning, a TEM study is currently under way.

In summary, polymorphism (denoted as Tc I and Tc II phases) is observed for all Tc films. The change in Davydov splitting addressed by absorption measurements can be assigned to varying Tc I : Tc II ratios with thicker films favoring growth in Tc I mode. This assumption is confirmed by XRD studies. AFM topography and SEM cross sections clearly show island formation of our Tc thin films. The actual growth mode, either the formation of an ultra-thin Tc layer prior to 3d island growth or nucleation with uncovered c-Si wafer regions remains an open question. From the here presented data for the 100 nm Tc film a maximum share of 0.1% of deep pinholes possibly reaching the c-Si substrate is extracted.

7.2 Dynamics of thin film Tc

The formation of long-lived triplet excited states in Tc via singlet fission is a key piece in our MEG hybrid device concept. As described in section 2.3.1, measuring time-resolved PL signal is an indirect but well established way to access long-lived triplet states [229, 227, 47, 45, 15]. To that end, time-correlated single photon counting (TCSPC) measurements on identical layer stacks as used for solar cell fabrication were conducted.
For the measurements an excitation wavelength of 500 nm of a pulsed laser source with a repetition rate of 500 kHz and an excitation density of about 1×10^{17} cm^{-3} was used. The PL signal was detected for wavelengths $\geq$ 540 nm using a long pass filter.
Figures 7.7 (a) and (b) show the measured PL transients of nominally 10 nm and 100 nm Tc films deposited on quartz glass and HF-dipped c-Si(111) substrates, respectively. Each thickness set was grown in the same evaporation run. The instrument response function (IRF) is plotted in grey. Its kinks are artifacts due to imperfect pulse picking. Obviously the recorded PL transients feature the same artifacts.
Upon photo-excitation, Tc has a population in the first excited state S_1. These singlets may decay via several processes: SF, fluorescence, or singlet-singlet annihilation (SSA). For Tc it has been shown that singlet fission, which is a first order process, is the predominant relaxation process. However, also second order SSA may occur [47, 46, 299]. Hence, the initial rapid decrease of PL intensity over several orders of magnitude is assigned to the fast depopulation of the emissive singlet state via SF. The delayed PL signal stems from the repopulation of the singlet state via

triplet-triplet fusion. Thus, the detection of a delayed signal component is the unambiguous proof that long-lived triplets are generated in the Tc layers under investigation [229, 227, 47, 45, 15]. Therefore, the basic requirement for MEG devices, the creation of long-lived triplet states via SF is proven.

Evaluation of PL transients

The ultimate goal for the analysis of measured PL transients is to understand the process producing luminescence by fitting a photo-physical SF kinetic model with realistic parameters. In a first modeling attempt rate equations as introduced in section 2.3.1 (Eqs. (2.7) - (2.9)) with additionally included second order singlet-singlet and triplet-triplet annihilation loss pathways, as well as non-radiative loss channels of the correlated triplet pair, $(T_1T_1)^l$, and free triplet, T_1, states were implemented. Unfortunately, within this model the fits never converged over the full dynamic range of experimental TCSPC data. Possible explanations therefore are: (i) samples are standardly translated during TCSPC measurements to minimize the exposure time at one spot which slows down beam induced degradation. Since thin film Tc is not uniform, as shown in the morphology study, this may effect measured transient PL spectra. (ii) Different phases of polycrystalline Tc thin films were observed. According to a recent study of D. H. Arias et al. [15], these different phases exhibit slightly different SF dynamics, which we cannot account for in the kinetic modeling.
Therefore, following Ref. [15], PL transients were fitted with an empirical multi-exponential decay model. In order to fit experimental data accurately it turned out that a series of four exponentials, which have to be convolved with the IRF is needed:

$$\text{Fit} = \text{IRF} \otimes \sum_{i=1}^{4} A_i \cdot e^{-\frac{t}{\tau_i}} \tag{7.1}$$

By visual inspection of Figure 7.7 (a,b), no significant quenching of the delayed PL signal is observed within each thickness data set. To prove that, a global fitting routine using Equation (7.1) with constant lifetimes τ_i was applied to each thickness set of data. As expected, within one thickness set, experimental data could be accurately modeled using equal lifetimes and only slightly varying amplitudes. Since the measured IRF is convolved with the empirical model, the fits feature the same artifacts and noise as the experimental data.
The corresponding fit parameters are summarized in Table 7.1. Because we are especially interested in the delayed first order decay, reflecting triplet lifetimes, the fitting routine was optimized in the range above 10 ns. The initial fast decay channel, which may also include second order processes, could not be modeled within the same accuracy in our four-exponential decay model.

Thus, by comparing the delayed PL transients of Tc layers with the same nominal thicknesses deposited on quartz, as well as on c-Si (cf. Fig. 7.7 (a,b) and Tab. 7.1), we do not observe a significant lifetime shortening of the long-lived component. If the triplet state would be efficiently depopulated via triplet exciton dissociation at the Tc/c-Si interface, a significant shortening of triplet lifetime with a delayed PL component decreasing to zero is expected. In other words,

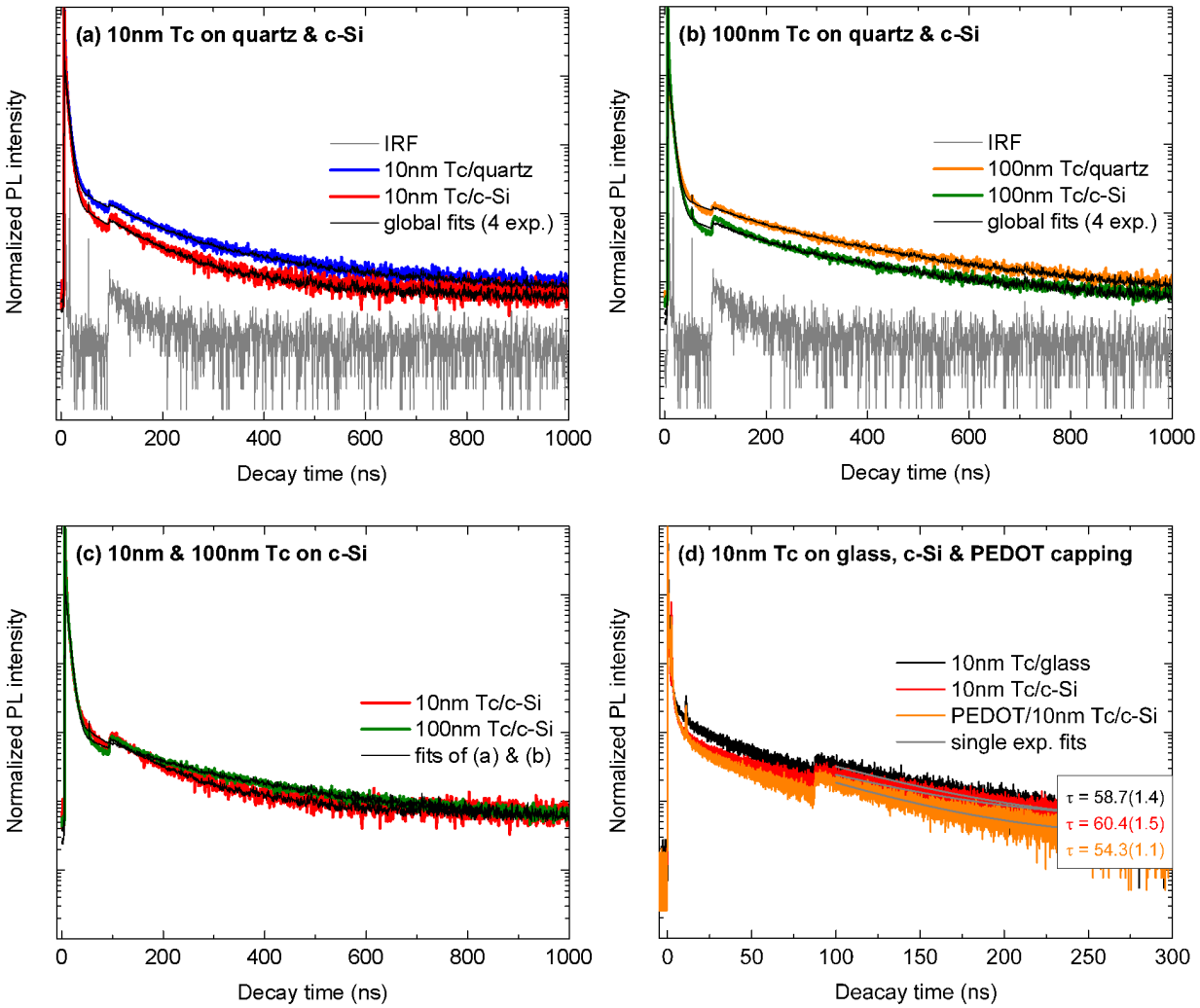

Figure 7.7: Normalized (Log10) transient PL spectra recorded by time-correlated single photon counting (TCSPC) measurements using a 500 kHz pulsed laser with an excitation wavelength of 500 nm and an excitation density of about 1×10^{17} cm^{-3}. The PL signal is detected for wavelengths $\geq$ 540 nm. In (a) PL transients of nominally 10 nm Tc, and (b) 100 nm Tc deposited on quartz and c-Si are shown (colored data). Using a four-exponential decay model (cf. Eq. (7.1)), global fitting was conducted by fixing lifetimes for each thickness set. The fits (black line) are convolved with the instrument response function (IRF, grey data). (c) Comparison of 10 nm and 100 nm Tc layers on c-Si. (d) Comparison of 10 nm Tc deposited on (i) glass and (ii) c-Si. (iii) Capped with PEDOT:PSS as it constitutes the device relevant hybrid layer stack.

Table 7.1: Fitted rate parameters using Equation (7.1) for nominally 10 nm and 100 nm Tc films deposited on quartz glass and c-Si(111) substrates, respectively. The amplitudes for the exponentials A_i are listed as $A_i/\sum_{j=1}^{4} A_j$. Global fitting with fixed lifetimes τ_i was conducted for each film thickness.

	10 nm Tc/quartz	10 nm Tc/c-Si	100 nm Tc/quartz	100 nm Tc/c-Si
A_1	0.986	0.990	0.995	0.994
τ_1 (ns)[a]	0.106	0.106	0.091	0.091
A_2	1.35E-2	1.02E-2	5.34E-3	5.61E-3
τ_2 (ns)[a]	5.53	5.53	6.08	6.08
A_3	1.51E-4	9.71E-5	4.40E-4	2.54E-5
τ_3 (ns)	**88.2**	**88.2**	**116**	**116**
A_4	3.99E-5	1.14E-5	3.08E-5	1.56E-5
τ_4 (ns)	**254**	**254**	**316**	**316**

[a]Since the focus was to fit the long-lived tail accurately (τ_3, τ_4, bold & dark grey shaded values), the short-lived components (τ_1, τ_2) are more inaccurately and should be treated with caution.

within this dynamic study no evidence for triplet exciton harvesting at the hybrid Tc/c-Si interface is found.

Figure 7.7 (c) displays the comparison of PL transients of "thin" (10 nm) and "thick" (100 nm) Tc layers deposited on the same substrate, here c-Si(111). In contrast to data of Figures 7.7 (a) and (b), long-lived tails are no more parallel, caused by slightly varying lifetimes. Fitted delayed lifetimes τ_3 and τ_4 moderately deviate within $\sim$20% (cf. Tab. 7.1). This can be attributed to morphology differences for various Tc layer thicknesses [15, 227] which was observed for Tc thin films under investigation (cf. section 7.1).

Finally, in Figure 7.7 (d) PL transients of 10 nm Tc, also deposited in the same evaporation run on (i) microscope slide glass, and (ii) H-passivated c-Si(111) are shown. (iii) Additionally, the Tc/c-Si stack was capped with PEDOT:PSS using the same fabrication steps, i.e. identical spin-coating parameters and annealing temperature/time, as for hybrid solar cell production. Although this experiment was carried out at the same experimental setup but roughly one year later as the measurements discussed so far (Fig. 7.7 (a)-(c)), optical adjustment and excitation density was slightly different resulting in a lower signal-to-noise ratio. Also in Figure 7.7 (d), no significant lifetime shortening of the delayed component is observed by eye. As a consistency check, this set of data was evaluated by assuming only first order decay in the delayed component above 100 ns. This justifies single exponential fits. We do not obtain pronounced differences, all samples exhibit comparable life times of τ = (57.4 $\pm$ 3.1) ns of the delayed component, corresponding to a maximum deviation less than 10%. Due to only marginal differences between samples with and

without capping layer of spin-coated PEDOT:PSS, it can be concluded that within the proposed device architecture and utilized fabrication steps, triplet excitons are not significantly parasitically quenched at the PEDOT:PSS/Tc interface.
This is an important result, since D. N. Congreve et al. [64] reported on the necessity of an interlayer placed in between the PEDOT:PSS hole conductive layer and the triplet exciton generating SF material. In their OPV devices P3HT is used. Their device architecture was already introduced in section 2.4 (cf. Fig 2.8 (a)). They assigned the functionality of this layer to prevent triplet diffusion to the anode and suppress parasitic recombination. Thus, this layer is called "exciton blocking layer." In a study by N. J. Thompson et al. [305, 304] it was shown by XRD measurements that the morphology of evaporated thin films is drastically influenced by the substrate with greatly increased percentage of crystallinity for films deposited on P3HT. Therefore, the boost in device performance was related to both, the improvement of crystallinity and triplet blocking. In contrast, in this thesis hybrid solar cells are fabricated by an inverse sequence compared to standard OPV device fabrication where layer stacks are deposited on ITO coated glass substrates (cf. Fig. 2.8 (a)). We evaporate Tc directly on c-Si, subsequently followed by spin-coating of PEDOT:PSS. Thus, different morphologies of thin film Tc is not an issue in the here presented hybrid cell concept. The results presented in Figure 7.7 (d) suggest that a significant parasitic loss of triplet excitons at the PEDOT:PSS/Tc interface is not present which supports the explanation of an increased OPV device performance due to a favorable Tc thin film morphology if evaporated on P3HT interlayer.

In summary, we clearly observe long-lived triplet states, although no significant quenching of triplets due to exciton dissociation and charge separation at the hybrid Tc/c-Si interface is detected. This is in accordance to a recently published dynamic study of G. B. Piland et al. [229]. Furthermore, it is shown that triplets are not significantly lost at the interface between the hole conductive PEDOT:PSS capping layer and Tc when cells are fabricated within the hybrid device concept as proposed in this thesis.
As it will be presented in section 7.4, the development of fully operating hybrid solar cells opens up the opportunity for additional experiments on device level to further assess whether the dissociation of triplet excitons and a charge transfer at the hybrid Tc/c-Si interface is a feasible scheme.

7.3 Energy level alignment at the Tc/c-Si interface

To assess the energy level alignment between H-passivated c-Si(111) and thin film Tc, as it is important for hole extraction from the c-Si absorber and charge separation at the Tc/c-Si interface, UPS experiments were performed.

In-system preparation

At the end station SurICat (BESSY II) an *in-system* sample preparation is provided. H-passivated c-Si(111) substrates were put into the load lock and evacuated as fast as possible ($\sim$10 min after

HF-dip). Three samples were investigated throughout the UPS study: (i) H-passivated c-Si reference, (ii) nominally 10 nm and (iii) 30 nm evaporated thin film Tc/c-Si samples. Subsequently after Tc film deposition samples were transferred into the analysis chamber without breaking vacuum. The results of UPS measurements using an excitation energy of 35 eV are depicted in Figure 7.8.
In panel (a) the secondary electron cut-off spectra, SECO, for determining the sample work function, Φ_w, are plotted. To clear the analyzer work function the samples were biased at -10 V. As depicted in the figure, all three samples exhibit a constant Φ_w = (4.3 $\pm$ 0.05) eV. It is determined by the intercept of linear fits between the steep rising signal edge and the background noise. For clarity, fits are not shown in the figure.
In panel (b) the HOMO(Tc)/VB(c-Si) region close to E_F, taken at 45° take-off angle for a better surface sensitivity, are plotted (bottom). In addition, for a more precicely HOMO level determination, the difference spectra (c-Si reference spectrum subtracted) are depicted (top). The extracted HOMO level of both Tc films are located at (1.1 $\pm$ 0.1) eV relative to E_F.
The valence band leading edge of the H-passivated c-Si substrate is shown in panel (c). As depicted, the valence band edge position is determined as the intercept of linear fits between the valence band leading edge and the background noise. Its position is estimated to (0.95 $\pm$ 0.1) eV relative to E_F.
Finally, based on the results presented above, combined with literature values for the Tc LUMO [134, 328] and E_g of c-Si [288], the energy level alignment at the Tc/c-Si interface is shown in Figure 7.8 (d). The obtained ionization energy of $\sim$5.4 eV for Tc is consistent with literature values [158, 112, 328, 134, 310]. The HOMO level of Tc and the VB maximum of H-passivated c-Si(111) are close to each other with an offset $\Delta E^{\mathrm{VB}}_{\mathrm{HOMO}} \approx 150$ meV.

Solar cell preparation

Furthermore, *ex-situ* grown, nominally 1 nm and 10 nm, Tc thin films on H-passivated c-Si(111) substrates, fabricated with identical deposition parameters and experimental setups as used for solar cell production, were investigated with lab-based UPS using an excitation energy of 21.2 eV (i.e. He-I$_\alpha$ radiation). Samples were transferred under inert gas atmosphere from the evaporator placed inside a glovebox to the UHV analysis chamber. The UV light intensity was attenuated by a factor of 10 in the case of the 10 nm film to minimize possible light-induced film degradation and sample charging.
Fig. 7.9 shows the measured SECO (a) and HOMO/valence band region spectra (b). A work function of Φ_w $\sim$4 eV in both cases is determined. The low binding energy onsets of emission of the HOMO is found at (1.2 $\pm$ 0.1) eV and (1.3 $\pm$ 0.1) eV for the monolayer and multilayer film, respectively. Accordingly, the ionization energy is $\sim$5.3 eV for multilayer (= bulk-like) Tc, consistent with literature values [158, 112, 328, 134, 310]. The slightly smaller ionization energy for the ultra-thin (1 nm) film might result from a more efficient photohole screening from Si when compared to the organic material. Such a film thickness-dependent shift is routinely observed at organic/metal interfaces [125, 311].

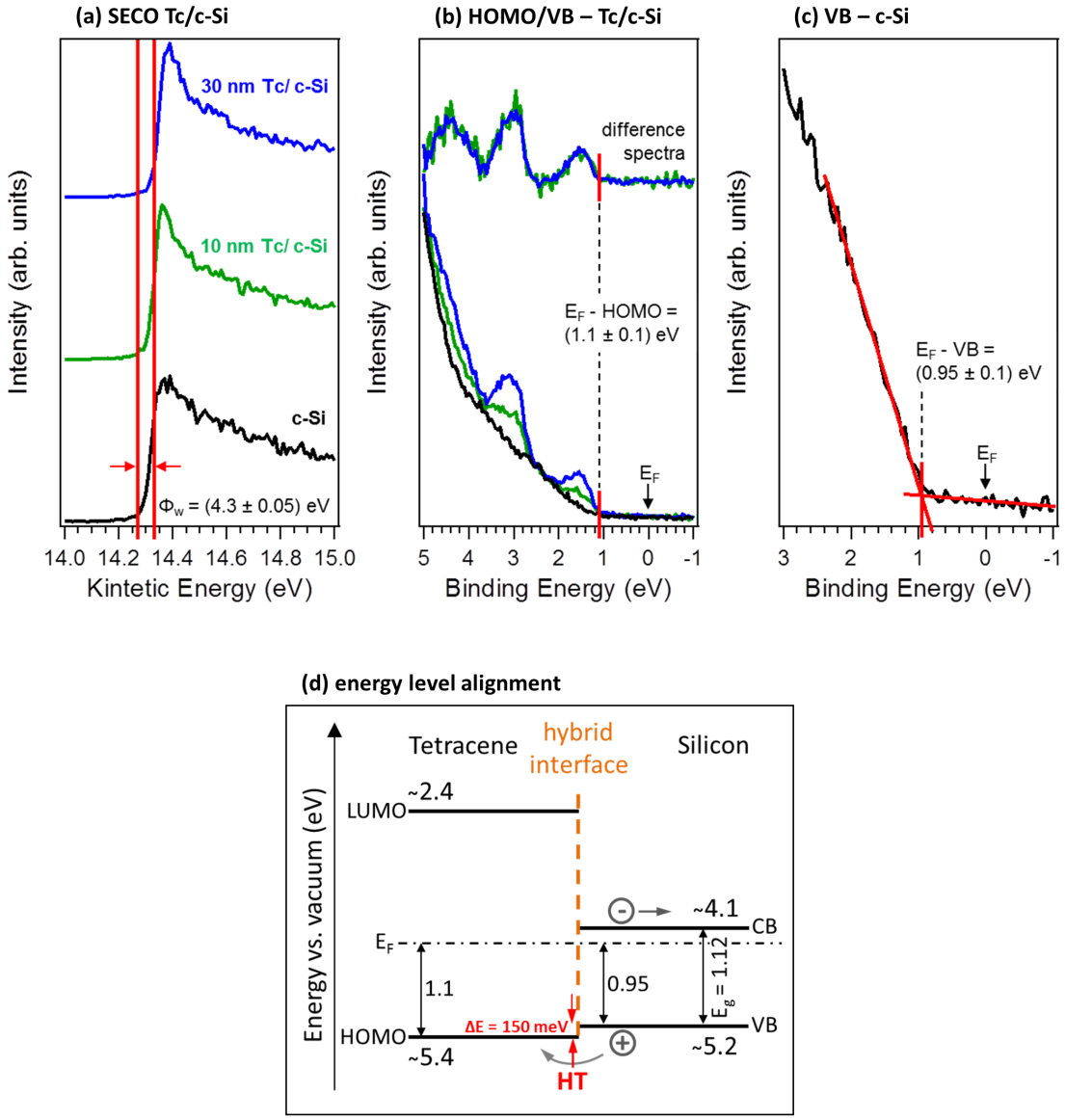

Figure 7.8: (a-c) UPS spectra recorded at SurICat end station (BESSY II) using an excitation energy of 35 eV. Samples were prepared *in-system*. Three samples were investigated: (i) H-passivated c-Si reference (put into load lock ∼10 min after HF-dip), (ii) nominally 10 nm and (iii) 30 nm evaporated thin film Tc/c-Si samples. (a) Secondary electron cut-off (SECO) region. (b) HOMO(Tc)/VB(c-Si) region close to E_F. Spectra are recorded with 45° take-off anlge (i.e., with increased surface sensitivity). (c) VB leading edge of H-passivated c-Si(111) substrate. Values extracted from the spectra are given in the figure. (d) Corresponding energy level alignment at the Tc/c-Si interface obtained by combining experimental and literature values. The LUMO is taken from Refs. [134, 328], E_g of c-Si from [288]. The determined offset between Tc HOMO and the VB of c-Si is $\Delta E^{\mathrm{VB}}_{\mathrm{HOMO}} \approx 150$ meV.

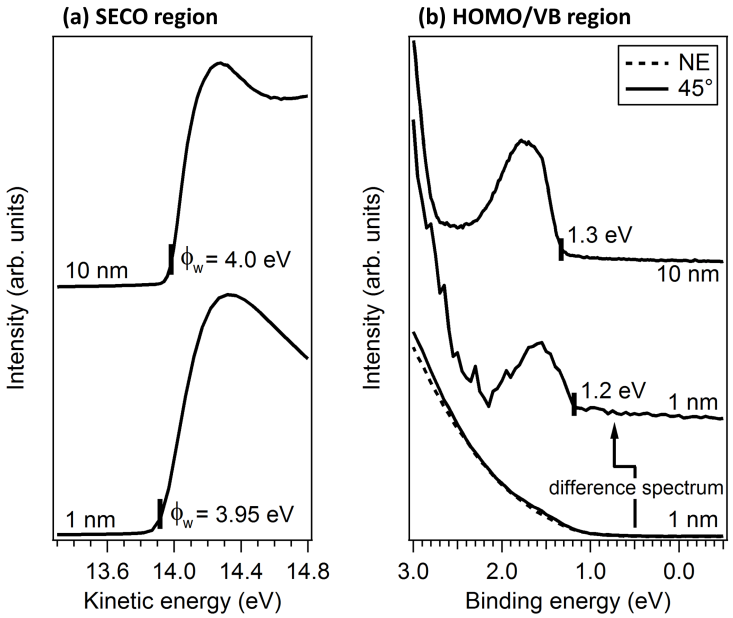

Figure 7.9: (a) UPS (21.2 eV excitation energy) results: Secondary electron cut-off, SECO, and (b) HOMO/VB region spectra of *ex-situ* grown Tc/c-Si(111) samples with Tc coverages as indicated. The data resulting form subtracting the spectra collected with 45° take-off angle (i.e., with increased surface sensitivity) from the one collected at normal emission (NE) is also included for the 1 nm film. Extracted values for work functions, Φ_w, and onsets of emission of the HOMO are given in the figure.

Discussion of UPS results

The extracted $|E_F$ - HOMO| of (1.3 $\pm$ 0.1) eV for the 10 nm Tc/c-Si *ex-situ* grown sample is 200 meV larger than (1.1 $\pm$ 0.1) eV determined for the *in-system* prepared sample. However, simultaneously the determined work function, Φ_w, shifts from (4.0 $\pm$ 0.05) eV to (4.3 $\pm$ 0.05) eV. Thus, the corresponding ionization energies are almost constant at $\sim$5.3 eV for the *ex-situ* and $\sim$5.4 eV for the *in-system* prepared sample, respectively. Such shifts of SECO and HOMO energy levels are observed in literature for organic/organic as well as organic/inorganic interfaces [283, 50, 51]. The authors relate this effect to differences in intermolecular packing and structural disorder in the organic film which is induced in those studies by a post diffusion of inert gas (N_2) into the film. In their model, gas molecules progressively penetrate into the organic film and the original intermolecular packing geometry is locally altered [50]. In our study, intermolecular packing of Tc thin films could be altered by various mechanisms comparing the two sample preparations: (i) N_2 gas atmosphere during sample transport for *ex-situ* prepared samples vs. vacuum transfer for *in-system* preparation, and (ii) altering evaporation conditions, e.g. specific evaporation rates and base pressures.

In summary, the here presented results, in accordance to literature, point out the importance of specific initial evaporation conditions. But also follow-up device fabrication processes, i.e. expo-

sure to various gas atmospheres, solution processing of PEDOT:PSS and various annealing steps may have a significant impact on the electronic properties of organic thin films and therefore overall device performance.
However, all UPS measurements on both, *ex-situ* and *in-system* prepared, Tc/c-Si solar cell precursor samples reveal an offset between the HOMO of Tc and the VB of H-passivated c-Si(111) in the order of $\Delta E^{\mathrm{VB}}_{\mathrm{HOMO}} \approx (200 \pm 200)$ meV. The large uncertainty of this value originates from the above described energy shifts observed for different sample preparations. The comparatively small offset, within the same order of magnitude as the a-Si:H/c-Si VB offset present in high efficient inorganic SHJ solar cells (cf. chapter 4), should not impose a significant barrier height for hole transport from the c-Si absorber across the hybrid interface to Tc.
A detailed discussion of triplet exciton harvesting at the hybrid Tc/c-Si interface, as it constitutes one of the fundamental prerequisites for the here proposed multi-exciton generation device approach, will be given in section 7.5.

7.4 PEDOT:PSS/Tc/c-Si hybrid solar cells

In the following section PEDOT:PSS/Tc/c-Si hybrid devices are analyzed and discussed by means of $j(V)$-characteristics and EQE measurements under various device conditions. Additionally, EQE spectra are evaluated by fitting experimental data within the singlet fission EQE optical model as presented in section 5.1.

7.4.1 j(V)-characteristics of PEDOT:PSS/Tc/c-Si solar cells

Figure 7.10 shows $j(V)$-curves of hybrid solar cells with various Tc layer thicknesses. The black curve corresponds to the PEDOT:PSS/c-Si reference cell without Tc, red and blue data correspond to cells with nominally 10 nm and 100 nm Tc thin films incorporated. AFM images taken on identically prepared Tc layers (without PEDOT:PSS capping layer) are also presented in the Figure. As described in section 7.1.2, for a nominally 10 nm film Tc islands cover $\sim$40% of the c-Si substrate, for the 100 nm layer a maximum share of 0.1% of deep pinholes possibly reaching the bare c-Si substrate are extracted from AFM images and a XPS study.
To the best of the author's knowledge, this is the first report of a working c-Si based hybrid solar cell with the singlet fission material Tc implemented within a hybrid layer stack. FFs of $\sim$70%, j_{sc}s of $\sim$22 mA/cm^2, and V_{oc}s of $\sim$645 mV result in PEDOT:PSS/Tc/c-Si device efficiencies exceeding 10%. As demonstrated in the optical simulation study (cf. chapter 5), due to parasitic absorption in PEDOT:PSS and reflection at hybrid layer stacks, the photocurrent strongly depends on specific organic layer thicknesses implemented on the solar cell's front side. Hence, the photocurrent extracted from $j(V)$-characteristics is insufficient to examine contributions of the Tc layer. Therefore, as it will be presented in the next section, an EQE analysis was additionally performed.

In order to keep solar cell fabrication for singlet fission hybrid devices simple, Ag was thermally evaporated directly onto the a-Si layer of the BSF, forming a more recombination active rear

contact compared to the optimized Ag/Ti/ITO/a-Si contact for highest efficiency SHJ solar cells, which was used for PEDOT:PSS/c-Si record devices. This explains the V_{oc} reduction from the reported 663 mV of the record PEDOT:PSS/c-Si solar cell (cf. section 6.3). Additionally, the here presented j_{sc} of ~22 mA/cm^2 is significantly lower compared to ~30 mA/cm^2 reported for the record PEDOT:PSS/c-Si cell. This is due to the fact that the front grid area is not subtracted in the $j(V)$-curves presented in Figure 7.10 which accounts for ~4 mA/cm^2. An additional j_{sc} reduction might stem from increased PEDOT:PSS layer thicknesses due to slightly different spin-coating parameters. Extracted from optical simulations (cf. Fig. 5.4, section 5.2) an increased PEDOT:PSS thickness of 150 nm reduces j_{sc} by ~4 mA/cm^2 compared to the optimized thickness of 80 nm.

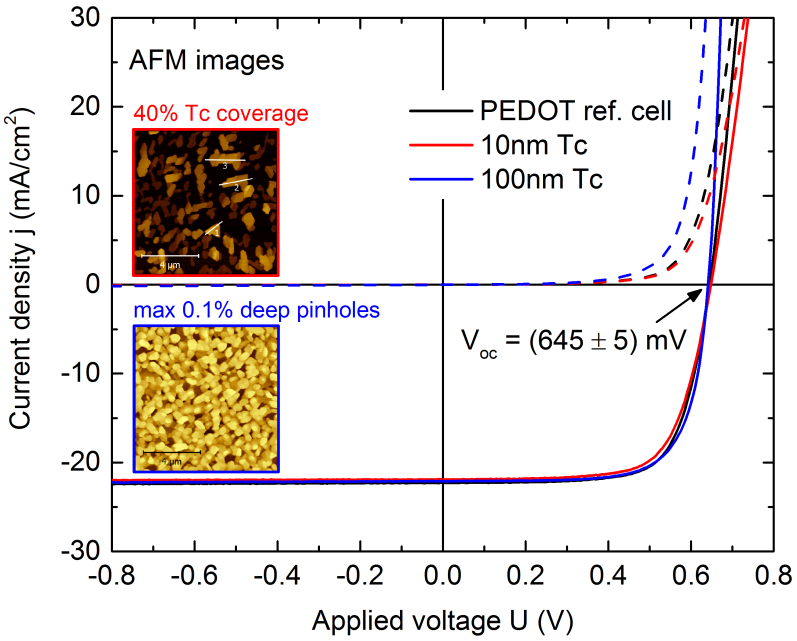

Figure 7.10: $j(V)$-characteristics under AM1.5G illumination (solid lines) and in the dark (dashed lines) for various hybrid devices. PEDOT:PSS/c-Si reference cell without Tc. PEDOT:PSS/Tc/c-Si cells with nominally 10 nm Tc, corresponding to 40% Tc island coverage and 100 nm Tc with a maximum share of deep pinholes of 0.1%, respectively. Coverages are extracted from AFM images. V_{oc} is constant at (645 ± 5) mV.

Discussion of j(V)-characteristics

The recombination current density, j_0, is a measure of overall recombination losses in a device [66]. As derived in Equation (2.2), $V_{oc} \propto ln\,(j_{ph}/j_0)$. Hence, passivation quality of the hybrid interface is directly reflected in solar cell's V_{oc}. Consequently, as V_{oc} = (645 ± 5) mV is constant for Tc coverages ranging from 0% (reference cell) to > 99% for the 100 nm Tc film, it is demonstrated that the passivation of the c-Si(111) surface by thermally evaporated thin film Tc

is comparable with the passivation quality of the hybrid PEDOT:PSS/SiO_x/c-Si interface.

Moreover, since j_{sc} is constant for all three hybrid cells, $j(V)$-characteristics imply that efficient extraction of holes generated in the c-Si main absorber is maintained for Tc layer thicknesses up to 100 nm. This allows to tune the Tc layer thickness in the relevant range regarding the triplet exciton diffusion length in polycrystalline Tc thin films with reported values of ∼100 nm [47].

The series resistance, R_s, in a solar cell has three causes: firstly, the movement of current through various device layers; secondly, contact resistances, R_c, at interfaces; and finally the resistance of the metal contacts. The main impact of R_s is to reduce the solar cell's FF.
From the $j(V)$-curves presented in Figure 7.10, overall hybrid device series resistances in the order of R_s^{total} ∼3 Ωcm^2 are extracted.
• With the conductivity σ_{PEDOT} = 470 S/cm [137][1] of the highly conductive polymer PEDOT:PSS and assuming 0.1% point contacts (cf. AFM/XPS analysis in section 7.1.2) with cylindrical rods of 100 nm height (polymer layer thickness) yield a resistance of point-contacted PEDOT:PSS rods of R_{PEDOT} ∼2 · 10^{-5} Ωcm^2. This is negligible compared to R_s^{total} ∼3 Ωcm^2.
• However, the contact resistance of PEDOT:PSS/c-Si, $R_c^{\text{P/Si}}$ = 50 mΩcm^2 [43][1], would increase to 50 Ωcm^2 assuming a 0.1% point-contacted PEDOT:PSS/Tc/c-Si solar cell. Thus, if hole extraction through 0.1% PEDOT:PSS/c-Si pinhole contacts would be the dominant pathway in the 100 nm Tc solar cell, from this consideration the FF is expected to be drastically reduced.
Since it is demonstrated by the $j(V)$-curves presented in Figure 7.10 that the FF is constant at ∼70%, this evaluation is an indication that there are no direct point contacts between PEDOT:PSS and c-Si in the 100 nm Tc device and therefore suggesting that holes which are generated in the c-Si absorber can be transferred across the hybrid Tc/c-Si interface and conducted through thin film Tc to be extracted at the PEDOT:PSS front contact. This is in line with the Tc-HOMO/c-Si-VB offset $\Delta E_{\text{HOMO}}^{\text{VB}}$ = (200 ± 200) meV[2] measured by UPS (cf. section 7.3).

Further analysis, e.g. EBIC experiments could help to spatially resolve the current flow in PEDOT:PSS/Tc/c-Si solar cells [170, 164].

7.4.2 EQE analysis of PEDOT:PSS/Tc/c-Si devices

In Figure 7.11 we compare the EQEs of PEDOT:PSS/Tc/c-Si solar cells with nominally 10 nm (red solid line) and 100 nm Tc (blue solid line) Tc incorporated with a PEDOT:PSS/c-Si reference cell (black solid line). As EQE spectra were recorded on the same devices as presented and discussed above, the color coding corresponds to the $j(V)$-curves depicted in Figure 7.10. Additionally, the approximated absorption spectra (100% - T) of thin film Tc deposited on glass in the same evaporation runs as for solar cell fabrication is plotted in dashed lines. Whereas EQE spectra of the reference and 10 nm Tc cells are very similar, the EQE with 100 nm Tc incorporated reveals strong deviations.
In the wavelength range below 550 nm, Tc absorption features are observed in the EQE, whereby absorption maxima coincide with EQE minima. Hence, Tc acts as an optical filter, but it does

[1] literature values measured for the solution PH 1000 mixed with 5% DMSO
[2] discussion of the large uncertainty, cf. section 7.3

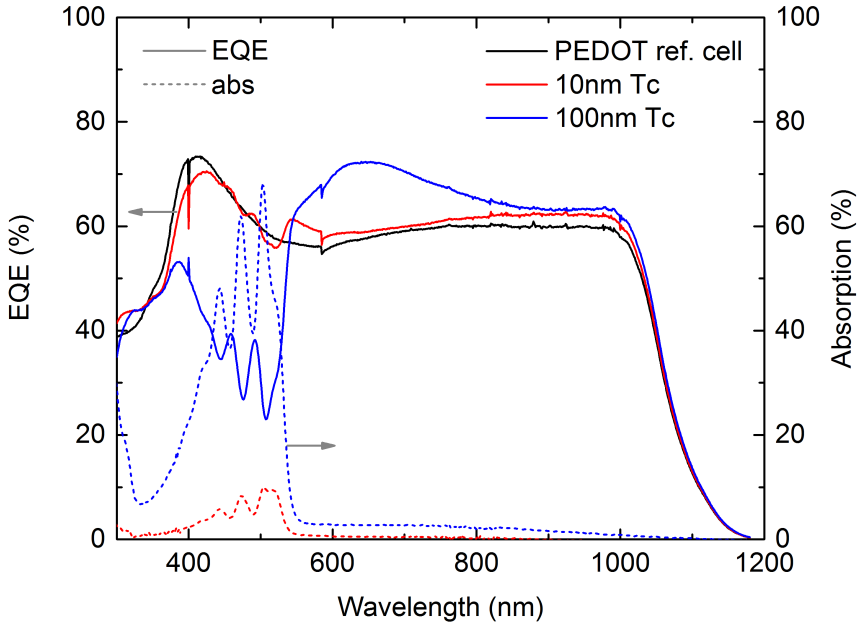

Figure 7.11: EQE spectra corresponding to $j(V)$-curves of Fig. 7.10 for the PEDOT:PSS/c-Si reference cell without Tc (black line), and 10 nm Tc (red line) and 100 nm Tc (blue line) PEDOT:PSS/Tc/c-Si hybrid devices. The spikes at ∼400 nm and ∼600 nm are setup artifacts. Approximated absorption spectra (100% - T) of thin film Tc deposited on glass in the same evaporation runs as for solar cell fabrication are plotted in dashed lines.

not hinder efficient charge carrier extraction from the c-Si absorber. This is seen in the long wavelength region above 550 nm where Tc does not absorb light. In this region, the EQE is not reduced compared to the PEDOT:PSS/c-Si reference cell. In fact, the EQE is even increased depending on Tc film thicknesses. This is attributed to optical effects such as altering reflection losses for different organic layer stack thicknesses, as simulated in section 5.3. Parasitic absorption losses of thicker Tc layers are compensated by a superior light management. Therefore, integration of the EQE explains the constant photocurrent observed in Figure 7.10.

In a nutshell, EQE spectra of Figure 7.11 reveal an "optical filter effect" of incorporated Tc layers. However, charge carrier extraction from the c-Si absorber is not hindered also for 100 nm Tc layers. Without further analysis, it is not possible to resolve contributions related to singlet fission in Tc. Small positive current contributions due to triplet exciton dissociation at the hybrid Tc/c-Si interface cannot be directly extracted from EQE spectra.

Fitting the singlet fission EQE optical model

To further evaluate the EQE spectra of Figure 7.11, experimental data of the 100 nm Tc cell were fitted with the singlet fission EQE optical model as introduced in section 5.1.
PEDOT:PSS is an optical anisotropic material. Experimentally derived (*n*-*k*) data of PEDOT:PSS, as already presented and discussed in section 5.1, are given in Figure 7.12 (a). If spin-coated on flat surfaces such as c-Si wafers, its extinction coefficient k reveals an ordinary and an extraordinary component, perpendicular and parallel to the surface plane, respectively [221, 222]. Consequently, for normal incidence of light only the ordinary component has to be taken into account. This has been prooven by the comparison of simulated and experimental EQE spectra of PEDOT:PSS/c-Si solar cells (cf. Fig. 6.12, section 6.3). However, AFM images confirm rough Tc layers with a RMS value of $\sim$16 nm and a $\sim$5% share of deep holes (cf. Fig. 7.5, section 7.1.2). Assuming that the PEDOT:PSS polymer chains are aligned along the Tc crystals, a mixing of both, ordinary and extraordinary components is expected under normal incidence of light.
Figure 7.12 (b) shows (*n*-*k*) data of polycrystalline thin film Tc as derived from reflection and transmission spectra (cf. section 5.1). The characteristic vibronic Tc absorption spectrum to the blue of 550 nm is reflected in k. As a guide for the eye, the vertical grey line separates the Tc absorption region in all three panels of the figure.
Finally, the influence on the simulated EQE for different ordinary/extraordinary (o/e) mixture ratios of PEDOT:PSS is depicted in Figure 7.12 (c). Obviously, only considering the ordinary component (pink data), oversimplifies the optics of the hybrid PEDOT:PSS/Tc/c-Si layer stack. However, EQEs for various (o/e) ratios demonstrate that the wavelength range $\gtrsim$ 550 nm is predominantly affected, whereas less influence is observed within the Tc absorption band width. This behavior is expected considering that the differences between ordinary and extraordinary component of birefringent PEDOT:PSS is steadily increasing towards the infrared. In the Tc absorption band width $\leq$ 550 nm deviations of ordinary and extraordinary components are only marginal (cf. Fig. 7.12 (a)). By comparison of experimental EQE (black data) with simulations,

the curvatures for different (o/e) mixtures suggest an ordinary component of less than 50% in the here presented hybrid device.
On that account, for fitting the experimental EQE the model was expanded by an additional (o/e) ratio parameter. For fitting, the Tc layer thickness was fixed to 110 nm as derived from (*n-k*) backwards calculation within the transfer matrix approach (cf. section 5.1). This is reasonable because the Tc film used for (*n-k*) determination was grown on a quartz glass substrate but with identical evaporation settings as used for solar cell fabrication. Thus, the only assumption made is that the same amount of Tc with similar morphology is deposited on quartz as on the c-Si(111) surface during identical evaporation runs. Furthermore, c-Si wafer and (i/n$^+$)a-Si:H back contact layer stack thicknesses were fixed to 280 μm and 5 nm/15 nm, respectively, as determined with spectral ellipsometry. Accordingly, four parameters remain which were fitted within the basic singlet fission EQE model: the PEDOT:PSS layer thickness, the (o/e) ratio parameter, and the efficiency parameters η_{MEG}^{Tc} and η_{el} as introduced in section 5.1.
Figure 7.13 (a) shows the comparison of experimental EQE and the best fit obtained within the optical model. The fit does not completely reproduce the experimental data over the full spectral range. Deviations mainly occur in the spectral region above 550 nm, while the valley-to-peak ratios in the Tc absorption region can be modeled fairly well. The fit was obtained for a PEDOT:PSS thickness of 190 nm, an (o/e) mixing ratio of 0.3, an electrical efficiency η_{el} = 90%, and a total MEG efficiency η_{MEG}^{Tc} = 10%. As introduced in section 5.1, η_{el} is the probability to extract generated free charge carriers from the solar cell. It is therefore determined by the full range EQE. η_{MEG}^{Tc} is defined as the overall efficiency due to singlet fission, diffusion of triplets to the interface, and their dissociation at the hybrid junction into extractable free charge carriers. Thus, η_{MEG}^{Tc} is only determined in the Tc absorption region $\lesssim$ 550 nm.
To visualize the effect of η_{MEG}^{Tc} on the modeled EQE spectra, the best fit for η_{MEG}^{Tc} = 10% is compared to efficiencies of 0% and 20%, respectively. The solid lines in Figure 7.13 (b) show simulated EQE spectra in the spectral range of interest of Tc absorption with various η_{MEG}^{Tc}, while keeping all the other model parameters constant. The spectrum for η_{MEG}^{Tc} = 0% (blue line) lies significant below the experimental data (dashed black line). The simulated spectrum for η_{MEG}^{Tc} = 20% (green line) is already significant above experimental EQE and also reveals significantly reduced valley-to-peak ratios of characteristic Tc absorption features. Additionally, simulated EQEs for various (o/e) mixing ratios (0%/ 50%/ 100%) are plotted in solid grey lines for η_{MEG}^{Tc} = 10% (best fit) illustrating its small effect within the Tc absorption region. Since the valley-to-peak ratios within the Tc absorption band width are reproduced fairly well in the best fit, optical modeling of the EQE spectra may indicate a small current contribution of Tc in the PEDOT:PSS/Tc/c-Si hybrid device under discussion with an overall efficiency of η_{MEG}^{Tc} $\sim$10%.

Evaluation of optical fitting

The optical fitting has to be treated with caution. AFM images demonstrate that Tc layers are rough with a RMS of $\sim$16 nm (cf. Fig. 7.5, section 7.1). Therefore, scattering effects at rough surfaces may disturb coherence conditions significantly, which are assumed in our optical simulations. At this stage of optical simulation, scattering is not included in the simple modeling

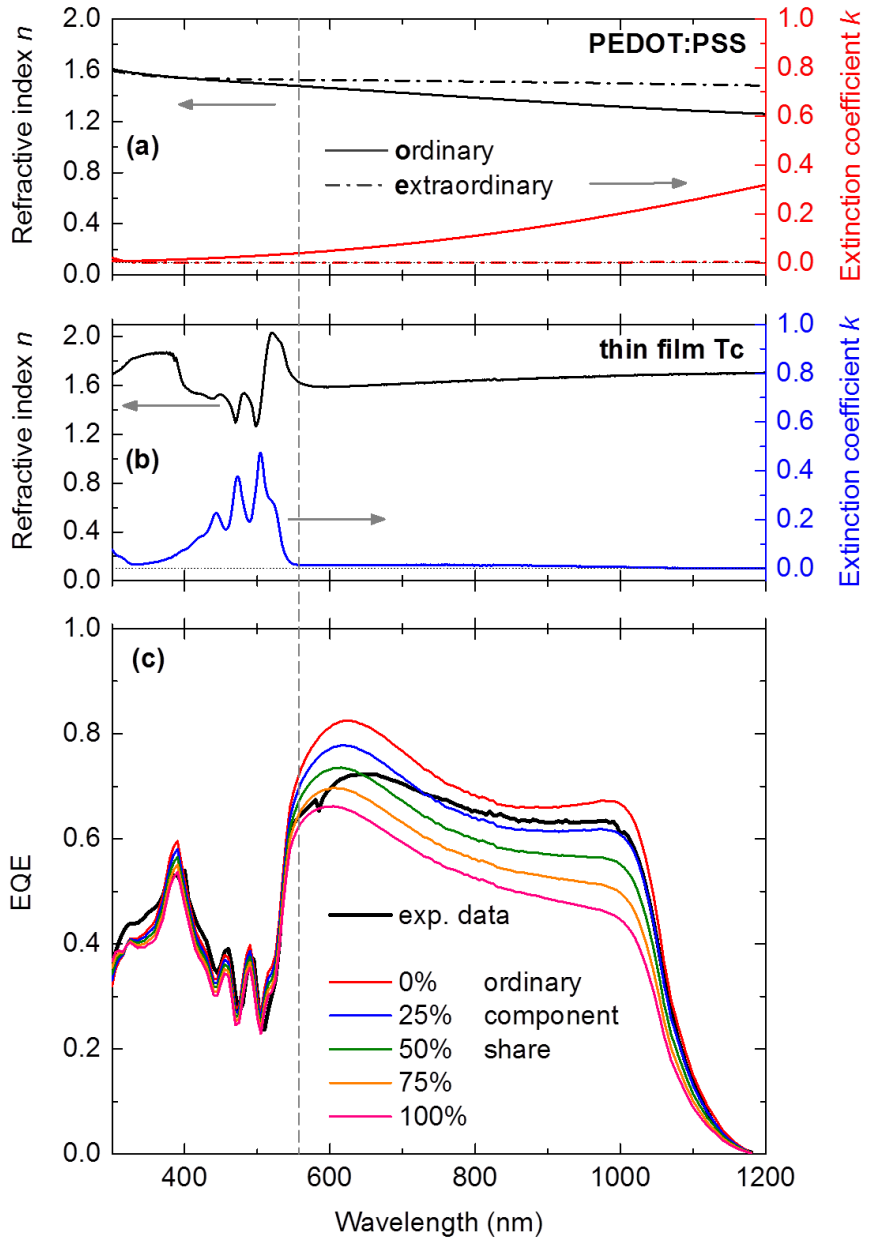

Figure 7.12: (a) (*n*-*k*) data of PEDOT:PSS as derived from spectroscopic ellipsometry following the analysis of L. A. A. Pettersson et al. [221, 222]. If spin-coated on flat substrates, PEDOT:PSS reveals an uniaxial anisotropy with an ordinary component perpendicular and an extraordinary component parallel to the surface plane. (b) (*n*-*k*) data of Tc derived from reflection and transmission spectra. Optical data are published in Ref. [136]. (c) Experimental EQE (black data) and simulated EQEs (colored data) within the singlet fission EQE model for (o/e) mixing ratios as indicated.

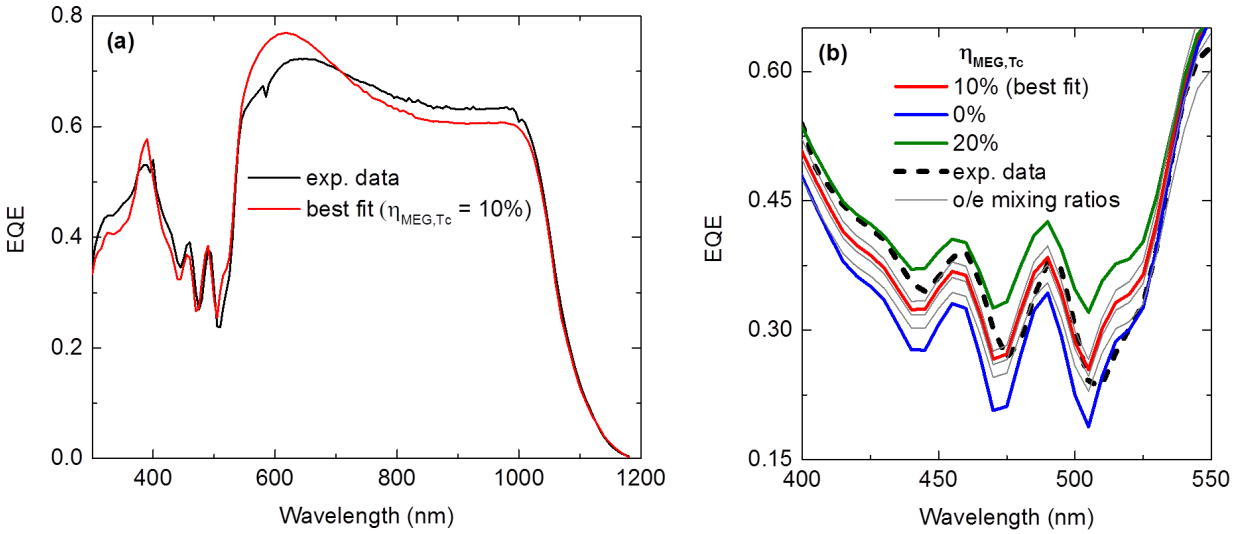

Figure 7.13: (a) Experimental EQE data and best optical fit within the singlet fission EQE optical model. The fit indicates a small current contribution stemming from Tc with total efficiency of η_{MEG}^{Tc} = 10%. (b) Zoom into Tc absorption region between 400 - 550 nm. Experimental data (dashed black line) and best fit (solid red line) with η_{MEG}^{Tc} = 10%. Additionally, efficiencies were fixed to 0% (solid blue line) and 20% (solid green line) while keeping all other model parameters constant. For comparison, simulated EQEs for various (o/e) ratios (0%/ 50%/ 100%) are plotted (solid grey lines) for η_{MEG}^{Tc} = 10%.

approach. In future, we aim to implement a scattering model which is possible within the here used simulation software "GENPRO4" [246, 144, 143]. The fitted PEDOT:PSS layer thickness is 190 nm. This is too high compared to experimentally determined values in the range of 100 - 150 nm. This may be either a result of scattering at rough surfaces and/or birefringence of PEDOT:PSS. The shape of experimental EQE to the red of 550 nm, where ordinary and extraordinary components of PEDOT:PSS deviate significantly, can only be modeled moderately. However, birefringence of PEDOT:PSS predominantly affects the wavelength range $\gtrsim$ 550 nm. The Tc absorption region $\lesssim$ 550 nm is less affected and the valley-to-peak ratios in the characteristic Tc absorption features can be modeled fairly well. Thus, fitting the experimental data with our basic singlet fission EQE optical model may indicate that a small current contribution originates from Tc with a total efficiency of $\eta_{MEG}^{Tc} \approx 10\%$.

As a final test, Figure 7.14 shows the simulated EQE assuming various contributions of singlet fission in the Tc layer expressed through the parameter η_{MEG}^{Tc} (cf. Eq. (5.3), section 5.1), ranging from 0% for purely parasitic absorption of Tc to its maximum value of 200% for a perfect MEG device with a singlet fission quantum yield of 200% and no losses during diffusion of triplet excitons and their dissociation at the hybrid interface.
Corresponding to Figure 7.13 experimental data and the best fit with η_{MEG}^{Tc} = 10% are plotted in solid black and red lines, respectively. As already discussed above, low efficiencies in the range $0\% \lesssim \eta_{MEG}^{Tc} \lesssim 20\%$ are hardly distinguishable within an EQE analysis calling for more sensitive experiments in this regime to resolve small Tc contributions to the photocurrent. However, for η_{MEG}^{Tc} = 50% the "filter effect" of Tc on the EQE is sufficiently diminished accompanied by significantly reduced valley-to-peak ratios of characteristic Tc absorption features which would allow to detect a current contribution stemming from Tc within an EQE analysis. Eventually, simulations predict that in the here presented hybrid PEDOT:PSS/Tc/c-Si device the EQE of unity, which is an unambiguous proof of MEG generation via singlet fission and triplet harvesting, is surpassed for $\eta_{MEG}^{Tc} \approx 125\%$ (data not shown in Fig. 7.14). For 150% the peak EQE yields ∼1.2. Ultimately, for the optimum efficiency of η_{MEG}^{Tc} = 200% a peak EQE of ∼1.5 is reached.
As already pointed out in section 5.3, the overall EQE could further be significantly raised by an improved light management by means of suitable AR-coatings and surface texturing, ideally accompanied by the reduction of parasitic absorption in thinner PEDOT:PSS layers.

The development of fully operating hybrid solar cells opens up the opportunity to further access the Tc/c-Si interface by performing EQE measurements under various device conditions such as external applied bias or temperature.

Field-assisted exciton separation

It is known from OPV literature that free charge carrier generation via exciton splitting at organic donor-acceptor interfaces can be significantly enhanced by external electric fields [59]. In particular, enhanced EQEs for applied reverse biases are reported for singlet fission Pc/C_{60} devices, e.g. Refs. [306, 171].
Figure 7.15 shows EQE spectra in the relevant Tc absorption region between 300 - 600 nm of

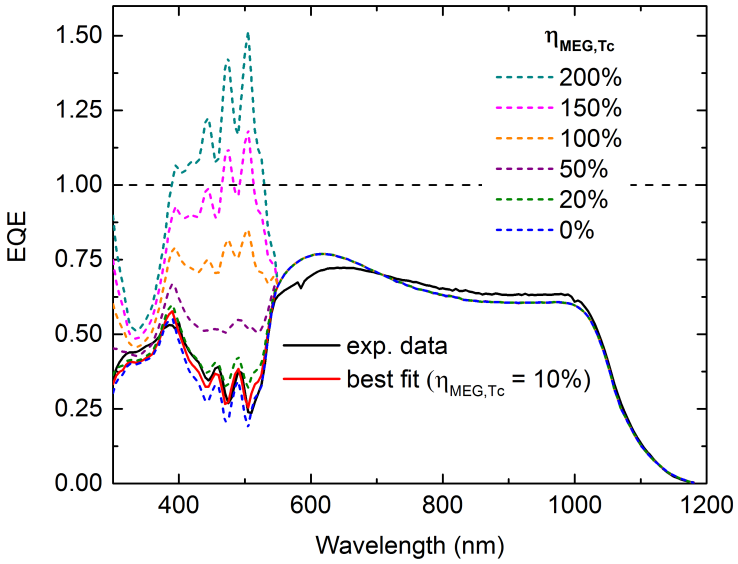

Figure 7.14: (solid lines) Measured EQE and best fit corresponding to Fig. 7.13. (dashed lines) Simulated EQEs for total MEG efficiencies ranging from $\eta_{MEG}^{Tc} = 0\%$, corresponding to purely parasitic absorption of Tc, to its maximum value of 200% for a perfect MEG device with a singlet fission quantum yield of 200% and no losses during diffusion of triplet excitons and their dissociation at the hybrid interface.

a PEDOT:PSS/Tc/c-Si solar cell recorded under external applied reverse biases. Obviously, no change in the EQE spectra is detected. Thus, within the here presented EQE analysis with applied biases up to -2.0 V, no field-assisted exciton separation is observed at the hybrid Tc/c-Si interface.
With the simulated width $d \approx 1$ μm of the depletion region using "AFORS-HET" [316], this corresponds to applied electric fields $|\vec{E}| = U_{bias}/d$ under reverse bias conditions of $\sim 10^6$ V/m.
A detailed discussion of the role of electric fields in driving charge dissociation will be given in the discussion of section 7.5.

Temperature-assisted exciton separation

Providing additional energy by means of temperature may also affect charge carrier generation [59]. Therefore, as shown in Figure 7.16 (left), EQE spectra of hybrid PEDOT:PSS/Tc/c-Si solar cells were recorded at room temperature (RT, black data), and stabilized at 80 °C (red data). The shift which is observed in the EQE spectra can be attributed to reversible temperature effects, as the PEDOT:PSS/c-Si reference cell reveals the same shift (green framed, Fig. 7.16 (right)). We speculate that the observed reversible temperature effect stems from the removal of water of already degraded PEDOT:PSS layers while heating. This will slightly change film thickness, thus changing reflection behavior of the layer stack as shown in the optical simulations. The effect is reversed due to uptake of water [90, 156] during 30 min interval in between both

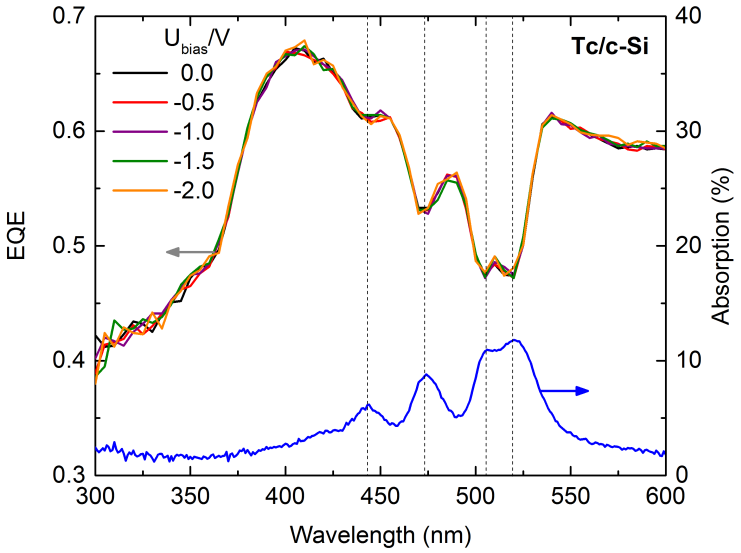

Figure 7.15: EQE spectra in the region of Tc absorption of PEDOT:PSS/Tc/c-Si solar cells, measured under indicated applied reverse biases U_{bias}. Devices are stable up to -2.0 V. For comparison, optical absorption of Tc is also plotted.

measurements. To check for this hypothesis, future measurements must be performed in inert gas atmosphere. Within the signal-to-noise ratio of the spectra presented in Figure 7.16, the Tc absorption feature ratios in the EQE do not change. Thus, the here presented EQE spectra recorded at high temperatures do not indicate any temperature-assisted exciton separation at the hybrid Tc/c-Si interface.
Also temperature effects will be included in the discussion of the following section.

7.5 Discussion – exciton harvesting at the hybrid Tc/c-Si interface

Experimental results and fits to the optical data from EQE modeling presented so far, reveal no clear evidence for bi-exciton splitting at the hybrid Tc/c-Si interface. As discussed in the previous section, small current contributions related to singlet fission in Tc are hard to detect within an EQE analysis, a total efficiency parameter $\eta_{MEG}^{Tc} \approx 10\%$ obtained by EQE modeling based on optical data has to be treated with caution. In the following, various possible exciton dissociation mechanisms and potential challenges which may hamper efficient triplet harvesting at the Tc/c-Si interface will be introduced and discussed.

As sketched in Figure 7.17, Frenkel excitons as observed in Tc are tightly bound (typical for organic materials E_{bind} = 0.1 - 1 eV) with the electron and hole localized on the same molecule [230, 59]. On the other hand, Wannier excitons, as they are present in c-Si, are highly delocalized with an exciton radius of $\sim$50 $\mathring{A}$ which is about 10$\times$ larger than the lattice constant. Wannier

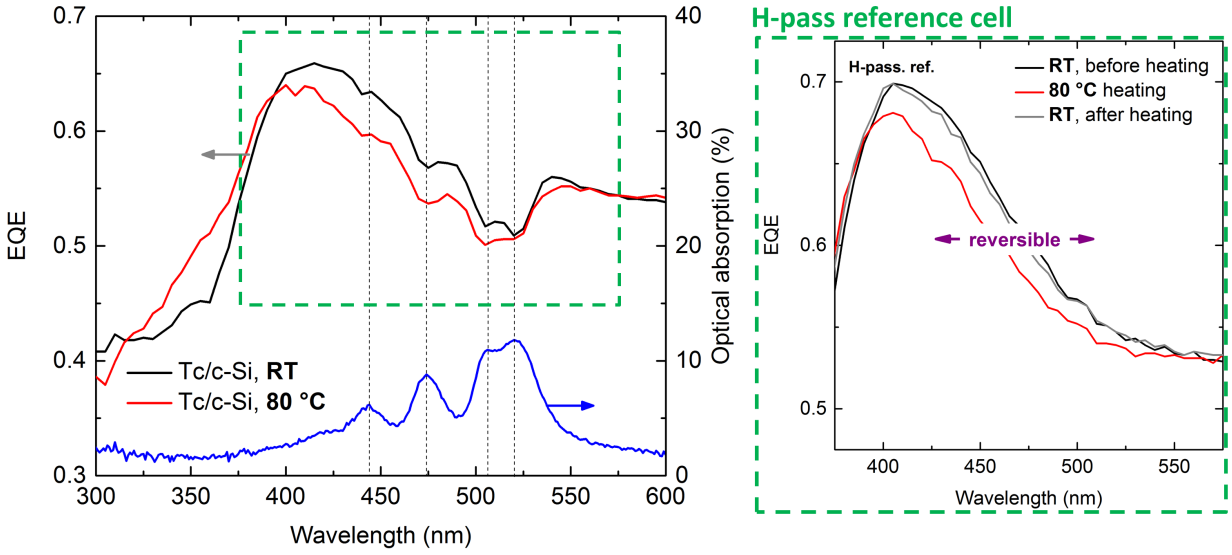

Figure 7.16: (left) EQE spectra in the region of Tc absorption of PEDOT:PSS/Tc/c-Si solar cells recorded at room temperature (RT) and 80 °C stabilized. For comparison, optical absorption of Tc is also plotted. (right) EQE zoom of a PEDOT:PSS/c-Si reference cell. A reversible EQE shift is observed while heating to 80 °C followed by cooling down back to RT.

excitons are weakly bound with $E_{\mathrm{bind}} \approx 0.01$ eV, resulting in free charge carriers already at room temperature ($k_B T = 0.025$ eV). The main reason for that is the difference of dielectric constants $\epsilon_r \approx 3.8$ for Tc [19] and $\epsilon_r \approx 12$ for c-Si [288].
The prerequisite for exciton separation is their diffusion to the hybrid interface. For singlet excitons reported diffusion lengths are in the range of 5 - 20 nm [223]. The diffusion length of long-lived triplet excitons can be much larger. Triplet diffusion is believed to originate by a Dexter-type energy transfer through phonon-assisted exciton hopping processes [282, 155, 293]. For polycrystalline thin film Tc, triplet diffusion lengths above 100 nm have been reported [47]. This indicates that a significant fraction of triplet excitons generated via singlet fission in the Tc layers reach both interfaces of a PEDOT:PSS/Tc/c-Si device. Since no pronounced shortening of triplet lifetime is observed on samples capped with PEDOT:PSS compared to pristine Tc films deposited on c-Si(111) substrates, it is concluded from transient PL measurements (cf. Fig. 7.7, section 7.2) that triplet excitons are neither significantly parasitically lost at the PEDOT:PSS/Tc interface nor split into free charges at the Tc/c-Si junction.

The consideration of momentum is a key factor in describing the excitation of electrons into the conduction band in indirect bandgap materials such as c-Si. The momentum of a plane wave in the far field is well-defined, i.e. the momentum of a photon is effectively zero. Hence, far-field photogeneration always needs to be phonon assisted to supply momentum to the electron system. However, it is shown in literature that organic molecules close to the c-Si surface with emission energies exceeding the band gap can non-radiatively transfer energy via near-field dipole-dipole interaction. An important feature of this Förster-type energy transfer mechanism, which occurs

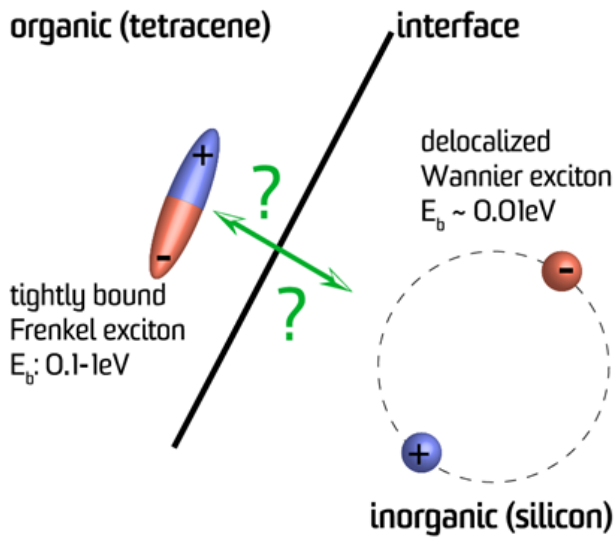

Figure 7.17: Sketch (not to scale) of a tightly bound Frenkel exciton in Tc –localized on the same molecule– and a delocalized Wannier exciton in c-Si. Typical exciton binding energies are given in the figure. For details see text.

from a localized excited state close to the absorber, is that it involves no strict momentum conservation [67, 95]. Efficient Förster-type energy transfer of singlets has been reported for dye films deposited on c-Si, e.g. Refs. [67, 95, 11, 96].
This non-radiative energy transfer from bright singlet states to c-Si is promising in terms of sensitizing c-Si devices with dyes or quantum dots. However, in the MEG device concept presented in this thesis we do not aim to harvest bright singlet states. If the singlet fission rate is fast, the formation of dark triplet excitons will outcompete singlet energy transfer to c-Si. Note that within the transient PL study efficient singlet state depopulation and the formation of long-lived triplet states via singlet fission was demonstrated in our Tc films (cf. Fig. 7.7, section 7.2). Since triplets are dark states, non-radiative Förster-type energy transfer via virtual photon exchange has no transition strength with the ground state of the molecule. To directly harvest non-emissive triplet excitons, there exist two transfer processes:

- Dexter-type **triplet energy transfer (TET)** which in the here presented device architecture requires a hole transfer (HT) back from c-Si.
- **Electron transfer** via localized **hybrid charge transfer (HCT)** states with the hole remaining on the Tc molecule.

In principle both mechanisms can exist at the Tc/c-Si interface. Both processes rely on particle exchange which in turn requires orbital overlap. The indirect band gap of c-Si should not constitute a problem for particle exchange, since (i) the DOS becomes very large just above the conduction band edge and (ii) localized donor states have a poorly-defined momentum [82].

Triplet energy transfer

Dexter-type TET of non-emissive triplet excitons from Pc and Tc to PbSe and PbS nanocrystals, respectively, was recently reported [307, 290, 133, 87]. TET efficiencies as high as 95% have been claimed [290]. It was demonstrated that the transfer rate is only efficient if the band gap

of the nanocrystals is resonant with the molecular triplet energy. TET from Tc (E_T^{Tc} = 1.25 eV) to PbS nanocrystals with band gaps in the range of 0.94 eV < E_g^{NC} < 1.23 eV with a maximum transfer efficiency for E_g^{NC} = 1.09 eV was observed [307]. Thus, resonance condition for c-Si (E_g^{Si} = 1.12 eV) should be fulfilled. In addition to resonance, also the band alignment is essential, since electrons and holes have to be transferred simultaneously.
With UPS measurements (cf. section 7.3) we have determined the HOMO level of Tc (5.4 ± 0.1) eV. This is close to the VB maximum of c-Si (5.2 ± 0.1) eV. The small offset, $\Delta E_{\mathrm{HOMO}}^{\mathrm{VB}} \approx$ (200 ± 200) meV, is within the range reported for various Pc/Tc-PbS/PbSe nanocrystal systems in which forward TET subsequently followed by hole transfer back is reported [133, 307, 290, 87]. This is summarized in Figure 7.18, which shows a possible triplet energy transfer process at the hybrid Tc/c-Si junction. Resonance condition between Tc triplet energy and c-Si band gap is fulfilled and Tc/c-Si HOMO-VB alignment should facilitate forward TET (step ①). After the triplet is transferred across the hybrid interface, charge carriers in c-Si are delocalized due to its high dielectric constant resulting in free charge carriers at room temperature. Obviously, a subsequent hole transfer back (step ②) is required. An efficient hole extraction from the c-Si absorber to the hole selective front contact in Tc/c-Si hybrid devices was demonstrated (cf. Figs. 7.10 & 7.11, section 7.4). Using standard back contact schemes adopted from the SHJ technology, efficient electron extraction from c-Si is achieved.

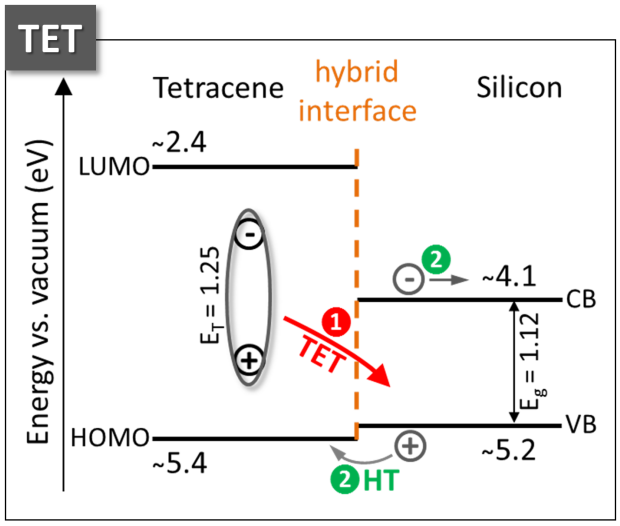

Figure 7.18: Sketch of principal charge separation mechanism by triplet energy transfer (TET). Energy level alignment at the hybrid Tc/c-Si junction. Energetic positions of the HOMO and VB were determined by UPS measurements, all other values are taken from literature [310, 54, 134, 328, 288]. ① Forward TET is sketched in red. ② Hole transfer (HT) back and electron extraction are sketched in green.

However, as discussed in the previous section, an EQE analysis is not sensitive enough to resolve small current contributions related to triplet harvesting. Thus, if TET takes place, its rate is rather low.

Electron transfer via hybrid charge transfer state

The second possible process to dissociate triplet excitons is electron transfer via an interfacial HCT state, sketched red in Figure 7.19. In a second step, the localized and Coulombically bound interfacial electron-hole pair has to be dissociated into free charge carriers to be extracted at the device contacts.

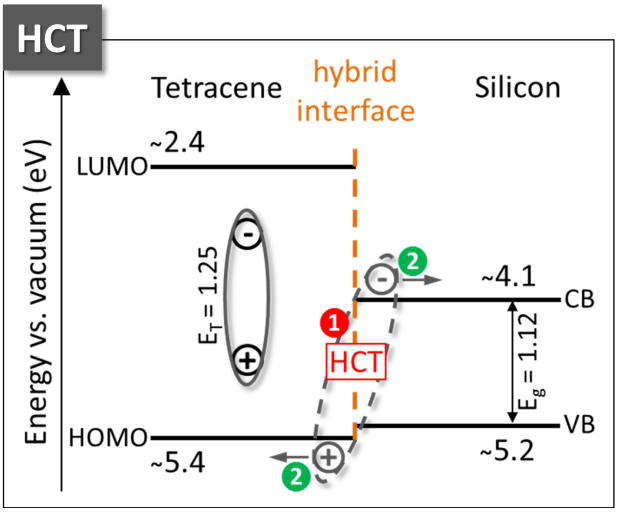

Figure 7.19: Sketch of principle charge separation mechanism by the formation of a hybrid charge transfer (HCT) state. Energy level alignment at the hybrid Tc/c-Si junction. Energetic positions of the HOMO and VB were determined by UPS measurements, all other values are taken from literature [310, 54, 134, 328, 288]. ① indicates the formation of an interfacial HCT state, ② its subsequent dissociation.

The difference to TET is that the hole remains on the Tc molecule. The energy difference between the CB maximum of c-Si and the HOMO level of Tc is $\Delta E^{\mathrm{CB}}_{\mathrm{HOMO}} \approx 1.3$ eV. This is a rough estimate of the HCT state energy at the hybrid Tc/c-Si junction; however, it neglects the binding energy of the HCT state [77]. Binding energies of CT states can be a few tenth of an eV at organic donor-acceptor interfaces [59]. Due to the low dielectric constants in purely organic junctions ($\epsilon_r < 4$, [59]), charge carriers are not efficiently screened from each other, forming Coulombically bound CT states. Given the high dielectric constant of c-Si ($\epsilon_r \approx 12$, [288]), the eventual formation of a HCT state between Tc and c-Si is considered to promote efficient decoupling of charge carriers due to the increased screening of electron-hole interaction. For organic-inorganic HCT states, Coulombic binding energies are estimated to be < 0.1 eV, thus reducing the driving force for charge carrier separation [20, 224, 318].
Since $\Delta E^{\mathrm{CB}}_{\mathrm{HOMO}} \approx \mathrm{E}_T^{Tc}$ is approximately isoenergetic, no driving force to form a HCT state is expected at the hybrid Tc/c-Si junction. On the other hand, the LUMO level of the electron acceptor C_{60} lies at ∼4.0 eV (large uncertainty of literature value [133, 328]), hence very close to the CB of c-Si at ∼4.1 eV. At the Tc/C_{60} interface, the formation of CT states and the harvesting of dark triplets has been suggested [52, 245, 328]. Thus, compared to the energy level alignment of the organic donor-acceptor Tc/C_{60} interface, the formation of a HCT state at the hybrid Tc/c-Si junction might be possible.

If interfacial CT states are formed, their dissociation into free charge carriers is competing with loss channels, e.g. geminate recombination. The competition depends upon the magnitude of the Coulombic attraction felt by CT states. In particular, L. Onsager proposed a definition for the so called Coulomb capture radius, r_c, which is defined as the distance where the Coulomb attraction energy equals the thermal energy $k_B T$ [214, 37, 59]:

$$r_c = \frac{e^2}{4\pi\epsilon_0\epsilon_r k_B T}\,, \tag{7.2}$$

with the permittivity of vacuum, ϵ_0, and the dielectric constant of the surrounding medium, ϵ_r. The dissociation probability increases for smaller r_c. Thus, Equation (7.2) emphasizes the importance of the dielectric constant. In the case of CT states at organic interfaces with $\epsilon_r < 4$ the Coulomb attraction between interfacial charges is rather high and the geminate recombination rate may constitute a significant loss channel [59]. By an external applied electric field, geminate recombination can be drastically reduced, resulting in more efficient charge carrier extraction [214, 37, 59, 171, 8, 49, 220]. In contrast, if an electron is transferred across an organic-inorganic junction, due to the delocalization of the electron in the inorganic counterpart ($\epsilon_r > 10$), geminate recombination at HCT states is expected to be rather small compared to organic CT states [318, 224].
To address the possible formation of HCT states, EQE measurements were conducted under applied external biases. The shape of EQE spectra of PEDOT:PSS/Tc/c-Si devices under reverse bias conditions up to -2 V does not change (cf. Fig. 7.15, section 7.4.2).
Three possible conclusions can be drawn from this bias dependent EQE analysis. (i) No HCT states are formed at the Tc/c-Si interface. (ii) HCT states are formed but possibly the applied electric field which is estimated to be $|\vec{E}| \approx 10^6$ V/m is not strong enough to significantly enhance HCT state dissociation. Note that typically electric fields in the order of $\sim 10^8$ V/m are applied to organic devices [59]. (iii) The Coulomb attraction of HCT states is so small due to the high dielectric constant of c-Si that interfacial charge dissociation is already efficient at the internal field under short-circuit condition.
Hypothesis (i) is supported by transient PL measurements in which no quenching of triplet excitons could be observed. Correspondingly, since no triplet lifetime shortening is detected which would be expected in the case of HCT formation, hypotheses (ii) and (iii) are rather unlikely. Anyhow, in the event of case (iii), HCT state formation and efficient dissociation into free charges, the effect must be very small with total efficiencies $\eta_{MEG}^{Tc} \lesssim 10\%$ as estimated by optical modeling of EQE data (cf. section 7.4.2).

Furthermore, to check for the influence of temperature as a driving force for charge dissociation [59], devices were heated during EQE measurements providing additional thermal energy to the system. However, as shown in Figure 7.16 (section 7.4.2), no indication of temperature-assisted exciton separation in Tc/c-Si hybrid devices upon heating to 80 °C was observed.

In a nutshell, it has been shown for various hybrid Tc/Pc - PbS/PbSe nanocrystal systems that efficient triplet energy transfer is possible in resonance conditions [307, 290, 133, 87] which are also fulfilled for the Tc/c-Si system.
The energy difference $\Delta E_{\mathrm{HOMO}}^{\mathrm{CB}}$ at the Tc/c-Si hybrid junction approximately equals the Tc triplet energy. Hence, no driving force for the formation of a HCT state is expected. However, Tc triplet exciton harvesting via CT states at the Tc/C_{60} interface is suggested [52, 245, 328], whereby the energy level positions of LUMO(C_{60}) $\approx$ CB(c-Si).
Thus, the band alignment is critical, but both, (i) triplet energy transfer or (ii) the formation of an interfacial HCT state at the Tc/c-Si interface might be possible.
Since EQE analysis, including optical modeling and measurements performed under reverse bias and high temperatures, is not sensitive enough to resolve possibly small current contributions of Tc due to exciton splitting at the Tc/c-Si interface, this calls for more sensitive experiments such

as magnetic field dependent current measurements, which can ideally monitor current contributions directly assigned to dissociation of triplet excitons created by singlet fission.

Besides the energy level alignment of the Tc/c-Si hybrid junction, other crucial aspects may be important for efficient triplet harvesting.
Particle exchange requires **orbital overlap**. At the hybrid Tc/c-Si interface, coupling of wave functions may strongly depend on (i) specific molecule arrangement at the semiconductor surface, and (ii) substrate surface conditions itself. For the Pc/C_{60} donor-acceptor pair charge transfer state energies were calculated for different molecule configurations using DFT calculations. The head-to-tail configuration appears likely to be able to dissociate triplet excitons from Pc, whereas CT state energy in the face-to-face configuration is too high [133]. Orbital overlap may also depend on substrate surface orientation and polarity, as it was modeled by DFT for the hybrid P3HT/GaAs interface [336]. To the best of the author's knowledge, no calculations for the hybrid Tc/c-Si interface have been reported. It is therefore possible that the lack of orbital overlap in our specific Tc/c-Si(111) hybrid interface formation hampers particle exchange processes.
The formation of a HCT state implies interfacial **localization**, at least for a short time. In contrast to purely organic CT states, the electron wave function in the inorganic part of the hybrid interface is very different. For c-Si it will be derived from delocalized band states. HCT states were experimentally observed at e.g. hybrid ZnO/organic interfaces [318, 224]. It is speculated that local defects at the ZnO surface may assist the initial localization of the electron state. Thus, trapping of excitons without degrading the c-Si interface may increase dissociation probability. The idea of realizing suitable trap states at the semiconductor surface was already mentioned in the original paper by D. L. Dexter in 1979 [82].
To that end, (i)a-Si:H passivation layers which exhibit localized states in the exponential band tail were implemented in hybrid devices (cf. next section).

7.6 Interlayer development

No clear evidence of exciton dissociation at the Tc/c-Si hybrid interface is found neither within an EQE analysis on device level nor by ultra-fast optical spectroscopy monitoring triplet exciton lifetimes in device relevant layer stacks. Results presented and discussed thus far were all obtained for Tc deposited on H-passivated c-Si(111) surfaces. In this work, further device engineering by means of interlayer development was conducted.

(i)a-Si:H passivation layer

The idea of an (i)a-Si:H passivation layer, as standardly used in the high-efficiency SHJ technology, is to trap long-lived triplet excitons at defect states located in the exponentially-decaying DOS in the a-Si:H band tail. It is speculated that suitable trap states may assist the formation of HCT states.
For that reason PECVD grown 5nm (i)a-Si:H passivation layers were implemented in hybrid solar cells. Prior to organic thin film deposition, the native oxide was removed by a HF-dip. Nominally 10 nm Tc was then evaporated onto the (i)a-Si:H layer followed by standard PEDOT:PSS

layer fabrication. Figure 7.20 shows the $j(V)$-characteristics of hybrid PEDOT:PSS/c-Si reference, PEDOT:PSS/(i)a-Si:H/c-Si, and PEDOT:PSS/Tc/(i)a-Si:H/c-Si cells, respectively. Pronounced s-shapes are observed for devices with (i)a-Si:H passivation layers incorporated. The inset of Figure 7.20 depicts a SEM cross section image of the hybrid layer stack. Tc island formation on (i)a-Si:H/c-Si substrates, as it was observed for Tc growth on bare, H-terminated c-Si(111) surfaces (cf. section 7.1), is observed. Note that the thin a-Si layer cannot be resolved with SEM.

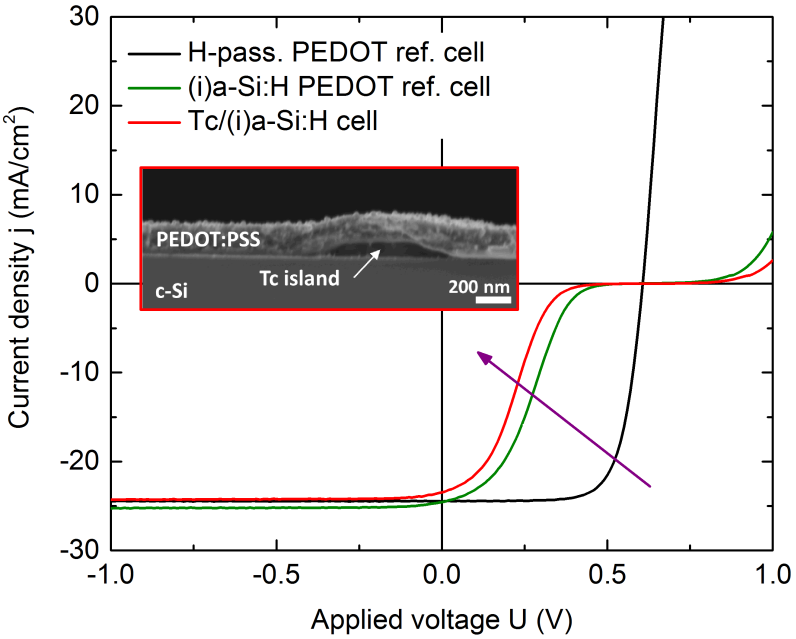

Figure 7.20: $j(V)$-curves of H-passivated PEDOT:PSS/c-Si reference cell (black line), PEDOT:PSS/(i)a-Si:H/c-Si (green line) and PEDOT:PSS/Tc/(i)a-Si:H/c-Si (red line) cells. For cells with 5 nm (i)a-Si:H passivation layer incorporated pronounced s-shapes are observed. The inset shows a SEM cross section image of Tc deposited on (i)a-Si:H/c-Si substrate capped with PEDOT:PSS. Tc island formation of a nominally 10 nm film is observed, as previously shown for Tc deposited on H-terminated c-Si(111).

Reflected in the pronounced s-shapes of both (i)a-Si:H devices, with and without Tc island layer, holes cannot be extracted efficiently at the hybrid front contact. A likely explanation therefore is the formation of a thick, wide band gap a-SiO_x hole blocking layer during cell fabrication. Providing water in the PEDOT:PSS suspension and heat during the mandatory polymer drying step constitute favorable conditions for a-SiO_x growth into the defect-rich amorphous silicon network [14, 325].
However, if assuming that hole blocking oxide formation is hindered beneath Tc islands, the fact that the s-shape is not reduced by the incorporation of a Tc island layer (∼40% coverage), no evidence for extraction of holes generated in the c-Si absorber across the Tc/(i)a-Si:H interface is given.

Finally, the corresponding EQE spectrum for the Tc/(i)a-Si:H/c-Si cell, due to the strong s-shape recorded at - 1 V reverse bias, is depicted in Figure 7.21. As for the H-passivated hybrid solar cells, Tc absorption is directly reflected as an "optical filter" in the EQE. If there is a positive contribution due to exciton separation at the Tc/(i)a-Si:H interface, it is small and cannot be resolved within an EQE analysis.

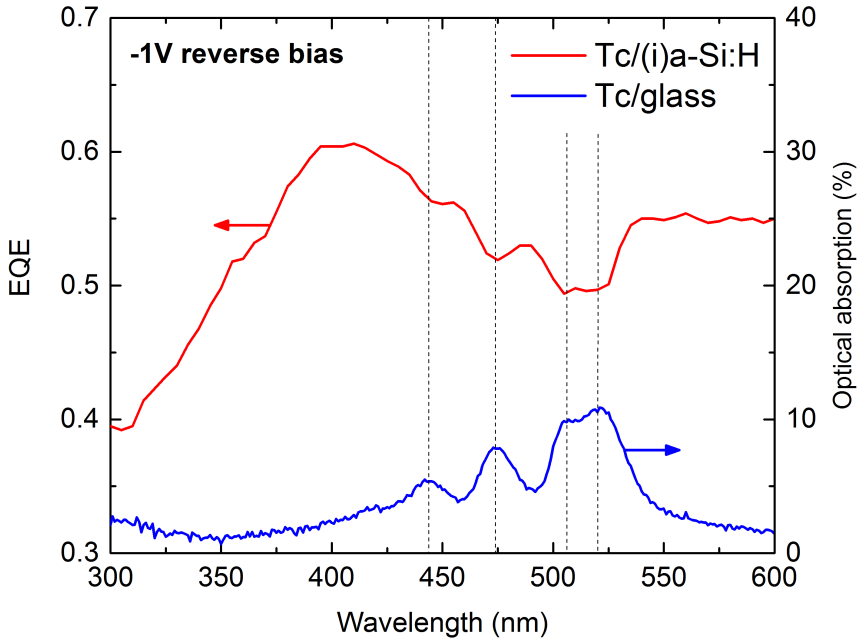

Figure 7.21: EQE spectrum of the PEDOT:PSS/Tc/(i)a-Si:Hc-Si solar cell recorded at -1 V revere bias (red line). The corresponding $j(V)$-characteristics of this cell is shown in Figure 7.20. For comparison, approximated absorption (100% - T) of a Tc film deposited on glass in the same evaporation run as for solar cell fabrication is plotted (blue line).

In future studies, to test the hypothesis of the formation of a hole blocking oxide layer, and to check if hole extraction through the Tc/(i)a-Si:H interface is possible, hybrid solar cells with varying Tc layer thicknesses and (i)a-Si:H surface coverages are essential.

Intermediate C_{60} layer

The second interlayer approach is the implementation of an intermediate C_{60} layer between Tc and c-Si. At the organic donor-acceptor Tc/C_{60} interface triplet excitons can be dissociated into free charge carriers. In literature CT state formation at the Tc/C_{60} interface has been reported [133, 52, 245]. On device level, photocurrent contribution from triplet exciton harvesting was demonstrated by magnetic field dependent changes in the photocurrent of Tc/C_{60} solar cells [134, 328]. Hole extraction to the PEDOT:PSS front contact is also confirmed.

The Tc/C_{60}/c-Si band alignment is depicted in Figure 7.22, whereby all processes confirmed in literature –namely CT state formation ① and its dissociation into free charge carriers ②– are

indicated in green. In a third step, the free electrons in C_{60} have then to be injected across the hybrid interface to c-Si. If wavefunction overlap is ensured, electron transfer (sketched red in Fig. 7.22) should be possible given the band lineup between the LUMO of C_{60} located at $\sim$ -4.0 eV [328] and the CB of c-Si at -4.05 eV [288]. The HOMO of C_{60} (approx. -6 eV, [328]) constitutes a large offset to the VB of c-Si (-5.2 eV), meaning that C_{60} would act as a hole blocking interlayer. Therefore, to ensure efficient extraction of holes generated in the c-Si absorber, which is essential in the device concept, two options for the C_{60} layer are possible: (i) a very thin layer that sustains hole tunneling, or (ii) a partially-closed layer, enabling hole extraction through point contact schemes.

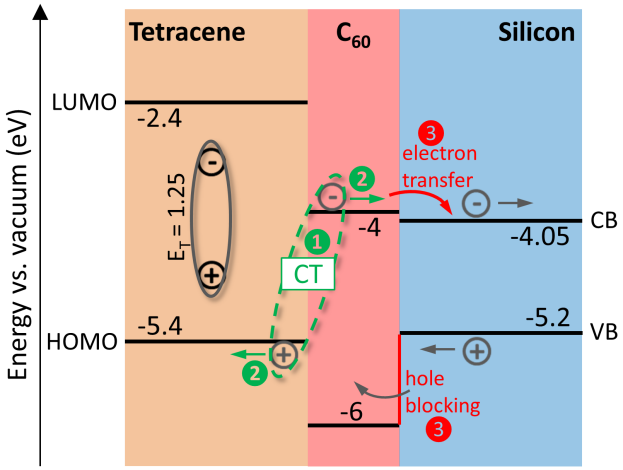

Figure 7.22: Band diagram of the Tc/C_{60}/c-Si interlayer approach. For details of charge separation and transfer processes see text.

For a first proof of concept hybrid PEDOT:PSS/Tc/C_{60}/c-Si solar cells on HF-dipped wafers with various C_{60} interlayer thicknesses were fabricated. For reference, a cell without C_{60} was also produced. On all devices nominally 10 nm thin film Tc was deposited in the same evaporation run.

Figure 7.23 (a) shows the $j(V)$-characteristics for three cells with 0 nm (= reference), nominal 1 nm and 3 nm intermediate C_{60} layers. V_{oc} is independent, thus c-Si surface passivation by C_{60} is sufficiently good and comparable to the Tc/c-Si interface. For 3 nm C_{60}, the $j(V)$-curve already exhibits a pronounced s-shape. As stated above, due to the large C_{60}-HOMO/c-Si-VB offset, this is likely related to an increasing hole blockade for thicker C_{60} layers.

The corresponding full range EQE spectra are plotted in Figure 7.23 (b). In the spectral range below 600 nm the EQE is slightly increasing for solar cells with C_{60} intermediate layers, whereas in the long wavelength range the EQE is independent. This might be an effect of both: (i) optical effects like light scattering which is more pronounced at shorter wavelengths, or (ii) possibly also due to harvesting of excitons at the Tc/C_{60} interface as proposed above.
To investigate this in more detail, we compare the EQE spectra of a PEDOT:PSS/Tc/c-Si reference and a PEDOT:PSS/Tc/3nmC_{60}/c-Si cell[3] recorded with a higher resolution (5 nm step width) and an improved signal-to-noise ratio by means of multiple scans. The results are depicted in Figure 7.24 (a) together with the approximated absorption (100% - T) of Tc/C_{60} layer stacks deposited on glass in the same evaporation runs as for solar cell fabrication.

[3] reproduced hybrid solar cell series

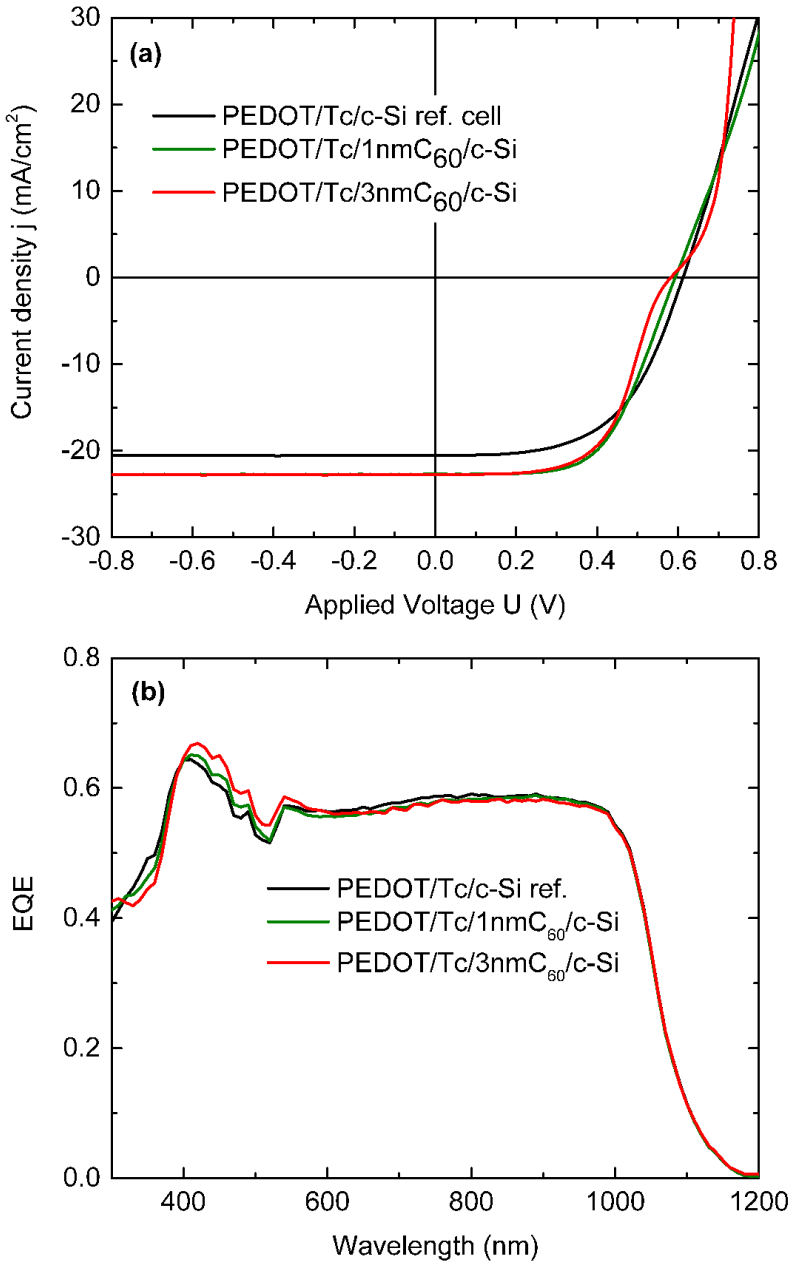

Figure 7.23: Intermediate C_{60} layer thickness variation (0 nm = reference, 1 & 3 nm C_{60}) of hybrid PEDOT:PSS/Tc/C_{60}/c-Si solar cells. (a) $j(V)$-characterisctics measured under AM1.5G, and (b) corresponding full range EQE spectra.

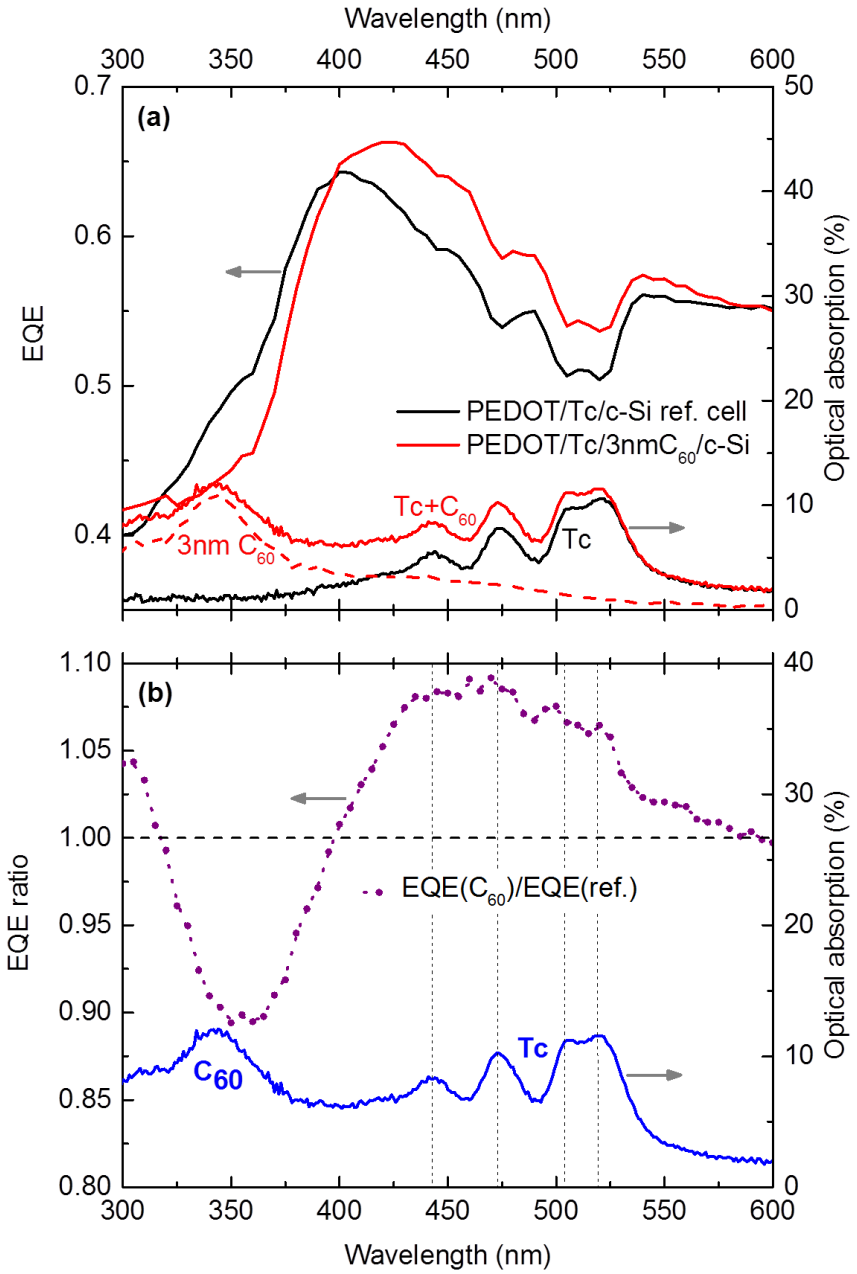

Figure 7.24: (a) EQE spectra (left axis) of PEDOT:PSS/Tc/c-Si reference cell (black data) and PEDOT:PSS/Tc/3nmC_{60}/c-Si cell (red data). Approximated absorption (100% - T) spectra (right axis) of various organic thin films deposited on glass substrates in the same evaporation runs as for solar cell production. (b) EQE ratio (violet dotted-line) obtained by division of EQE(C_{60}-cell)/EQE(ref.-cell).

Comparing EQE spectra of the reference cell without C_{60} with the 3 nm C_{60} incorporated device, a significant increase of the EQE in the spectral range between 400 - 550 nm, where Tc predominantly absorbs, is observed. In the range between 300 - 400 nm, which is dominated by absorption of C_{60}, the EQE decreases. This observation might be dominated by optical effects such as scattering or slightly varying anti-reflex behavior. However, just by visual inspection peak-to-dip ratio in the EQE of the Tc/3nm C_{60} device seems to be slightly reduced compared to the reference cell without C_{60}.
To verify this assumption, in Figure 7.24 (b) the two EQE spectra are divided. The corresponding ratio of EQE(C_{60}-cell)/EQE(ref.-cell) (violet dotted-line) reveals a positive region with an EQE ratio > 1 which coincide with the spectral range of Tc absorption. On the other hand, between 300 - 400 nm where the absorption of C_{60} becomes dominant, the EQE ratio is < 1. This might be indicative for parasitic light absorption of C_{60}. However, the promising feature in Figure 7.24 (b) is that characteristic Tc absorption maxima coincide with maxima of the EQE ratio, as indicated by the vertical grey dashed lines. While the broad range features could be also evoked by optical effects, the overlaid narrow peaks appearing in the EQE ratio and reproducing the vibrational structure of Tc absorption are indicative for a small current contribution related to Tc, stemming from exciton harvesting at the Tc/C_{60} interface and electron injection into c-Si base, as proposed above.

Although EQE analysis of this study is promising, the effect is still very small and further experiments have to be performed to unambiguously check for a positive Tc contribution arising from triplet exciton dissociation and to exclude optical effects.

7.7 Summary

A promising multi-exciton generation concept is to take advantage of the singlet fission process. By reducing thermalization losses, device efficiencies above the single-junction limit are theoretically possible. Tc is a promising SF material for the combination with a c-Si main absorber as the Tc triplet energy is slightly above the band gap energy of c-Si.

In this work Tc was incorporated in hybrid PEDOT:PSS/Tc/c-Si solar cells. Device efficiencies $\gtrsim 10\%$ are reported. Thereby a constant V_{oc} = (645 $\pm$ 5) mV is measured for devices with various Tc coverage ratios of the c-Si surface, ranging from 0% (reference cell) to > 99% ($\sim$100 nm Tc layer). This indicates a sufficiently good surface passivation of c-Si wafers by Tc comparable to the passivation quality of the PEDOT:PSS/SiO_x/c-Si interface (cf. chapter 6).

An evaluation of $j(V)$-curves considering the impact of series resistance on solar cell fill factors indicates that there are no direct point contacts between PEDOT:PSS and c-Si for the 100 nm Tc device. This implies that holes can be transferred from c-Si across the Tc/c-Si interface and conducted through the Tc film to be extracted at the PEDOT:PSS front contact. This is in line with the Tc-HOMO/c-Si-VB offset, $\Delta E^{\mathrm{VB}}_{\mathrm{HOMO}}$ = (200 $\pm$ 200) meV, measured by UPS. The comparatively small offset, within the same order of magnitude as the a-Si:H/c-Si valence band offset present in high efficient inorganic SHJ solar cells (cf. chapter 4), should not impose a significant

barrier height for hole transport.

The key issue in the here proposed MEG device concept is to directly harvest non-emissive triplet excitons at the hybrid Tc/c-Si interface. Delayed fluorescence measurements prove the formation of long-lived triplet states via singlet fission in thin film Tc on cell relevant precursor layer stacks. However, no significant quenching of triplet lifetimes is observed and hence no evidence for triplet exciton harvesting at the Tc/c-Si interface is given. This is in accordance to EQE spectra which reveal an *"optical filter effect"* of Tc incorporated in hybrid devices. Although fitting of experimental EQE spectra within a basic singlet fission optical model may indicate very small current contributions related to light absorption in Tc with a total MEG parameter of $\eta_{MEG}^{Tc} \approx 10\%$[4], such small contributions cannot be adequately resolved with EQE analysis. Furthermore, no field-assisted exciton separation up to -2.0 V applied reverse bias and no indications for temperature-assisted exciton separation are detected within EQE studies.

Since experimental results reveal no clear evidence for a photocurrent contribution due to triplet harvesting at the Tc/c-Si interface, two interlayer approaches were tested:

(i) The implementation of an (i)a-Si:H passivation layer. Exciton dissociation rate might be facilitated by trapping triplets at localized mid-gap defect states in the exponential decaying DOS in the band tail of a-Si:H.
Operative hybrid PEDOT:PSS/Tc/(i)a-Si:H/c-Si solar cells are presented, although $j(V)$-curves with incorporated (i)a-Si:H exhibit strong s-shapes. A likely explanation therefore is the formation of a thick, insulating a-SiO_x layer as water in the PEDOT:PSS suspension and heat during the mandatory drying step provide favorable oxide growth conditions. EQE analysis reveals an *"optical filter effect"* of Tc.

(ii) The incorporation of an intermediate C_{60} layer. It is demonstrated in literature that triplets are dissociated at the Tc/C_{60} interface. Since the HOMO of Tc exhibits a large offset with respect to the VB of c-Si, C_{60} layers have to be ultra-thin for efficient hole extraction.
Absorption peaks of Tc coincide with maxima of the EQE ratio comparing C_{60} interlayer devices with a reference cell. This indicates a positive current contribution related to Tc. However, the effect is still very small and has to be confirmed with more sensitive experimental techniques.

EQE spectra of all hybrid devices reveal an *"optical filter effect"* of incorporated Tc layers. Analysis of EQE spectra is insufficiently robust to resolve possible small current contributions due to singlet fission in Tc and triplet exciton harvesting. The development of operative devices opens up the possibility to conduct sensitive magnetic field dependent photocurrent, $I(B)$, measurements in future. Due to the magnetic field dependence of the SF process itself, $I(B)$ measurements should allow to identify small current contributions of Tc to the total hybrid cell photocurrent. Furthermore, by the shape of $I(B)$, it is possible to differentiate between current contributions related to triplet or singlet exciton harvesting [328, 134] (see also section 2.3.1).

[4] η_{MEG}^{Tc} accounts for the SF efficiency, diffusion of created triplets to the interface and their dissociation

8 Conclusions and outlook

Photovoltaics (PV) is a fast growing industrial market. With silicon (Si) being the most abundant inorganic semiconductor material, it is dominated by crystalline Si (c-Si) wafer based technologies yielding more than 90% of the global market share in 2015 [99]. The current world record for single-junction c-Si based solar cells of 26.33% was reported in 2016 [91, 338]. Those very high efficiencies, already close to the fundamental single-junction limit of ∼30% [267, 243], can be achieved by charge selective and excellent passivated Si heterojunction (SHJ) contacts. Tolerable PV system costs scale with efficiency. About 1%-point efficiency gain allows ∼25% higher cell processing costs [206, 123]. Therefore, the development of high efficiency concepts is important. The objective of this work is to further exploit the already mature c-Si based PV technology. Three strategies are investigated:

1. Wide band gap a-SiO_x passivation layers in Si heterojunction solar cells

One drawback of the conventional SHJ solar cell technology is parasitic light absorption in the amorphous, hydrogenated Si (a-Si:H) layers in the front contacts[1] [129]. Thus, one possibility to further improve this high efficiency technology is to reduce the parasitic absorption by implementing wider band gap materials. Obviously a change of optical band gap modifies the band alignment at the heterojunction which is important for charge selectivity. Within the scope of this thesis, wide band gap amorphous Si sub-oxides (a-SiO_x:H) ranging from pure a-Si:H to near-stoichiometric a-SiO_2, were investigated. A continuous increase of the valence band offset starting from ΔE_V = 270 meV for the a-Si:H/c-Si to 4.3 eV for the a-SiO_2/c-Si heterointerface was determined. All layers reveal a sufficient surface passivation. Furthermore, SHJ solar cells with identically prepared passivation layers were fabricated allowing to relate ΔE_V to device efficiency. Rising ΔE_V causes an increased transport barrier for holes. This is reflected in decreasing solar cell fill factors. Although large valence band offsets constitute a general transport problem for SHJ solar cells, it is demonstrated that a stacked passivation layer approach, referred to as "staircase", mitigates the transport problem. Therefore, splitting the valence band offsets is

[1] relevant in both-side contacted device architectures

shown to be a promising concept for the incorporation of wide band gap Si alloys.

Outlook – In this work only a two-step "staircase" passivation layer stack was fabricated. However, a gradually varying amorphous Si alloy layer is another possible concept. Especially, the combination of medium band gap passivation with high band gap hole contact layers may allow the successful application of wide band gap Si alloys in SHJ solar cells. Recently, SHJ research interest has shifted towards the development of tunnel oxides and alternative charge carrier selective contact materials to improve efficiencies. Excellent passivating tunnel oxide layers can be grown by e.g. ozonized DI-water or by UV radiation induced photo oxidation [198, 199], thus omitting the more costly plasma enhanced chemical vapor deposition (PECVD) processes. Parasitic absorption in those ultra-thin layers is minimized due to their wide band gap and thickness of only $\sim$1 nm. Furthermore, high work function metal oxides like MoO_x or WoO_x were already successfully incorporated as hole selective contacts in SHJ solar cells replacing the p-doped a-Si:H layer [35, 24, 191]. In future works the obvious combination of both, SHJ solar cells with ultra-thin tunnel oxide passivation and high band gap metal oxide layers as the hole selective contact should be investigated.

2. Hybrid PEDOT:PSS/c-Si solar cells

The polymer PEDOT:PSS is commonly used as a hole selective contact in organic PV devices. Recently it was shown that PEDOT:PSS can also be successfully applied as a hole selective contact in c-Si based solar cells [232]. The hybrid PEDOT:PSS/(n)c-Si junction can be described as an abrupt p^+n-heterojunction giving rise to high open-circuit voltages (V_{oc}) [138]. Since PEDOT:PSS is highly conductive no transparent conductive oxide layer (TCO) is needed, as required for charge carrier extraction in conventional SHJ solar cells. As part of this work this novel PEDOT:PSS/(n)c-Si solar cell approach was investigated in great detail. A band diagram was constructed showing that c-Si is strongly inverted at the hybrid interface, thus providing a good selectivity. However, besides the proper band alignment of a heterojunction a good interface passivation is essential. PEDOT:PSS/(n)c-Si solar cells using planar, high quality wafers and a superior, well passivated electron selective back contact adopted from the conventional SHJ technology reach an efficiency of 14.8% with best V_{oc} of 663 mV. An interface recombination velocity of $\sim$400 cm/s at the hybrid PEDOT:PSS/c-Si interface was estimated. This corresponds well to the photoelectron spectroscopy study probing the buried interface. Device and spectroscopy results both indicate the formation of an interfacial, sub-stoichiometric and moderately passivating SiO_x layer. Moreover, it is observed that this SiO_x layer is not stable. Although when stored in an inert gas atmosphere its thickness and oxidation state increases with time which may deteriorate the initial electronic quality of the hybrid interface. Optical simulations point out the importance of optimized light management. Significant current losses of $\sim$4.6 mA/cm^2 due to parasitic absorption in PEDOT:PSS and $\sim$11.2 mA/cm^2 due to reflection at the planar hybrid layer stack are predicted.

Outlook – An enhanced passivation quality to reduce interface recombination losses and a long-term stability of the hybrid PEDOT:PSS/c-Si junction should be guaranteed by the incorporation of a well-defined, stoichiometric and stable SiO_2 tunnel oxide layer [279, 199, 97] grown be-

tween the polymer and the Si wafer. To minimize parasitic absorption losses PEDOT:PSS has to be fabricated as thin as possible while maintaining its electrical properties. Simultaneously, optimized anti-reflection layers, e.g. by the implementation of MoO_x or LiF layers, and the use of textured Si wafers are essential to minimize reflection losses.
Ultimately, the use of PEDOT:PSS is technologically interesting because fabrication does not require costly vacuum deposition methods and high-temperature processes. PEDOT:PSS layer fabrication is cheaply solution processed, is large area scalable, and only requires a low temperature annealing step below 150 °C . If further optimized, it could possibly compete with or replace ITO sputtering and a-Si PECVD processes needed for conventional SHJ solar cell fabrication.

3. Multi-exciton generating hybrid PEDOT:PSS/Tc/c-Si device concept

In the singlet fission (SF) process a singlet exciton, created by the absorption of a photon, is split into two triplet excitons with approximately half the energy of the initial excitation [276]. If those triplets can be harvested, SF-mediated multi-exciton generation (MEG) solar cells have the potential to overcome the fundamental single-junction limit by reducing thermalization losses [269]. The MEG device concept followed in this thesis is based on the direct harvesting of triplet excitons. Thus, the basic requirement is the diffusion of the triplets to an appropriate interface to be dissociated into free charges there. To the best of the author's knowledge, there is no report on the implementation of a SF material in c-Si based solar cells to date. In this work, thermally evaporated thin films of polycrystalline tetracene (Tc), being a promising SF material with triplet energies matching the band gap energy of c-Si [310] and a very high SF quantum yield with reported values close to 100% [47], could be incorporated in c-Si based hybrid devices. In the presented device architecture Tc is integrated between the (n)c-Si main absorber and the hole selective front contact PEDOT:PSS. Hybrid solar cells yield efficiencies above 10%. The constant V_{oc} of (645 $\pm$ 5) mV independent of Tc coverages ranging from 0% to >99% indicates a sufficiently good c-Si surface passivation comparable to the PEDOT:PSS/SiO_x/c-Si interface. Moreover, an efficient hole extraction from the c-Si absorber is observed for application relevant Tc layer thicknesses up to $\sim$100 nm. In a dynamic study conducted on various solar cell precursor layer stacks the formation of long-lived triplet states via SF is demonstrated, but no significant quenching of triplet lifetimes is observed. Hence, no evidence for triplet harvesting at the hybrid Tc/c-Si interface is given. This is in accordance to the external quantum efficiency (EQE) of PEDOT:PSS/Tc/c-Si solar cells in which light-absorption in Tc functions as an optical filter in the spectra. However, optical modeling of the EQE may indicate a small Tc contribution with $\eta_{MEG}^{Tc} \lesssim 10\%$[2].

Outlook – Within an EQE analysis such small effects related to triplet harvesting are not clearly resolvable, calling for more sensitive experimental analyzing methods to be conducted. One possibility, commonly used in literature, is to measure magnetic field modulated photocurrent changes. Those measurements should (i) be sensitive enough to resolve small current changes below 0.1%, and (ii) additionally enable to distinguish between singlet and triplet harvesting [134, 133, 64, 172, 328].

[2] η_{MEG}^{Tc} accounts for the SF efficiency, diffusion of created triplets to the interface and their dissociation

Lastly, it is important to keep in mind that for the realization of a MEG device –in this thesis via SF in thin film Tc– the MEG medium has obviously to be incorporated on the front side of the main absorber, here c-Si. This device architecture implies that for a successful implementation with an overall positive effect the photocurrent contribution due to MEG and triplet harvesting has to overcompensate the current losses in the c-Si main absorber caused by light absorption in the Tc layer. Results obtained so far reveal no, or only a very little share of exciton harvesting at the Tc/c-Si interface calling for further work on interface modification. It is reported that self-assembled monolayers (SAMs) can tune the work function at inorganic material surfaces significantly, e.g. Refs. [224, 168]. Therefore, the use of SAMs feature possible playgrounds for further modifications of the Tc/c-Si interface.
Ultimately, as pointed out by optical simulations, for the potential to overcome the fundamental single-junction limit, optical device optimization by means of suitable anti-reflection layers and surface structuring has to be ensured.

Abstract

The photovoltaic (PV) market is dominated by crystalline Si (c-Si) based solar cell technologies. Device efficiencies >26%, already close to the theoretical single-junction limit of ∼30%, have been reported. The work in this thesis aims to further reduce the costs of electricity of the already mature c-Si based PV technology by (i) increasing the efficiency by the incorporation of wide band gap contact layers, (ii) reducing costs by exploring new contact materials that can be processed at lower cost, and (iii) the implementation of multi-exciton generating (MEG) layers, thus featuring the potential to overcome the single-junction limit by reducing thermalization losses.

One possibility to improve highly efficient conventional Si heterojunction (SHJ) solar cells is to reduce parasitic absorption in the thin, hydrogenated amorphous Si (a-Si:H) layers by using wider band gap materials. In this work Si suboxides (a-SiO_x:H) within the full stoichiometry range ($0 \leq x \lesssim 2$) were investigated. A continuous increase of the valence band offset (ΔE_V) starting from ∼0.3 eV for the a-Si:H/c-Si to >4 eV for the a-SiO_2/c-Si heterointerface is determined. A decrease in SHJ solar cell fill factor coinciding with increasing ΔE_V at the a-SiO_x:H/c-Si interface is observed. The reason is an increasing barrier height for holes at the SHJ and a simultaneous change of the hole transport mechanism from thermionic emission to tunneling processes. Furthermore, it is demonstrated that as compared to a single layer, larger barrier heights can be tolerated in a stack of high band gap materials and a material with lower band gap, forming a *"staircase"* of band offsets. This may allow the application of wider band gap Si alloys in SHJ solar cells.

As an alternative hole selective contact to conventional inorganic SHJs, the highly conductive polymer PEDOT:PSS is a promising organic material forming a hybrid p^+n-heterojunction with n-type c-Si. The use of PEDOT:PSS is technologically interesting because it is cheaply solution processed. Hybrid PEDOT:PSS/c-Si/a-Si heterojunction solar cells with efficiencies up to 14.8% and high open-circuit voltages (V_{oc}) exceeding 660 mV are fabricated. A recombination velocity at the PEDOT:PSS/c-Si interface of $\nu_I \approx 400$ cm/s is estimated. Device and spectroscopy results indicate the formation of an interfacial, sub-stoichiometric and moderately passivating SiO_x layer at the c-Si surface. This limits V_{oc}. For planar devices with an optimal PEDOT:PSS layer thickness of 80 nm, optical simulations quantify significant photocurrent losses of 11.2 mA/cm^2 due to reflection at the hybrid layer stack and 4.6 mA/cm^2 related to parasitic absorption in the polymer. The results emphasize the importance of (i) an improved hybrid interface passivation quality, and (ii) an optimized light management to further increase PEDOT:PSS/c-Si device efficiencies.

A promising MEG concept is to take advantage of the singlet fission (SF) process in thin film tetracene (Tc) implemented on top of c-Si absorbers. In such a device high energy photons deposit their energy in the Tc film as singlet excitons. One singlet is then converted via SF into two triplets of lower energy. In order to contribute to the overall photocurrent, triplet excitons have to diffuse to an appropriate interface to be dissociated into free charges there. In the device concept presented in this thesis, Tc is incorporated in between the hole selective PEDOT:PSS and the c-Si main absorber. Hybrid solar cells yield efficiencies above 10%. The constant V_{oc} of (645 ± 5) mV independent of Tc surface coverage indicates a sufficiently good Tc/c-Si interface passivation. Efficient hole extraction from the c-Si absorber for application relevant Tc layer thicknesses up to ∼100 nm is demonstrated. However, based on delayed fluorescence measurements, no evidence for triplet harvesting at the Tc/c-Si interface is given. This is in accordance to external quantum efficiency (EQE) spectra which reveal an *"optical filter effect"* of Tc incorporated in hybrid devices. Optical modeling of the EQE may indicate a small Tc contribution with $\eta_{MEG}^{Tc} \lesssim 10\%^*$. Such small effects, which are not clearly resolvable within an EQE analysis, require (i) more sensitive experimental analyzing methods, and (ii) further work on interface modifications to be conducted in future.

$^*\eta_{MEG}^{Tc}$ accounts for the SF efficiency, triplet diffusion to the interface and their dissociation into free charges

Kurzfassung

Die Photovoltaikbranche (PV) wird von Technologien basierend auf kristallinem Silizium (c-Si) dominiert. Solarzellenwirkungsgrade >26% nahe des theoretischen Einfachzellenlimits von ∼30% wurden bereits erzielt. Ziel dieser Arbeit ist es die Stromerzeugungskosten der bereits ausgereiften c-Si basierten PV Technologie weiter zu senken. Dazu wurden drei Strategien verfolgt: (i) Effizienzsteigerung durch Implementierung von Kontaktschichten aus Materialien mit größerer Bandlücke. (ii) Produktionskostensenkung durch die Erforschung von neuartigen und kostengünstigeren Kontaktschichten. (iii) Verwendung von multi-Exziton generierenden (MEG) Schichten. Hierbei kann durch geringere Thermalisationsverluste das Einfachzellenlimit theoretisch übertroffen werden.

Durch die Implementierung von Materialien mit größeren Bandlücken können Absorptionsverluste in den dünnen, hydrogenisierten amorphen (a-Si:H) Schichten verringert werden, was die Effizienz konventioneller hocheffizienz Si-Heterokontakt (SHJ) Solarzellen steigern kann. In dieser Arbeit wurden Si-Suboxide (a-SiO_x:H) mit Stöchiometrien $0 \leq x \lesssim 2$ untersucht. Stetig steigende Valenzband-Diskontinuitäten (ΔE_V), beginnend bei ∼0,3 eV für den a-Si:H/c-Si bis >4 eV für den a-SiO_2/c-Si Heterokontakt, wurden bestimmt. Einhergehend mit steigender ΔE_V wurden sinkende Füllfaktoren an SHJ Solarzellen gemessen. Grund dafür ist eine erhöhte Transportbarriere für Löcher an der SHJ und eine damit einhergehende Änderung des zugrundeliegenden Ladungstransportmechanismus von thermionischer Emission hin zu Tunnelprozessen. Des Weiteren wurde gezeigt, dass –im Vergleich zu einem einfachen Heterokontakt– durch einen Mehrschicht-Heterokontaktstapel mit abgestuften Banddiskontinuitäten höhere Barrieren toleriert werden können. Dieser Ansatz könnte den Einsatz von Si Verbindungen mit größeren Bandlücken in SHJ Solarzellen ermöglichen.

Das hochleitfähige Polymer PEDOT:PSS ist eine vielversprechende Alternative zu konventionellen anorganischen Lochkontakten. Kürzlich wurde gezeigt, dass sich ein hybrider p^+n-Heterokontakt zwischen PEDOT:PSS und n-dotierten c-Si ausbildet. Die Prozessierung von PEDOT:PSS ist billig und lösungsmittelbasiert, was es zu einem vielversprechenden Material für die Solarzellenfertigung macht. Hybride PEDOT:PSS/c-Si/a-Si Heterokontakt-Solarzellen mit Wirkungsgraden bis zu 14,8% und hohen Leerlaufspannungen (V_{oc}) über 660 mV wurden hergestellt. Die Rekombinationsgeschwindigkeit an der PEDOT:PSS/c-Si Grenzfläche konnte auf $\nu_I \approx 400$ cm/s geschätzt werden. Zell- und Spektroskopieergebnisse deuten auf die Ausbildung einer sub-stöchiometrisch und moderat passivierenden SiO_x Grenzflächenschicht an der c-Si Oberfläche hin, was V_{oc} limitiert. Durch optische Simulationen an planaren Zellstrukturen konnten signifikante Photostromverluste von 11,2 mA/cm^2 durch Reflektion am hybriden Schichtstapel und 4,6 mA/cm^2 auf Grund parasitärer Absorption im Polymer quantifiziert werden. Die Ergebnisse zeigen, dass (i) eine verbesserte Grenzflächenpassivierung und (ii) ein optimiertes Lichtmanagement sichergestellt werden müssen um PEDOT:PSS/c-Si Zellwirkungsgrade weiter zu verbessern.

Ein vielversprechender MEG Ansatz ist die Ausnutzung des Singlet Fission (SF) Prozesses in dünnen Tetrazen (Tc) Schichten. Singlet Exzitonen werden durch Absorption hochenergetischer Photonen im Tc erzeugt. Durch SF werden aus einem Singlet zwei Triplets niedrigerer Energie generiert. Um zum Zellgesamtstrom beizutragen müssen Triplets zu einer geeigneten Grenzfläche diffundieren und dort in freie Ladungen aufgespaltet werden. In dem in dieser Arbeit verfolgten Ansatz wird Tc zwischen dem Loch selektiven PEDOT:PSS Vorderseitenkontakt und dem c-Si Hauptabsorber integriert. Hybride Solarzellen weisen einen Wirkungsgrad von über 10% auf. Die konstante V_{oc} von (645 ± 5) mV, unabhängig vom Tc Oberflächenbedeckungsgrad, deutet auf eine ausreichend gute Tc/c-Si Grenzflächenpassivierung hin. Es wurde gezeigt, dass im c-Si Absorber generierte Löcher bis zu einer anwendungsrelevanten Tc Schichtdicke von ∼100 nm effizient am Vorderseitenkontakt extrahiert werden können. Zeitaufgelöste Fluoreszenzmessungen ergaben jedoch keinen Hinweis auf Tripletspaltung an der Tc/c-Si Grenzfläche. Dies ist in Übereinstimmung mit externen Quanteneffizienz (EQE) Spektren, in welchen ein *"optischer Filtereffekt"* der in hybriden Zellen integrierten Tc Schichten beobachtet wurde. Optische Modellierung der EQE-Spektren deuten auf einen geringen Tc Beitrag mit $\eta_{MEG}^{Tc} \lesssim 10\%^*$ hin. Derart kleine Effekte können jedoch nicht eindeutig in einer EQE-Analyse aufgelöst werden. Deshalb müssen in zukünftigen Experimenten sensitivere Messmethoden angewendet werden. Die Untersuchung von potentiellen Grenzflächenmodifikationen für eine effiziente Tripletspaltung ist unumgänglich.

$^*\eta_{MEG}^{Tc}$ ergibt sich aus: SF-Effizienz, Diffusion der Triplets zur Grenzfläche und dessen Trennung in freie Ladungsträger

List of Symbols and Abbreviations

Symbols

A^{**}	effective Richardson constant
D_{it}	interface defect density
Δ	amplitude change angle of ellipsometry
ΔE_C	conduction band offset
ΔE_V	valence band offset
$\Delta E_{\mathrm{HOMO}}^{\mathrm{VB}}$	HOMO - valence band offset
Δn	excess carrier concentration (electrons)
Δp	excess carrier concentration (holes)
e	elementary charge: 1.6021766208(98) $\times$ 10^{-19} C
ϵ_0	permittivity in vacuum
ϵ_r	dielectric constant
η	efficiency
η_{FRET}	Förster resonance energy transfer efficiency
E_{bind}	binding energy
E_{ex}	excitation energy
E_F	Fermi level/edge
$E_{\mathrm{F,n}}$	quasi-Fermi level of electrons
$E_{\mathrm{F,p}}$	quasi-Fermi level of holes
E_{g}	band gap energy
E_I	intrinsic Fermi level
E_{kin}	kinetic energy
E_{kin}^0	constant final state kinetic energy
$E(\lambda)$	monochromatic illumination power density
$\mathrm{e}\varphi$	band bending
E_{phot}	photon energy
E_{vac}	vacuum level
$E_V^{\mathrm{a-Si}}$	valence band maximum of a-Si
E_{VBM}	valence band maximum
$E_V^{\mathrm{c-Si}}$	valence band maximum of c-Si
$E_{0\mathrm{V}}$	Urbach energy
$I_{\mathrm{tot}}^{\mathrm{CFSY}}\,(E_{\mathrm{kin}}^0, h\nu)$	photoelectron current
iV_{oc}	implied open-circuit voltage
j_{mpp}	current at maximum power point
j_{ph}	photocurrent density
j_{sc}	short-circuit current density delivered by a solar cell under illumination

$j(V)$ . . . . . current voltage characteristics
j_0 . . . . . recombination current density
$\vec{k}$ . . . . . wave vector
k_B . . . . . Boltzmann constant: 8.6173303(50) $\times$ 10^{-5} eV/K
k_{nrad} . . . . . non-radiative decay rate constant
k_{SF} . . . . . singlet fission rate constant
k_{TF} . . . . . triplet fusion rate constant
λ . . . . . wavelength
μ_h . . . . . hole mobility
μ_n . . . . . electron mobility
$\vec{n}$ . . . . . surface normal
N_C . . . . . effective density of states in the conduction band
N_D . . . . . doping concentration
n_d . . . . . ideality factor
$N_d(E)$ . . . . . defect distribution
n_{dark} . . . . . electron density in the dark
$n_{\mathrm{el}}(h\nu)$ . . . . . photoelectron flux
n_i . . . . . intrinsic carrier concentration
n_{illum} . . . . . electron density under illumination
$n_{\mathrm{phot}}(h\nu)$ . . . . . incident photoelectron flux
$n_{\mathrm{refl}}(h\nu)$ . . . . . reflected photoelectron flux
$n(t)$ . . . . . photon distribution
$N_V^t(E)$ . . . . . valence band tail
Φ_w . . . . . work function
Φ_{det} . . . . . work function of photoelectron detector
p_{illum} . . . . . hole density under illumination
P_{in} . . . . . incident power density
p_{dark} . . . . . hole density in the dark
Ψ_{bi} . . . . . built-in potential
Ψ_{el} . . . . . phase change angle of ellipsometry
Q_{it} . . . . . interface charge
R . . . . . reflectivity
R_c . . . . . contact resistance
r_c . . . . . Coulomb capture radius
R_s . . . . . series resistance
R_{sh} . . . . . shunt resistace
R_0 . . . . . Förster distance
$\tilde{r}$ . . . . . complex Fresnel reflection coefficient
σ_d^2 . . . . . Gaussian dangling bond distribution
σ_L . . . . . photoconductance
$SR(\lambda)$ . . . . . spectral response
τ_{Auger} . . . . . Auger lifetime
τ_{eff} . . . . . effective lifetime

τ_{rad} . . . . . radiative lifetime
τ_{SRH} . . . . . Shockley-Read-Hall lifetime
τ_{surface} . . . . . surface lifetime
V_{mpp} . . . . . voltage at maximum power point
V_{oc} . . . . . open-circuit voltage of a solar cell under illumination
V_{SPV} . . . . . photovoltage pulse
$V_{\mathrm{SPV,corr}}$ . . . . . Dember corrected photovoltage pulse
ν_I . . . . . interface recombination velocity
ν_S . . . . . surface recombination velocity
$Y_{\mathrm{int}}(E^0_{\mathrm{kin}}, h\nu)$ . . . internal photoelectron yield
χ . . . . . electron affinity

Abbreviations

A . . . . . absorption
A . . . . . acceptor
AFM . . . . . atomic force microscope
ALD . . . . . atomic layer deposition
AM1.5G . . . . . standard global air mass solar spectrum
AR . . . . . anti-reflex
AZO . . . . . aluminium doped zinc-oxide
a-Si . . . . . amorphous silicon
a-Si:H . . . . . hydrogenated amorphous silicon
a-SiO_x . . . . . amorphous silicon suboxide
a-SiO_x:H . . . . . amorphous silicon suboxide
BSF . . . . . back surface field
B_2H_6 . . . . . diborane
CB . . . . . conduction band
CFSYS . . . . . constant final state yield spectroscopy
CO_2 . . . . . carbon dioxide
CT . . . . . charge transfer
C_{60} . . . . . fullerene
c-Si . . . . . crystalline silicon
C-V . . . . . capacitance-voltage
D . . . . . donor
DB . . . . . dangling bond
DMSO . . . . . dimethyl sulfoxide
DFT . . . . . density functional theory
DOS . . . . . density of states
EBIC . . . . . electron beam-induced current
EQE . . . . . external quantum efficiency
ET . . . . . electron transfer

FF . . . . . fill factor
FRET . . . . . FÃ¶rster resonance energy transfer
HAXPES . . . . . hard X-ray photoelectron spectroscopy
HCT . . . . . hybrid charge transfer
HF . . . . . hydrofluoric acid
HIKE . . . . . high kinetic energy electron spectroscopy
HJ . . . . . heterojunction
HOMO . . . . . highest occupied molecular orbital
HT . . . . . hole transfer
IBC . . . . . interdigitated back contact
IL . . . . . inversion layer
IMPF . . . . . inelastic mean free path
IPES . . . . . inverse photoelectron spectroscopy
IRF . . . . . instrumental response function
ITO . . . . . indium tin oxide
IQE . . . . . internal quantum efficiency
KMC-1 . . . . . double crystal monochromator beamline at BESSY II
LUMO . . . . . lowest occupied molecular orbital
MEG . . . . . multi-exciton generation
MIS . . . . . metal-insulator-semiconductor
NC . . . . . nano crystals
ND . . . . . neutral density
OPV . . . . . organic photovoltaic
Pc . . . . . Pentacene
PCD . . . . . Photoconductance decay
PECVD . . . . . plasma enhanced chemical vapor deposition
PEDOT:PSS . . . . poly(2,4-ethylenedioxythiophene)-poly(styrene sulfonate)
PES . . . . . photoelectron spectroscopy
PH_3 . . . . . phosphine
PL . . . . . photoluminescence
PV . . . . . photovoltaics
QSSPC . . . . . quasi-steady-state photoconductance decay
R . . . . . reflection
RCA . . . . . standard cleaning process by Radio Company of America
RMS . . . . . root mean square
RT . . . . . room temperature
SAMs . . . . . self-assembled monolayers
SE . . . . . spectroscopic ellipsometry
SECO . . . . . secondary electron cutoff
SEM . . . . . scanning electron microscopy
SF . . . . . singlet fission
SHJ . . . . . silicon heterojunction
SiH_4 . . . . . silane

SiO_2 . . . . . silicon dioxide
SRH . . . . . Shockley-Read-Hall recombination
SPV . . . . . surface photovoltage
SSA . . . . . singlet-singlet annihilation
T . . . . . transmission
Tc . . . . . tetracene
TCSPC . . . . . time-correlated single photon counting
TCO . . . . . transparent conductive oxide
TE . . . . . thermionic emission
TEM . . . . . tunnel electron microscopy
TET . . . . . triplet energy transfer
TH . . . . . tunnel-hopping
TT . . . . . triplet transfer
$(T_1T_1)^l$ . . . . . correlated triplet pair state
UC . . . . . upconversion
UHV . . . . . ultra high vacuum
UPS . . . . . ultraviolet photoelectron spectroscopy
VB . . . . . valence band
XPS . . . . . X-ray photoelectron spectroscopy
XRD . . . . . X-ray diffraction

Bibliography

[1] Data Sheet No. 81076210, *CLEVIOS^{TM} PH 1000*, Heraeus Clevios GmbH, Leverkusen/Germany, 2010.

[2] Data Sheet No. 81098168, *CLEVIOS^{TM} S V 3 Stab*, Heraeus Clevios GmbH, Leverkusen/Germany, 2016.

[3] Data Sheet No. 81138655, *CLEVIOS^{TM} HTL Solar 3*, Heraeus Clevios GmbH, Leverkusen/Germany, 2016.

[4] A. G. Aberle, *Surface passivation of crystalline silicon solar cells: a review*, Progress in Photovoltaics: Research and Applications **8** (2000), 473.

[5] U.S. Energy Information Administration, *International Energy Outlook 2016*, published online, May 2016.

[6] V. Ai Dao, Y. Lee, S. Kim, J. Cho, S. Ahn, Y. Kim, N. Lakshminarayan, and J. Yi, *Effect of Valence Band Offset and Surface Passivation Quality in the Silicon Heterojunction Solar Cells*, Journal of The Electrochemical Society **158** (2011), H1129.

[7] H. Aibin, W. Wenwu, and X. Qiuxia, *$(NH_4)_2S$ treatment of the Si (100) surface and its effects on Al/Si Schottky barrier heights*, Journal of Semiconductors **30** (2009), 084001.

[8] S. Albrecht, S. Janietz, W. Schindler, J. Frisch, J. Kurpiers, J. Kniepert, S. Inal, P. Pingel, K. Fostiropoulos, N. Koch, and D. Neher, *Fluorinated Copolymer PCPDTBT with Enhanced Open-Circuit Voltage and Reduced Recombination for Highly Efficient Polymer Solar Cells*, Journal of the American Chemical Society **134** (2012), 14932.

[9] S. Albrecht, M. Saliba, J.-P. Correa-Baena, K. Jäger, L. Korte, A. Hagfeldt, M. Grätzel, and B. Rech, *Towards optical optimization of planar monolithic perovskite/silicon-heterojunction tandem solar cells*, Journal of Optics **18** (2016), 064012.

[10] S. Albrecht, M. Saliba, J. P. Correa Baena, F. Lang, L. Kegelmann, M. Mews, L. Steier, A. Abate, J. Rappich, L. Korte, R. Schlatmann, M. K. Nazeeruddin, A. Hagfeldt, M. Grätzel, and B. Rech, *Monolithic perovskite/silicon-heterojunction tandem solar cells processed at low temperature*, Energy & Environmental Science **9** (2016), 81.

[11] A. P. Alivisatos, M. F. Arndt, S. Efrima, D. H. Waldeck, and C. B. Harris, *Electronic energy transfer at semiconductor interfaces. I. Energy transfer from two-dimensional molecular films to Si(111)*, The Journal of Chemical Physics **86** (1987), 6540.

[12] I. An, H. Arwin, C. Chen, R. W. Collins, A. S. Ferlauto, J. N. Hilfiker, J. Humlicek, E. A. Irene, G. E. Jellison, J. Lee, F. A. Modine, A. Röseler, M. Schubert, H. G. Tompkins, and J. A. Zapien, *Handbook of Ellipsometry*, William Andrew Publishing/Springer, 2005.

[13] H. Angermann, W. Henrion, M. Rebien, K. Kliefoth, D. Fischer, and J.-T. Zettler, *Evolution of electronically active defects during the formation of SiSiO2 interface monitored by combined surface photovoltage and spectroscopic ellipsometry measurements*, Microelectronic Engineering **36** (1997), 43.

[14] H. Angermann, W. Henrion, A. Röseler, and M. Rebien, *Wet-chemical passivation of Si(111)- and Si(100)-substrates*, Materials Science and Engineering: B **73** (2000), 178.

[15] D. H. Arias, J. L. Ryerson, J. D. Cook, N. H. Damrauer, and J. C. Johnson, *Polymorphism influences singlet fission rates in tetracene thin films*, Chemical Science **7** (2016), 1185.

[16] A. J. Arvia and R. C. Salvarezza, *An Interdisciplinary Approach to the Electrochemistry at Solid Electrodes*, Journal of the Brazilian Chemical Society **8** (1997), 91.

[17] N. W. Ashcroft and N. Mermin, *Solid State Physics*, Saunders College, 1976.

[18] A. Avila, I. Montero, L. Galán, J. M. Ripalda, and R. Levy, *Behavior of oxygen doped SiC thin films: An x-ray photoelectron spectroscopy study*, Journal of Applied Physics **89** (2001), 212.

[19] H. Baessler, G. Herrmann, N. Riehl, and G. Vaubel, *Space-charge-limited currents in tetracene single-crystals*, Journal of Physics and Chemistry of Solids **30** (1969), 1579.

[20] N. Bansal, L. X. Reynolds, A. MacLachlan, T. Lutz, R. S. Ashraf, W. Zhang, C. B. Nielsen, I. McCulloch, D. G. Rebois, T. Kirchartz, M. S. Hill, K. C. Molloy, J. Nelson, and S. A. Haque, *Influence of Crystallinity and Energetics on Charge Separation in Polymer–Inorganic Nanocomposite Films for Solar Cells*, Scientific Reports **3** (2013), 1531.

[21] C. J. Bardeen, *The Structure and Dynamics of Molecular Excitons*, Annual Review of Physical Chemistry **65** (2014), 127.

[22] C. J. Bardeen, *Triplet excitons: Bringing dark states to light*, nature materials **13** (2014), 1001.

[23] C. Battaglia, A. Cuevas, and S. De Wolf, *High-efficiency crystalline silicon solar cells: status and perspectives*, Energy & Environmental Science **9** (2016), 1552.

[24] C. Battaglia, S. M. de Nicolás, S. De Wolf, X. Yin, M. Zheng, C. Ballif, and A. Javey, *Silicon heterojunction solar cell with passivated hole selective MoO_x contact*, Applied Physics Letters **104** (2014), 113902.

[25] E. Bauer, *Phänomenologische Theorie der Kristallabscheidung an Oberflächen. I*, Zeitschrift fur Kristallographie **110** (1958), 372.

[26] K. E. Bean, *Anisotropic etching of silicon*, IEEE Transactions on Electron Devices **25** (1978), 1185.

[27] M. C. Beard, *Multiple Exciton Generation in Semiconductor Quantum Dots*, The Journal of Physical Chemistry Letters **2** (2011), 1282.

[28] M. C. Beard, J. C. Johnson, J. M. Luther, and A. J. Nozik, *Multiple exciton generation in quantum dots versus singlet fission in molecular chromophores for solar photon conversion*, Philosophical Transactions of the Royal Society of London A **373** (2015), 20140412.

[29] M. C. Beard, K. P. Knutsen, P. Yu, J. M. Luther, Q. Song, W. K. Metzger, R. J. Ellingson, and A. J. Nozik, *Multiple Exciton Generation in Colloidal Silicon Nanocrystals*, Nano Letters **7** (2007), 2506.

[30] W. Becker, *Advanced Time-Corelated Single Photon Counting Techniques*, Springer, Berlin, 2005.

[31] ———, *The bh TCSPC Handbook*, Becker & Hickl GmbH, Berlin, 2015.

[32] T. Bekkay, E. Sacher, and A. Yelon, *Surface reaction during the argon ion sputter cleaning of surface oxidized crystalline silicon (111)*, Surface Science **217** (1989), L377.

[33] D. Bertho and C. Jouanin, *Polaron and bipolaron excitations in doped polythiophene*, Physical Review B **35** (1987), 626.

[34] J. Bian, L. Zhang, W. Guo, D. Wang, F. Meng, and Z.n Liu, *Improved passivation effect at the amorphous/crystalline silicon interface due to ultrathin SiO_x layers pre-formed in chemical solutions*, Applied Physics Express **7** (2014), 065504.

[35] M. Bivour, J. Temmler, H. Steinkemper, and M. Hermle, *Molybdenum and tungsten oxide: High work function wide band gap contact materials for hole selective contacts of silicon solar cells*, Solar Energy Materials and Solar Cells **142** (2015), 34.

[36] M. Boccard and Z. C. Holman, *Amorphous silicon carbide passivating layers for crystalline-silicon-based heterojunction solar cells*, Journal of Applied Physics **118** (2015), 065704.

[37] C. L. Braun, *Electric field assisted dissociation of charge transfer states as a mechanism of photocarrier production*, The Journal of Chemical Physics **80** (1984), 4157.

[38] J. L. Brédas, F. Wudl, and A. J. Heeger, *Polarons and bipolarons in doped polythiophene: A theoretical investigation*, Solid State Communications **63** (1987), 577.

[39] J. L. Brédas, B. Thémans, J. G. Fripiat, J. M. André, and R. R. Chance, *Highly conducting polyparaphenylene, polypyrrole, and polythiophene chains: An ab initio study of the geometry and electronic-structure modifications upon doping*, Physical Review B **29** (1984), 6761.

[40] T. M. Brown, C. Bittencourt, M. Sebastiani, and F. Evangelisti, *Electronic states and band lineups in c-Si(100)/a-*$Si_{1-x}C_x$*:H heterojunctions*, Physical Review B **55** (1997), 9904.

[41] D. A. G. Bruggemann, *Dielektrizitätskonstanten und Leitfähigkeiten der Mischkörper aus isotropen und anisotropen Substanzen*, Annalen der Physik **5** (1935), 636.

[42] O. Bubnova, Z. U. Khan, H. Wang, S. Braun, D. R. Evans, M. Fabretto, P. Hojati-Talemi, D. Dagnelund, J.-B. Arlin, Y. H. Geerts, S. Desbief, D. W. Breiby, J. W. Andreasen, R. Lazzaroni, W. M. Chen, I. Zozoulenko, M. Fahlman, P. J. Murphy, M. Berggren, and X. Crispin, *Semi-metallic polymers*, nature materials **13** (2014), 190.

[43] J. Bullock, Y. Wan, M. Hettick, J. Geissbühler, A. J. Ong, D. Kiriya, D. Yan, T. Allen, J. Peng, X. Zhang, C. M. Sutter-Fella, S. De Wolf, C. Ballif, A. Cuevas, and A. Javey, *Survey of Dopant-Free Carrier-Selective Contacts for Silicon Solar Cells*, IEEE conference proceedings PVSEC43 (2016), 210.

[44] J. J. Burdett and C. J. Bardeen, *Quantum Beats in Crystalline Tetracene Delayed Fluorescence Due to Triplet Pair Coherences Produced by Direct Singlet Fission*, Journal of the American Chemical Society **134** (2012), 8597.

[45] ———, *The Dynamics of Singlet Fission in Crystalline Tetracene and Covalent Analogs*, Accounts of Chemical Research **46** (2013), 1312.

[46] J. J. Burdett, D. Gosztola, and C. J. Bardeen, *The dependence of singlet exciton relaxation on excitation density and temperature in polycrystalline tetracene thin films: Kinetic evidence for a dark intermediate state and implications for singlet fission*, The Journal of Chemical Physics **135** (2011), 214508.

[47] J. J. Burdett, A. M. Müller, D. Gosztola, and C. J. Bardeen, *Excited state dynamics in solid and monomeric tetracene: The roles of superradiance and exciton fission*, The Journal of Chemical Physics **133** (2010), 144506.

[48] J. J. Burdett, G. B. Piland, and C. J. Bardeen, *Magnetic field effects and the role of spin states in singlet fission*, Chemical Physics Letters **585** (2013), 1.

[49] G. F. Burkhard, E. T. Hoke, Z. M. Beiley, and M. D. McGehee, *Free Carrier Generation in Fullerene Acceptors and Its Effect on Polymer Photovoltaics*, The Journal of Physical Chemistry C **116** (2012), 26674.

[50] F. Bussolotti, S. Kera, K. Kudo, A. Kahn, and N. Ueno, *Gap states in Pentacene Thin Film Induced by Inert Gas Exposure*, Physical Review Letters **110** (2013), 267602.

[51] F. Bussolotti, J. Yang, A. Hinderhofer, Y. Huang, W. Chen, S. Kera, A. T. S. Wee, and N. Ueno, *Origin of the energy level alignment at organic/organic interfaces: The role of structural defects*, Physical Review B **89** (2014), 115319.

[52] I. H. Campbell and B. K. Crone, *Improving an organic photodiode by incorporating a tunnel barrier between the donor and acceptor layers*, Applied Physics Letters **101** (2012), 023301.

[53] W.-L. Chan, M. Ligges, A. Jailaubekov, L. Kaake, L. Miaja-Avila, and X.-Y. Zhu, *Observing the Multiexciton State in Singlet Fission and Ensuing Ultrafast Multielectron Transfer*, Science **334** (2011), 1541.

[54] W.-L. Chan, M. Ligges, and X.-Y. Zhu, *The energy barrier in singlet fission can be overcome through coherent coupling and entropic gain*, nature chemistry **4** (2012), 840.

[55] W.-L. Chan, J. R. Tritsch, and X.-Y. Zhu, *Harvesting Singlet Fission for Solar Energy Conversion: One- versus Two-Electron Transfer from the Quantum Mechanical Superposition*, Journal of the American Chemical Society **134** (2012), 18295.

[56] D. M. Chapin, C. S. Fuller, and G. L. Pearson, *A New Silicon p-n Junction Photocell for Converting Solar Radiation into Electrical Power*, Journal of Applied Physics **25** (1954), 676.

[57] Z. Chen, S. K. Pang, K. Yasutake, and A. Rohatgi, *Plasma-enhanced chemical-vapor-deposited oxide for low surface recombination velocity and high effective lifetime in silicon*, Journal of Applied Physics **74** (1993), 2856.

[58] T.-R. Chou, S.-H. Chen, Y.-T. Chiang, Y.-T. Lin, and C.-Y. Chao, *Highly conductive PEDOT:PSS films by post-treatment with dimethyl sulfoxide for ITO-free liquid crystal display*, Journal of Materials Chemistry C **3** (2015), 3760.

[59] T. M. Clarke and J. R. Durrant, *Charge Photogeneration in Organic Solar Cells*, Chemical Reviews **110** (2010), 6736.

[60] M. W. M. van Cleef, F. A. Rubinelli, R. Rizzoli, R. Pinghini, R. E. I. Schropp, and W. F. van der Weg, *Amorphous Silicon Carbide/Crystalline Silicon Heterojunction Solar Cells: A Comprehensive Study of the Photocarrier Collection*, Japanese Journal of Applied Physics **37** (1998), 3926.

[61] G. Cody, T. Tiedje, B. Abeles, B. Brooks, and Y. Goldstein, *Disorder and the Optical-Absorption Edge of Hydrogenated Amorphous Silicon*, Physical Review Letters **47** (1981), 1480.

[62] G. D. Cody, *Urbach Edge, Disorder, and Absorption On-set in a-Si:H*, MRS Proceedings **862** (2005), A1.3.

[63] A. Colsmann, M. Reinhard, T.-H. Kwon, C. Kayser, F. Nickel, J. Czolk, U. Lemmer, N. Clark, J. Jasieniak, A. B. Holmes, and D. Jones, *Inverted semi-transparent organic solar cells with spray coated, surfactant free polymer top-electrodes*, Solar Energy Materials and Solar Cells **98** (2012), 118.

[64] D. N. Congreve, J. Lee, N. J. Thompson, E. Hontz, S. R. Yost, P. D. Reusswig, M. E. Bahlke, S. Reineke, T. Van Voorhis, and M. A. Baldo, *External Quantum Efficiency Above 100% in a Singlet-Exciton-Fission–Based Organic Photovoltaic Cell*, Science **340** (2013), 334.

[65] R. S. Crandall, E. Iwaniczko, J. V. Li, and M. R. Page, *A comprehensive study of hole collection in heterojunction solar cells*, Journal of Applied Physics **112** (2012), 093713.

[66] A. Cuevas, *The Recombination Parameter J_0*, Energy Procedia **55** (2014), 53.

[67] L. Danos, R. Greef, and T. Markvart, *Efficient fluorescence quenching near crystalline silicon from Langmuir-Blodgett dye films*, Thin Solid Films **516** (2008), 7251.

[68] A. Datta, M. Rahmouni, M. Nath, R. Boubekri, P. Roca i Cabarrocas, and P. Chatterjee, *Insights gained from computer modeling of heterojunction with instrinsic thin layer "HIT" solar cells*, Solar Energy Materials and Solar Cells **94** (2010), 1457.

[69] S. Dauwe, J. Schmidt, and R. Hezel, *Very low surface recombination velocities on p- and n-type silicon wafers passivated with hydrogenated amorphous silicon films*, Conference Record of the 29^{th} IEEE (2002), 1246.

[70] A. S. Davydov, *Theory of Molecular Excitons*, Plenum Press, New York, 1971.

[71] C. G. Van de Walle and L. H. Yang, *Band discontinuities at heterojunctions between crystalline and amorphous silicon*, Journal of Vacuum Science and Technology B **13** (1995), 1635.

[72] S. De Wolf, A. Descoeudres, Z. C. Holman, and C. Ballif, *High-efficiency silicon heterojunction solar cells: A review*, Green **2** (2012), 7.

[73] S. De Wolf and M. Kondo, *Abruptness of a-Si:H/c-Si interface revealed by carrier lifetime measurements*, Applied Physics Letters **90** (2007), 042111.

[74] ———, *Nature of doped a-Si:H/c-Si interface recombination*, Journal of Applied Physics **105** (2009), 103707.

[75] S. De Wolf, S. Olibet, and C. Ballif, *Stretched-exponential a-Si:H/c-Si interface recombination decay*, Applied Physics Letters **93** (2008), 032101.

[76] C. Deetuam, D. Weise, C. Samthong, P. Praserthdam, R. R. Baumann, and A. Somwangthanaroj, *Electrical conductivity enhancement of spin-coated PEDOT:PSS thin film via dipping method in low concentration aqueous DMSO*, Journal of Applied Polymer Science **132** (2015), 1.

[77] C. Deibel, T. Strobel, and V. Dyakonov, *Role of the Charge Transfer State in Organic Donor-Acceptor Solar Cells*, Advanced Materials **22** (2010), 4097.

[78] B. Demaurex, S. De Wolf, A. Descoeudres, Z. Charles Holman, and C. Ballif, *Damage at hydrogenated amorphous/crystalline silicon interfaces by indium tin oxide overlayer sputtering*, Applied Physics Letters **101** (2012), 171604.

[79] H. Dember, *Über eine photoelektronische Kraft in Kupferoxydul-Kristallen*, Physikalische Zeitschrift **32** (1931), 554.

[80] A. Descoeudres, L. Barraud, S. De Wolf, B. Strahm, D. Lachenal, C. Guérin, Z. C. Holman, F. Zicarelli, B. Demaurex, J. Seif, J. Holovsky, and C. Ballif, *Improved amorphous/crystalline silicon interface passivation by hydrogen plasma treatment*, Applied Physics Letters **99** (2011), 123506.

[81] D. L. Dexter, *A Theory of Sensitized Luminescence in Solids*, The Journal of Chemical Physics **21** (1953), 836.

[82] D. L. Dexter, *Two ideas on energy transfer phenomena: Ion-pair effects involving the OH stretching mode, and sensitization of photovoltaic cells*, Journal of Luminescence **18** (1979), 779.

[83] K. Ding, U. Aeberhard, F. Finger, and U. Rau, *Optimized amorphous silicon oxide buffer layers for silicon heterojunction solar cells with microcrystalline silicon oxide contact layers*, Journal of Applied Physics **113** (2013), 134501.

[84] J. Dziewior and W. Schmid, *Auger coefficients for highly doped and highly excited silicon*, Applied Physics Letters **31** (1977), 346.

[85] M. Edwards, S. Bowden, U. Das, and M. Burrows, *Effect of texturing and surface preparation on lifetime and cell performance in heterojunction silicon solar cells*, Solar Energy Materials and Solar Cells **92** (2008), 1373.

[86] B. Ehrler, K. P. Musselman, M. L. Böhm, R. H. Friend, and N. C. Greenham, *Hybrid pentacene/a-silicon solar cells utilizing multiple carrier generation via singlet exciton fission*, Applied Physics Letters **101** (2012), 153507.

[87] B. Ehrler, B. J. Walker, M. L. Böhm, M. W. B. Wilson, Y. Vaynzof, R. H. Friend, and N. C. Greenham, *In situ measurement of exciton energy in hybrid singlet-fission solar cells*, nature communications **3** (2012), 1019.

[88] B. Ehrler, M. W. B. Wilson, A. Rao, R. H. Friend, and N. C. Greenham, *Singlet Exciton Fission-Sensitized Infrared Quantum Dot Solar Cells*, Nano Letters **12** (2012), 1053.

[89] F. Einsele, W. Beyer, and U. Rau, *Analysis of sub-stoichiometric hydrogenated silicon oxide films for surface passivation of crystalline silicon solar cells*, Journal of Applied Physics **112** (2012), 054905.

[90] A. Elschner, S. Kirchmeyer, W. Lovenich, U. Merker, and K. Reuter, *PEDOT: Principles and Applications of an Intrinsically Conductive Polymer*, CRC Press, 2010.

[91] New Energy and Kaneka Corporation Industrial Technology Developement Organization (NEDO), *World's Highest Conversion Efficiency of 26.33% Achieved in a Crystalline Silicon Solar Cell - A World First in a Practical Cell Size* -, press release, 14-09-2016.

[92] A. S. Erickson, A. Zohar, and D. Cahen, *n-si-organic inversion layer interfaces: A low temperature deposition method for forming a p-n homojunction in n-si*, Advanced Energy Materials **4** (2014), 1301724.

[93] V. Ern and R. E. Merrifield, *Magnetic Field Effect on Triplet Exciton Quenching in Organic Crystals*, Physical Review Letters **21** (1968), 609.

[94] J. M. Essick, Z. Nobel, Y.-M. Li, and M. S. Bennett, *Conduction- and valence-band offsets at the hydrogenated amorphous silicon-carbon/crystalline silicon interface via capacitance techniques*, Physical Review B **54** (1996), 4885.

[95] L. Fang, N. Alderman, L. Danos, and T. Markvart, *Silicon sensitisation using light harvesting layers*, Materials Research Innovations **18** (2014), 494.

[96] L. Fang, K. S. Kiang, N. P. Alderman, L. Danos, and T. Markvart, *Photon tunneling into a single-mode planar silicon waveguide*, Optical Express **23** (2015), A1528.

[97] F. Feldmann, M. Simon, M. Bivour, C. Reichel, M. Hermle, and S. W. Glunz, *Carrier-selective contacts for Si solar cells*, Applied Physics Letters **104** (2014), 181105.

[98] Fraunhofer Institute for Solar Energy Systems, *New world record for solar cell efficiency at 46%*, press release, 01-12-2014.

[99] _____, *Photovoltaics Report*, published online, updated: 06-06-2016.

[100] F. C. Frank and J. H. van der Merwe, *One-Dimensional Dislocations. I. Static Theory*, Proceedings of the Royal Society of London A **198** (1949), 205.

[101] T. Förster, *Zwischenmolekulare Energiewanderung und Fluoreszenz*, Annalen der Physik **437** (1948), 55.

[102] H. Fujiwara, T. Kaneko, and M. Kondo, *Application of hydrogenated amorphous silicon oxide layers to c-Si heterojunction solar cells*, Applied Physics Letters **91** (2007), 133508.

[103] H. Fujiwara and M. Kondo, *Real-time monitoring and process control in amorphous/crystalline silicon heterojunction solar cells by spectroscopic ellipsometry and infrared spectroscopy*, Applied Physics Letters **86** (2005), 032112.

[104] _____, *Effects of a-Si:H layer thicknesses on the performance of a-Si:H/c-Si heterojunction solar cells*, Journal of Applied Physics **101** (2007), 054516.

[105] _____, *Impact of epitaxial growth at the heterointerface of a-Si:H/c-Si solar cells*, Applied Physics Letters **90** (2007), 013503.

[106] K. M. Gad, D. Vössing, P. Balamou, D. Hiller, B. Stegemann, H. Angermann, and M. Kasemann, *Improved Si/SiO$_x$ interface passivation by ultra-thin tunneling oxide layers prepared by rapid thermal oxidation*, Applied Surface Science **353** (2015), 1269.

[107] N. Geacintov, M. Pope, and F. Vogel, *Effect of Magnetic Field on the Fluorescence of Tetracene Crystals: Exciton Fission*, Physical Review Letters **22** (1969), 593.

[108] J. Geissbühler, J. Werner, S. Martin de Nicolas, L. Barraud, A. Hessler-Wyser, M. Despeisse, S. Nicolay, A. Tomasi, B. Niesen, S. De Wolf, and C. Ballif, *22.5% efficient silicon heterojunction solar cell with molybdenum oxide hole collector*, Applied Physics Letters **107** (2015), 081601.

[109] S. W. Glunz, F. Feldmann, A. Richter, M. Bivour, C. Reichel, H. Steinkemper, J. Benick, and M. Hermle, *The Irresistible Charm of a Simple Current Flow Pattern – 25% with a Solar Cell Featuring a Full-Area Back Contact*, 31st European Photovoltaic Solar Energy Converence and Exhibition (2015), 259.

[110] M. Gohlke, *Documentation of APCSA Program*, Soft-Matter Group, University of Potsdam, 2012.

[111] M. Gorgoi, S. Svensson, F. Schäfers, G. Öhrwall, M. Mertin, P. Bressler, O. Karis, H. Siegbahn, A. Sandell, H. Rensmo, W. Doherty, C. Jung, W. Braun, and W. Eberhardt, *The high kinetic energy photoelectron spectroscopy facility at BESSY progress and first results*, Nuclear Instruments and Methods in Physics Research Section A: Accelerators, Spectrometers, Detectors and Associated Equipment **601** (2009), 48.

[112] K. R. Graham, P. Erwin, D. Nordlund, K. Vandewal, R. Li, G. O. Ngongang Ndjawa, E. T. Hoke, A. Salleo, M. E. Thompson, M. D. McGehee, and A. Amassian, *Re-evaluating the Role of Sterics and Electronic Coupling in Determining the Open-Circuit Voltage of Organic Solar Cells*, Advanced Materials **25** (2013), 6076.

[113] G. Greczynski, T. Kugler, M. Keil, W. Osikowicz, M. Fahlman, and W. R. Salaneck, *Photoelectron spectroscopy of thin films of PEDOT-PSS conjugated polymer blend: a mini-review and some new results*, Journal of Electron Spectroscopy and Related Phenomena **121** (2001), 1.

[114] M. A. Green, *Limits on the open-circuit voltage and efficiency of silicon solar cells imposed by intrinsic Auger processes*, IEEE Transactions on Electron Devices **31** (1984), 671.

[115] ———, *Third Generation Photovoltaics: Advanced Solar Energy Conversion*, Springer, Heidelberg, 2003.

[116] D. Gräf, M. Grundner, R. Schulz, and L. Mühlhoff, *Oxidation of HF-treated Si wafer surfaces in air*, Journal of Applied Physics **68** (1990), 5155.

[117] R. N. Hall, *Electron-Hole Recombination in Germanium*, Physical Review **87** (1952), 387.

[118] User Handbook, *16-Channel TCSPC / FLIM Detectors*, Becker & Hickl GmbH, Berlin, 2016.

[119] M. C. Hanna and A. J. Nozik, *Solar conversion efficiency of photovoltaic and photoelectrolysis cells with carrier multiplication absorbers*, Journal of Applied Physics **100** (2006), 074510.

[120] B. Harbecke, *Coherent and incoherent reflection and transmission of multilayer structures*, Applied Physics B **39** (1986), 165.

[121] J. Haschke, N. Mingirulli, and B. Rech, *Progress in Point Contacted Rear Silicon Heterojunction Solar Cells*, Energy Procedia **27** (2012), 116.

[122] K. Heilig, *Determination of doping factor, mobility ratio and excess concentration using photovoltages at extreme band bendings*, Solid-State Electronics **21** (1978), 975.

[123] M. Hermle, *Silicon solar cells – current production and future concepts*, Fraunhofer Institute for Solar Energy Systems ISE; talk at BESSY II Foreseight Workshop on Energy Materials Research, Berlin, 10-10-2016.

[124] S. Hüfner, *Photoelectron Spectroscopy - Principles and Applications*, Springer, Berlin, 2003.

[125] I. G. Hill, A. J. Mäkinen, and Z. H. Kafafi, *Initial stages of metal/organic semiconductor interface formation*, Journal of Applied Physics **88** (2000), 889.

[126] F. J. Himpsel, F. R. McFeely, A. Taleb-Ibrahimi, J. A. Yarmoff, and G. Hollinger, *Microscopic structure of the* SiO_2*/Si interface*, Physical Review B **38** (1988), 6084.

[127] T. Hänel, *Spannungs- und Intensitätsabhängige spektrale Empfindlichkeit von poly-Si Dünnschichtsolarzellen*, Diploma thesis, Fachhochschule für Technik und Wirtschaft Berlin, 2008.

[128] W. Hofberger, *Structure and optical properties of polycrystalline evaporated tetracene films*, physica status solidi (a) **30** (1975), 271.

[129] Z. C. Holman, A. Descoeudres, L. Barraud, F. Z. Fernandez, J. P. Seif, S. De Wolf, and C. Ballif, *Current Losses at the Front of Silicon Heterojunction Solar Cells*, IEEE Journal of Photovoltaics **2** (2012), 7.

[130] Z. C. Holman, M. Filipič, A. Descoeudres, S. De Wolf, F. Smole, M. Topič, and C. Ballif, *Infrared light management in high-efficiency silicon heterojunction and rear-passivated solar cells*, Journal of Applied Physics **113** (2013), 013107.

[131] J. Huang, P. F. Miller, J. S. Wilson, A. J. deMello, J. C. deMello, and D. D. C. Bradley, *Investigation of the Effects of Doping and Post-Deposition Treatments on the Conductivity, Morphology, and Work Function of Poly(3,4-ethylenedioxythiophene)/Poly(styrene sulfonate) Films*, Advanced Functional Materials **15** (2005), 290.

[132] J. Hwang, F. Amy, and A. Kahn, *Spectroscopic study on sputtered PEDOT PSS: Role of surface PSS layer*, Organic Electronics **7** (2006), 387.

[133] P. J. Jadhav, P. R. Brown, N. Thompson, B. Wunsch, A. Mohanty, S. R. Yost, E. Hontz, T. Van Voorhis, M. G. Bawendi, V. Bulovic, and M. A. Baldo, *Triplet Exciton Dissociation in Singlet Exciton Fission Photovoltaics*, Advanced Materials **24** (2012), 6169.

[134] P. J. Jadhav, A. Mohanty, J. Sussman, J. Lee, and M. A. Baldo, *Singlet Exciton Fission in Nanostructured Organic Solar Cells*, Nano Letters **11** (2011), 1495.

[135] K. Jäger, C. Barth, M. Hammerschmidt, S. Herrmann, S. Burger, F. Schmidt, and C. Becker, *Simulations of sinusoidal nanotextures for coupling light into c-Si thin-film solar cells*, Optics Express **24** (2016), A569.

[136] S. Jäckle, M. Liebhaber, C. Gersmann, M. Mews, K. Jäger, S. Christiansen, and K. Lips, *Potential of PEDOT:PSS as a hole selective front contact for silicon heterojunction solar cells*, `http://arxiv.org/abs/1701.05368` (2017).

[137] S. Jäckle, M. Liebhaber, J. Niederhausen, M. Büchele, R. Félix, R. G. Wilks, M. Bär, K. Lips, and S. Christiansen, *Unveiling the Hybrid n-Si/PEDOT:PSS Interface*, ACS Applied Materials & Interfaces **8** (2016), 8841.

[138] S. Jäckle, M. Mattiza, M. Liebhaber, G. Brönstrup, M. Rommel, K. Lips, and S. Christiansen, *Junction formation and current transport mechanisms in hybid n-Si/PDEOT:PSS solar cells*, Scientific Reports **5** (2015), 13008.

[139] G. E. Jellison and F. A. Modine, *Parameterization of the optical functions of amorphous materials in the interband region*, Applied Physics Letters **69** (1996), 371.

[140] N. Jensen, R. M. Hausner, R. B. Bergmann, J. H. Werner, and U. Rau, *Optimization and Characterization of Amorphous/Crystalline Silicon Heterojunction Solar Cells*, Progress in Photovoltaics: Research and Applications **10** (2002), 1.

[141] H. Jeong, H. Song, Y. Pak, I. K. Kwon, K. Jo, H. Lee, and G. Y. Jung, *Enhanced Light Absorption of Silicon Nanotube Arrays for Organic/Inorganic Hybrid Solar Cells*, Advanced Materials **26** (2014), 3445.

[142] S. Jeong, E. C. Garnett, S. Wang, Z. Yu, S. Fan, M. L. Brongersma, M. D. McGehee, and Y. Cui, *Hybrid Silicon Nanocone-Polymer Solar Cells*, Nano Letters **12** (2012), 2971.

[143] K. Jäger, *On the Scalar Scattering Theory for Thin-Film Solar Cells*, Ph.D. thesis, Delft University of Technology, 2012.

[144] K. Jäger, M. Fischer, R. A. C. M. M. van Swaaij, and M. Zeman, *A scattering model for nano-textured interfaces and its application in opto-electrical simulations of thin-film silicon solar cells*, Journal of Applied Physics **111** (2012), 083108.

[145] P. B. Johnson and R. W. Christy, *Optical Constants of the Noble Metals*, Physical Review B **6** (1972), 4370.

[146] R. C. Johnson and R. E. Merrifield, *Effects of Magnetic Fields on the Mutual Annihilation of Triplet Excitons in Anthracene Crystals*, Physical Review B **1** (1970), 896.

[147] D. Jurbergs, E. Rogojina, L. Mangolini, and U. Kortshagen, *Silicon nanocrystals with ensemble quantum yields exceeding 60%*, Applied Physics Letters **88** (2006), 233116.

[148] A. Kanevce and W. K. Metzger, *The role of amorphous silicon and tunneling in heterojunction with intrinsic thin layer (HIT) solar cells*, Journal of Applied Physics **105** (2009), 094507.

[149] M. Kasha, *Energy Transfer Mechanisms and the Molecular Exciton Model for Molecular Aggregates*, Radiation Research **20** (1963), 55.

[150] M. Kasha, H. R. Rawls, and M. Ashraf El-Bayoumi, *The Exciton Model in Molecular Spectroscopy*, Pure and Applied Chemistry **11** (1965), 371.

[151] J. W. Keister, J. E. Rowe, J. J. Kolodziej, H. Niimi, T. E. Madey, and G. Lucovsky, *Band offsets for ultrathin SiO_2 and Si_3N_4 films on Si(111) and Si(100) from photoemission spectroscopy*, Journal of Vacuum Science and Technology B **17** (1999), 1831.

[152] W. Kern, *The Evolution of Silicon Wafer Cleaning Technology*, Journal of the Electrochemical Society **137** (1990), 1887.

[153] M. J. Kerr and A. Cuevas, *General parameterization of Auger recombination in crystalline silicon*, Journal of Applied Physics **91** (2002), 2473.

[154] M. J. Kerr and A. Cuevas, *Very low bulk and surface recombination in oxidized silicon wafers*, Semiconductor Science and Technology **17** (2002), 35.

[155] A. Köhler and H. Bassler, *What controls triplet exciton transfer in organic semiconductors?*, Journal of Materials Chemistry **21** (2011), 4003.

[156] Y. H. Kim, C. Sachse, M. L. Machala, C. May, L. Müller-Meskamp, and K. Leo, *Highly Conductive PEDOT:PSS Electrode with Optimized Solvent and Thermal Post-Treatment for ITO-Free Organic Solar Cells*, Advanced Functional Materials **21** (2011), 1076.

[157] N. Koch, A. Vollmer, and A. Elschner, *Influence of water on the work function of conducting poly(3,4-ethylenedioxythiophene)/poly(styrenesulfonate)*, Applied Physics Letters **90** (2007), 043512.

[158] M. Kochi, Y. Harada, T. Hirooka, and H. Inokuchi, *Photoemission from Organic Crystal in Vacuum Ultraviolet Region. IV*, Bulletin of the Chemical Society of Japan **43** (1970), 2690.

[159] L. Korte, *Die elektronische Struktur des amorph-kristallinen Silizium-Heterostruktur-Kontakts*, Ph.D. thesis, Philipps-Universität Marburg, 2006.

[160] L. Korte, A. Laades, K. Lauer, R. Stangl, D. Schaffarzik, and M. Schmidt, *Surface photovoltage investigation of recombination at the a-Si/c-Si heterojunction*, Thin Solid Films **517** (2009), 6396.

[161] L. Korte, A. Laades, and M. Schmidt, *Electronic states in a-Si:H/c-Si heterostructures*, Journal of Non-Crystalline Solids **352** (2006), 1217.

[162] L. Korte and M. Schmidt, *Investigation of gap states in phosphorous-doped ultra-thin a-Si:H by near-UV photoelectron spectroscopy*, Journal of Non-Crystalline Solids **354** (2008), 2138.

[163] L. Korte and M. Schmidt, *Doping type and thickness dependence of band offsets at the amorphous/crystalline silicon heterojunction*, Journal of Applied Physics **109** (2011), 063714.

[164] L. Kranz, C. Gretener, J. Perrenoud, R. Schmitt, F. Pianezzi, F. La Mattina, P. Blösch, E. Cheah, A. Chirila, C. M. Fella, H. Hagendorfer, T. Jäger, S. Nishiwaki, A. R. Uhl, S. Buecheler, and A. N. Tiwari, *Doping of polycrystalline CdTe for high-efficiency solar cells on flexible metal foil*, Nature Communications **4** (2013), 2306.

[165] M. V. Kurik, *Urbach rule*, physica status solidi (a) **8** (1971), 9.

[166] National Renewable Energy Laboratory, *Best Research-Cell Efficiencies*, published online, 01-01-2017.

[167] F. Lang, M. A. Gluba, S. Albrecht, J. Rappich, L. Korte, B. Rech, and N. H. Nickel, *Perovskite Solar Cells with Large-Area CVD-Graphene for Tandem Solar Cells*, The Journal of Physical Chemistry Letters **6** (2015), 2745.

[168] I. Lange, S. Reiter, M. Pätzel, A. Zykov, A. Nefedov, J. Hildebrandt, S. Hecht, S. Kowarik, C. Wöll, G. Heimel, and D. Neher, *Tuning the Work Function of Polar Zinc Oxide Surfaces using Modified Phosphonic Acid Self-Assembled Monolayers*, Advanced Functional Materials **24** (2014), 7014.

[169] Andreas Langner, Annegret Hauschild, Sonja Fahrenholz, and Moritz Sokolowski, *Structural properties of tetracene films on Ag(111) investigated by SPA-LEED and TPD*, Surface Science **574** (2005), 153.

[170] H. J. Leamy, *Charge collection scanning electron microscopy*, Journal of Applied Physics **53** (1982), R51.

[171] J. Lee, P. Jadhav, and M. A. Baldo, *High efficiency organic multilayer photodetectors based on singlet exciton fission*, Applied Physics Letters **95** (2009), 033301.

[172] J. Lee, P. Jadhav, P. D. Reusswig, S. R. Yost, N. J. Thompson, D. N. Congreve, E. Hontz, T. Van Voorhis, and M. A. Baldo, *Singlet Exciton Fission Photovoltaics*, Accounts of Chemical Research **46** (2013), 1300.

[173] C. Leendertz, N. Mingirulli, T. F. Schulze, J. P. Kleider, B. Rech, and L. Korte, *Discerning passivation mechanisms at a-Si:H/c-Si interfaces by means of photoconductance measurements*, Applied Physics Letters **98** (2011), 202108.

[174] C. Leendertz, R. Stangl, T. F. Schulze, M. Schmidt, and L. Korte, *A recombination model for a-Si:H/c-Si heterostructures*, physica status solidi (c) **7** (2010), 1005.

[175] M. A. Lieberman and A. J. Lichtenberg, *Principles of Plasma Discharges and Materials Processing*, Wiley, 2005.

[176] M. Liebhaber, M. Mews, L. Korte, T. F. Schulze, B. Rech, and K. Lips, *Valence band offset and hole transport across a-SiO_x (0<x<2) passivation layers in silicon heterojunction solar cells*, 31st European Photovoltaic Solar Energy Converence and Exhibition (2015), 770.

[177] M. Liebhaber, M. Mews, T. F. Schulze, L. Korte, B. Rech, and K. Lips, *Valence band offset in heterojunctions between crystalline silicon and amorphous silicon (sub)oxides (a-SiO_x:H, 0<x<2)*, Applied Physics Letters **106** (2015), 031601.

[178] D. Liu, Y. Zhang, X. Fang, F. Zhang, T. Song, and B. Sun, *An 11%-Power-Conversion-Efficiency Organic-Inorganic Hybrid Solar Cell Achieved by Facile Organic Passivation*, IEEE Electron Device Letters **34** (2013), 345.

[179] R. Liu, S.-T. Lee, and B. Sun, *13.8% Efficiency Hybrid Si/Organic Heterojunction Solar Cells with MoO_3 Film as Antireflection and Inversion Induced Layer*, Advanced Materials **26** (2014), 6007.

[180] S. Lombardo and S. U. Campisano, *Electrical and optical properties of semi-insulating polycrystalline silicon thin films: the role of microstructure and doping*, Materials Science and Engineering: R: Reports **17** (1996), 281.

[181] P. Löper, S.-J. Moon, S. Martin de Nicolas, B. Niesen, M. Ledinsky, S. Nicolay, J. Bailat, J.-H. Yum, S. De Wolf, and C. Ballif, *Organic–inorganic halide perovskite/crystalline silicon four-terminal tandem solar cells*, Physical Chemistry Chemical Physics **17** (2015), 1619.

[182] M. Lu, S. Bowden, U. Das, and R. Birkmire, *Interdigitated back contact silicon heterojunction solar cell and the effect of front surface passivation*, Applied Physics Letters **91** (2007), 063507.

[183] H. A. Macleod, *Thin-Film Optical Filters*, Taylor and Francis Group, 2010.

[184] M. S. Mahajan, D. M. Marathe, S. S. Ghosh, V. Ganesan, and J. V. Sali, *Changes in in-plane electrical conductivity of PEDOT:PSS thin films due to electric field induced dipolar reorientation*, Royal Society of Chemistry Advances **5** (2015), 86393.

[185] L. Mazzarella, S. Kirner, B. Stannowski, L. Korte, B. Rech, and R. Schlatmann, *p-type microcrystalline silicon oxide emitter for silicon heterojunction solar cells allowing current densities above 40 mA/cm^2*, Applied Physics Letters **106** (2015), 023902.

[186] H. Mäckel and A. Cuevas, *Determination of the surface recombination velocity of unpassivated silicon from spectral photoconductance measurements*, 3^{rd} World Conference on Photovoltaic Energy Conversion (2003), 71.

[187] D. P. McMeekin, G. Sadoughi, W. Rehman, . E. Eperon, M. Saliba, M. T. Hörantner, A. Haghighirad, N. Sakai, L. Korte, B. Rech, M. B. Johnston, L. M. Herz, and H. J. Snaith, *A mixed-cation lead mixed-halide perovskite absorber for tandem solar cells*, Science **351** (2016), 151.

[188] R. E. Merrifield, *Theory of Magnetic Field Effects on the Mutual Annihilation of Triplet Excitons*, The Journal of Chemical Physics **48** (1968), 4318.

[189] R. E. Merrifield, P. Avakian, and R. P. Groff, *Fission of singlet excitons into pairs of triplet excitons in tetracene crystals*, Chemical Physics Letters **3** (1969), 155.

[190] M. Mews, *Interfaces in amorphous/crystalline silicon heterojunction solar cells*, Ph.D. thesis, Technische Universität Berlin, 2016.

[191] M. Mews, L. Korte, and B. Rech, *Oxygen vacancies in tungsten oxide and their influence on tungsten oxide/silicon heterojunction solar cells*, Solar Energy Materials and Solar Cells **158** (2016), 77.

[192] M. Mews, C. Leendertz, M. Algasinger, S. Koynov, and L. Korte, *Amorphous/crystalline silicon heterojunction solar cells with black silicon texture*, physica status solidi RRL **8** (2014), 831.

[193] M. Mews, M. Liebhaber, B. Rech, and L. Korte, *Valence band alignment and hole transport in amorphous/crystalline silicon heterojunction solar cells*, Applied Physics Letters **107** (2015), 013902.

[194] M. Mews, T. F. Schulze, N. Mingirulli, and L. Korte, *Amorphous Silicon Passivation of Surfaces Promoting Epitaxy*, Energy Procedia **38** (2013), 855.

[195] O. V. Mikhnenko, P. W. M. Blom, and T.-Q. Nguyen, *Exciton diffusion in organic semiconductors*, Energy & Environmental Science **8** (2015), 1867.

[196] A. Mishra, R. K. Behera, P. K. Behera, B. K. Mishra, and G. B. Behera, *Cyanines during the 1990s: A Review*, Chemical Reviews **100** (2000), 1973.

[197] J. Mitchell, D. Macdonald, and A. Cuevas, *Thermal activation energy for the passivation of the n-type crystalline silicon surface by hydrogenated amorphous silicon*, Applied Physics Letters **94** (2009), 162102.

[198] A. Moldovan, F. Feldmann, G. Krugel, M. Zimmer, J. Rentsch, M. Hermle, A. Roth-Fölsch, K. Kaufmann, and C. Hagendorf, *Simple Cleaning and Conditioning of Silicon Surfaces with UV/Ozone Sources*, Energy Procedia **55** (2014), 834.

[199] A. Moldovan, F. Feldmann, M. Zimmer, J. Rentsch, J. Benick, and M. Hermle, *Tunnel oxide passivated carrier-selective contacts based on ultra-thin SiO_2 layers*, Solar Energy Materials and Solar Cells **142** (2015), 123.

[200] N. Monahan and X.-Y. Zhu, *Charge Transfer-Mediated Singlet Fission*, Annual Review of Physical Chemistry **66** (2015), 601.

[201] M. Morita, T. Ohmi, E. Hasegawa, M. Kawakami, and K. Suma, *Control factor of native oxide growth on silicon in air or in ultrapure water*, Applied Physics Letters **55** (1989), 562.

[202] K. A. Nagamatsu, S. Avasthi, J. Jhaveri, and J. C. Sturm, *A 12 % Efficient Silicon/PEDOT:PSS Heterojunction Solar Cell Fabricated at < 100 °C*, IEEE Journal of Photovoltaics **4** (2014), 260.

[203] K. A. Nagamatsu, S. Avasthi, G. Sahasrabudhe, G. Man, J. Jhaveri, A. H. Berg, J. Schwartz, A. Kahn, S. Wagner, and J. C. Sturm, *Titanium dioxide/silicon hole-blocking selective contact to enable double-heterojunction crystalline silicon-based solar cell*, Applied Physics Letters **106** (2015), 123906.

[204] R. K. Nahm and J. R. Engstrom, *Unexpected Effects of the Rate of Deposition on the Mode of Growth and Morphology of Thin Films of Tetracene Grown on SiO_2*, The Journal of Physical Chemistry C **120** (2016), 7183.

[205] H. Nohira, A. Omura, M. Katayama, and T. Hattori, *Valence band edge of ultra-thin silicon oxide near the interface*, Applied Surface Science **123** (1998), 546.

[206] S. Nold, N. Voigt, L. Friedrich, D. Weber, I. Hädrich, M. Mittag, H. Wirth, B. Thaidigsmann, I. Brucker, M. Hofmann, J. Rentsch, and R. Preu, *Cost Modeling of Silicon Solar Cell Production Innovation along the PV Value Chain*, 31st European Photovoltaic Solar Energy Converence and Exhibition (2012), 1084.

[207] A. J. Nozik, *Quantum dot solar cells*, Physica E **14** (2002), 115.

[208] A. J. Nozik, M. C. Beard, J. M. Luther, M. Law, R. J. Ellingson, and J. C. Johnson, *Semiconductor Quantum Dots and Quantum Dot Arrays and Applications of Multiple Exciton Generation to Third-Generation Photovoltaic Solar Cells*, Chemical Reviews **110** (2010), 6873.

[209] D. V. O´Connor and D. Phillips, *Time-correlated single photon counting*, Academic Press, London, 1984.

[210] National Institute of Standards and USA 2012 Technology: Gaithersburg, MD, *NIST database X-ray photoelectron spectroscopy database*, published online, 22-08-2016.

[211] K. Ohdaira, T. Oikawa, K. Higashimine, and H. Matsumura, *Suppression of the epitaxial growth of Si films in Si heterojunction solar cells by the formation of ultra-thin oxide layers*, Current Applied Physics **16** (2016), 1026.

[212] H. Ohigashi, I. Shirotani, H. Inokuchi, and S. Minomura, *Effect of Pressure on Davydov Splitting of Tetracene Crystals*, The Journal of Chemical Physics **43** (1965), 314.

[213] S. Olibet, E. Vallat-Sauvain, and C. Ballif, *Model for a-Si:H/c-Si interface recombination based on the amphoteric nature of silicon dangling bonds*, Physical Review B **76** (2007), 035326.

[214] L. Onsager, *Initial Recombination of Ions*, Physical Review **54** (1938), 554.

[215] M. R. Page, E. Iwaniczko, Y.-Q. Xu, L. Roybal, F. Hasoon, Q. Wang, and R. S. Crandall, *Amorphous/crystalline silicon heterojunction solar cells with varying i-layer thickness*, Thin Solid Films **519** (2011), 4527.

[216] A. Panda, C. K. Renshaw, A. Oskooi, K. Lee, and S. R. Forrest, *Excited state and charge dynamics of hybrid organic/inorganic heterojunctions. II. Experiment*, Physical Review B **90** (2014), 045303.

[217] A. K. Pandey, S. Dabos-Seignon, and J.-M. Nunzi, *Pentacene: PTCDI-$C_{13}H_{27}$ molecular blends efficiently harvest light for solar cell applications*, Applied Physics Letters **89** (2006), 113506.

[218] J. I. Pankove and M. L. Tarng, *Amorphous silicon as a passivant for crystalline silicon*, Applied Physics Letters **34** (1979), 156.

[219] J. Perrin, O. Leroy, and M. C. Bordage, *Cross-Sections, Rate Constants and Transport Coefficients in Silane Plasma Chemistry*, Contributions to Plasma Physics **36** (1996), 3.

[220] A. Petersen, A. Ojala, T. Kirchartz, T. A. Wagner, F. Würthner, and U. Rau, *Field-dependent exciton dissociation in organic heterojunction solar cells*, Physical Review B **85** (2012), 245208.

[221] L. A. A. Pettersson, F. Carlsson, O. Inganäs, and H. Arwin, *Spectroscopic ellipsometry studies of the optical properties of doped poly/3,4-ethylenedioxythiophene): an anisotropic metal*, Thin Solid Films **313-314** (1998), 356.

[222] L. A. A. Pettersson, S. Ghosh, and O. Inganäs, *Optical anisotropy in thin films of poly(3,4-ethylenedioxythiophene)-poly(4-styrenesulfonate)*, Organic Electronics **3** (2002), 143.

[223] P. Peumans, A. Yakimov, and S. R. Forrest, *Small molecular weight organic thin-film photodetectors and solar cells*, Journal of Applied Physics **93** (2003), 3693.

[224] F. Piersimoni, R. Schlesinger, J. Benduhn, D. Spoltore, S. Reiter, I. Lange, N. Koch, K. Vandewal, and D. Neher, *Charge Transfer Absorption and Emission at ZnO/Organic Interfaces*, The Journal of Physical Chemistry Letters **6** (2015), 500.

[225] M. Pietsch, M. Y. Bashouti, and S. Christiansen, *The Role of Hole Transport in Hybrid Inorganic/Organic Silicon/Poly(3,4-ethylenedioxy-thiophene):Poly(styrenesulfonate) Heterojunction Solar Cells*, The Journal of Physical Chemistry C **117** (2013), 9049.

[226] M. Pietsch, S. Jäckle, and S. Christiansen, *Interface investigation of planar hybrid n-Si/PEDOT:PSS solar cells with open circuit voltages up to 645 mV and efficiencies of 12.6 %*, Applied Physics A **115** (2014), 1109.

[227] G. B. Piland and C. J. Bardeen, *How Morphology Affects Singlet Fission in Crystalline Tetracene*, The Journal of Physical Chemistry Letters **6** (2015), 1841.

[228] G. B. Piland, J. J. Burdett, R. J. Dillon, and C. J. Bardeen, *Singlet Fission: From Coherences to Kinetics*, The Journal of Physical Chemistry Letters **5** (2014), 2312.

[229] G. B. Piland, J. J. Burdett, T.-Y. Hung, P.-H. Chen, C.-F. Lin, T.-L. Chiu, J.-H. Lee, and C. J. Bardeen, *Dynamics of molecular excitons near a semiconductor surface studied by fluorescence quenching of polycrystalline tetracene on silicon*, Chemical Physics Letters **601** (2014), 33.

[230] M. Pope and C. E. Swenberg, *Electronic Processes in Organic Crystals and Polymers*, Oxford University Press, New York, 1999.

[231] M. J. Powell and S. C. Deane, *Improved defect-pool model for charged defects in amorphous silicon*, Physical Review B **48** (1993), 10815.

[232] M. J. Price, J. M. Foley, R. A. May, and S. Maldonado, *Comparison of majority carrier charge transfer velocities at Si/polymer and Si/metal photovoltaic heterojunctions*, Applied Physics Letters **97** (2010), 083503.

[233] A. Pucci and G. Ruggeri, *Mechanochromic polymer blends*, Journal of Materials Chemistry **21** (2011), 8282.

[234] P. R. Pudasaini, M. Sharma, F. Ruiz-Zepeda, and A. A. Ayon, *Efficiency improvement of a nanostructured polymer solar cell employing atomic layer deposited Al_2O_3 as a passivation layer*, Microelectronic Engineering **119** (2014), 6.

[235] D. Pysch, C. Meinhardt, K. U. Ritzau, M. Bivour, K. Zimmermann, C. Schetter, M. Hermle, and S. W. Glunz, *Comparison of intrinsic amorphous silicon buffer layers for silicon heterojunction solar cells deposited with different PECVD techniques*, IEEE Journal of Photovoltaics (2010), 003570.

[236] P. Rahe, R. Lindner, M. Kittelmann, M. Nimmrich, and A. Kuhnle, *From dewetting to wetting molecular layers: C_{60} on $CaCO_3(1014)$ as a case study*, Physical Chemistry Chemical Physics **14** (2012), 6544.

[237] M. Rahmouni, A. Datta, P. Chatterjee, J. Damon-Lacoste, C. Ballif, and P. R. i Cabarrocas, *Carrier transport and sensitivity issues in heterojunction with intrinsic thin layer solar cells on N-type crystalline silicon: A computer simulation study*, Journal of Applied Physics **107** (2010), 054521.

[238] A. D. Rakić, J. M. Elazar, and A. B. Djurišić, *Acceptance-probability-controlled simulated annealing: A method for modeling the optical constants of solids*, Physical Review E **52** (1995), 6862.

[239] A. Rao, M. W. B. Wilson, J. M. Hodgkiss, S. Albert-Seifried, H. Bässler, and R. H. Friend, *Exciton Fission and Charge Generation via Triplet Excitons in Pentacene/C_{60} Bilayers*, Journal of the American Chemical Society **132** (2010), 12698.

[240] F. Reinert and S. Hüfner, *Photoemission spectroscopy–from early days to recent applications*, New Journal of Physics **7** (2005), 97.

[241] C. K. Renshaw and S. R. Forrest, *Excited state and charge dynamics of hybrid organic/inorganic heterojunctions. I. Theory*, Physical Review B **90** (2014), 045302.

[242] P. D. Reusswig, D. N. Congreve, N. J. Thompson, and M. A. Baldo, *Enhanced external quantum efficiency in an organic photovoltaic cell via singlet fission exciton sensitizer*, Applied Physics Letters **101** (2012), 113304.

[243] A. Richter, M. Hermle, and S. W. Glunz, *Reassessment of the Limiting Efficiency for Crystalline Silicon Solar Cells*, IEEE Journal of Photovoltaics **3** (2013), 1184.

[244] R. Rößler, C. Leendertz, L. Korte, N. Mingirulli, and B. Rech, *Impact of the transparent conductive oxide work function on injection-dependent a-Si:H/c-Si band bending and solar cell parameters*, Journal of Applied Physics **113** (2013), 144513.

[245] S. Sampat, A. D. Mohite, B. Crone, S. Tretiak, A. V. Malko, A. J. Taylor, and D. A. Yarotski, *Tunable Charge Transfer Dynamics at Tetracene/LiF/C_{60} Interfaces*, The Journal of Physical Chemistry C **119** (2015), 1286.

[246] R. Santbergen, A. H. M. Smets, and M. Zeman, *Optical model for multilayer structures with coherent, partly coherent and incoherent layers*, Optics Express **21** (2013), A262.

[247] F. Schaefers, M. Mertin, and M. Gorgoi, *KMC-1: A high resolution and high flux soft x-ray beamline at BESSY*, Review of Scientific Instruments **78** (2007), 123102.

[248] J. Schmidt, A. Merkle, R. Brendel, B. Hoex, M. C. M. van de Sanden, and W. M. M. Kessels, *Surface passivation of high-efficiency silicon solar cells by atomic-layer-deposited Al_2O_3*, Progress in Photovoltaics: Research and Applications **16** (2008), 461.

[249] J. Schmidt, V. Titova, and D. Zielke, *Organic-silicon heterojunction solar cells: Open-circuit voltage potential and stability*, Applied Physics Letters **103** (2013), 183901.

[250] J. Schmidt, D. Zielke, W. Lövenich, M. Hörteis, and A. Elschner, *Organic-Silicon Heterojunctions: a promising new concept for high-efficiency solar cells*, 6^{th} World Conference on Photovoltaic Energy Conversion (2014), 869.

[251] M. Schmidt, A. Schoepke, L. Korte, O. Milch, and W. Fuhs, *Density distribution of gap states in extremely thin a-Si:H layers on crystalline silicon wafers*, Journal of Non-Crystalline Solids **338** (2004), 211.

[252] G. D. Scholes, *Long-range resonance energy transfer in molecular systems*, Annual Review of Physical Chemistry **54** (2003), 57.

[253] G. D. Scholes and G. Rumbles, *Excitons in nanoscale systems*, nature materials **5** (2006), 683.

[254] J.-W. A. Schüttauf, K. H. M. van der Werf, I. M. Kielen, W. G. J. H. M. van Sark, J. K. Rath, and R. E. I. Schropp, *Excellent crystalline silicon surface passivation by amorphous silicon irrespective of the technique used for chemical vapor deposition*, Applied Physics Letters **98** (2011), 153514.

[255] T. F. Schulze, *Structural, electronic and transport properties of amorphous/crystalline silicon heterojunctions*, Ph.D. thesis, Technische Universität Berlin, 2011.

[256] T. F. Schulze, H. N. Beushausen, C. Leendertz, A. Dobrich, B. Rech, and L. Korte, *Interplay of amorphous silicon disorder and hydrogen content with interface defects in amorphous/crystalline silicon heterojunctions*, Applied Physics Letters **96** (2010), 252102.

[257] T. F. Schulze, L. Korte, and B. Rech, *Impact of a-Si:H hydrogen depth profiles on passivation properties in a-Si:H/c-Si heterojunctions*, Thin Solid Films **520** (2012), 4439.

[258] T. F. Schulze, L. Korte, F. Ruske, and B. Rech, *Band lineup in amorphous/crystalline silicon heterojunctions and the impact of hydrogen microstructure and topological disorder*, Physical Review B **83** (2011), 165314.

[259] T. F. Schulze and T. W. Schmidt, *Photochemical upconversion: present status and prospects for its application to solar energy conversion*, Energy & Environmental Science **8** (2015), 103.

[260] M. P. Seah and W. A. Dench, *Quantitative electron spectroscopy of surfaces: A standard data base for electron inelastic mean free paths in solids*, Surface and Interface Analysis **1** (1979), 2.

[261] M. Sebastiani, L. Di Gaspare, G. Capellini, C. Bittencourt, and F. Evangelisti, *Low-Energy Yield Spectroscopy as a Novel Technique for Determining Band Offsets: Application to the c-Si(100)/a-Si:H Heterostructure*, Physical Review Letters **75** (1995), 3352.

[262] J. P. Seif, A. Descoeudres, M. Filipič, F. Smole, M. Topič, Z. C. Holman, S. De Wolf, and C. Ballif, *Amorphous silicon oxide window layers for high-efficiency silicon heterojunction solar cells*, Journal of Applied Physics **115** (2014), 024502.

[263] O. E. Semonin, J. M. Luther, S. Choi, H.-Y. Chen, J. Gao, A. J. Nozik, and M. C. Beard, *Peak External Photocurrent Quantum Efficiency Exceeding 100% via MEG in a Quantum Dot Solar Cell*, Science **334** (2011), 1530.

[264] M. Shahidul Haque, H. A. Naseem, and W. D. Brown, *Interaction of aluminum with hydrogenated amorphous silicon at low temperatures*, Journal of Applied Physics **75** (1994), 3928.

[265] J. Shi and X. R. Qin, *Flux dependence of the morphology of a tetracene film on hydrogen-passivated Si(100)*, Physical Review B **73** (2006), 121303.

[266] D. A. Shirley, *High-resolution x-ray photoemission spectrum of the valence bands of gold*, Physical Review B **5** (1972), 4709.

[267] W. Shockley and H. J. Queisser, *Detailed Balance Limit of Efficiency of p-n Junction Solar Cells*, Journal of Applied Physics **32** (1961), 510.

[268] W. Shockley and W. T. Read, *Statistics of the Recombinations of Holes and Electrons*, Physical Review **87** (1952), 83.

[269] H. Shpaisman, O. Niitsoo, I. Lubomirsky, and D. Cahen, *Can up- and down-conversion and multi-exciton generation improve photovoltaics?*, Solar Energy Materials and Solar Cells **92** (2008), 1541.

[270] K. Siegbahn, *Electron Spectroscopy for Chemical Analysis, Atomic, Molecular and Solid State Structure Studies by Means of Electron Spectroscopy*, Almquist abd Wiksells, Uppsala, 1967.

[271] S. Singh, W. J. Jones, W. Siebrand, B. P. Stoicheff, and W. G. Schneider, *Laser Generation of Excitons and Fluorescence in Anthracene Crystals*, The Journal of Chemical Physics **42** (1965), 330.

[272] R. A. Sinton and A. Cuevas, *Contactless determination of current-voltage characteristics and minority-carrier lifetimes in semiconductors from quasi-steady-state photoconductance data*, Applied Physics Letters **69** (1996), 2510.

[273] _____, *A quasi-steady-state open-circuit voltage method for solar cell characterization*, 16th European Photovoltaic Solar Energy Converence (2000), 1.

[274] A. Smets, K. Jäger, O. Isabella, van Swaaij. R. A., and M. Zeman, *Solar energy: The physics and engineering of photovoltaic conversion, technologies and systems*, UIT Cambrige, England, 2016.

[275] G. C. Smith, *Surface Analysis by Electron Spectroscopy*, Plenum Press, New York, 1994.

[276] M. B. Smith and J. Michl, *Singlet Fission*, Chemical Reviews **110** (2010), 6891.

[277] M. B. Smith and J. Michl, *Recent Advances in Singlet Fission*, Annual Review of Physical Chemistry **64** (2013), 361.

[278] C. M. Soukoulis, M. H. Cohen, and E. N. Economou, *Exponential Band Tails in Random Systems*, Physical Review Letters **53** (1984), 616.

[279] B. Stegemann, K. M. Gad, P. Balamou, D. Sixtensson, D. Vössing, M. Kasemann, and H. Angermann, *Ultra-thin silicon oxide layers on crystalline silicon wafers: Comparison of advanced oxidation techniques with respect to chemically abrupt SiO_2/Si interfaces with low defect densities*, Applied Surface Science **395** (2017), 78.

[280] I. N. Stranski and L. Krastanov, *Zur Theorie der orientierten Ausscheidung von Ionenkristallen aufeinander*, Sitzungsberichte der Akadademie der Wissenschaften in Wien **146** (1938), 797.

[281] M. Stutzmann, *The defect density in amorphous silicon*, Philosophical Magazine Part B **60** (1989), 531.

[282] L. Sudha Devi, M. K. Al-Suti, C. Dosche, M. S. Khan, R. H. Friend, and Anna Köhler, *Triplet energy transfer in conjugated polymers. I. Experimental investigation of a weakly disordered compound*, Physical Review B **78** (2008), 045210.

[283] T. Sueyoshi, H. Kakuta, M. Ono, K. Sakamoto, S. Kera, and N. Ueno, *Band gap states of copper phthalocyanine thin films induced by nitrogen exposure*, Applied Physics Letters **96** (2010), 093303.

[284] Y. Sun, Z. Yang, P. Gao, J. He, X. Yang, J. Sheng, S. Wu, Y. Xiang, and J. Ye, *Si/PEDOT:PSS Hybrid Solar Cells with Advanced Antireflection and Back Surface Field Designs*, Nanoscale Research Letters **11** (2016), 1.

[285] A. Suna, *Kinematics of Exciton-Exciton Annihilation in Molecular Crystals*, Physical Review B **1** (1970), 1716.

[286] C. E. Swenberg and N. E. Geacintov, *Organic Molecular Photophysics*, John Wiley & Sons, Bristol, 1973.

[287] C. E. Swenberg and W. T. Stacy, *Bimolecular radiationless transitions in crystalline tetracene*, Chemical Physics Letters **2** (1968), 327.

[288] S. M. Sze and K. Ng. Kwok, *Physics of Semiconductor Devices*, John Wiley & Sons, Hoboken, New Jersey, 2007.

[289] M. Tabachnyk, B. Ehrler, S. Bayliss, R. H. Friend, and N. C. Greenham, *Triplet diffusion in singlet exciton fission sensitized pentacene solar cells*, Applied Physics Letters **103** (2013), 153302.

[290] M. Tabachnyk, B. Ehrler, S. Gelinas, M. L. Böhm, B. J. Walker, K. P. Musselman, N. C. Greenham, R. H. Friend, and A. Rao, *Resonant energy transfer of triplet excitons from pentacene to PbSe nanocrystals*, nature materials **13** (2014), 1033.

[291] M. Taguchi, K. Kawamoto, S. Tsuge, T. Baba, H. Sakata, M. Morizane, K. Uchihashi, N. Nakamura, S. Kiyama, and O. Oota, *HIT^{TM} Cells–High-Efficiency Crystalline Si Cells with Novel Structure*, Progress in Photovoltaics: Research and Applications **8** (2000), 503.

[292] M. Taguchi, A. Yano, S. Tohoda, K. Matsuyama, Y. Nakamura, T. Nishiwaki, K. Fujita, and E. Maruyama, *24.7% Record Efficiency HIT Solar Cell on Thin Silicon Wafer*, IEEE Journal of Photovoltaics **4** (2014), 96.

[293] Y. Tamai, H. Ohkita, H. Benten, and S. Ito, *Exciton Diffusion in Conjugated Polymers: From Fundamental Understanding to Improvement in Photovoltaic Conversion Efficiency*, The Journal of Physical Chemistry Letters **6** (2015), 3417.

[294] M. Tanaka, M. Taguchi, T. Matsuyama, T. Sawada, S. Tsuda, S. Nakano, H. Hanafusa, and Y. Kuwano, *Development of New a-Si/c-Si Heterojunction Solar Cells: ACJ-HIT (Artificially Constructed Junction-Heterojunction with Intrinsic Thin-Layer)*, Japanese Journal of Applied Physics **31** (1992), 3518.

[295] C. W. Tang, *Two-layer organic photovoltaic cell*, Applied Physics Letters **48** (1986), 183.

[296] S. Tanuma, C. J. Powell, and D. R. Penn, *Calculations of electron inelastic mean free paths*, Surface and Interface Analysis **37** (2005), 1.

[297] ———, *Calculations of electron inelastic mean free paths (QUASES-IMPF-TPP2M code, Version 2.2)*, Surface and Interface Analysis **37** (2005), 1.

[298] J. Tauc, R. Griborovici, and A. Vancu, *Optical Properties and Electronic Structure of Amorphous Germanium*, physica status solidi **15** (1966), 627.

[299] M. J. Y. Tayebjee, R. G. C. R. Clady, and T. W. Schmidt, *The exciton dynamics in tetracene thin films*, Physical Chemistry Chemical Physics **15** (2013), 14797.

[300] M. J. Y. Tayebjee, A. A. Gray-Weale, and T. W. Schmidt, *Thermodynamic Limit of Exciton Fission Solar Cell Efficiency*, The Journal of Physical Chemistry Letters **3** (2012), 2749.

[301] M. J. Y. Tayebjee, D. R. McCamey, and T. W. Schmidt, *Beyond Shockley-Queisser: Molecular Approaches to High-Efficiency Photovoltaics*, The Journal of Physical Chemistry Letters **6** (2015), 2367.

[302] M. J. Y. Tayebjee, A. Mahboubi Soufiani, and G. J. Conibeer, *Semi-Empirical Limiting Efficiency of Singlet-Fission-Capable Polyacene/Inorganic Hybrid Solar Cells*, The Journal of Physical Chemistry C **118** (2014), 2298.

[303] A. Tersigni, J. Shi, D. T. Jiang, and X. R. Qin, *Structure of tetracene films on hydrogen-passivated Si(001) studied via STM, AFM, and NEXAFS*, Physical Review B **74** (2006), 205326.

[304] N. J. Thompson, *Singlet Exciton Fission: Applications to Solar Energy Harvesting*, Ph.D. thesis, Massachusetts Institute of Technology, 2014.

[305] N. J. Thompson, D. N. Congreve, D. Goldberg, V. M. Menon, and M. A. Baldo, *Slow light enhanced singlet exciton fission solar cells with a 126% yield of electrons per photon*, Applied Physics Letters **103** (2013), 263302.

[306] N. J. Thompson, E. Hontz, D. N. Congreve, M. E. Bahlke, S. Reineke, T. Van Voorhis, and M. A. Baldo, *Nanostructured Singlet Fission Photovoltaics Subject to Triplet-Charge Annihilation*, Advanced Materials **26** (2014), 1366.

[307] N. J. Thompson, M. W. B. Wilson, D. N. Congreve, P. R. Brown, J. M. Scherer, T. S. Bischof, M. Wu, N. Geva, M. Welborn, T. Van Voorhis, V. Bulovic, M. G. Bawendi, and M. A. Baldo, *Energy harvesting of non-emissive triplet excitons in tetracene by emissive PbS nanocrystals*, nature materials **13** (2014), 1039.

[308] R. Thornagel, R. Klein, and G. Ulm, *The electron storage ring BESSY II as a primary source standard from the visible to the the X-ray range*, Metrologia **38** (2001), 385.

[309] D. Timmerman, J. Valenta, K. Dohnalova, W. D. A. M. de Boer, and T. Gregorkiewicz, *Step-like enhancement of luminescence quantum yield of silicon nanocrystals*, nature nanotechnology **6** (2011), 710.

[310] Y. Tomkiewicz, R. P. Groff, and P. Avakian, *Spectroscopic Approach to Energetics of Exciton Fission and Fusion in Tetracene Crystals*, The Journal of Chemical Physics **54** (1971), 4504.

[311] I. F. Torrente, K. J. Franke, and J. I. Pascual, *Spectroscopy of C_{60} single molecules: the role of screening on energy level alignment*, Journal of Physics: Condensed Matter **20** (2008), 184001.

[312] L. Tsetseris and S. T. Pantelides, *Atomic-scale mechanisms of selective adsorption and dimerization of pentacene on Si surfaces*, Applied Physics Letters **87** (2005), 233109.

[313] N. K. Unsworth, I. Hancox, C. Argent Dearden, P. Sullivan, M. Walker, R. S. Lilley, J. Sharp, and T. S. Jones, *Comparison of dimethyl sulfoxide treated highly conductive poly(3,4-ethylenedioxythiophene):poly(styrenesulfonate) electrodes for use in indium tin oxide-free organic electronic photovoltaic devices*, Organic Electronics **15** (2014), 2624.

[314] F. Urbach, *The Long-Wavelength Edge of Photographic Sensitivity and of the Electronic Absorption of Solids*, Physical Review **92** (1953), 1324.

[315] M. W. M. van Cleef, R. E. I. Schropp, and F. A. Rubinelli, *Significance of tunneling in p^+ amorphous silicon carbide n crystalline silicon heterojunction solar cells*, Applied Physics Letters **73** (1998), 2609.

[316] R. Varache, C. Leendertz, M. E. Gueunier-Farret, J. Haschke, D. Muñoz, and L. Korte, *Investigation of selective junctions using a newly developed tunnel current model for solar cell applications*, Solar Energy Materials and Solar Cells **141** (2015), 14.

[317] Y. P. Varshni, *Band-to-Band Radiative Recombination in Groups IV, VI, and III-V Semiconductors (I)*, physica status solidi (b) **19** (1967), 459.

[318] Y. Vaynzof, A. A. Bakulin, S. Gélinas, and R. H. Friend, *Direct Observation of Photoinduced Bound Charge-Pair States at an Organic-Inorganic Semiconductor Interface*, Physical Review Letters **108** (2012), 246605.

[319] A. Vollmer, O. D. Jurchescu, I. Arfaoui, I. Salzmann, T. T. M. Palstra, P. Rudolf, J. Niemax, J. Pflaum, J. P. Rabe, and N. Koch, *The effect of oxygen exposure on pentacene electronic structure*, The European Physical Journal E **17** (2005), 339.

[320] M. Volmer and A. Weber, *Keimbildung in übersättigten Gebilden*, Zeitschrift für Physikalische Chemie **119** (1926), 277.

[321] C. D. Wagner, L. E. Davis, M. V. Zeller, J. A. Taylor, R. H. Raymond, and L. H. Gale, *Empirical Atomic Sensitivity Factors for Quantitative Analysis by Electron Spectroscopy for Chemical Analysis*, Surface and Interface Analysis **3** (1981), 211.

[322] X. Wallart, C. Henry de Villeneuve, and P. Allongue, *Truly Quantitative XPS Characterization of Organic Monolayers on Silicon: Study of Alkyl and Alkoxy Monolayers on H-Si(111)*, Journal of the American Chemical Society **127** (2005), 7871.

[323] H. Wang, J. Wang, and Rusli, *Hybrid Si nanocones/PEDOT:PSS solar cell*, Nanoscale Research Letters **10** (2015), 1.

[324] F. Werner, B. Veith, V. Tiba, P. Poodt, F. Roozeboom, R. Brendel, and J. Schmidt, *Very low surface recombination velocities on p- and n-type c-Si by ultrafast spatial atomic layer deposition of aluminum oxide*, Applied Physics Letters **97** (2010), 162103.

[325] E. L. Williams, G. E. Jabbour, Q. Wang, S. E. Shaheen, D. S. Ginley, and E. A. Schiff, *Conducting polymer and hydrogenated amorphous silicon hybrid solar cells*, Applied Physics Letters **87** (2005), no. 22, 223504.

[326] M. Wimmer, M. Bär, D. Gerlach, R. G. Wilks, S. Scherf, C. Lupulescu, F. Ruske, R. Félix, J. Hüpkes, G. Gavrila, M. Gorgoi, K. Lips, W. Eberhardt, and B. Rech, *Hard x-ray photoelectron spectroscopy study of the buried Si/ZnO thin-film solar cell interface: Direct evidence for the formation of Si-O at the expense of Zn-O bonds*, Applied Physics Letters **99** (2011), 152104.

[327] P. Würfel, *Physics of Solar Cells: From Basic Principles to Advanced Concepts*, WILEY-VCH Verlag, Weinheim, 2009.

[328] T. C. Wu, N. J. Thompson, D. N. Congreve, E. Hontz, S. R. Yost, T. Van Voorhis, and M. A. Baldo, *Singlet fission efficiency in tetracene-based organic solar cells*, Applied Physics Letters **104** (2014), 193901.

[329] X. Wu, J. Liu, and G. He, *A highly conductive PEDOT:PSS film with the dipping treatment by hydroiodic acid as anode for organic light emitting diode*, Organic Electronics **22** (2015), 160.

[330] J. Wünsche, G. Tarabella, S. Bertolazzi, M. Bocoum, N. Coppede, L. Barba, G. Arrighetti, L. Lutterotti, S. Iannotta, F. Cicoira, and C. Santato, *The correlation between gate dielectric, film growth, and charge transport in organic thin film transistors: the case of vacuum-sublimed tetracene thin films*, Journal of Materials Chemistry C **1** (2013), 967.

[331] Y. Xia, K. Sun, and J. Ouyang, *Solution-Processed Metallic Conducting Polymer Films as Transparent Electrode of Optoelectronic Devices*, Advanced Materials **24** (2012), 2436.

[332] H. Xu, R. Chen, Q. Sun, W. Lai, Q. Su, W. Huang, and X. Liu, *Recent progress in metal-organic complexes for optoelectronic applications*, Chemical Society Reviews **43** (2014), 3259.

[333] H. Yan and H. Okuzaki, *Effect of solvent on PEDOT/PSS nanometer-scaled thin films: XPS and STEM/AFM studies*, Synthetic Metals **159** (2009), 2225.

[334] Y. Yan, M. Page, T. H. Wang, M. M. Al-Jassim, H. M. Branz, and Q. Wang, *Atomic structure and electronic properties of c-Si/a-Si:H heterointerfaces*, Applied Physics Letters **88** (2006), 121925.

[335] L. Yang, M. Tabachnyk, S. L. Bayliss, M. L. Böhm, K. Broch, N. C. Greenham, R. H. Friend, and B. Ehrler, *Solution-Processable Singlet Fission Photovoltaic Devices*, Nano Letters **15** (2015), 354.

[336] J. Yin, D. B. Migas, M. Panahandeh-Fard, S. Chen, Z. Wang, P. Lova, and C. Soci, *Charge Redistribution at GaAs/P3HT Heterointerfaces with Different Surface Polarity*, The Journal of Physical Chemistry Letters **4** (2013), 3303.

[337] S. Yoo, B. Domercq, and B. Kippelen, *Efficient thin-film organic solar cells based on pentacene/C_{60} heterojunctions*, Applied Physics Letters **85** (2004), 5427.

[338] K. Yoshikawa, *Crystalline silicon heterojunction solar cell exceeding 26% conversion efficiency*, Joint Foresight & HERCULES Workshop, talk, Berlin, 11-10-2016.

[339] P. Yu, C.-Y. Tsai, J.-K. Chang, C.-C. Lai, P.-H. Chen, Y.-C. Lai, P.-T. Tsai, M.-C. Li, H.-T. Pan, Y.-Y. Huang, C.-I. Wu, Y.-L. Chueh, S.-W. Chen, C.-H. Du, S.-F. Horng, and H.-F. Meng, *13% Efficiency Hybrid Organic/Silicon-Nanowire Heterojunction Solar Cell via Interface Engineering*, ACS Nano **7** (2013), 10780.

[340] D.-J. Yun, H. Ra, J. Kim, I. Hwang, J. Lee, S.-W. Rhee, and J. Chung, *Characterizing Annealing Effect of Poly (3,4-ethylenedioxythiophene) Polymerized with Poly (4-styrenesulfonate) Conjugated Film on the Molecular Arrangement and Work Function by Core-Level and Valence-Level Band Spectra*, ECS Journal of Science and Technology **1** (2012), M10.

[341] M. Zellmeier, S. Kühnapfel, B. Rech, N. H. Nickel, and J. Rappich, *Enhanced stability of P3HT/polycrystalline Si thin film hybrid solar cells*, physica status solidi (a) **213** (2016), 1904.

[342] D. Zhai, W. Xu, L. Zhang, and Y.-T. Chang, *The role of "disaggregation" in optical probe development*, Chemical Society Reviews **43** (2014), 2402.

[343] D. Zhang, D. Deligiannis, G. Papakonstantinou, R. A. C. M. M. van Swaaij, and M. Zeman, *Optical Enhancement of Silicon Heterojunction Solar Cells With Hydrogenated Amorphous Silicon Carbide Emitter*, IEEE Journal of Photovoltaics **4** (2014), 1326.

[344] F. Zhang, D. Liu, Y. Zhang, H. Wei, T. Song, and B. Sun, *Methyl/Allyl Monolayer on Silicon: Efficient Surface Passivation for Silicon-Conjugated Polymer Hybrid Solar Cell*, ACS Applied Materials & Interfaces **5** (2013), 4678.

[345] F. Zhang, B. Sun, T. Song, X. Zhu, and S. Lee, *Air Stable, Efficient Hybrid Photovoltaic Devices Based on Poly(3-hexylthiophene) and Silicon Nanostructures*, Chemistry of Materials **23** (2011), 2084.

[346] Y. Zhu, T. Song, F. Zhang, S.-T. Lee, and B. Sun, *Efficient organic-inorganic hybrid Schottky solar cell: The role of built-in potential*, Applied Physics Letters **102** (2013), 113504.

[347] D. Zielke, C. Niehaves, W. Lövenich, A. Elschner, M. Hörteis, and J. Schmidt, *Organic-silicon Solar Cells Exceeding 20% Efficiency*, Energy Procedia **77** (2015), 331.

[348] D. Zielke, A. Pazidis, F. Werner, and J. Schmidt, *Organic-silicon heterojunction solar cells on n-type silicon wafers: The BackPEDOT concept*, Solar Energy Materials and Solar Cells **131** (2014), 110.

[349] P. M. Zimmerman, Z. Zhang, and C. B. Musgrave, *Singlet fission in pentacene through multi-exciton quantum states*, nature chemistry **2** (2010), 648.

Publications

Paper publications

In the framework of this thesis

[1] M. Liebhaber, M. Mews, T. F. Schulze, L. Korte, B. Rech, and K. Lips, *Valence band offset in heterojunctions between crystalline silicon an amorphous silicon (sub)oxides (a-SiO_x, 0<x<2)*, Applied Physics Letters **106** (2015), 031601, http://dx.doi.org/10.1063/1.4906195.

[2] M. Mews, M. Liebhaber, B. Rech, and L. Korte, *Valence band alignment and hole transport in amorphous/crystalline silicon heterojunction solar cells*, Applied Physics Letters **107** (2015), 013902, http://dx.doi.org/10.1063/1.4926402.

[3] S. Jäckle, M. Mattiza, M. Liebhaber, G. Brönstrup, M. Rommel, K. Lips, and S. Christiansen, *Junction formation and current transport mechanisms in hybrid n-Si/PEDOT:PSS solar cells*, Scientific Reports **5** (2015), 13008, http://dx.doi.org/10.1038/srep13008.

[4] M. Liebhaber, M. Mews, L. Korte, T. F. Schulze, B. Rech, and K. Lips, *Valence band offset and hole transport across a-SiO_x (0<x<2) passivation layers in silicon heterojunction solar cells*, 31st European Photovoltaic Solar Energy Conference and Exhibition (2015), 770, http://dx.doi.org/10.4229/EUPVSEC20152015-2AV.3.26.

[5] S. Jäckle, M. Liebhaber, J. Niederhausen, M. Büchele, R. Félix, R. G. Wilks, M. Bär, K. Lips, and S. Christiansen, *Unveiling the hybrid n-Si/PEDOT:PSS interface*, ACS Applied Materials & Interfaces **8** (2016), 8841, http://dx.doi.org/10.1021/acsami.6b01596.

[6] S. Jäckle, M. Liebhaber, C. Gersmann, M. Mews, K. Jäger, S. Christiansen, and K. Lips, *Potential of PEDOT:PSS as a hole selective front contact for silicon heterojunction solar cells*, submitted to Scientific Reports (2017), http://arxiv.org/abs/1701.05368.

Not in the framework of this thesis

[1] M. Liebhaber, U. Bass, P. Bayersdorfer, J. Geurts, E. Speiser, J. Räthel, A. Baumann, S. Chandola, and N. Esser, *Surface phonons of the Si(111)-(7×7) reconstruction observed by Raman spectroscopy*, Physical Review B **89** (2014), 045313.

[2] M. Liebhaber, B. Halbig, U. Bass, J. Geurts, S. Neufeld, S. Sanna, and W. G. Schmidt, E. Speiser, J. Räthel, S. Chandola, and N. Esser, *Vibration Eigenmodes of the Au-(5×2)/Si(111) surface studied by Raman spectroscopy and first-principles calculations*, Physical Review B **94** (2016), 235304.

Conference, workshop & seminar contributions

(as 1st author)

[1] M. Liebhaber, *Analysis of a-SiO_x:H/c-Si hetero interfaces*, 5th Joint HZB-FZJ Workshop, Hirschegg, Kleinwalsertal, Austria (2014), **workshop talk**.

[2] M. Liebhaber, M. Mews, T. F. Schulze, L. Korte, and K. Lips, *Valence band offset in heterojunctions between crystalline silicon and amorphous silicon (sub)oxides*, DPG spring meeting, Berlin, Germany (2015), **conference talk**.

[3] M. Liebhaber, M. Mews, T. F. Schulze, L. Korte, B. Rech, and K. Lips, *Valence band offset and hole transport across crystalline silicon/amorphous silicon (sub)oxide heterojunctions* E-MRS Spring Meeting, Lille, France (2015), **conference talk**.

[4] M. Liebhaber, M. Mews, L. Korte, T. F. Schulze, B. Rech, and K. Lips, *Valence band offset and hole transport across a-SiO_x (0<x<2) passivation layers in silicon heterojunction solar cells*, EU PVSEC, Hamburg, Germany (2015), **conference poster**.

[5] M. Liebhaber, M. Mews, T. F. Schulze, B. Rech, L. Korte, and K. Lips, *Valence band offset an hole transport at the crystalline silicon/amorphous silicon suboxide heterojunction*, ICANS26, Aachen, Germany (2015), **conference talk**.

[6] M. Liebhaber, *3^{rd} generation Tetracene/c-Si hybrid solar cells – multi-exciton generation via singlet fission –*, HZB PhD seminar, Berlin, Germany (2015), **seminar talk**.

[7] M. Liebhaber, *High efficiency silicon heterojunction solar cells: From conventional concepts to a 3^{rd} generation bi-triplet exciton generating hybrid device*, SPREE Public Research Seminar, University of New South Wales, Sydney, Australia (2015), **invited public seminar talk**.

[8] M. Liebhaber, R. W. MacQueen, M. J. Y. Tayebjee, T. F. Schulze, J. Niederhausen, C. Gersmann, J. Behrends, T. W. Schmidt, and K. Lips, *Multi-exciton generation via Singlet Fission – In search of charge separation in Tetracene/c-Si hybrid solar cells*, QUANTSOL 2016, Rauris, Salzburg, Austria (2016), **workshop talk**.

[9] M. Liebhaber, R. W. MacQueen, M. J. Y. Tayebjee, T. F. Schulze, J. Niederhausen, C. Gersmann, T. W. Schmidt, and K. Lips, *Multi-exciton generation via Singlet Fission – In search of charge separation at Tetracene/c-Si hybrid devices*, ISPF^2, Gothenburg, Sweden (2016), **conference poster**.

[10] M. Liebhaber, *In search of charge separation in Tc/Si hybrid solar cells - device realization & interlayer development*, HZB PhD seminar, Berlin, Germany (2016), **seminar talk**.

Acknowledgments

The research presented in this thesis was carried out under the supervision of Prof. Dr. **Klaus Lips** (Institute for Nanospectroscopy) in assistance with Prof. Dr. **Bernd Rech**, Dr. **Lars Korte** and Dr. **Tim Schulze** (Institute for Silicon Photovoltaics), all from Helmholtz-Zentrum Berlin. Thank you for the constant guidance and support throughout this project, as well as for critical discussions, assistance in talk preparation, paper writing, and reading the thesis.

I particularly appreciate the delightful working atmosphere in the labs of the Institute for Silicon Photovoltaics. It was always a pleasure to work together and discuss (not only about physics) with all of you guys. At this point, I would also like to thank **Marion Krusche**, **Jutta Proszak** and **Andreas von Kozierowski** for their excellent and patient administration support.

Thanks to:

Klaus Lips for the excellent supervision throughout the whole PhD project. Thank you for your extremely helpful tips regarding presentations and publications, as well as for fruitful scientific discussions. Thanks for various parties at your home.

Lars Korte for your scientific support, cosy evenings at Ostkreutz bars and barbeque on the roof top, and for being the substitutional supervisor after the resignation of **Tim Schulze**. Thank you Tim for the great supervision during my first year and for inspiring me in the exciting singlet fission Tc/c-Si hybrid project.

Murad Tayebjee and **Rowan MacQueen** for the excellent DAAD co-operation with a wonderful stay at UNSW in Sydney/Australia. Thanks for your support regarding experiments and discussions on singlet fission dynamics. Thank you Rowan for your assistance in data analysis and interpretation, and for proof-reading my thesis.

Clemens Gersmann for your excellent work in the lab. It was always a pleasure to collaborate with you. Thanks for all the effort you put into the multi-exciton generating Tc/c-Si hybrid solar cell project. Parts of his Master's project also contributed to this work.

Florian Ruske for assistance in the analysis of ellipsometry data and **Klaus Jäger** for the realization of optical simulations.

The colleagues form HZB Wannsee, namely **Holger Kropf** for FIB preparations and SEM studies, **Markus Wollgarten** for TEM analysis, and **Klaus Schwarzburg** for TCSPC measurements. The results obtained in your labs generated significant scientific added value.

Andreas Popp for monochromized XPS measurements and **Jens Niederhausen** for UPS measurements and HIKE/SurICat beamtime collaboration. Thank you Jens for fruitful discussions

regarding tricky organic-inorganic hybrid interfaces. Thanks to **David Eisenhauer** for AFM images.

The **"Glovebox crew"** of EE-IS (Matthias, Felix, Oleksandra, Steve, Moritz, Marko, Eva, Lukas, Clemens...). We are all sitting in the same boat, "fighting" for spin-coating and evaporation time, and struggling with gross motor skills and perspiration in the gloves. However, finally all our samples degrade quite quickly.

Marcus Bär's **"HIKE crew"** for giving us the opportunity to perform various HAXPES test measurements during commissioning time. Thanks for your assistance in HAXPES data analysis and interpretation.

All **technicians of EE-IS and PVcomB**. Your experimental assistance really pushes and facilitates research. At this point, I would especially like to to appreciate the competent and always very fast technical support by **Thomas Lußky**.

HZB "Energy Converter" runners group for extreme fun at various team relay races and the Cross fit obstacle run.

Special thanks to:

Paul Sonntag for the best conference trip including couchsurfing, Orval and Crevette. Thank you for exploring and hanging out with you in Berlin, thank you for organizing delicious beer tests.

Sara Jäckle and **Mathias Mews** being the best co-operation partners I can imagine. We generated quite a lot of scientific output. But also thanks for unforgettable bike tour/accident experiences, board game parties, looong night shifts at HIKE, and the legendary user meeting at BESSY.

Mein ganz besonderer Dank gilt schließlich **all meinen Freunden und Familie** für die Unterstützung in all den Jahren meines Studiums. Ohne euch, **Eve, Alex, Richi und Shizzle** wäre die Phase des Zusammenschreibens schwieriger gewesen. Ihr seid die besten!

Selbstständigkeitserklärung

gemäß § 7, Abs. 4 der Promotionsordnung
des Fachbereichs Physik
der Freien Universität Berlin
(Amtsblatt 34/2013, 2. September 2013)

Hiermit versichere ich alle Hilfsmittel und Hilfen angegeben zu haben, auf deren Grundlagen die Arbeit selbstständig verfasst wurde.

Die vorliegende Arbeit wurde nicht in einem früheren Promotionsverfahren angenommen oder als ungenügend beurteilt.

Berlin, den

.....
(Martin Liebhaber)